



MSc Thesis – Space Engineering

AOTF – Development and Validation of a 3D Optical Simulation Model

Aleksandr Pavlov (5003458)

Supervisor: Dr. ir. Jurgen A.M. Vanhamel

Page left blank intentionally.

DELFT UNIVERSITY OF TECHNOLOGY
FACULTY OF AEROSPACE ENGINEERING
AE5822
THESIS SPACE

Master Thesis

Development and validation of a 3D optical simulation model for the
Acousto-Optic Tunable Filter (AOTF)

by

Aleksandr Pavlov

to obtain the degree of Master of Science
at the Delft University of Technology,
to be defended on Thursday, November 28th, 2024, at 14:00.

Student number:	5003458	
Institution:	Delft University of Technology	
Faculty:	Faculty of Aerospace Engineering, Delft	
Thesis committee:	Dr. ir. J.A.M. Vanhamel,	TU Delft, Daily Supervisor
	Dr. ir. J. Bouwmeester,	TU Delft, Committee Chair
	Dr. ir. B.R. Brandl,	TU Delft, Examiner
	Dr. ir. N. Bhattacharya,	TU Delft, Additional Member

An electronic version of this thesis is available at <http://repository.tudelft.nl/>.



Page left blank intentionally.

Preface

This thesis has been one of the most challenging tasks I have tackled as an Aerospace Engineering student. The challenge came not only from diving into a completely new field of Acousto-Optics, but also from the project's sheer size—and my own perfectionism sometimes getting in the way. But where there is a challenge, there is growth, and I can honestly say I have learned a lot during this process. I enjoyed the learning, especially when things came together in developing my analytical model, and by the end, I felt truly pleased with what I was able to accomplish.

I wanted to thank my supervisor, Jurgen Vanhamel, for guiding me through this project, helping me structure my thoughts on AOTF, and supporting me when things got overwhelming. It was a great opportunity for me to work with optical hardware and to create something new in the academic world.

I want to extend my gratitude to the friends I have made over the past five years at TU Delft: The 2D Bois, Systems Eng. Fan club, Torius, my roommates, and many more. I am lucky to have so many ambitious and supportive friends who joined me on this unforgettable university journey. Thank you all for supporting me through the tough times, helping me improve in every aspect, and, most importantly, making my university life fun and memorable. Without you, I would not have made it this far.

Finally, I want to thank my family for supporting me throughout my university journey. Even from afar, you were always there for me, cheering me on and making sure I stayed on the right path. Your encouragement and guidance meant everything to me, and I could not have achieved this much without you.

*Aleksandr Pavlov
Delft, November 2024*

Table of Contents

Table of Contents	i
List of Figures	iv
List of Tables	vii
List of Symbols and Abbreviations	ix
Abstract	xiii
1 Introduction	1
1.1 Acousto-Optic Tunable Filter	1
1.2 Applicability of AOTF in space missions	2
1.3 Motivation to study AOTF simulation	2
1.4 Thesis structure	3
2 AOTF Theory	4
2.1 AOTF materials	4
2.2 AOTF configurations	5
2.3 Configuration and material choice for the AOTF simulation	6
2.4 Crystallographic axis and ray diffraction of TeO ₂	7
2.4.1 Definition of polarization states	9
2.4.2 Crystallographic planes	10
2.5 Optical properties of Tellurium Dioxide	11
2.6 AO interaction and momentum-matching condition	12
2.6.1 Factors affecting the tuning frequency	14
2.6.2 Eigenmode polarization state changes during AO interaction	17
2.7 Optical activity and gyration	18
2.7.1 Rotatory Power	18
2.7.2 Gyration tensor and relation in the crystallographic axis	21
2.7.3 Impact of polarization change on refractive indices	22
2.7.4 Conclusion on rotatory power	24
2.8 Electrical components	25
2.8.1 Electrical setup overview	25
2.8.2 VSWR and transducer bandwidth	26
3 Research Description	27
3.1 Research objective/question	27
3.2 Requirements for analytical model and testing	28
4 AOTF analytical model description	30
4.1 Rotational matrices	30
4.2 Notations and the Three surface model	32
4.2.1 Directional cosine matrix	32
4.2.2 Three surface model and key crystal angles definitions	33
4.2.3 Variable notation for the analytical model	34
4.2.4 Stage and ray terminologies	35
4.3 Analytical Model	36

4.3.1	Entrance ray definition	37
4.3.2	First surface - Entering Crystal's medium	39
4.3.3	Second surface - the AO interaction	42
4.3.4	Third surface - Exit AOTF facet	45
4.4	Extraordinary ray simulation	48
4.4.1	E-ray surface interactions	49
4.4.2	E-ray AO interaction	50
4.5	AOTF rotation	51
4.5.1	Surface rotations	52
4.5.2	Crystallographic axis rotation	54
4.6	Ray propagation visualisation and verification	55
4.7	Conclusion on the analytical model	57
5	Simulation verification	59
5.1	Experimental results	59
5.2	Analytical model results	60
5.3	Conclusion and results evaluation	61
6	Testing methodology for AOTF and geometry analysis	63
6.1	AOTF's allowed frequency range	63
6.2	AOTF geometrical dimension calculations	65
6.3	Setup description	68
6.3.1	Setup components	68
6.3.2	Setup alignment procedure	70
6.3.3	Polarisation classification	73
6.4	Diffraction testing procedure	73
6.5	Power testing procedure	77
6.6	Conclusion	79
7	Model validation — experimental results	81
7.1	Power testing validation	81
7.1.1	Incident e-ray power test	81
7.1.2	Incident o-ray power test	83
7.2	Crystallographic axis identification	85
7.2.1	Incident e-ray frequency-matching	85
7.2.2	Incident o-ray frequency-matching	86
7.2.3	Conclusion on AOTF characterisation method	87
7.3	Diffraction test validation	87
7.3.1	Incident e-ray diffraction test results	88
7.3.2	Incident o-ray diffraction test results	89
7.3.3	Model's evaluation and result discrepancies	91
7.4	AOTF's rotatory power influence	91
7.5	Model validation and experimental results conclusion	93
8	Model optimisation and AOTF characterisation	95
8.1	Procedure and Brimrose AOTF schematics	95
8.2	Solution with optimisation	97
8.2.1	Optimisation algorithm choice	98
8.2.2	Objective function and bounds selection	99
8.3	Evaluation of the optimisation results	100
8.4	Conclusion on optimisation	103
9	Conclusion	104
10	Recommendations and Future Works	106

10.1 Analytical model based recommendations	106
10.1.1 Change in coordinate system	106
10.1.2 Multiple transducers AOTF designs	106
10.1.3 Model adaptation for other AOTF types and materials	106
10.1.4 Far-off axis simulation attempt	107
10.2 Test related recommendations	108
10.2.1 Test setup recommendations	108
10.2.2 Test analysis recommendations	108
References	110
A Derivation of refractive index with gyration tensor (G)	I
B Diffraction testing raw data	II
B.1 Incident e-ray diffraction test	II
B.2 Incident o-ray diffraction test	III
C Power testing raw data	IV
C.1 Power tests - bright setting	IV
C.2 Power tests - Dark room setting	IV
C.3 Optical lab - horizontal polarization power test	V
C.4 Optical lab - vertical polarization power test	VI
D Samuel Verification results	VII
D.1 Experimental Results	VII
D.2 Analytical Model Results E-ray	VII
E Brimrose tests for AOTF characterisation	VIII

List of Figures

1.1	Principle of work of an AO device.	1
1.2	A working principle illustration of the AOTF - adapted from [8].	2
2.1	Non-collinear AOTF working with the polarized light [7].	5
2.2	A working principle illustration of the collinear AOTF with incident polarized light [7].	5
2.3	Non-collinear TeO ₂ based AOTF top view schematic for e-ray diffraction with the addition of crystallographic axes.	7
2.4	3D view of the AOTF diffraction and polarization of light beams	8
2.5	Non-collinear TeO ₂ based AOTF top view schematic for o-ray diffraction with the addition of crystallographic axes.	8
2.6	Polarization visualization [19].	9
2.7	(a) Linearly polarized light (b) Oscillating field diagram showing the intensity and direction of the overall electric field vector [18].	10
2.8	Crystallographic axis of AOTF, according to [22].	11
2.9	Variation of the ordinary and extraordinary refractive indices with optical wavelength for TeO ₂ [23].	11
2.10	Variation of birefringence with optical wavelength for TeO ₂ [23].	12
2.11	AO interaction schematic inside the AOTF crystal -adapted from [10].	13
2.12	Wave vector diagram of the momentum-(mis)matching conditions in TeO ₂ . The incident (\mathbf{k}_i) and diffracted (\mathbf{k}_d) light waves, and the acoustic (\mathbf{k}_a) wave are represented.	14
2.13	Tuning curve with varying wavelength for an AOTF based on TeO ₂ [27].	15
2.14	Experimental results for tuning frequency for peak diffraction in relation with the varying angle of incidence for ordinary and extraordinary polarized rays [26].	16
2.15	Frequency dependence on the cut angle α and the incident angle, in case of the Bragg diffraction in the TeO ₂ crystal for 633nm optical wavelength [28].	16
2.16	Eigenmode polarization state changes in birefringent AO interaction [15]	18
2.17	Rotatory power effect with a sample [35].	19
2.18	Power Law relation based on the experimental data from the experiment done by Uchida (1971) [23].	20
2.19	(a) Rotation of the plane polarization in the optically active medium, where the right circularly polarized wave rotates faster $n_r < n_l$. (b) if the wave from (a) is reflected back to the medium, the plane of polarization rotates in the opposite direction. [39]	20
2.20	Rotatory power relation with a variable angle away from the optical axis [001].	22
2.21	New refractive indices ellipses based on Voloshinov/Fresnel's relations shown in colours (solid lines for Voloshinov and dashed lines for Fresnel), and relations by Gass are shown in black.	23
2.22	The difference in refractive index for extraordinary ray between Voloshinov and Gass (in green), and between Fresnel and Gass (in Red)	24
2.23	Electrical setup preceding the AOTF	25
2.24	Piezoelectric transducer with impedance matching, adapted from [4].	26
4.1	Effect of the rotational matrix around X-axis in (a) axis system view and (b) vector view.	31
4.2	Effect of the rotational matrix around Y-axis in (a) axis system view and (b) vector view.	32
4.3	Representation of the ray vector orientation with respect to DCM angles, adapted from [49].	33
4.4	Main AOTF surfaces and variables used, also the positioning of the global (black) and crystallographic (blue) coordinate systems in the AOTF.	34
4.5	Stages and substages of ray propagation in the AOTF model, showing ordinary (blue) and extraordinary (green) rays with key AOTF angles and directions labeled.	36
4.6	Base equation of the initial ray propagating along the optical axis.	37
4.7	Steering the initial ray by θ_0 in the YZ -plane.	38
4.8	Steering the initial ray by ϕ_0 in the XZ -plane.	38

4.9	Closer view of stage one, involving the rays and substages involved in the model.	39
4.10	Snell's law at the entrance facet schematic.	40
4.11	(a) Initial ray depiction and (b) coordinate system transformation for the intermediate stage a . . .	40
4.12	(c) Application of the Snell's law and (d) transformation back to the global coordinate system. . .	41
4.13	Closer view of stage two, involving the rays and substages involved in the model.	42
4.14	Two-dimensional wave vector diagram during the AO interaction in O-XY'Z' axis system - adapted from [47].	43
4.15	Wave vector diagram during the AO interaction in O-XY'Z' axis system	44
4.16	Closer view of stage three, involving the rays and substages involved in the model.	46
4.17	Snell's law at the third surface schematic.	46
4.18	Coordinate system transformation at the substage \mathbf{u}_{3g}	47
4.19	Coordinate system transformation at the substage \mathbf{u}_{3h} and the ray \mathbf{r}_3	47
4.20	Wave vector diagram for the extraordinary polarization AO interaction.	50
4.21	AOTF angles with the moved crystallographic axis system.	51
4.22	Rotated AOTF by an angle ζ_{rot} clockwise.	52
4.23	Snell's law at the entrance facet schematic, including the ζ_{rot} rotation.	52
4.24	(a) New initial ray depiction and (b) coordinate system transformation for the intermediate stage a with angle ζ_{rot} included.	53
4.25	(c) Application of Snell's law on the ray with a larger normal angle, and (d) transformation back to the global coordinate system.	54
4.26	AO interaction to verify the results with the results from Voloshinov (2007), $\beta=0^\circ$, and $\gamma=0^\circ$	56
4.27	Ray propagations throughout the crystal with a 700nm laser input angle of 0 degrees, $\beta=0^\circ$, and $\gamma=0^\circ$	57
5.1	AOTF variables for the test conducted at UPHF.	59
6.1	The SWR over Frequency graph for the AA opto-electronics AOTF (AA.AOTF.4C 284–97.07) . .	64
6.2	The SWR over Frequency graph for the Brimrose AOTF (TEAF10-55-1.0-MSD)	64
6.3	AOTF being analysed in image analysis software — Tracker [63].	66
6.4	AOTF length dimensions obtained from the image analysis.	66
6.5	AOTF angles obtained from the image analysis.	67
6.6	Comparison between initial and revised identification of the β angle.	68
6.7	Experimental setup schematic for the power testing for the incident e-ray.	69
6.8	Experimental setup schematic for the incident e-ray diffraction test.	69
6.9	Iris Diaphragm and elliptical incident laser profile	70
6.10	Laser alignment along the optical axis.	71
6.11	Notation used for the positioning of the beams at the ruler	72
6.12	Adjusting AOTF to be perpendicular to the optical axis.	72
6.13	Global coordinate system with the setup used	73
6.14	Experimental setup schematic for the incident o-ray diffraction test.	74
6.15	Ray separation by birefringence into ordinary and extraordinary rays, sending a horizontally polarized light (e-ray).	75
6.16	Top view of an AOTF diffraction at 0 degrees of rotation.	76
6.17	Top view of an AOTF when rotation by an angle ζ_{rot} is introduced, changing a reference point (Y_{0n}) for the angle calculation.	77
6.18	Experimental setup schematic for the incident o-ray power test.	78
6.19	Optical setup for the power testing.	79
7.1	Zoomed-in VSWR curve for the AA Opto-Electronics AOTF, focusing on 90-110 MHz range and highlighting the unobstructed ray region during e-ray power test.	83
7.2	Zoomed-in VSWR curve for the AA Opto-Electronics AOTF, focusing on 90-110 MHz range and highlighting the unobstructed ray region during o-ray power test.	84
7.3	Frequency tuning over rotational angle matching curves for incident e-ray.	86
7.4	Frequency tuning over rotational angle matching curves for incident o-ray.	87

7.5	Diffracted angles (θ_{3o}) as a function of rotational angle for e-ray diffraction test.	88
7.6	Undiffracted angles (θ_{3e}) as a function of rotational angle for e-ray diffraction test.	89
7.7	Diffracted angles (θ_{3e}) as a function of rotational angle for o-ray diffraction test.	90
7.8	Undiffracted angles (θ_{3o}) as a function of rotational angle for o-ray diffraction test.	90
7.9	Polarization rotation experiment.	92
7.10	AA opto-electronics AOTF polarization angle change	93
8.1	Brimrose Entrance View	96
8.2	Brimrose Exit View	96
8.3	Physical pictures of the Brimrose TEAF10-0.55-1.0-MSD AOTF	96
8.4	Brimrose AOTF diffraction when a vertically polarised light is shone onto the AOTF.	96
8.5	Top view schematic of the AOTF crystal in the experimental setup.	97
8.6	AOTF inverted along the z-axis	97
8.7	Simplified multimodal example where finding global minimum is challenging for Newton methods — adapted from [73]	99
8.8	Momentum-matching frequencies as a function of AOTF rotational angle for the o-ray diffraction test on the Brimrose AOTF.	101
8.9	Undiffracted ray angles (θ_{3o}) as a function of AOTF rotational angle for the o-ray diffraction test on the Brimrose AOTF.	102
8.10	Diffracted ray angles (θ_{3e}) as a function of AOTF rotational angle for the o-ray diffraction test on the Brimrose AOTF.	102
10.1	Comparison of on-axis and off-axis AO interaction in the AOTF with $\alpha = 10^\circ$, $\zeta_{rot} = 0^\circ$	107
10.2	Example of (a) Close to the optical axis AO interaction and (b) Far-off axis AO interaction [51].	107

List of Tables

2.1	Properties of the AO materials [7].	5
4.1	Definitions of key variables used in the analytical model.	35
4.2	Examples of variable notation in the model.	35
4.3	Stages of AOTF Surface Simulation	36
4.4	First Stage Simulation: Sub-stage Notation and Transformations	42
4.5	Second Stage Simulation: Sub-stage Notation and Transformations	45
4.6	Substage Notation and Transformations for o-ray	48
4.7	Substage Notation and Transformations for e-ray	48
4.8	Substage Notation and Transformations for Incident e-ray	49
4.9	AOTF parameter inputs from Voloshinov et al. paper [53]	55
4.10	AOTF parameter outputs from Voloshinov et al. paper [53]	55
4.11	Comparison of AOTF parameter outputs from Voloshinov et al. [53] and the analytical model	56
5.1	Experimental Results for AOTF diffraction at different wavelengths, conducted at UPHF.	60
5.2	Input Parameters for the Analytical Model	60
5.3	Separation Angle Comparison Table	61
5.4	Frequency Difference Comparison Table	61
6.1	Test Requirements and Achievements	80
7.1	Optical Lab Testing incident e-ray - Coarse Power Testing	82
7.2	Optical Lab Testing incident e-ray - Fine Power Testing	82
7.3	Vertical Polarization Testing - Coarse Results	84
7.4	Comparison of e-ray and o-ray test results (Maximum DE, Tuning Frequency, and SWR)	84
7.5	Comparison between e-ray and o-ray coarse testing results (Rotational Angle, RF Signal, and DE)	85
7.6	Methods summary to characterise θ_c and α angles for e-ray and o-ray incident cases.	87
7.7	Bounds of differences for diffracted and undiffracted angles	91
7.8	Polarizer rotation and intensity power measurements for horizontally polarized incident light	92
7.9	Polarizer rotation and intensity power measurements for vertically polarized incident light	92
7.10	Validation Requirements and Achievements	94
8.1	Brimrose AOTF Specifications	95
8.2	optimisation Variables and Their Bounds	100
8.3	Brimrose AOTF Optimised Parameters	100
8.4	characterisation Requirements and Achievements	103
9.1	Brimrose AOTF Optimised Parameters	105
B.1	Reference parameters for the AA opto-electronics for the incidence e-ray diffraction testing	II
B.2	Diffraction Test — incident e-ray raw data	II
B.3	Reference parameters for the AA opto-electronics for the incidence o-ray diffraction testing	III
B.4	Diffraction Test — incident o-ray raw data	III
C.1	Power Testing Results - Part 1	IV
C.2	Power Testing Results - Part 2	IV
C.3	Power Testing Results in Dark Room - Coarse search	V
C.4	Power Testing Results in Dark Room - Fine Search	V
C.5	Optical Lab Testing incident e-ray - Coarse Power Testing	V

C.6	Optical Lab Testing incident e-ray - Fine Power Testing	V
C.7	Vertical Polarization Testing - Coarse Results	VI
D.1	Experimental Results	VII
D.2	Simulation Results - e-ray	VII
D.3	Simulation Results - e-ray gyration no adaptation (Uchida)	VII
D.4	Simulation Results - e-ray gyration adaptation	VII
E.1	Reference parameters used for the Brimrose diffraction testing	VIII
E.2	Incident o-ray Brimrose Diffraction Testing	VIII

List of Symbols and Abbreviations

- 3D** - Three dimensional
- AODs** - Acousto-Optic Deflectors
- AOMs** - Acousto-Optic Modulators
- AOTF** - Acousto-Optic Tunable Filter
- AO** - Acousto-Optic
- CO₂** - Carbon Dioxide
- COTS** - Commercial-Off-The-Shelf
- CO** - Carbon Monoxide
- CubeSats** - Miniaturized Satellites
- DCM** - Directional Cosine Matrix
- DE** - Diffraction efficiency
- EM** - Electromagnetic
- FoV** - Field of View
- FWHM** - Full Width at Half Maximum
- Hg₂Cl₂** - Mercurous chloride
- IR** - Infrared
- KDP** - Potassium Dihydrogen Phosphate (KH₂PO₄)
- L-BFGS-B** Limited-memory Broyden-Fletcher-Goldfarb-Shanno algorithm, with box constraints
- NIR** - Near-Infrared
- NO₂** - Nitrogen Dioxide
- RF** - Radio Frequency
- TeO₂** - Tellurium Dioxide
- Tl₃AsSe₃** - Thallium Arsenic Selenide
- UPHF** - Université Polytechnique Hauts-de-France
- UV** - Ultraviolet
- VIS** - Visible Spectrum
- VNA** Vector Network Analyser

VSWR Voltage Standing Wave Ratio

α	Tilt-angle between the [110] axis and the transducer's positioning	degrees
β	AOTF's exit facet inclination angle	degrees
$\delta\theta_2$	Separation angle inside the AOTF's crystal	degrees
$\delta\theta_3$	Separation angle at the AOTF's exit facet	degrees
Δn	Birefringence	-
$\Delta\lambda$	Bandpass from the Central Wavelength	nm
ϵ	Material's permittivity	F/m
ϵ_{rot}	Estimated shift of the new reference point on the optical axis	mm
γ	AOTF's entrance facet inclination angle	degrees
λ	Optical Wavelength	nm
\mathbf{k}_d	Diffracted wave vector	m^{-1}
\mathbf{k}_i	Incident wave vector	m^{-1}
\mathbf{k}_{2c}	Substage representig an incident wave vector at the second surface	-
\mathbf{k}_{2d}	Substage representig a diffracted wave vector at the second surface	-
\mathbf{r}_{0e}	Initial incident ray at stage 0 (extraordinarily polarized)	-
\mathbf{r}_{0o}	Initial incident ray at stage 0 (ordinarily polarized)	-
\mathbf{r}_1	Ray exiting entrance facet surface (surface 1)	-
\mathbf{u}_{1a}	Substage expressing the ray relative to the entrance surface inclination	-
\mathbf{u}_{1b}	Substage after applying the Snell's law at the entrance surface	-
ω	Angular frequency of the wave	rad/s
ρ	Rotatory power	degrees/mm
ρ_{mat}	AO material's mass density	kg/m^3
θ'_c	Effective crystallographic axis angle	degrees
θ_c	Crystallographic axis angle	degrees
θ_i	Incidence angle	degrees
θ_s	Separation angle	degrees
θ_{3e}	Output angle for the extraordinary ray	degrees
θ_{3o}	Output angle for the ordinary ray	degrees
ξ	Angle between AOTF's bottom surface and optical axis	degrees
ζ_{rot}	AOTF's rotation angle	degrees
E_x	Amplitude of light's electromagnetic wave in the x-direction	V/m

E_y	Amplitude of light's electromagnetic wave in the y-direction	V/m
E_{diff}	Error for diffracted angles	-
E_{freq}	Error for momentum-matching frequency	-
E_{inc}	Incident voltage	V
E_{max}	Maximum voltage wave	V
E_{min}	Minimum voltage wave	V
E_{ref}	Reflected voltage	V
E_{total}	Total error	-
E_{undiff}	Error for undiffracted angles	-
f	Frequency tuning (refers to the momentum-matching frequency)	Hz
G	Gyration tensor	-
g_{ij}	Gyration vector	-
k	Wave number	m^{-1}
k_a	Acoustic wave vector	m^{-1}
L	Directional cosine along the x -axis	-
M	Directional cosine along the y -axis	-
M_2	Figure of Merit	-
N	Directional cosine along the z -axis	-
n_e	Refractive Index for the Extraordinary Ray	-
n_o	Refractive Index for the Ordinary Ray	-
n_{e1}	Effective refractive index for the extraordinary ray based on the P. Gass model	-
n_{e2}	Effective refractive index for the extraordinary ray based on the Voloshinov's model	-
n_{e3}	Effective refractive index for the extraordinary ray based on the Fresnel's model	-
n_i	Incident ray's refractive index	-
n_l	Refractive index for the left-hand circularly polarized eigenmode	-
n_r	Refractive index for the right-hand circularly polarized eigenmode	-
$R_x(\theta_c)$	Rotation matrix around the x -axis by angle θ_c	-
$R_y(\phi)$	Rotation matrix around the y -axis by angle ϕ	-
t	Time variable	s
V	Acoustic wave phase velocity	m/s
V_{001}	Acoustic wave phase velocity along [001] crystallographic axis	m/s
V_{110}	Acoustic wave phase velocity along [110] crystallographic axis	m/s
Y_0	Point on the optical axis	mm

Y_e	Point of the recorded diffracted beam	mm
O-XY'Z'	Crystallographic coordinate system	
O-XYZ	Global coordinate system	

Abstract/Executive Summary

To support the integration of Acousto-Optic Tunable Filters (AOTFs) in optical systems and lay the groundwork for further research, this report presents the development and validation of an analytical model for a non-collinear AOTF based on tellurium dioxide (TeO_2). The AOTFs are compact solid-state devices that filter desired optical wavelengths by applying an appropriate RF signal. Their compactness and quick tunability make them particularly appealing for Earth observation missions, where an AOTF can be integrated into small platforms like CubeSats [1].

However, there is a significant gap in the availability of comprehensive optical AOTF simulations that can predict the behaviour of AOTFs, and specify the momentum-matching frequencies required for the highest diffraction efficiency (DE) to occur. This report addresses that gap by developing a detailed three-dimensional (3D) analytical model for the non-collinear AOTFs based on TeO_2 , the most commercially available and widely used AOTF configuration. The analytical model, developed in this report, aims to facilitate the design and optimization of AOTFs for optical systems used in various fields, particularly in space-based instruments.

The core of the AOTF's analytical model can be broken down into three main stages: the entrance facet, the acoustic field, and the exit facet. The interaction of light with these three stages is simulated by rays, the direction of which is determined by the Directional Cosine Matrices (DCMs). The model performs calculations to describe the path of incoming rays as they enter, propagate through, and exit the AOTF crystal. Special attention is given to simulating the Acousto-Optic (AO) interaction within the crystal, where a diffracted light is produced. Furthermore, the model calculates the momentum-matching frequency and outputs the propagation of a newly created diffracted light through the AO interaction.

The developed model is adapted to operate for both incident polarisation types, ordinary and extraordinary. Furthermore, the model can simulate the AOTF's behaviour as it is rotated, allowing further versatility of AOTF's placement in the optical design. The model, as well as the adaptations, were first verified with the data from the Voloshinov et al. paper, where it accurately predicted both the separation angles and the momentum-matching frequencies. Further verification was performed with known AOTF parameters at various optical wavelengths with the help of an experiment performed at Université Polytechnique Hauts-de-France (UPHF).

Furthermore, the model was validated through diffraction testing, where it successfully simulated the AOTF's behaviour, predicting both diffracted and undiffracted ray angles with an accuracy of 0.1° . Testing was conducted at various rotational angles and for both incident polarization types, with the model's predictions closely matching the experimental data. Based on the testing, it was possible to determine the frequency-matching method used in characterising the essential AOTF angles that dictate the AOTF's behaviour.

The analytical model was further enhanced by incorporating an optimisation algorithm, which automates the characterization of key AOTF variables for newly acquired devices. The algorithm characterises the crystallographic axis angle, tilt angle, and facet inclination angles. These parameters are typically not provided by manufacturers, leaving the AOTF's behaviour largely unknown. However, by characterising these variables with the model created, it becomes possible to extrapolate the AOTF's performance for any incident optical wavelength within the visible spectrum.

The study of Acousto-Optics (AO) has a relatively short history, starting in 1922 with Brillouin predicting that the light can be diffracted by an acoustical wave [2]. This field has quickly expanded however in the recent decades with their initial prevalent application in laser systems such as light modulation, Q-switching, pulse picking and many more [3]. At the present time, there are multiple classifications of AO devices, which are distinguished based on the AO interaction, material choice and the selection of the acoustical mode [3].

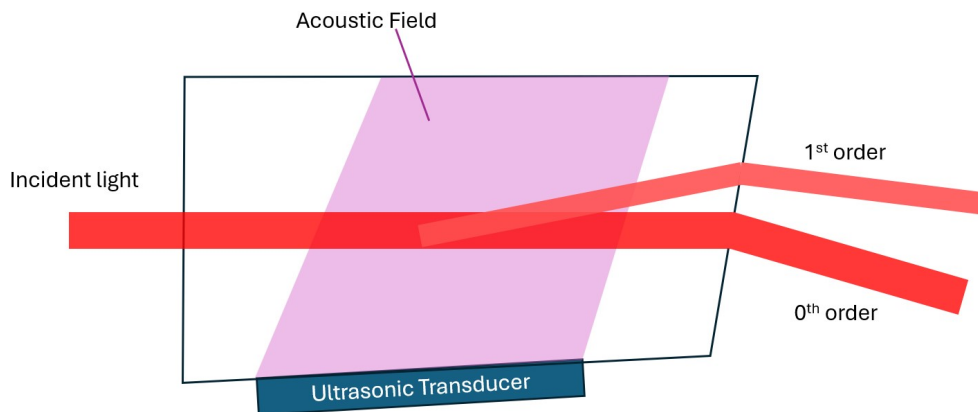


Figure 1.1: Principle of work of an AO device.

A working principle of an AO device is illustrated in Figure 1.1, which is based on the elasto-optic or photoelastic effect [4]. A piezoelectric transducer is typically bonded to the bottom surface of the AO material and generates an acoustical wave based on the RF signal sent to it. This acoustic wave is launched inside the crystal, which induces local strains in a pattern corresponding to the propagating acoustical wave. These strains affect the electric susceptibility of the crystal and change the refractive index of the material through this elasto-optic effect [5].

When the incident optical beam reaches the acoustic field, it is susceptible to the AO interaction, which can be described as a diffraction of the optical wave by the periodical phase grating induced by the acoustical wave inside the crystal. The difference between an ordinary grating and a phase grating is that the latter is not stationary but travels at the speed of sound, depending on the medium of the AO material. This travelling acoustical wave Doppler shifts the optical beam passing through the acoustic field, and this effect can either be used to deflect, modulate or filter the incident optical beam [4]. The names of the devices responsible for these properties are AO deflectors (AODs), AO Modulators (AOMs), and AO tunable filters (AOTFs), respectively. However, the design and the choice of materials vary significantly between these three devices [4].

1.1 Acousto-Optic Tunable Filter

This report will focus on the Acousto-Optic Tunable Filter (AOTF) which is a compact (few cubic centimetres), solid-state device designed for optical wavelength or frequency tuning of electromagnetic spectra in real-time [6]. In other words, this device can filter a desired optical wavelength from a spectrum of light when the correct RF signal is applied [7]. This device is often preferred in applications such as spectroscopy, remote sensing, and hyper-spectral imaging due to the device's ability to quickly change the spectral filtering properties in a matter of milliseconds [6], if the RF signal change is automated.

An illustration of the AOTF's working principle is shown in Figure 1.2. The acoustic wave inside the AOTF's crystal can be tuned via the piezoelectric transducer by adjusting a radio-frequency (RF) signal. This allows

users to select which wavelength bandpass will be influenced by the AO interaction, resulting in two distinct beams exiting the AOTF: one with diffracted and polarized photons at the tuned wavelength, and the other with the remaining wavelengths [7]. The diffracted photons can then be sent onto a detector, and be analysed for the presence of bandgaps and the consequent gas concentration calculation. If another wavelength is desired to be analysed, the user or the automated computer can tune to the new desired wavelength and repeat the process.

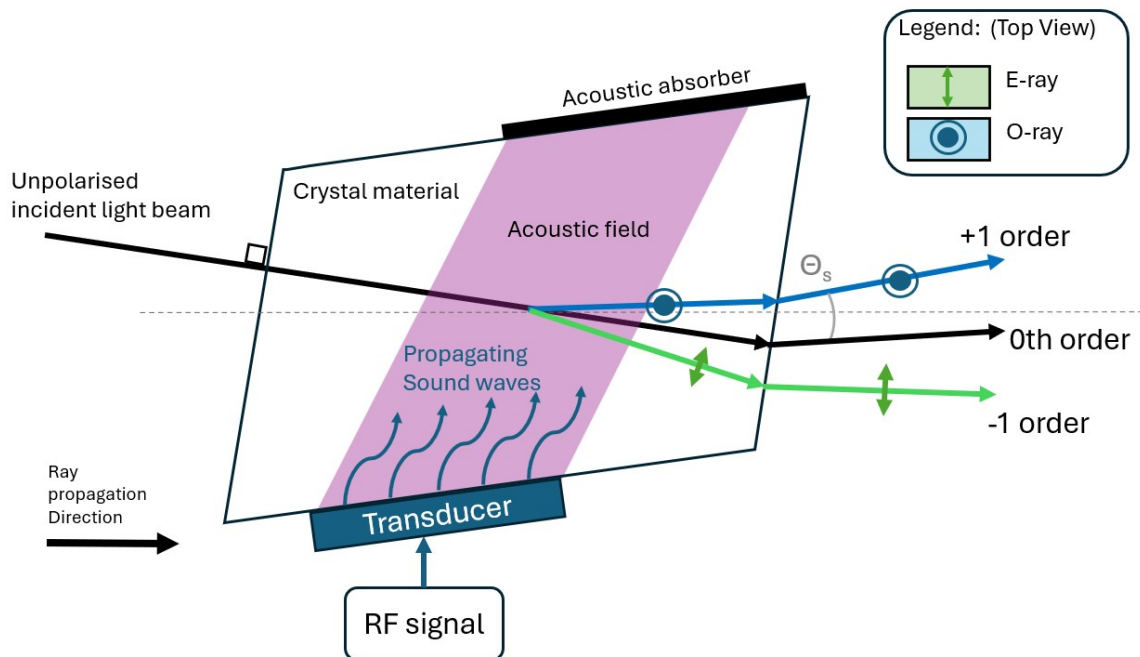


Figure 1.2: A working principle illustration of the AOTF - adapted from [8].

The RF signal and power can be controlled by varying the frequency and power level with the RF generator and amplifier, respectively [8]. The component positioned on top of the AO material in Figure 1.2 is the acoustic absorber, which is an element positioned on the opposite side of the crystal to prevent acoustic wave reflections, which may cause the creation of standing waves. Otherwise, such a scenario would limit the tunability of the AOTF device [9].

1.2 Applicability of AOTF in space missions

The AOTFs' compact size and relatively low price make these filters appealing for use in CubeSat applications and other small satellites to perform Earth observation missions [1]. Such missions are of great interest to the research institutes, which seek global Earth coverage and an increased passage frequency over the areas of interest [1]. These missions allow the institutes to report on the progression of pollution sources such as coal plumes [10], water pollution [11], or can help with aerosol detection [1].

The CubeSats have experienced increased demand in the past few years due to the reduced cost and development time compared to larger satellites [12]. This trend can be attributed to the use of Commercial-Off-The-Shelf (COTS) components, miniaturization of subsystems and the possibility of launching multiple CubeSats with a single launch, which can further lead to missions with a constellation of observational CubeSats [12].

The AOTFs have already been used for applications such as spectroscopy, remote sensing and hyper-spectral imaging [6], due to the filter's ability to quickly synchronise acquisitions of spectral images [10]. Previous usability and market availability make the AOTF an appealing device to be used for space spectroscopy applications on CubeSat and other satellites.

1.3 Motivation to study AOTF simulation

However, implementing AOTF into an optical setup of a CubeSat, or other use cases, is not trivial. Especially, when currently there is no open-source AOTF optical model freely available, to the knowledge of the author. An optical model is an important tool in planning optical setups, before testing or already implementing in

the optical product. It allows the user to foresee the expected optical behaviour of the system, and highlight potential flaws that in the worst-case scenario can lead to equipment damage.

Typically, the AOTF is tested multiple times in the lab for a specific wavelength, where the diffracted angle and the applied RF signal are recorded. These experimental results are then incorporated into a model, which simulates the AOTF's behaviour as a prism that diffracts light only at the test wavelength. While this approach is reliable, it is time-consuming and limited to a single wavelength. Extending this method to cover a full spectrum would be even more labour-intensive. Thus, there is a significant need for a simulation that can accurately model the AOTF's behaviour across a range of wavelengths.

Simulating the AOTF device is not trivial, as multiple factors come into play. Not only the incident optical wavelength, and the refractive index of the material matter, but also under which conditions the efficient diffraction occurs. To achieve a Bragg diffraction for instance where the diffraction efficiency is the highest for a desired wavelength, a so-called momentum-matching condition needs to be passed which is dependent as well on multiple parameters. Namely, the propagation angle of the incident light relative to the material's optic axis, the suitable RF signal which needs to be applied, the polarization of the incident light and so on.

1.4 Thesis structure

With the lack of knowledge on the topic of the AOTF simulation identified, it was decided that it would be beneficial for the research community to have a working AOTF simulation model that can work at multiple optical wavelengths. To achieve this, Chapter 2 will firstly go into the detailed working principle of the AOTFs, with a closer look into the types of AOTF, AO interaction, and polarization. Followed by a research description in Chapter 3, where the main research questions and requirements are stated. Additionally, Chapter 4 will go into the analytical model behind the simulation which involves the use of directional cosines to represent rays of light that propagate through three distinct surfaces of the AOTF, namely the entrance, acoustic field and exit surface.

Afterwards, the analytical model is verified in Chapter 5. Using an experiment from UPHF, the experimental results are compared with the model for the RF signal required for Bragg diffraction and the separation angle between the two outgoing rays from the AOTF. Chapter 6 goes into the experimental procedures that will be used to validate the model. The model validation itself is conducted in Chapter 7, where physical experiments are performed on an AOTF with an unknown crystal structure but known geometry. Besides validation, the second goal of these experiments is to establish a method for identifying the crystal properties of the AOTF. The report provides the final bits of new content in Chapter 8 by demonstrating a further use case of the analytical model. Where, a new AOTF is tested and characterized in terms of its crystal geometry, with the help of an optimisation algorithm. Finally, Chapter 9 concludes the report and Chapter 10 provides the recommendations for future works.

AOTF Theory 2

Before developing the analytical model and simulating the AOTF's behaviour, it is essential to first understand the underlying theory of how the AOTF operates. This chapter begins with an overview of the materials commonly used in AOTFs, presented in Section 2.1. Next, Section 2.2 outlines the various configurations of AOTFs, followed by Section 2.3, which discusses the selection of the appropriate AOTF configuration and material for further model development.

Section 2.4 will describe the crystallographic axes critical for Acousto-Optic (AO) interactions, along with the polarisation types that are relevant to these interactions. This is followed by Section 2.5, which details the optical properties of TeO₂. The theory behind AO interactions is presented in Section 2.6, discussing the key factors influencing the momentum-matching frequency and provide a brief mathematical description of the AO interaction. Section 2.7 examines the optical activity phenomenon, which can alter the polarisation of the incident wave as it propagates through the material, and its implications for AO calculations.

Finally, Section 2.8 delves into the theory behind the transducers and highlights important electrical considerations to take into account during the physical experiments.

2.1 AOTF materials

There are several important parameters that the material should satisfy for the efficient operation as an AOTF material. Firstly, the material should be optically transparent in the wavelength region of interest [7]. The TeO₂ crystals for instance are used for visible (VIS) and near-infrared (NIR) spectra applications. For spectra in the shorter wavelength such as ultraviolet (UV) spectra, the crystal TeO₂ is not compatible since it is not transparent for the wavelengths below 350 nm [5]. For the UV spectrum, it is potentially possible to use the KH₂PO₄ (KDP) crystal, but careful attention towards a manufacturing process is required [5]. For the wavelengths in the infrared (IR) range, mercurous chloride (Hg₂Cl₂) can also be used [7].

Generally, the materials with high density and slow acoustic velocity, produce well-defined acoustic waves which improve the efficiency of the AO material. For this, the figure of merit (M_2) parameter is often used to compare the AO materials. The greater M_2 value is a reflection of the AOTF's efficiency [7]. The parameter M_2 can be calculated by Equation 2.1, where ρ_{mat} is the AO material's mass density, V is the acoustic velocity, p is the photoelastic coefficient of the material, and n_e with n_o are the refractive indices for ordinary and extraordinary rays [13].

$$M_2 = \frac{n_e^3 n_o^3 p^2}{\rho_{mat} V^3} \quad (2.1)$$

For the reasons of having low acoustic velocity, significant birefringence, and the resulting high M_2 value. The non-collinear AOTF configuration is popular in use. The most commonly used material for the AOTFs is TeO₂, also known as paratellurite. Table 2.1 summarises the AO properties of the most commonly used materials for AOTFs, where quartz and thallium arsenic selenide (Tl₃AsSe₃) have also shown to be promising for the ultraviolet and infrared spectra respectively [7].

Table 2.1: Properties of the AO materials [7].

Crystal	Lattice	Transmission range (μm)	Refractive indices at 633nm*	Acoustic velocity (m/s)	AO figure of merit ($\times 10^{-18} \text{ s}^3/\text{kg}$)	AOTF type
α -Quartz	L	0.12 – 6.5	$n = 1.539$ $n_e = 1.548$	5960	1.51	Collinear Non-collinear
LiNbO ₃	L[X]	0.4 – 4.5	$n_o = 2.29$ $n_e = 2.20$	6570	6.95	Collinear
TeO ₂	S[110]	0.35 – 4.5	$n_o = 2.26$ $n_e = 2.41$	616	1200	Non-collinear
Tl ₃ AsSe ₃	L[100]	1.25 – 17	$n_o = 3.34$ $n_e = 3.15$	2050	628	Collinear Non-collinear
Hg ₂ Cl ₂	S[110]	0.4 – 20	$n_o = 1.96$ $n_e = 2.62$	347	1060	Non-collinear

*except quartz, which was quoted at 589 nm.

From Table 2.1, it can be observed that the figure of merit is the highest for Tellurium Dioxide (TeO₂). Considering that the parameter M_2 is directly related to the efficiency of the material for the AO interaction, it makes sense why the majority of the AOTFs use TeO₂ for the visible and near-infrared optical range [14]. Furthermore, these types of the AOTF are the most commercially available. These two facts combined suggest that TeO₂ based AOTF is the most desired AOTF type to be simulated, and there is also potential to physically validate the analytical model.

2.2 AOTF configurations

From Table 2.1 it is shown that different AOTF types exist; collinear or non-collinear. The term non-collinear is used due to the non-collinear interaction between the incident beam and the launched acoustic beam. Meaning that when these two beams interact, their propagation vectors do not lie along the same line, and are almost perpendicular to each other as can be seen in Figure 2.1. Contrary, the collinear configuration makes sure that the interaction between the incident and the acoustic beam lies along the same optical line [7], almost parallel to each other, as can be seen in Figure 2.2.

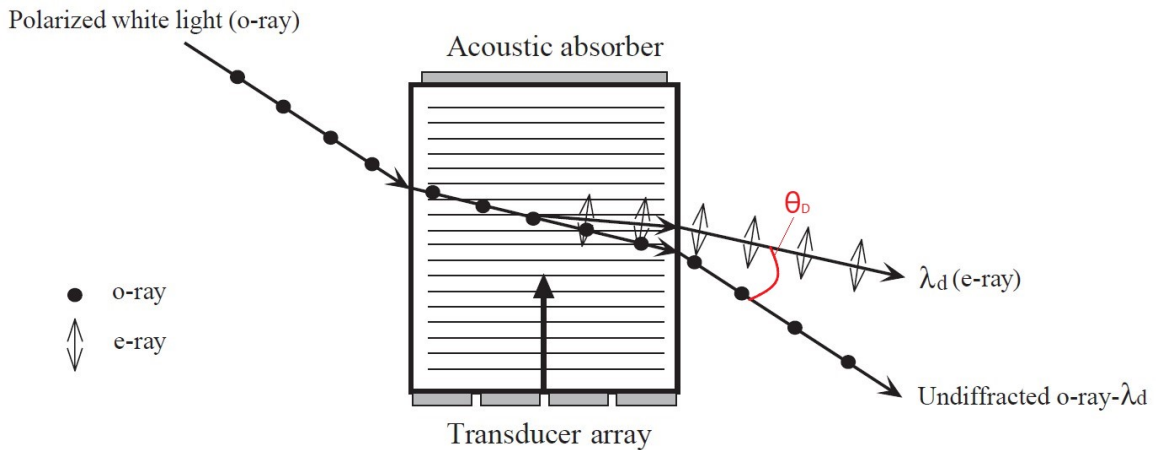


Figure 2.1: Non-collinear AOTF working with the polarized light [7].

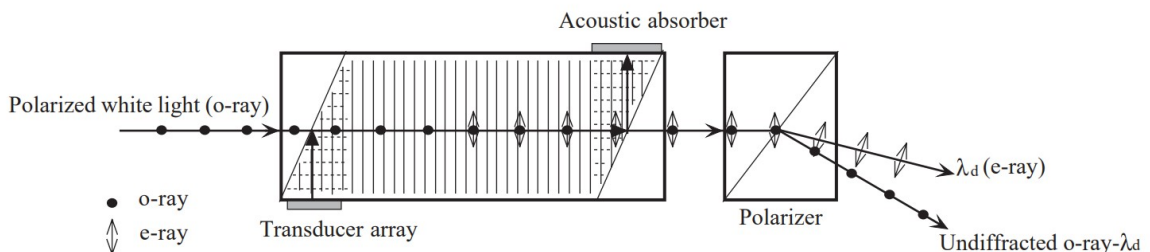


Figure 2.2: A working principle illustration of the collinear AOTF with incident polarized light [7].

Both AOTF configurations typically require the incident light to be polarized, either ordinarily or extraordinarily, for the AO interaction to occur. In both cases, the diffracted ray will have a perpendicular polarization to the incident beam. This diffracted ray then goes to the detector to save the recording for the filtered wavelength. The main differences between the two configurations is that the collinear AOTF typically has a smaller bandpass ($\Delta\lambda$) from the central wavelength, which improves the spectral resolution when multiple tuning samples are taken [7].

While the AOTFs are designed to filter a particular central wavelength (λ), diffraction can occur at the wavelength which is not perfectly matched with the acoustic wave inside the AO material. In that case, the diffracted wavelength can be slightly smaller or larger than the central wavelength. This range of the diffracted radiation band is called the bandpass ($\Delta\lambda$) and can be defined as the full-width at half-maximum intensity (FWHM) of the diffracted light [7].

$$\Delta\lambda = \frac{0.9\lambda^2}{\Delta n L \sin^2(\theta_i)} \quad (2.2)$$

The bandpass relation can be described by Equation 2.2, where the longer interaction length (L), between the acoustic beam and the light beam, results in a smaller bandpass [7]. This smaller bandpass allows filtering out precise wavelengths of interest, which increases the resolution of the search spectra after multiple tuning samples have been collected. Collinear devices typically have a larger interaction length, which allows them to give outputs with higher resolution in comparison to Non-collinear AOTFs [7]. However, this trait in non-collinear AOTF can also be improved by increasing the size of the transducer, which also increases the interaction length between the light and acoustic beams.

However, not all the materials are suitable for collinear AOTFs. If the material has a significant difference between the refractive indexes for the ordinary (n_o) and extraordinary rays (n_e) representing the material's birefringence, it is convenient to use it for the non-collinear configuration. Alternatively, if the material does not possess high birefringence, but has a non-symmetrical (L) lattice structure, then this material can be a good candidate for collinear AOTF configuration [7].

It could be seen, from Table 2.1, that the TeO_2 is typically used for the non-collinear AOTFs, which also has advantages. Typically, non-collinear AOTFs have a larger angle of acceptance, and subsequently larger apertures [7], in comparison to the collinear types. This advantage, allows a larger field of view (FoV) and higher versatility in the positioning inside the optical design, which is advantageous for the absorption spectroscopy if the instrument is operating on a space orbit. Furthermore, the non-collinear AOTFs are easier to manufacture in comparison to the collinear AOTFs, where the difficulty lies in ensuring a prolonged propagation of the acoustical wave along the crystal.

2.3 Configuration and material choice for the AOTF simulation

By studying the typical AO materials and the AOTF configurations that are in use, everything points out that the most prominent choice for future simulation is the non-collinear AOTF based on tellurium dioxide (TeO_2). Not only the material has the highest figure of merit in comparison to the other AO materials, which improves the efficiency of the AOTF's work, but also the non-collinear configuration provides two major advantages by enabling a larger angle of acceptance together with an easier manufacturing process in comparison to the collinear AOTFs [7].

The choice is even further solidified by the fact that this type of AOTF is the most commercially available, which would make the AOTF simulation applicable to a larger application field, as well as it would make it easier to perform a validation on such an AOTF.

The only reason why other materials could be considered for an AOTF is when the wavelengths of interest for filtering are outside the materials' transmission range. In other words, the optical wavelength is being absorbed by the material instead of passing through it. However, for this report, considering there is already a lack of information on the AOTF simulations, testing an AOTF in infrared or ultraviolet spectrum would increase the complexity of the validation procedure. Therefore, a final choice was made for a TeO_2 non-collinear AOTF, as TeO_2 can be used in the visible domain, simplifying the testing.

2.4 Crystallographic axis and ray diffraction of TeO₂

Before going into the theory of optical wave diffraction, some basic information on the AOTF's material (TeO₂) and polarisation needs to be described. TeO₂ is a birefringent material with a positively uniaxial axis system. The latter means that the material TeO₂ does not have the same material's permittivity (ϵ) along one of the axes [15]. In other words, the material exhibits different resistance to the electric field, in this case is due to the optical light, along one of its axes. For TeO₂, the crystallographic axis [110] shows varying permittivity. Consequently, the refractive index (Equation 2.3) along the [110] axis is higher for electromagnetic (EM) waves polarized parallel to this crystallographic plane [15], due to the increased permittivity along that axis.

$$n = \frac{c}{\nu} = \left(\frac{\epsilon}{\epsilon_0} \right)^{1/2} \quad (2.3)$$

From a physical perspective, this means that inside of the birefringent crystal of TeO₂, the [110] crystallographic plane has a denser population of molecules, making the electromagnetic (EM) wave propagation along this plane more difficult. This creates a higher refractive index for the EM wave, which is polarized parallel to this plane [15]. This type of polarized wave is considered to be the extraordinary polarized wave (e-wave), and the refractive index for such a wave is denoted as n_e .

In literature, the crystallographic axis perpendicular to the [110] is denoted as the [001] axis. Along the [001] axis, the refractive index acting on the EM wave is always the same, it is considered to be the fast axis as the light experiences the lowest refractive index along [001] axis [16]. The typical positioning of these two axes in the AOTF is presented in Figure 2.3, where a top view of an AOTF crystal is presented. The combination of the [001] and [110] axis is called a crystallographic axis system, and typically it is positioned at an angle (θ_c) in comparison to the global axis system, the system where the light rays are propagating. The subscript 'c' in the notation stands for crystallographic. Another important angle concerning the crystallographic axis system is α , which is measured between the [110] axis and the transducer's positioning and will become important when AO interaction is studied.

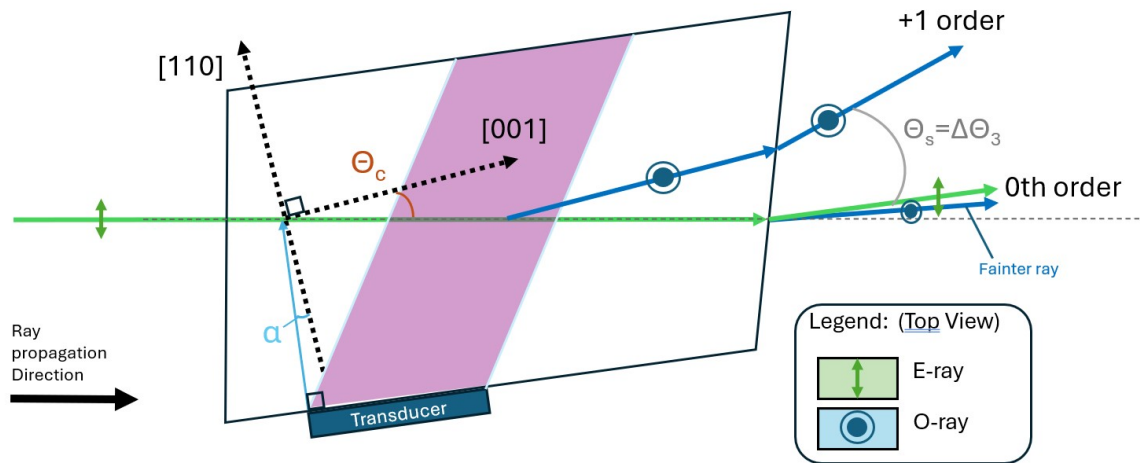


Figure 2.3: Non-collinear TeO₂ based AOTF top view schematic for e-ray diffraction with the addition of crystallographic axes.

Typically, in the experiment a linearly polarised ray of light is sent into an AOTF, meaning that the light's electromagnetic field vector is oscillating along one linear plane. In Figure 2.3, the incident ray is horizontally polarized which is largely parallel to the [110] axis, meaning that this type of ray is extraordinarily polarized. This can be further visualised in Figure 2.4, where a 3D visualisation with polarization notation and crystallographic axis are shown.

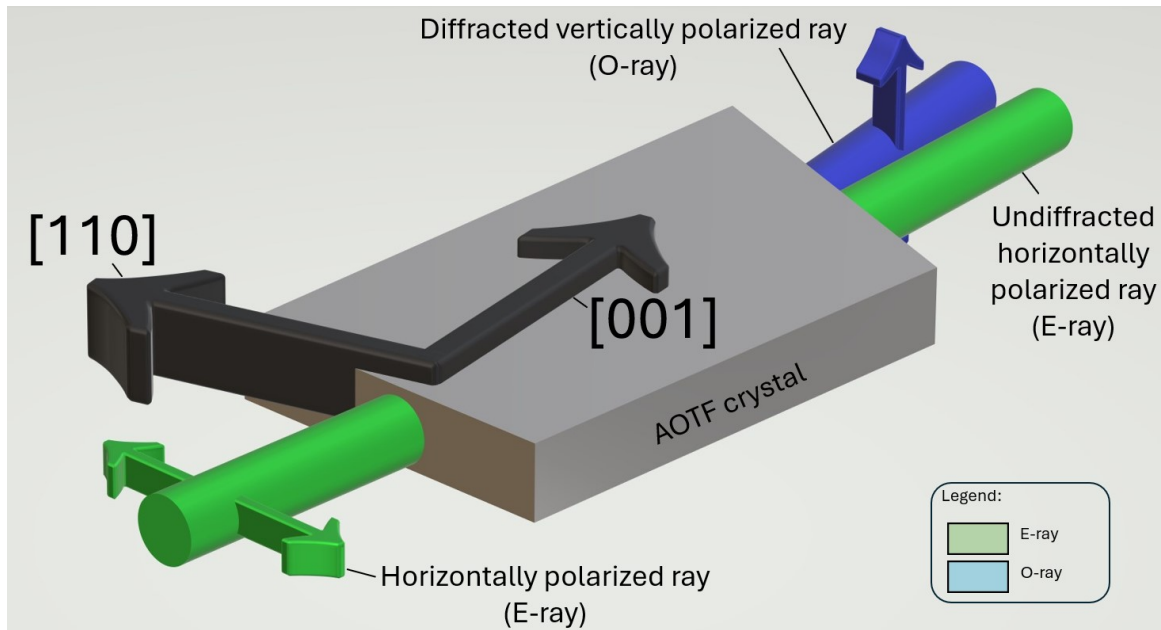


Figure 2.4: 3D view of the AOTF diffraction and polarization of light beams

Considering, that from the top view, it can be seen that the horizontally polarized light is not fully parallel to the [110] axis, a small part of the light changes its polarization due to the birefringence of the TeO₂. This can be visualised in Figure 2.3, where a faint ordinary ray appears close to the e-ray at the crystal's exit surface. Consequently, the larger the angle θ_c , the brighter the separated ray due to the material's birefringence. Those two rays, marked as 0th order, are the undiffracted rays.

Birefringence is the difference between the extraordinary and ordinary refractive indices of the material, which can be quantified by using Equation 2.4 [17]. TeO₂ material is considered to behave as positive uniaxial material, meaning that $n_o < n_e$ [15], therefore the value of birefringence will be positive.

$$\Delta n = n_e - n_o \quad (2.4)$$

However, the main interest in the AOTF is the diffracted ray, which appears only after the AO interaction between the acoustical beam and the light ray. The diffracted ray has a perpendicular polarization to the incident ray [5], and in the case shown in Figure 2.3 the diffracted ray has an ordinary polarisation. The ordinarily polarised ray (o-ray) propagates in the same ways as it would in the isotropic medium, same refractive index along each axis, and experiences the ordinary refractive index (n_o) inside the AO material [15]. When this type of ray is a product of diffraction, the diffraction order is +1, which can be seen in Figure 2.3.

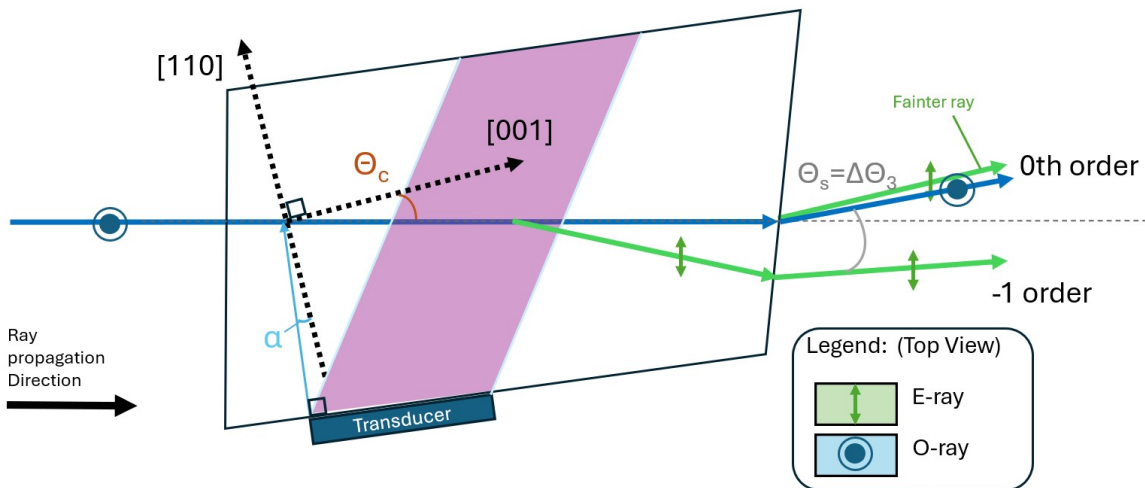


Figure 2.5: Non-collinear TeO₂ based AOTF top view schematic for o-ray diffraction with the addition of crystallographic axes.

Similarly, the ordinarily polarized light can be sent into the AOTF, which would be a vertically polarised light according to the notation used and the propagation of rays will look as shown in Figure 2.5. The diffracted light in this case will be extraordinarily polarised and will appear below the incident ordinary ray after the AO interaction. The orientation of the diffracted ray based on the incident polarisation will make sense after the AO interaction is studied. The diffracted ray in this case has a -1 order notation, and the angular difference between the diffracted and undiffracted ray is called a separation angle which is denoted as θ_s , or for future convenience with the analytical model $\Delta\theta_3$.

2.4.1 Definition of polarization states

From the description of ray diffraction in AOTFs, it can be noted that the ray's polarization state plays an important role. Here, a more elaborate explanation of what is a polarization state is provided. Light is an electromagnetic (EM) wave, which is a combination of oscillating magnetic and electric fields that are perpendicular to each other and the wave's propagation vector. By convention, the polarisation of the EM wave is the direction of the electric field vector [18]. The polarization state is the evolution of the electromagnetic field vector through time at one point in space [19].

For an electromagnetic wave, Maxwell's equations can be used, where an expression can be derived for an electric field vector (\vec{E}) represented in Equation 2.5. The light propagates along the optical axis, which for this explanation will be the z-axis. Furthermore, this expression is used for the monochromatic plane waves, meaning it can be used for each wavelength individually.

$$\vec{E} = E_x \cos(kz - \omega t) \vec{x}_0 + E_y \cos(kz - \omega t + \phi) \vec{y}_0 \quad (2.5)$$

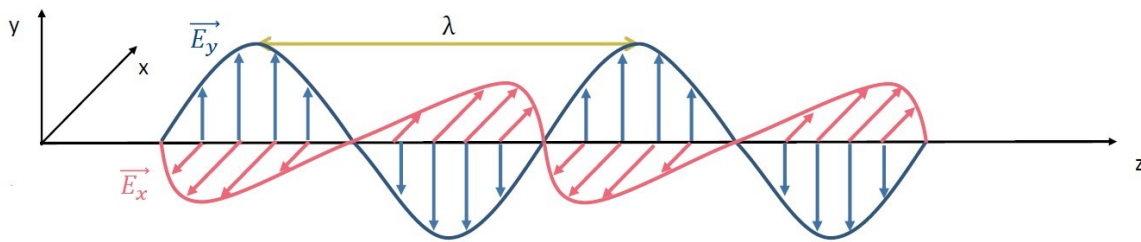


Figure 2.6: Polarization visualization [19].

The electric field vector representation in Equation 2.5, characterizes the light's electromagnetic wave in terms of amplitudes in the x and y directions, E_x and E_y respectively, and the vector directions of these two amplitudes. An illustration of the polarization terminology can be seen in Figure 2.6. The other terms represent the propagation variance of the waves over time (t), where k represents the wave number and ω represents the wave's angular frequency.

Finally, it is important to note that the electric field propagation of x and y components may not always be in phase with each other. Therefore, the ϕ component is added to one of the vector components, which represents the phase shift. If the ϕ was 0 or 2π , then the x and y components would be in phase and the light would be considered linearly polarized, as the electric field vector would be oscillating along the same intensity vector line. As can be seen in Figure 2.7, where part (a) shows the light propagating along the z-axis and (b) shows the electric field vector change with time. Based on this notation, when the phase shift angle is zero, the light has horizontal linear polarization, and when $\phi = \pi/2$ the light has vertical linear polarization.

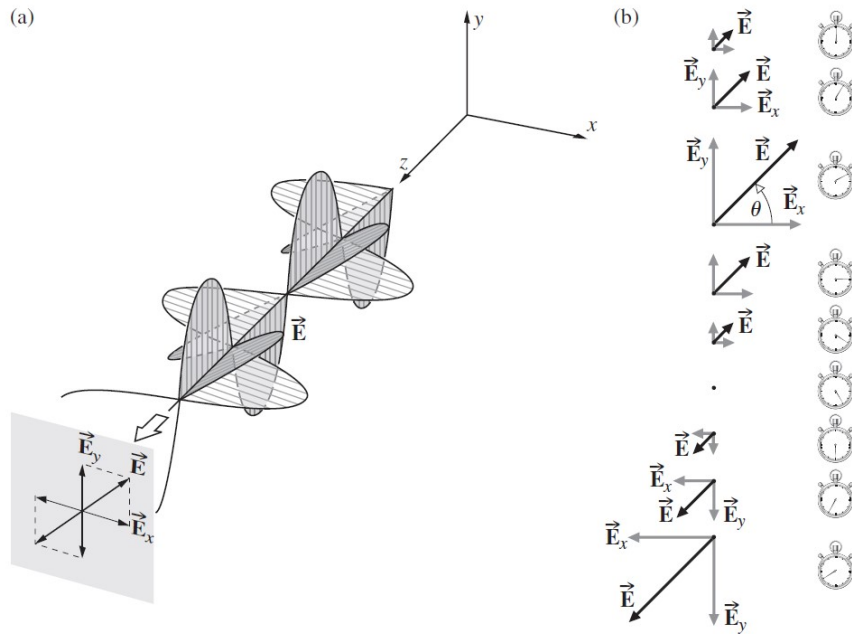


Figure 2.7: (a) Linearly polarized light (b) Oscillating field diagram showing the intensity and direction of the overall electric field vector [18].

The other case where the light would also be linearly polarized is when one of the magnitude vectors is set to zero, meaning that the light is propagating purely along the x or y-axis plane. The other polarization state is circular, where the magnitudes of the electric field along the x and y-axis are the same and the two electromagnetic field components are out of phase by $\pi/2$. Finally, the general case, of polarization is elliptical where the magnitude of the electromagnetic field components (E_x and E_y) is not the same and their oscillation is out of phase [18].

2.4.2 Crystallographic planes

Considering that crystallographic planes [001] and [110] were brought up during the AOTFs principle of work and how they help to figure out which incident ray is extraordinarily or ordinarily polarized. It is important to provide a brief explanation of what these planes mean. The numbers inside the squared brackets are the Miller indices, which are used to describe the orientation of the material crystal axis plane [20].

Tellurium Dioxide exists in two types of crystal structure, orthorhombic or tetragonal [21]. For AOTF purposes, the tetragonal (422) crystal structure is used [3], where two of the three Miller axes are equal in length and are all perpendicular to each other [20]. This results in two lattice planes [20], or in other words, planes of symmetry. The plane of symmetry where two of the three miller axes are equal is [110], and the plane of symmetry orthogonal to it is [001].

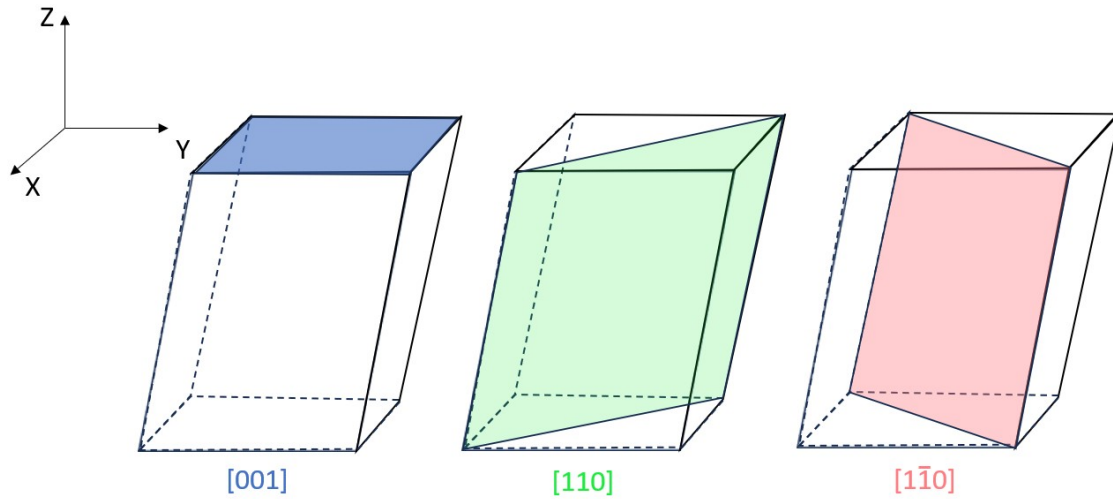


Figure 2.8: Crystallographic axis of AOTF, according to [22].

The relevant crystallographic planes, in Miller's space, are pictured in Figure 2.8. For this explanation, the light is propagating along the X-axis (which will not be the same coordinate system as used in the optical testing). As has been previously shown, for the AOTFs the light wave and the slow acoustic wave are usually both confined within the [110] and [001] (Z-axis plane) [15]. The incident light propagates closely parallel to the Z-axis plane (shown in blue) and in the TeO₂ AOTF the acoustic wave is normally sent along the [110] axis, shown in green.

2.5 Optical properties of Tellurium Dioxide

The ordinary and extraordinary refractive indices were mentioned multiple times in the explanation of the AOTF principles of work. However, these values have not yet been quantified, which will be useful for the AO interaction and the future analytical model. Both of the refractive indices are dependent on the optical wavelength (λ) entering the crystal. The relation of the refractive index varies with the wavelength and is visualised in Figure 2.9, where the ordinary refractive index is shown in blue and the extraordinary in green.

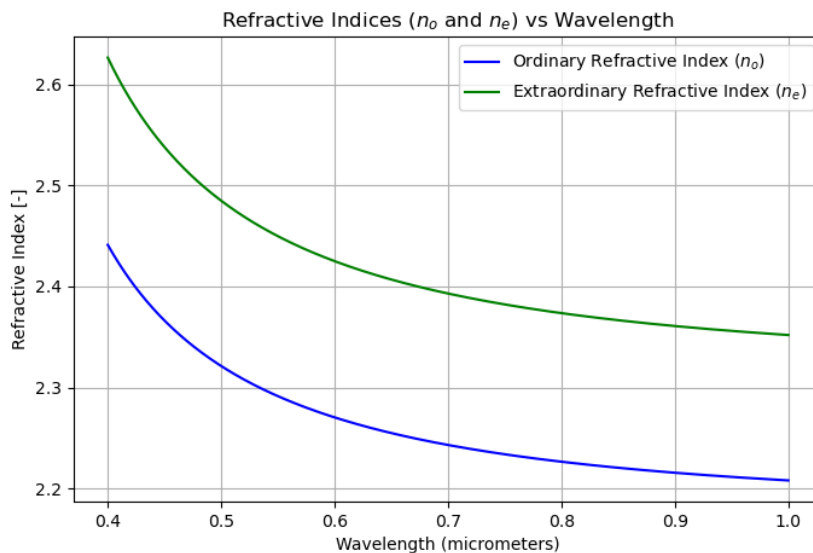


Figure 2.9: Variation of the ordinary and extraordinary refractive indices with optical wavelength for TeO₂ [23].

$$n_o(\lambda) = \sqrt{1 + \frac{2.584}{1 - \left(\frac{0.1342}{\lambda}\right)^2} + \frac{1.157}{1 - \left(\frac{0.2638}{\lambda}\right)^2}} \quad (2.6)$$

$$n_e(\lambda) = \sqrt{1 + \frac{2.823}{1 - \left(\frac{0.1342}{\lambda}\right)^2} + \frac{1.542}{1 - \left(\frac{0.2631}{\lambda}\right)^2}} \quad (2.7)$$

The data for both of the refractive indices were taken from a paper by Uchida [23], where the author has measured the indices experimentally, and calculated analytically with the help of two-term Sellmeier's dispersion formula [23]. A full study on Sellmeier's formula was outside the scope of this research, and therefore simplified relations were taken instead based on the experimental values provided by the Uchida. The simplified relation for the ordinary refractive index (n_o) is shown in Equation 2.6, and for the extraordinary refractive index in Equation 2.7. The relations were obtained from a database by Polyanskiy [24], and verified with the experimental values from Uchida.

Based on Figure 2.9, it could be observed that both of the refractive indices decrease as the optical wavelength increases. Furthermore, it could be observed that the birefringence also follows a similar trend, which can be better visualised in Figure 2.10. This information will become important further in the research.

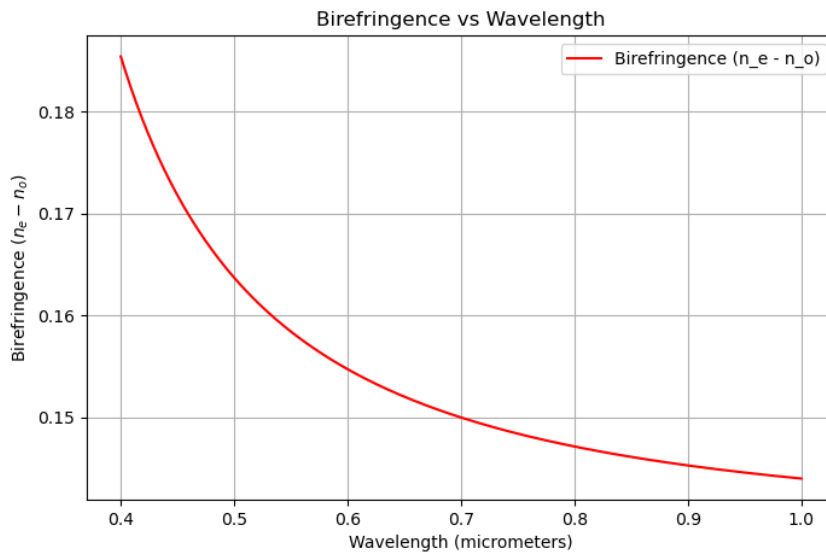


Figure 2.10: Variation of birefringence with optical wavelength for TeO₂ [23].

2.6 AO interaction and momentum-matching condition

Going one step further in understanding the AO interaction at the acoustic column between the acoustical and light beams, Figure 2.11 shows an exaggerated schematic where an extraordinarily polarized light ray enters a noncollinear AOTF crystal at an angle. A similar graphic can be drawn for the ordinary incident ray, but to avoid confusion the extraordinary incident light case will be examined here. The mathematics behind the AO interaction happen in the crystallographic axis system, and the rays of light need to be converted into the wave vectors, where the incident wave vector is \mathbf{k}_i , the diffracted wave vector is \mathbf{k}_d , and the acoustic wave vector is \mathbf{k}_a .

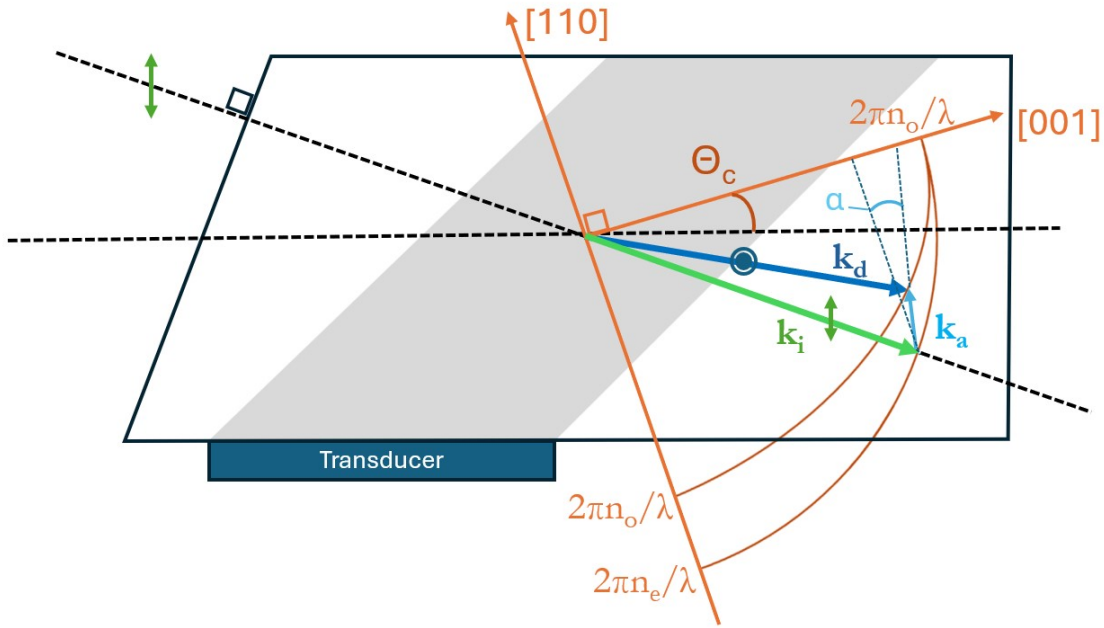


Figure 2.11: AO interaction schematic inside the AOTF crystal -adapted from [10].

The interest in this report is to create a simulation where the diffraction of light happens at the highest efficiency, and to tell the user at which incidence angle (θ_i) and RF signal (f) such condition can be achieved. Such a condition is called momentum-matching, or Bragg regime [25], where up to 100% of optical light intensity ($I_1(\lambda)$) of a selected wavelength can be diffracted by an angle θ_d [25].

To satisfy such a condition, mathematically, Equation 2.8 is provided [25], which means that the acoustical wave vector (\mathbf{k}_a) should cover the distance between the two refractive ellipses, drawn in Figure 2.11. The magnitude of the vector \mathbf{k}_a is controlled by the RF frequency signal (f) applied and the acoustical wave phase velocity (V). If the magnitude of the vector \mathbf{k}_a is not sufficient to cover such a distance, a momentum-mismatch condition is applied ($\Delta\mathbf{k}_a \neq 0$), where the diffraction efficiency (DE), presented in Equation 2.10, decreases following a sinc^2 function as the value of $\Delta\mathbf{k}_a$ increases [25].

$$\Delta\mathbf{k}_a = \mathbf{k}_i + \mathbf{k}_a - \mathbf{k}_d = 0 \quad (2.8)$$

$$\mathbf{k}_i = \frac{2\pi n_i}{\lambda_0}, \quad \mathbf{k}_d = \frac{2\pi n_o}{\lambda_0}, \quad \mathbf{k}_a = \frac{2\pi f}{V} \quad (2.9)$$

$$DE = \frac{I_1(\lambda)}{I_0(\lambda)} \quad (2.10)$$

To show the differences between the two conditions, Figure 2.12 shows the two rays from the previous example, in the wave vector space of the AOTF crystal. Figure 2.12a shows a momentum-matching condition where the wave vector \mathbf{k}_a has a sufficient magnitude to connect the wave vectors of the incident and the diffracted rays together. Oppositely, Figure 2.12b shows the momentum-mismatch condition, where a variable $\Delta\mathbf{k}_a$ is added to connect the two wave vectors together.

It could be noticed that the wave vector diagrams have these refractive index ellipses, one for ordinary ray and the other for extraordinary ray, which both start at the same value ($2\pi n_o/\lambda$) if the measuring is done at [001] axis. For TeO_2 , the ordinary refractive index ellipse, the smaller one, has the same refractive index value (n_o) no matter the positioning along the crystallographic axis. However, the refractive index for the incident extraordinarily polarized ray (n_i) changes depending on the angle with the [001] axis, which progressively increases and reaches the maximum (n_e) if the extraordinarily polarized ray propagates parallel to the [110].

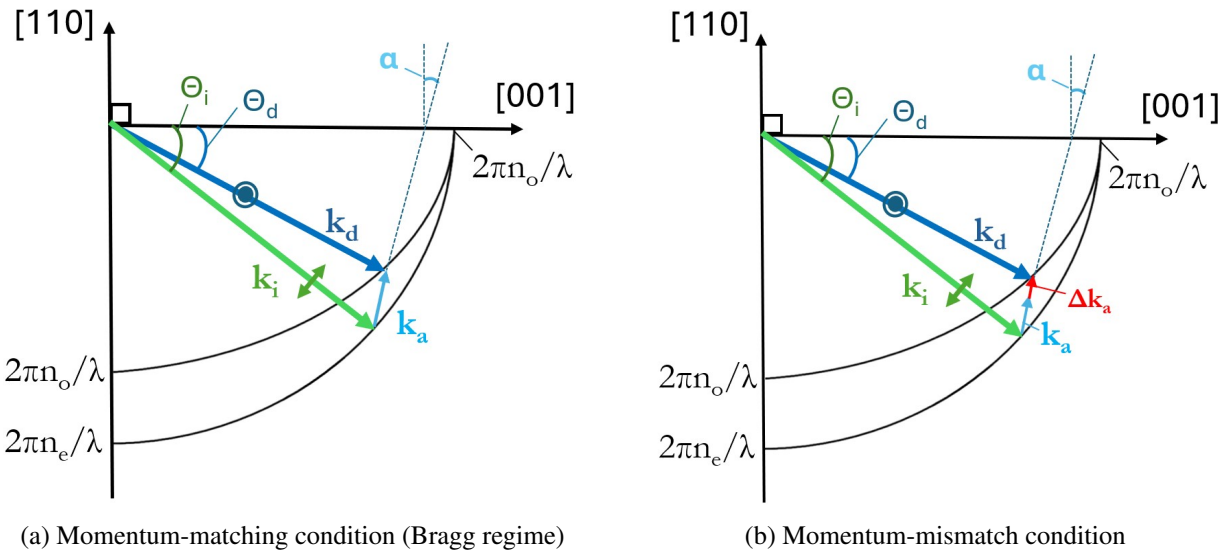


Figure 2.12: Wave vector diagram of the momentum-(mis)matching conditions in TeO₂. The incident (\mathbf{k}_i) and diffracted (\mathbf{k}_d) light waves, and the acoustic (\mathbf{k}_a) wave are represented.

There are three different ways to express the refractive index for the anisotropic crystals, such as TeO₂, that were found in the literature. All the methods have an angle θ between the optic axis [001] and the ray vector's direction propagating inside the crystal. The first method uses the refractive ellipses which both have the same value at [001] axis as shown in Figure 2.12, and this method is the most commonly used in literature which was introduced by P. A. Gass and J. R. Sambles [26]. In this method, the refractive index for ordinary ray (n_{o1}) stays the same throughout the ellipse, and the index for extraordinary ray (n_{e1}) follows the relation presented in Equation 2.12. The subscript, '1', stands for the first method in this case.

$$n_{o1} = n_o \quad (2.11)$$

$$n_{e1}(\theta) = \left(\frac{\cos^2(\theta)}{n_o^2} + \frac{\sin^2(\theta)}{n_e^2} \right)^{-1/2} \quad (2.12)$$

By looking at Equation 2.12, if the value of $\theta = 0^\circ$ is taken then the extraordinary ray's refractive index will be n_o , similarly as $\theta = 90^\circ$ it will be n_e , which does go inline with the observation made previously.

2.6.1 Factors affecting the tuning frequency

Based on the AO interaction theory, it is desired in the optical setup that the AOTF is operating in the momentum-matching condition, since it allows achieving the highest diffraction efficiency [25]. However, this condition depends on multiple parameters, requiring a delicate balance in AOTF's tuning and positioning. This subsection will focus on AOTF tuning and explain how factors such as optical wavelength λ , incident ray angle θ_i , and the cut angle α influence the frequency tuning f .

Starting with the dependence of frequency tuning on the optical wavelength. It was previously mentioned that to satisfy the momentum-matching condition, the vector \mathbf{k}_a should have sufficient magnitude, which can be increased or decreased by a tuning value f based on Equation 2.9, to cover the distance between the two refractive ellipses. The distance between the two ellipses, is determined based on the birefringence of the material. As it was learned from Figure 2.10 for TeO₂ based on the results from Uchida, the birefringence is the highest for lower optical wavelengths, in the visible spectrum. Meaning that the distance between the two refractive index ellipses would be higher at lower wavelengths. Consequently, the distance that needs to be covered by vector \mathbf{k}_a would also increase, meaning that the RF frequency signal (f) needs to be higher for lower wavelengths to satisfy the momentum-matching condition. This trait of TeO₂ can be seen from experimental results in Figure 2.13 where the frequency tuning curve increases for the lower optical wavelengths [27].

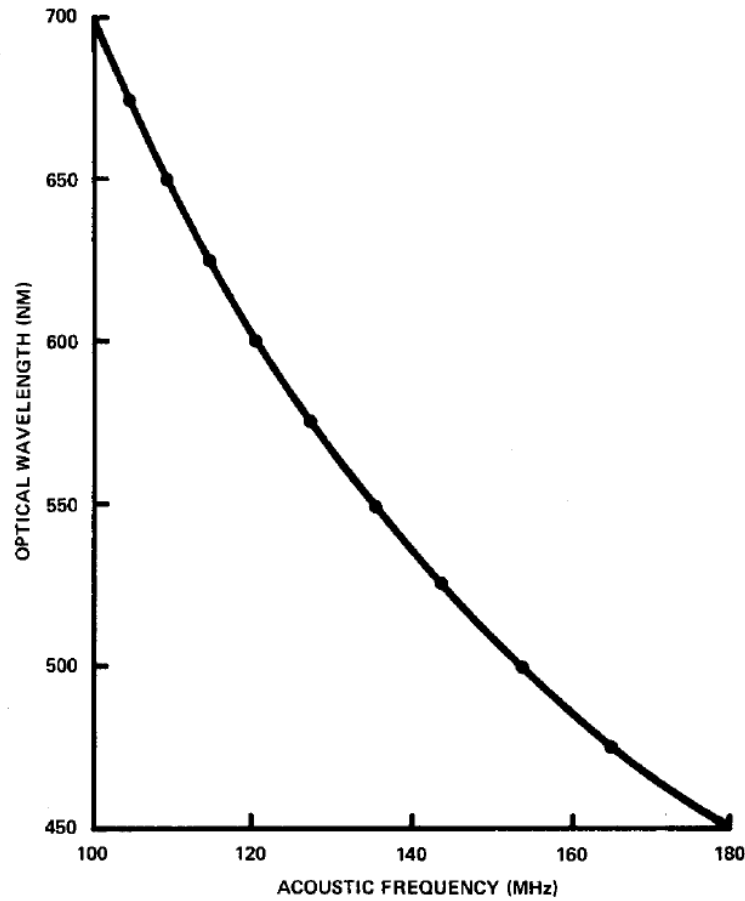


Figure 2.13: Tuning curve with varying wavelength for an AOTF based on TeO_2 [27].

Continuing on the trend of covering the distance between the ellipses, with the acoustical wave vector in the wave vector space. The other factor that influences this distance is the incidence angle θ_i , which is shown in the experimental data by P.Gass in Figure 2.14 [26]. The angle θ_i is measured in the crystallographic axis system, and it increases if the optical ray's entrance angle θ_1 is further away from the [001] axis, as can be seen from Figure 2.11 and be illustrated by Equation 2.13. At higher angles of θ_i , the difference between the refractive ellipses is getting larger. Which, similarly to the previous point, means that the magnitude of \mathbf{k}_a should be increasing as the angle θ_i increases, to satisfy the momentum-matching condition.

$$\theta_i = \theta_c + \theta_1 \quad (2.13)$$

However, it can be seen in Figure 2.14 that the tuning curve has trough at a certain angle of incidence, only after which the RF signal starts to increase. There is not much literature on how to mathematically find this trough point, but there is evidence that the cut angle α influences the frequency curve, as can be seen in Figure 2.15. Based on AOTF testing performed, the AOTFs are usually designed to have this trough point when the θ_1 angle is around zero degrees. Meaning that if the incidence angle θ_1 increases, the RF signal required for peak diffraction also increases.

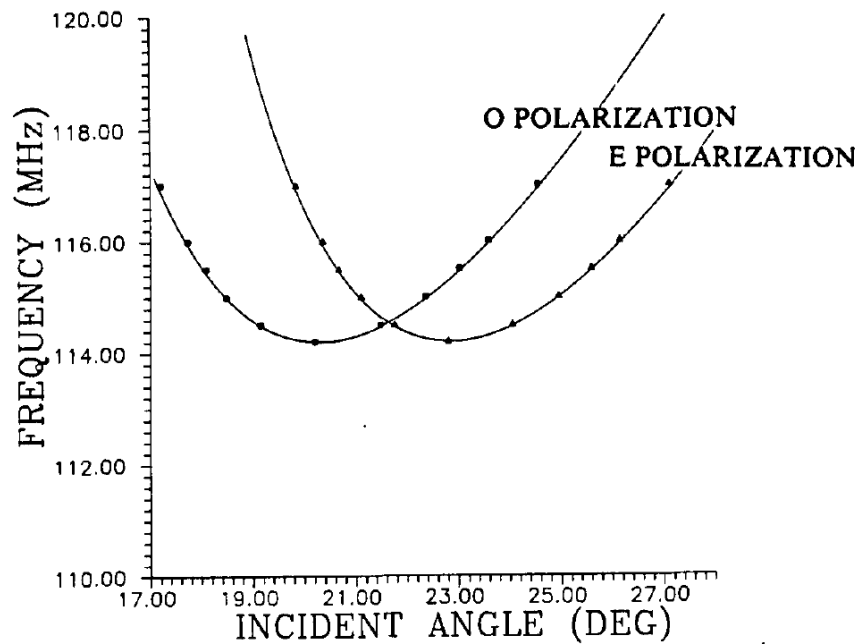


Figure 2.14: Experimental results for tuning frequency for peak diffraction in relation with the varying angle of incidence for ordinary and extraordinary polarized rays [26].

The other influence on the tuning frequency for the momentum-matching condition is related to the manufacturing of the AOTF itself. The cut angle α made between the transducer's positioning and [110] axis, as pictured in Figure 2.3, determines the direction of the acoustic wave in the crystallographic space. By looking at the wave-vector diagrams in Figure 2.12, it is shown that the shortest distance between the two refractive index ellipses can be achieved when angle α is equal to zero. The choice of angle α varies per AOTF device, but what all AOTF designs strive to achieve is to minimize the dependence of the desired diffracted wavelength on the incidence angle [26], and the non-collinear AOTF with $\alpha = 0^\circ$ are almost never described in literature.

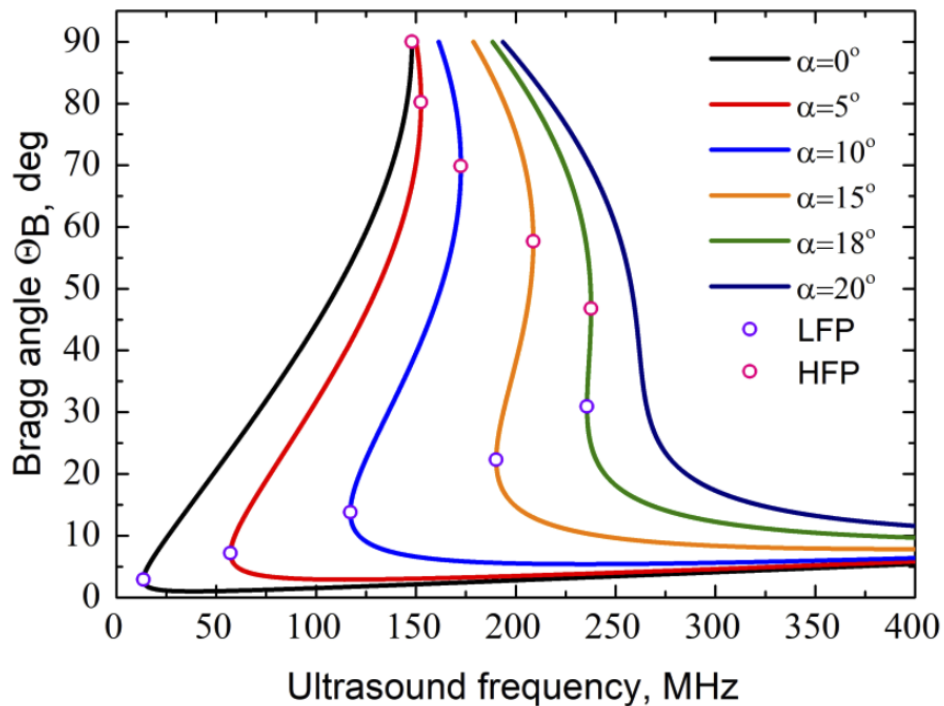


Figure 2.15: Frequency dependence on the cut angle α and the incident angle, in case of the Bragg diffraction in the TeO_2 crystal for 633nm optical wavelength [28].

From Figure 2.15 it is shown that the larger acoustic cut angle α causes the tuning curve to shift towards higher

frequencies as well. This phenomenon is not only related to the fact that the acoustical vector \mathbf{k}_a travels a larger distance in a wave vector diagram, if a larger α angle is chosen. The other factor is related to the acoustical velocity (V) inside the crystal, where for TeO₂ velocity along the [110] axis is $V_{110} = 616m/s$ and along [001] axis is $V_{001} = 2104m/s$ [29]. The acoustical phase velocity can be found by Equation 2.14 [30], where if the angle α is larger the acoustical wave propagates more along [001] axis causing the value of acoustical velocity to increase too, as $V_{110} > V_{001}$.

$$V^2 = V_{110}^2 \cos^2(\alpha) + V_{001}^2 \sin^2(\alpha) \quad (2.14)$$

The conclusion on the frequency tuning for momentum-matching condition is that finding a suitable frequency is challenging as this variable is dependent on angle of incidence, the incoming optical wavelength, and also on how the AOTF was built. The latter one is often unknown to the user. To conclude, the frequency required for momentum-matching condition does increase if either the angle of incidence is further away from [001] axis, the wavelength for diffraction is decreased, or finally if the AOTF's tilt-angle α is larger.

2.6.2 Eigenmode polarization state changes during AO interaction

As mentioned previously, in an anisotropic medium like the birefringent crystal, the entering light is decomposed based on two eigenmodes, the ordinary and extraordinary [15]. Each wave entering the medium is decomposed between these two eigenmode components, based on the polarization of the wave.

In Figure 2.16, a practical example is shown with polarization ellipsoids along crystallographic planes. Where the ellipsoids with the larger area are for n_e and circular eigenmodes represent the n_o .

The e-light, in the example shown in Figure 2.16, is polarized along the same axis as the sending of an acoustic wave, the [110] axis, meaning the electric field oscillation is happening in this direction. The o-light is then polarized oppositely, along the $[\bar{1}10]$ [15]. The overline symbol on the first number means that the crystallographic plane starts from the negative x-axis, for demonstration this orientation would look similar to the red plane shown in Figure 2.8, but shown behind it.

Both of these planes are 90 degrees from each other, and the property of the birefringent crystals is that oscillation along a certain plane would be different in terms of the phase change. The e-light (extraordinary polarized light) will experience a greater refractive index compared to the o-light, which means that the e-light would propagate slower in the medium. This birefringence will already create a phase shift between the eigenmodes before the AO interaction [31].

In cases of light diffraction by the shear acoustic wave. The shear acoustic wave sent by the transducer is sent at 45 degrees with respect to the polarization vectors of the eigenmodes [31]. It can also be sent with a slight deviation from the plane by a few degrees [32], caused by a crystal's tilt angle, or in the notation of this report the crystallographic axis angle θ_c , during the manufacturing of AOTF crystal.

In the example case shown in Figure 2.16, the acoustic grating is sent along the [110] crystallographic axis which can be broken down into axis components of X [100] and Y [010]. These two axes are exactly 45 degrees compared to the o-light and e-light eigenmodes.

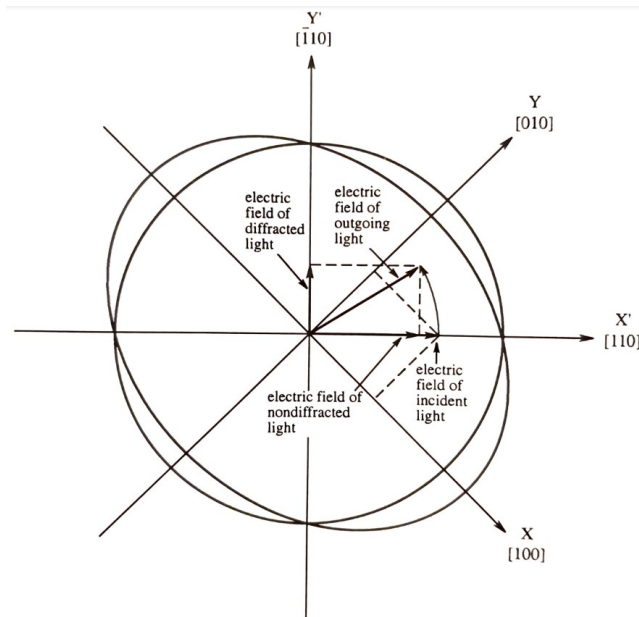


Figure 2.16: Eigenmode polarization state changes in birefringent AO interaction [15]

The acoustic waves contain strains due to the previously mentioned elasto-optic effect. These strains act as a grating where the gratings are shifted with respect to each other by half-wavelength [31], this parameter can be tuned by the frequency sent to a piezoelectric transducer. The grating's amplitudes of the refractive index periodically change based on the material's birefringence. This shift between the gratings gives a phase shift.

This strain causes the waves to propagate along other principal axes, in the current example along X [100] and Y [010]. This principle axis change happens due to the material's elasto-optic coefficient (p_{44}) which was used for the calculation of the material's figure of merit in Equation 2.1, and causes the eigenmodes to become more elliptical along the new principle axes, as seen in Figure 2.16. The p_{44} term causes the eigenmode polarization directions to be reoriented along a new axis system from $X'Y'$ to XY [15].

The previously e-polarized light travelling along [110], now has to be decomposed along a new axis system, causing the polarization direction of the outgoing light to rotate as it propagates through the medium [15]. Part of the light is diffracted from the original e-polarized wave. To compensate for the polarization direction the diffracted light has a 90-degree polarization to the e-light [15], and the diffracted light according to the definition is the o-light.

2.7 Optical activity and gyration

In Section 2.6 it was mentioned that there are two other methods to identify the refractive index in the crystallographic axis system. Those two methods are related to the optical activity of the crystal, and some background information is required first. While doing testing, it was found that the AOTF crystal made of TeO_2 has a noticeable optical activity effect by the name of the rotatory power [33].

This section will delve into the rotatory power phenomenon in Subsection 2.7.1, then look how it changes depending on the ray's position inside the crystal (Subsection 2.7.2), and finally quantify the impact of the rotatory power on the refractive index ellipses and provide the remaining two methods for refractive index calculation, based on literature.

2.7.1 Rotatory Power

Rotatory power is a phenomenon, where a linearly polarized light rotates its polarization direction as the wave travels through the medium. This effect can occur in the optically active solids, isotropic media and crystalline solids [34]. An illustration of the rotatory power is seen in Figure 2.17, where vertically polarized light enters the optically active sample under number five. The polarization of light rotates anticlockwise, in this example, and reaches the observer at a new polarization angle.

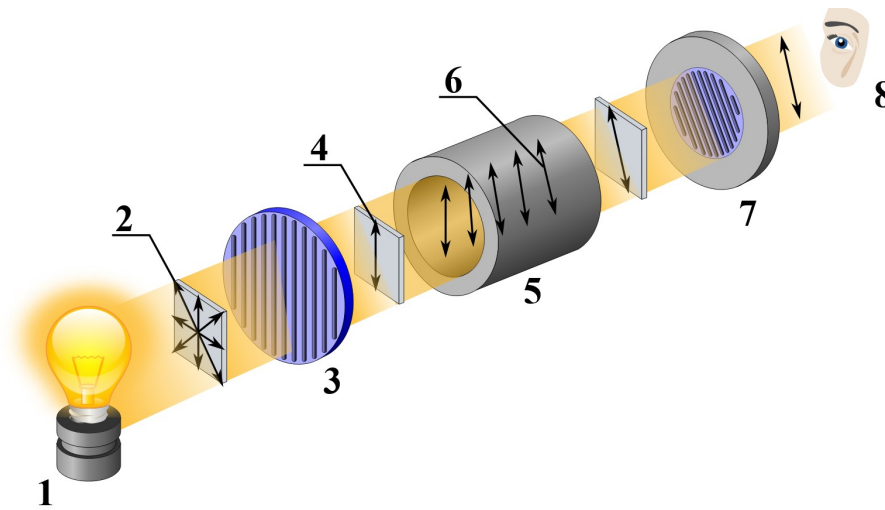


Figure 2.17: Rotatory power effect with a sample [35].

To simplify, the TeO_2 crystal has an ability to change the polarization state of the incoming polarized light. This optical activity is wavelength dependent, according to the Uchida [23] where an experiment and an analytical model were introduced to study this optical property of the TeO_2 material.

From the experiment a set of data points were provided, and in order to make the relation of rotatory power with wavelength continuous for the analytical mode, a fit function was used. A power law function fitted the experimental data the best, which can be seen in Figure 2.18 where the wavelengths from 370 until 1100nm were taken, producing the relation seen in Equation 2.15.

$$|\rho| = 8.18\lambda^{-4.2} + 25.68 \quad (2.15)$$

$$|\rho| = 15.914\lambda^{-3.282} + 15.303 \quad (2.16)$$

It can be noticed that at the lower wavelengths in the visible range, the rotatory power can reach up to 600 degrees of rotation per millimetre of sample length, and for the wavelength of 635nm, the wavelength used in the AOTF experiments, the rotatory power was around 86 deg/mm. This effect is measured along the [001] axis, where the rotatory power is the strongest [36].

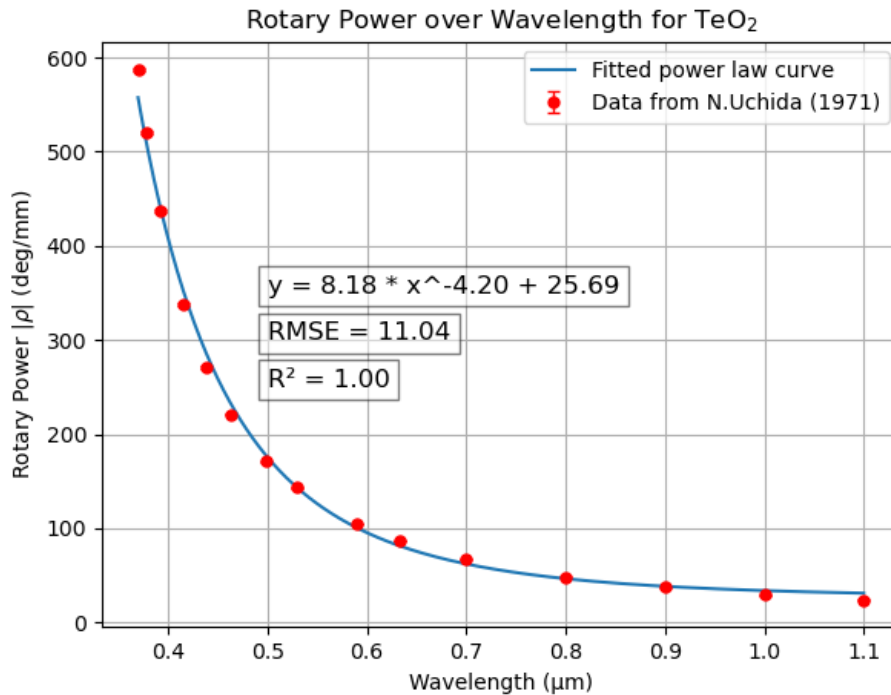


Figure 2.18: Power Law relation based on the experimental data from the experiment done by Uchida (1971) [23].

The rotatory power values provided by Uchida seemed high at the first glance, however, after looking at the Equation 2.17, it can be seen that there is a division by a small value of λ making the rotatory power ($|\rho|$) to appear large. The refractive indices n_r and n_l represent the right-hand and left-hand circularly polarized eigenmodes [37], convention is while looking at the source.

$$|\rho| = \frac{\pi}{\lambda} |n_r - n_l| \quad (2.17)$$

According to the Jones polarization vectors, every linear polarization can be represented as a superposition of two oppositely oriented circular polarizations [38], which can be observed in Figure 2.19. If the refractive index of n_r is higher than, the ray's polarization will be rotated anti-clockwise if looking in the ray's direction as shown in Figure 2.19(a), and vice versa [34]. Similarly, if $n_r = n_l$ then there is no rotation in polarization present.

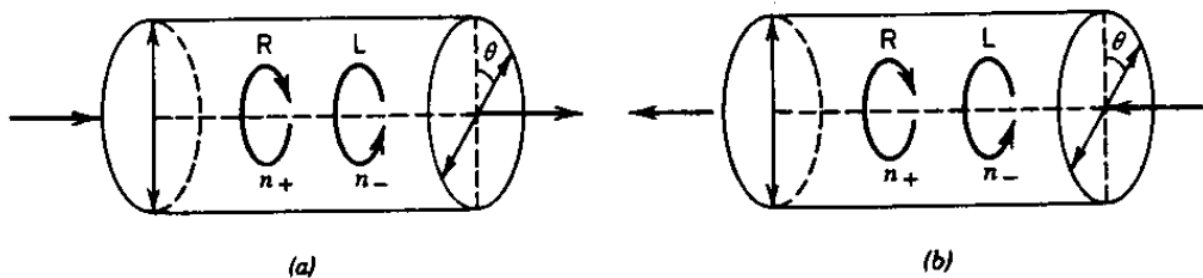


Figure 2.19: (a) Rotation of the plane polarization in the optically active medium, where the right circularly polarized wave rotates faster $n_r < n_l$. (b) if the wave from (a) is reflected back to the medium, the plane of polarization rotates in the opposite direction. [39]

In case of TeO_2 , the material is dextrorotatory, meaning that the optical rotation is expected to be anti-clockwise in the ray's direction [40]. This material property will be tested in the experiment.

2.7.2 Gyration tensor and relation in the crystallographic axis

The values found from Uchida were surprisingly high, and it was quite hard to believe that the polarization changes 86 degrees per mm inside the material for the wavelength of 635nm. Therefore, this topic was studied further, and it was found that this effect significantly reduces if the ray is propagating further away from the crystal's [001] axis.

It was found that the rotatory power (ρ) is dependent on the material's gyration tensor (G), which can be illustrated by Equation 2.18 [38]. Equation 2.18 is only applicable for the optically active material where $G \ll n_o$, where TeO_2 does fit these criteria [39].

$$\rho = \frac{\pi G}{\lambda n_o} \quad (2.18)$$

The gyration tensor is responsible for the rotation of the polarization plane going through the material, and it varies in magnitude depending on the ray's direction. It could be found using the Equation 2.19, where the gyration vector (g_{ij}) is multiplied by the quadratic function of directional cosines ($s_i s_j$). The directional cosines, do represent the direction of the ray in the crystallographic axis system [001] and [110], the one which is used in the analytical model in Chapter 4.

The shape of the gyration vector (g_{ij}), is material dependent, TeO_2 has tetragonal 422 shape which corresponds to the gyration vector represented in Equation 2.20 [38], where the value g_{33} represent gyration along the optical axis ([001]) and $g_{11} = g_{22}$ for the other two crystal's axes [40].

$$G = g_{ij} s_i s_j \quad i, j = x, y, z \quad (2.19)$$

$$g_{ij} = \begin{pmatrix} g_{11} & 0 & 0 \\ 0 & g_{11} & 0 \\ 0 & 0 & g_{33} \end{pmatrix} \quad (2.20)$$

The g_{33} value is significantly larger, according to Maak et al. (1999) $g_{33} = 678 \times 10^{-6}$ and $g_{11} = 1 \times 10^{-7}$ at $\lambda = 633nm$ [36]. This does make sense, as the rotational effect is the strongest along the optical axis [001]. Measuring the optical activity for gyration tensor perpendicular to optical axis (g_{11}) is complicated due to TeO_2 high birefringence, which makes it difficult to experimentally test the true variable's value [3].

Considering the fact that the variable g_{33} is along the optical axis, the magnitude of this variable is directly correlated with the power curve shown in Figure 2.18, for the rotatory power according to Uchida (ρ_u). By using Equation 2.18, the wavelength dependent variable g_{33} can be found, and is illustrated in Equation 2.21.

With the g_{11} variable in relation to the wavelength, due to the lack of information, a scalar multiplication was used shown in Equation 2.22, where values at 633nm according to Maak et al. were used and multiplied with the g_{33} value found in Equation 2.21.

$$g_{33}(\lambda) = \frac{\rho_u(\lambda) n_o \lambda}{\pi} \quad (2.21)$$

$$g_{11}(\lambda) = \frac{g_{33}(\lambda)}{g_{33}(633nm)} g_{11}(633nm) \quad (2.22)$$

Using these relations, a gyration tensor vector (g_{ij}) could be constructed and by varying directional cosines vector with an angle θ defined as zero at [001] axis. A relation could be drawn, which is shown in Figure 2.20, where a higher angle away from the optical axis [001] causes the rotatory power to be decreased.

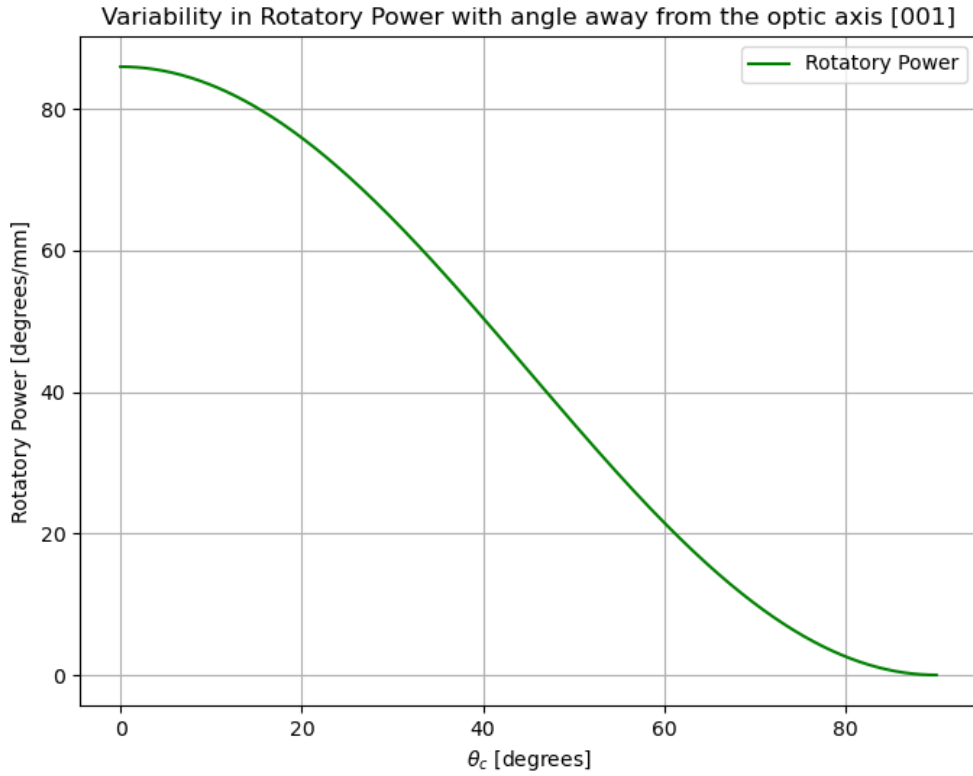


Figure 2.20: Rotatory power relation with a variable angle away from the optical axis [001].

From Figure 2.20, it can be seen that the rotatory power does significantly decrease as the angle from the optical axis increases. The value can decrease even further, however, if the AOTF has been in use previously, and it could have been irradiated during this time, which does reduce the gyration effect [41]. In either of the cases, the value for rotatory power remains significant even at 60 degrees away from the optical axis [001], and the rotatory power effect on the refractive index ellipses should be investigated.

2.7.3 Impact of polarization change on refractive indices

The second method, of finding the effective refractive indices in the crystallographic axis space, includes the rotatory power effect. This method has been used by the Voloshinov et al. (2017) [37]. This method is a simplified approach to involve the gyration effect on the refractive index, and it is a good approximation for the θ angles of 5° or below [37]. In this method, the shape of the ellipse is altered at an optic axis [001] by a value σ , calculation of which can be seen in Equation 2.23.

The parameter σ represents the change of refractive index due to the rotatory power. The rotatory power, in the meantime, is wavelength dependent (Equation 2.15). For the ordinary ray, the refractive index value along the optic axis is reduced and contrary for the extraordinary ray. This relation can be seen in Equation 2.24 and Equation 2.25, respectively. Alternatively, these relations are visualised in Figure 2.21, where the new relation for the ordinary ray is represented in blue colour and for the extraordinary ray in green colour.

$$\sigma = \frac{\rho(\lambda)\lambda}{2\pi} \quad (2.23)$$

$$n_{o2}(\theta) = \left(\frac{\cos^2(\theta)}{(n_o - \sigma)^2} + \frac{\sin^2(\theta)}{n_o^2} \right)^{-1/2} \quad (2.24)$$

$$n_{e2}(\theta) = \left(\frac{\cos^2(\theta)}{(n_o + \sigma)^2} + \frac{\sin^2(\theta)}{n_e^2} \right)^{-1/2} \quad (2.25)$$

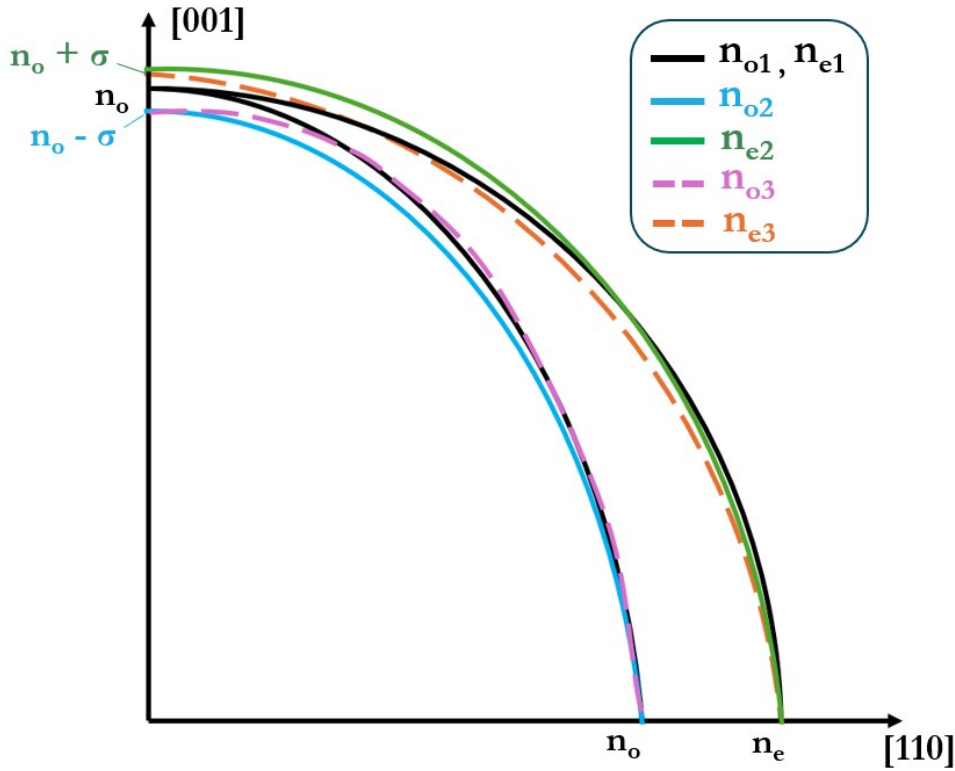


Figure 2.21: New refractive indices ellipses based on Voloshinov/Fresnel's relations shown in colours (solid lines for Voloshinov and dashed lines for Fresnel), and relations by Gass are shown in black.

The third method, is dependent on the gyration tensor, introduced in Subsection 2.7.2. The method follows the Fresnel's equation, which for uniaxial crystals follows the relation presented in Equation 2.26 [38], where n_i represents the refractive index of an incident ray, the parameter of interest. This method consists of two steps, where firstly it is required to find variables n_{o1} and n_{e1} based on the previously used relation from Gass and to find the gyration tensor (G) using the relation presented in Equation 2.19.

$$(n_i^2 - n_{o1}^2)(n_i^2 - n_{e1}^2(\theta)) = G^2 \quad (2.26)$$

After finding relevant variables, refractive indices can be derived from the Fresnel's relation, which are presented in Equation 2.27 for the ordinary ray and in Equation 2.28 for an extraordinary ray. A full derivation of these refractive indices can be found in Appendix A, which involves the use of the quadratic formula.

$$n_{o3}(\theta) = \left(\frac{(n_{e1}^2(\theta) + n_{o1}^2) - \sqrt{(n_{e1}^2(\theta) + n_{o1}^2)^2 - 4(n_{o1}^2 n_{e1}^2(\theta) - G^2)}}{2} \right)^{1/2} \quad (2.27)$$

$$n_{e3}(\theta) = \left(\frac{(n_{e1}^2(\theta) + n_{o1}^2) + \sqrt{(n_{e1}^2(\theta) + n_{o1}^2)^2 - 4(n_{o1}^2 n_{e1}^2(\theta) - G^2)}}{2} \right)^{1/2} \quad (2.28)$$

The Fresnel's formulation of refractive indices is the most accurate and at the same time the most complex from the formulations presented. The refractive indices follow an irregular ellipse pattern, which were visualised in Figure 2.21 with dashed lines.

However, to visualise the difference between the methods mathematically, Figure 2.22 has been presented where the methods were compared for the extraordinary refractive index. The green line represents the refractive index difference between the Voloshinov's value and the value found using the Gass's method, similarly the red line represent the difference between Fresnel's equation.

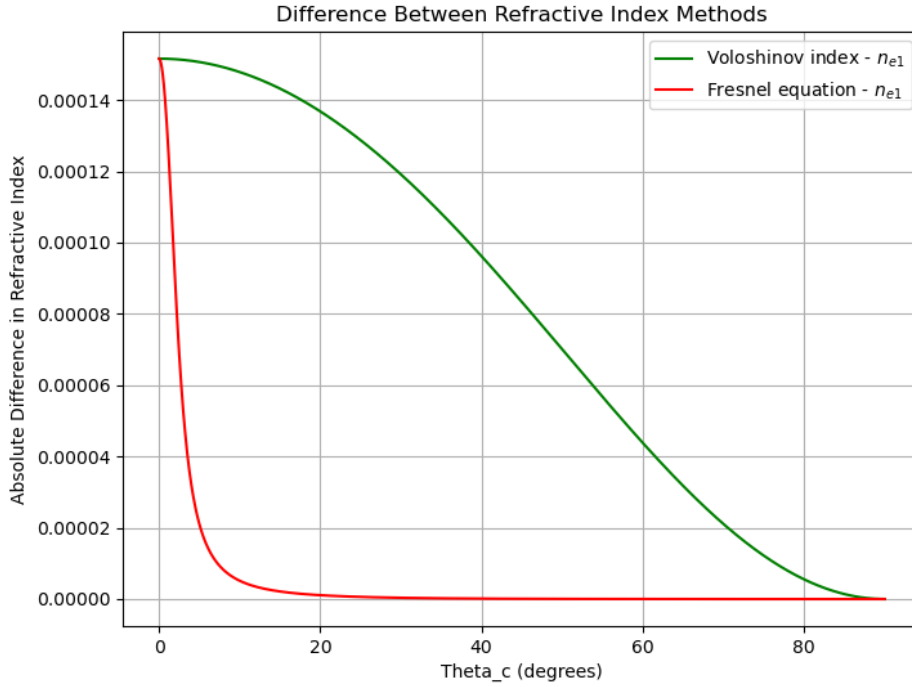


Figure 2.22: The difference in refractive index for extraordinary ray between Voloshiov and Gass (in green), and between Fresnel and Gass (in Red)

It can be noticed, that the red line quickly decreases as the angle from the optical axis increases. At an angle around ten degrees, the difference between the Fresnel's equation and the Gass becomes minimal. This finding does go inline with the statement provided by Voloshinov [37]. Considering that most of the AOTF's have a crystallographic axis angle θ_c larger than ten degrees, then it does make sense that most of the equations describing AOTF's behaviour use the relation's presented by Gass.

Another observation from Figure 2.22, it can be seen that even along the [001] axis ($\theta = 0$), the increase of the refractive index due to the rotatory power only equals to $\delta n = 1.4 \times 10^{-4}$. It is a surprising find, considering that rotatory power was found to be significant in experimental values and especially in the theoretical values provided by Uchida.

However, this minor change can still have an influence on the AO interaction, as converting the values to the wave vector space ($k_i = 2\pi n_i/\lambda$), involves a division by wavelength which can make a difference in refractive indices significant.

2.7.4 Conclusion on rotatory power

Based on the literature studied on the rotatory power, it could be said that TeO₂ is indeed highly optically active material that can rotate the polarization state while the ray of light is propagating. The rotatory power is the highest along the TeO₂ optical axis, along which the material has the lowest refractive index, in other words the [001] axis. The rotatory power reduces, if the angle between the ray and the [001] axis increases, the reduction in rotatory power is dependent on the gyration tensor G .

The impact of the rotatory power on the refractive indices can be calculated with two new methods, a simplified method proposed by Voloshinov and a more complex method involving the Fresnel's method depending on the gyration tensor and the directional cosine multiplication. If these two methods are compared with the originally used P.Gass formulation, it could be noticed that the change in refractive index becomes insignificant already at 10 degrees ray propagation away from the [001] axis. However, this optical activity still impacts the shape of the refractive ellipses, which can affect the calculations for the AO interaction as it involves the use of wave vectors. This TeO₂ should be tested experimentally, and the impact of the optical activity on the refractive results should be studied.

2.8 Electrical components

The final theory concerns the electrical components in the AOTF that precede the launch of the acoustic waves that create the wavefronts inside the material [7], required for the AO interaction. Even though the theory on the electrical components will not be used in the optical simulation, it is an important part of the theory with regard to the physical testing in order to avoid damaging the electrical equipment.

Subsection 2.8.1 will firstly go over the electrical components used to operate an AOTF device, and briefly describe the role of the electrical components in the electrical setup preceding the AOTF's crystal. Subsection 2.8.2 will go over two practicalities which are needed to be kept in mind during an AOTF testing, namely the voltage standing wave ratio (VSWR) and the transducer bandwidth. The latter describes the RF frequency range in which the AOTF functions.

2.8.1 Electrical setup overview

In case of the AOTF, the goal of an electrical setup is to generate, amplify and send the RF signal towards the transducer, while making sure that the acoustical and electrical impedance in the setup are within safe margins [4]. The setup's main components are the RF generator, RF amplifier and impedance-matching network. For illustration, the Figure 2.23 will be used in this section to explain the main components in further detail.

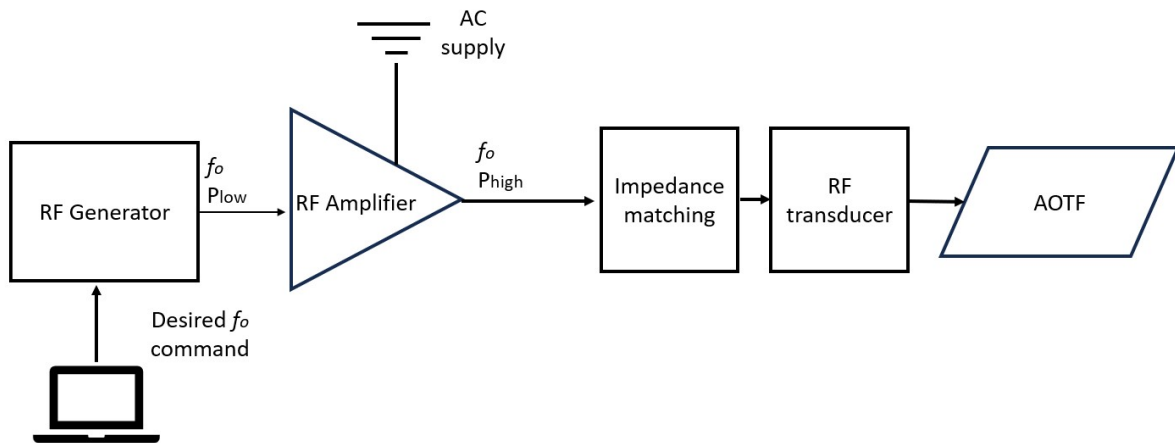


Figure 2.23: Electrical setup preceding the AOTF

The setup first starts with the user sending a command with a desired frequency, the RF generator takes this signal and generates a sin wave with the desired frequency, the power level of this signal is limited to around 0 dBm [42]. This amount of power is insufficient for the transducer to generate an acoustic wave for the AOTF, as the transducer's power requirement ranges between 100 mW to 3 W [5], depending on the AOTF and used AO material.

Therefore, the RF amplifier is connected in series with the generator [42], which increases the amplitude of the RF sin wave previously generated and subsequently increases the signal's power level [42]. However, to amplify the generated RF signal, the RF amplifier needs to take the power from somewhere else. Therefore, the RF amplifiers are typically connected to the AC source [43].

The RF transducer and the impedance matching network are going to be discussed simultaneously. The transducer is the material responsible for converting electrical (RF) energy into the mechanical energy, in this case the acoustical energy, by the means of a piezoelectric layer [44]. The impedance matching for the AOTF is commonly passive, meaning it uses thin layers of material bonding between the piezoelectric material to suffice the acoustical and electric impedance matching [4]. This is achieved due to the combination of materials which all have different inductive properties which allow matching the impedances. An example of such bonding being illustrated in Figure 2.24.

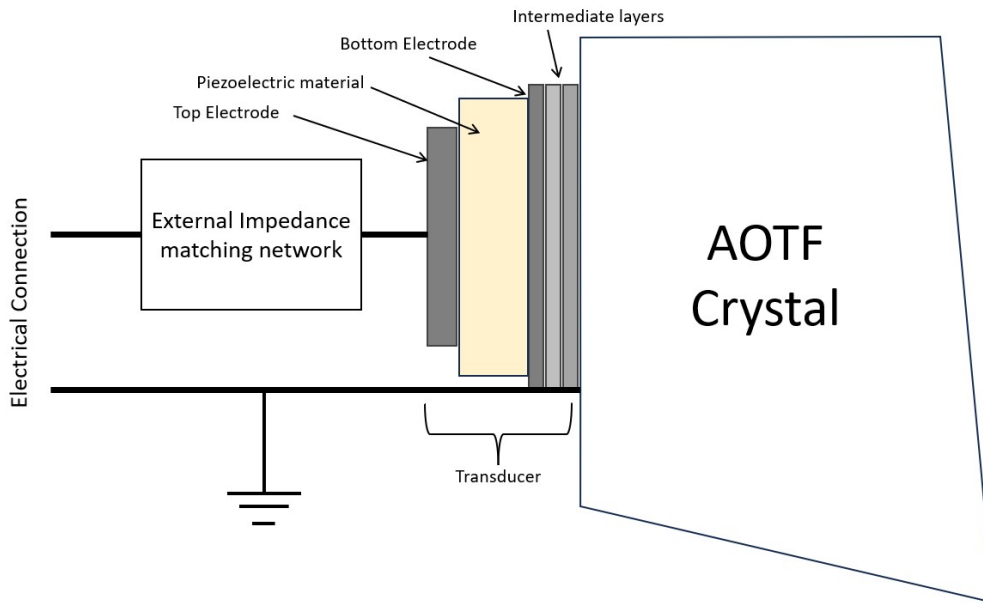


Figure 2.24: Piezoelectric transducer with impedance matching, adapted from [4].

The commonly used piezoelectric material for the AO devices is Lithium niobate (LiNbO_3) primarily because of its high electromechanical coupling factor (k) [4], that indicates the effectiveness of conversion of electrical energy to mechanical energy and the other way around [45]. However, due to the high values of k for LiNbO_3 , in ranges between 0.49-0.68, it becomes cumbersome to choose correct material layers and thicknesses to satisfy both electrical and acoustical impedances [4].

The other reason for choosing LiNbO_3 piezoelectric material, is the relatively high power handling ability (around 500mW without damage) [4]. In either way, however, it is important to make sure that the input power is within the transducer's power handling limits.

2.8.2 VSWR and transducer bandwidth

This report will not go into selection of materials for impedance matching, neither for electrical nor acoustical side of impedance matching. However, during the testing, it is important to know the AOTF's transducer bandwidth and voltage standing wave ratio (VSWR). The transducer bandwidth is the frequency range for which the electrical matching of the device is done properly [13], meaning that an acceptable amount of power is reflected back to the RF amplifier.

VSWR measures the voltage reflectance of the transducer [46], which can be calculated by Equation 2.29. This reflectance is related to the difference between the amplifier impedance output and transducer impedance input. If these impedances match, there is no voltage reflectance to the amplifier and VSWR value is equal to one, meaning that all the power is transferred to the transducer.

$$VSWR = \frac{|E_{max}|}{|E_{min}|} = \frac{|E_{inc}| + |E_{refl}|}{|E_{inc}| - |E_{refl}|} \quad (2.29)$$

Alternatively, if the impedance mismatch is present, there is a possibility that the incident voltage is reflected back to the source. The incident (E_{inc}) and the reflected (E_{refl}) voltages can resonate and be responsible for the voltage standing wave creation [4]. The ratio of the voltage wave maximum (E_{max}) and the voltage wave minimum (E_{min}) of such a standing wave is used in the voltage standing wave ratio (VSWR) terminology.

The VSWR value changes depending on the RF frequency signal applied, it is desired to operate the AOTF at the low VSWR values, below 3 [46]. Therefore, before testing an AOTF, it needs to be electrically characterised by using Vector Network Analyser (VNA) which allows determining the frequency range where the VSWR value stays below the value of 3 [46]. This consideration, together with a low power input of 100 mW, should avoid damaging the RF amplifier connected to the AOTF.

Research Description 3

Considering the outlined motivation to study the topic of AOTF simulation, a proper outline needs to be provided of what exactly is desired to be achieved. For this reason, a research description is provided which will state the research objective, the main research question and the sub-questions that follow from it. Furthermore, a list of requirements will be given for reference throughout the research provided in this report.

3.1 Research objective/question

The research objective of this report is to address the existing gap in knowledge regarding Acousto-Optic Tunable Filters (AOTFs). Specifically, there is a lack of comprehensive simulations capable of characterising the behaviour of AOTFs across a selected band of the light spectrum. This report aims to develop and validate an analytical model for a non-Collinear AOTF that is effective within the visible light spectrum (400-1100nm).

Research Objective:

“To develop and validate a comprehensive analytical model of a non-collinear Acousto-Optic Tunable Filter (AOTF) based on tellurium dioxide (TeO_2) that is operational in the visible spectrum of light (400-1100 nm).”

The reason for choosing a non-collinear type of AOTF based on tellurium dioxide (TeO_2), comes down to the fact that these AOTF types are the most common in the industry and are the most available commercially for validation [3]. Extending the model to other AOTF types or alternative Acousto-Optic (AO) materials would require a different theoretical framework for AO interactions. This emphasizes the importance of only focusing on the non-collinear type in this research. This leads to the main research question aimed to be answered in this report, which is closely connected to the research objective.

Main Research Question:

“How can the performance of the non-collinear Acousto-Optic Tunable Filter (AOTF) based on tellurium dioxide (TeO_2) be accurately simulated, be physically validated, and be effectively characterised?”

The main research question encompasses three key areas: analytical model development, validation, and AOTF characterisation. To provide clarity, it is divided into specific sub-questions. Sub-questions 1–3 address the model development, while sub-questions 4–6 focus on the model validation and the AOTF characterization.

Sub-Questions:

1. Which AOTF parameters are essential for building the analytical model for AOTF optical simulation?
2. How is the propagation through the crystal of the diffracted and undiffracted rays simulated in the analytical model?
3. How can the Acousto-Optic interaction be simulated and provide the RF signal required for the momentum-matching condition to occur?
4. What test methodology would be sufficient to validate the outputs of the AOTF analytical model for a specific wavelength?

5. Can the analytical model created be used to characterise a commercially bought AOTF, in terms of crystallographic axis angles (θ_c and α) and facet geometrical angles (γ and β)?
6. Does the diffraction efficiency stay the same for all incidence angles in the momentum-matching condition, and if not, what factors influence it?

3.2 Requirements for analytical model and testing

Based on the research questions outlined, it is important to specify the requirements that will help answer these questions and also to quantify whether the analytical model is performing to the expected standard. The requirements can be broken down into four main categories. The first one is related to the analytical model, where in essence it needs to be ensured that the model works in 3D, does not break down when the user specifies a wavelength within the visible range, and can provide versatility to the user.

The second category focuses on the verification of the analytical model, making sure that the model's output is in line with the experimental results. The third category concerns the validation process, which involves setting up a reliable test environment to measure the AOTF behaviour at various incident angles. Finally, the fourth category addresses the characterisation of the AOTF. This involves developing methods to accurately determine the crystallographic angles and automating the characterisation process for commercially available AOTFs.

Overall Requirements for Analytical Model

The analytical model requirements, presented below, will be targeted in Chapter 4, where the analytical model will be developed and explained.

- [SIM-REQ-001] The analytical model shall be integrable into Zemax or other ray tracing software.
- [SIM-REQ-002] The analytical model should be continuous in terms of:
 - Optical wavelength within the visible spectrum of light.
 - Refractive indices.
 - Optical activity (gyration).
- [SIM-REQ-003] The analytical model should be applicable to both ordinary and extraordinary incident ray polarization states.
- [SIM-REQ-004] The analytical model shall include the capability to rotate the AOTF, providing versatility in optical design and alignment.
- [SIM-REQ-005] The analytical model shall operate in 3D to incorporate potential inclinations in both vertical and transverse direction.

Requirements for Analytical Model Verification

The analytical model verification is performed by comparing the model's outputs, with either results from literature or the experiment performed at UPHF. The verification analysis is performed at Chapter 5, where the model's outputs should satisfy the requirements below:

- [VER-REQ-001] The separation angle difference between the analytical model's output and the experimentally obtained values should be below 0.02 degrees.
- [VER-REQ-002] The difference in the applied RF signal value for achieving the momentum-matching condition should be below 0.5 MHz when compared to experimental results.

Requirements for testing methodology and validation

The validation of the analytical model involves the physical testing on the AOTF (Chapter 6), and then comparing the results from the experiment to the model's outputs. The requirements can be split into two categories. Requirements for the testing methodology are marked with TEST, and requirements for the model's validation are marked with VAL.

Testing methodology:

- [TEST-REQ-001] The optical test setup must be properly aligned to ensure accurate measurement of output angles.
- [TEST-REQ-002] A test setup must be devised that can accurately quantify both diffracted and undiffracted ray angles for varying incident ray angles.
- [TEST-REQ-003] The test environment should be in a dark setting to accurately identify the highest intensity of the diffracted ray.
- [TEST-REQ-004] A test setup should include a measurement of diffracted ray intensity.
- [TEST-REQ-005] The RF signal applied to the AOTF should be within VSWR range.
- [TEST-REQ-006] The RF signal shall be recorded when the highest intensity of diffracted ray is observed.
- [TEST-REQ-007] The method for varying the incidence angle inside the crystal shall be implemented in the optical testing design.
- [TEST-REQ-008] The applied power during AOTF testing shall be within transducer's power handling abilities.

Validation:

- [VAL-REQ-001] The model shall produce realistic results at various rotational angles.
- [VAL-REQ-002] The model accuracy for diffracted and undiffracted angles shall be within 0.1° in comparison to experimental results.
- [VAL-REQ-003] The model shall work for both incident extraordinary and ordinary polarizations
- [VAL-REQ-004] The factors affecting the diffraction efficiency shall be identified.

The accuracy for the validation is lower than in the verification requirements, due to the unknowns with the crystallographic angles.

Requirements for AOTF characterisation

AOTF characterisation requirements tackle finding the AOTF angles that determine the AOTF's behaviour for diffraction and ray propagations of the exit rays. These requirements will be tackled in Chapter 7 and Chapter 8.

- [CHAR-REQ-001] A method must be developed to characterise the crystallographic angles θ_c and α of the AOTF.
- [CHAR-REQ-002] The characterisation process for commercially available AOTFs must be automated, focusing on determining crystallographic and geometric angles.

AOTF analytical model description 4

After learning about the theory on different types of AOTFs, polarization, optical properties, and AO interaction, the simulation part comes in. This chapter aims to provide a detailed explanation of the analytical model, from a mathematical perspective, that will be used in the simulation tool that will describe optical behaviour of an AOTF. The goal of the analytical model is to provide a ray tracing model where the user can specify an input ray's direction, polarization and the ray's wavelength. As an output, the model then provides the user the ray's optical path through the AOTF as well as ray tracing of the diffracted ray, accompanied with the frequency signal required for the momentum-matching condition. The final goal is to have a model which is valid for a range of incident wavelengths.

As mentioned previously, in literature, there is a limitation of papers that create a simulation of an AOTF, or similarly, there are no open source simulations of the AOTF from an optical perspective. However, there is an AOTF simulation proposed by Zhao et al. (2014), where the authors split the AOTF into three separate surfaces, and provided mathematical equations for an analytical model using directional cosines in 3D [47]. In this chapter, their model has been used as initial guidance and adapted to make equations more user-friendly, as well as to provide explanations of what the equations represent. Furthermore, several adaptations were implemented to the analytical model, which would allow simulating diffractions for both incident ordinary and extraordinary rays, as well as the implementation of the AOTF rotation, allowing further versatility in the optical design planning.

To start describing the analytical model, a basic recap of rotational matrices will firstly be provided in Section 4.1, which will be needed for transformations between the global axis system and the crystallographic axis. Afterwards, considering that the analytical model involves multiple computational stages, an overview of those stages and the three main AOTF surfaces are presented in Section 4.2. Section 4.3 goes into the analytical model itself, with subsections describing the substages required for the three AOTF's surfaces, namely the entrance facet, AO field, and the exit field. The model is then further adapted in Section 4.4 and Section 4.5, where the analytical model could work for extraordinary polarized ray and include the rotation of the AOTF's positioning, respectively. Afterwards, Section 4.6 provides a visualised ray tracing output of the model for an incident ordinary polarization ray.

4.1 Rotational matrices

The rotational matrices are a tool that will be used in this simulation to either rotate the coordinate system in which the rays are propagating or to rotate the ray vector's direction by the desired angle. There are only two axes around which the rotations will be performed in the analytical, the X axis (Figure 4.1) and the Y axis (Figure 4.2). These rotations will be performed in 3-Dimensional space, and will be required for multiple substages throughout the model. Therefore, this section will discuss how these rotational matrices work, and provide an example on how the switch between the global and crystallographic axis systems is performed, before advancing to how the model works.

The first rotational matrix is the rotation around the X-axis, visualised in Figure 4.1 in the left-handed coordinate system. The reason for choosing this type of system instead of the conventional right-handed system comes to the fact that the reference simulation by Zhao et al. have used this type of system [47], making it easier to reference for the initial steps of building the AOTF analytical model.

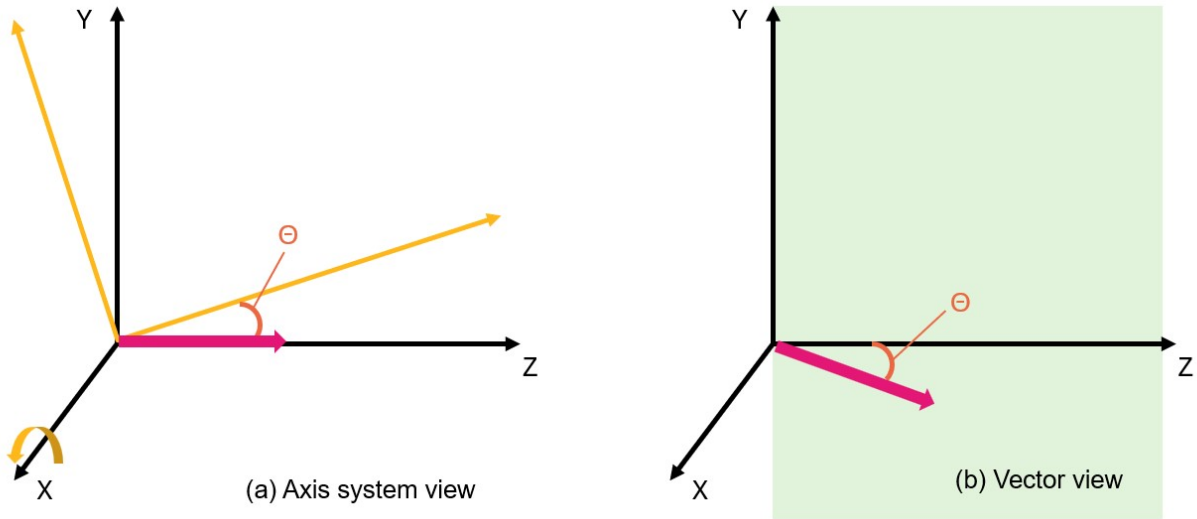


Figure 4.1: Effect of the rotational matrix around X-axis in (a) axis system view and (b) vector view.

To perform a rotation around the x -axis in the left-handed system Equation 4.1 is used [48], where the notation $\mathbf{R}_x(\theta)$ is used to show that the rotation is around the x -axis by an angle θ . The rotation around x -axis can either mean the axis-system transformation (ex: switching between the global axis system and the crystallographic axis system), such transformation can be seen in part (a) of Figure 4.1 [48]. Alternatively, it may be desired to change the ray's direction (example: to change propagation of the incident ray), in this case $\mathbf{R}_x(\theta)$ will rotate the propagation vector in the YZ -space by an angle θ , as shown in part (b) of Figure 4.1

$$\mathbf{R}_x(\theta) = \begin{bmatrix} 1 & 0 & 0 \\ 0 & \cos \theta & -\sin \theta \\ 0 & \sin \theta & \cos \theta \end{bmatrix} \quad (4.1)$$

Similar rotation can be performed around the y -axis by a rotation matrix $\mathbf{R}_y(\phi)$ presented in Equation 4.2 [48]. In this case, the axis system can be rotated around y -axis as shown in part (a) of Figure 4.2. Similarly, the same rotational matrix can be used to rotate the direction of a vector by an angle ϕ in the XZ -space, as shown in part (b) of Figure 4.2.

$$\mathbf{R}_y(\phi) = \begin{bmatrix} \cos \phi & 0 & -\sin \phi \\ 0 & 1 & 0 \\ \sin \phi & 0 & \cos \phi \end{bmatrix} \quad (4.2)$$

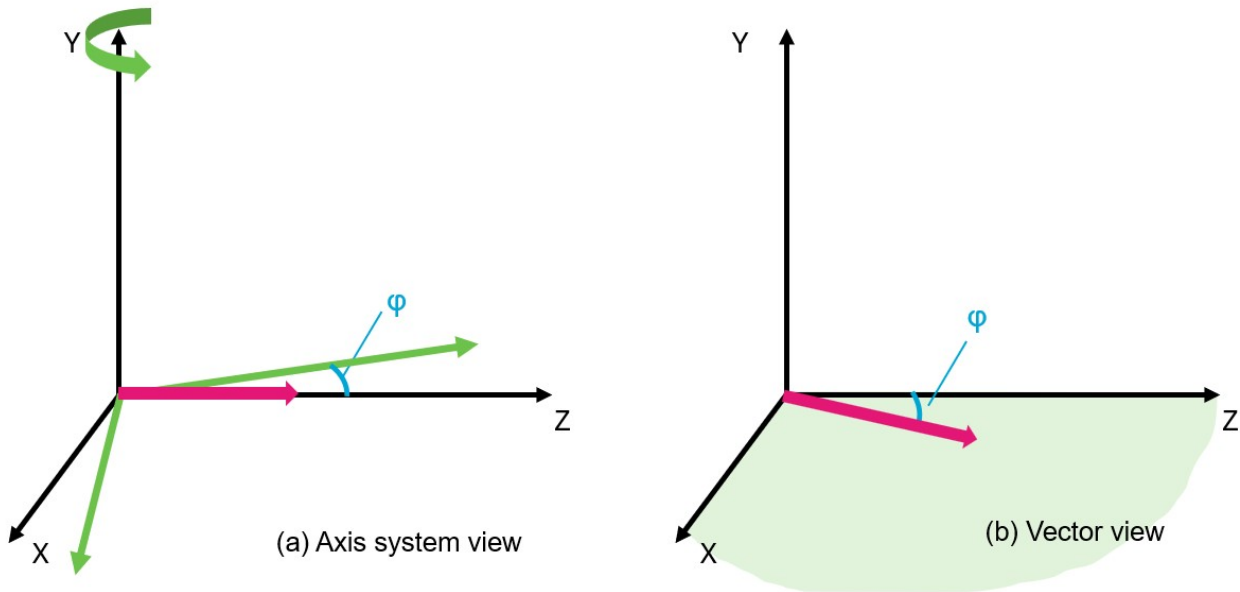


Figure 4.2: Effect of the rotational matrix around Y-axis in (a) axis system view and (b) vector view.

The convenience of this system is that both of the rotational matrices can also perform the rotation in the opposite direction, by changing a sign of the angle. This allows the analytical model to easily switch between the coordinate systems by applying $\mathbf{R}_x(\theta)$ to make iterations in one coordinate system and then transform back to the original coordinate system by applying $\mathbf{R}_x(-\theta)$.

4.2 Notations and the Three surface model

After outlining how do the rotational matrices work. This section provides an overview of the notation used in the analytical model. Given the model's multiple intermediate steps, tracking progress in the simulation can be challenging. Therefore, before delving into the mathematical calculations, this section outlines the model's structure and explains the notations used.

Subsection 4.2.1 provides an explanation of directional cosine matrix notation, which will be used to represent the rays in 3-dimensional vector space. Afterwards, Subsection 4.2.2 provides the three main AOTF surfaces and key AOTF crystal's angle definitions. Subsection 4.2.3 provides the notation used for different rays and substages used in the model, and finally Subsection 4.2.4 provides a sequential positioning of rays and substages in the model.

4.2.1 Directional cosine matrix

To represent the ray's direction in 3D space, a directional cosine matrix (DCM) will be used in the analytical model. DCM is a fundamental way to describe an attitude of an object in a three-dimensional space [49], in this case the object is the ray of light propagating in the AOTF. Direction cosines are the cosines of angles, between the vector and the coordinate frame [49], a representation of which can be seen in Figure 4.3. In simple words, DCM projects a directional unit vector along the reference axis frame [49]. The reference axis frame will be changed multiple times throughout the analytical model.

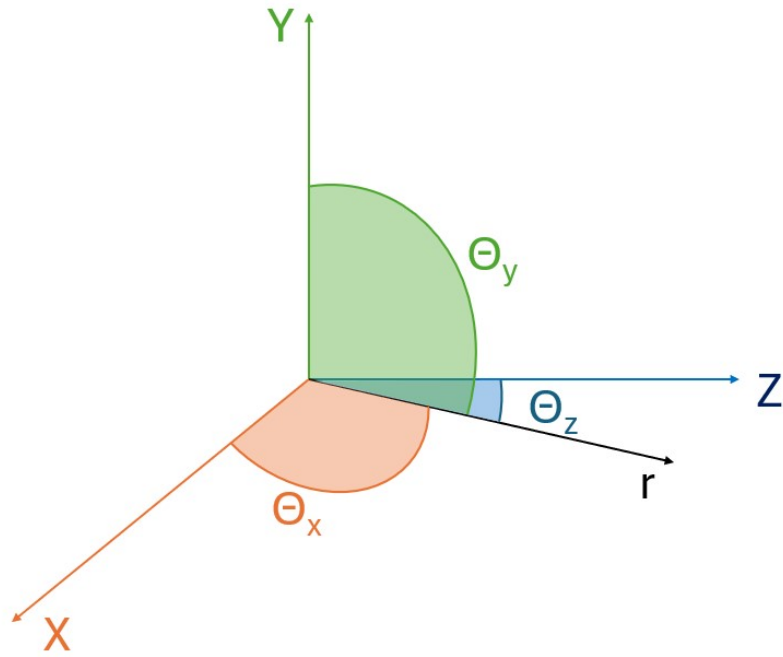


Figure 4.3: Representation of the ray vector orientation with respect to DCM angles, adapted from [49].

The DCM for each light ray r is represented as a 3x3 matrix with variables L , M , and N representing directional cosine value along x , y and z axes respectively (Equation 4.3). The rays in the model will mainly be propagating along the z -axis (optical axis), therefore it will be expected that the N variable will have the largest value for ray representations, or analogously θ_z will be the smallest angle from the 3 axis angles used.

$$\mathbf{r} = \begin{bmatrix} L \\ M \\ N \end{bmatrix} = \begin{bmatrix} \cos \theta_x \\ \cos \theta_y \\ \cos \theta_z \end{bmatrix} \quad (4.3)$$

4.2.2 Three surface model and key crystal angles definitions

The AOTF's analytical model can be broken down into three main surfaces, which are depicted in Figure 4.4. The first surface is the AOTF's entrance facet, which has an inclination angle γ . The second surface is the acoustic column where the AO interaction is happening, and two types of beams are produced, the diffracted and undiffracted rays. These two beams continue propagating inside the crystal but this time under different refractive indices, since the diffracted ray has an orthogonal polarization to the undiffracted ray [5]. The final third surface is the exit facet of the AOTF's crystal, where an angle β is introduced at the exit facet relative to the optical axis. The angle β is responsible for reducing the variation of the diffracted angles at different wavelengths [47], which is an important property for spectroscopic applications.

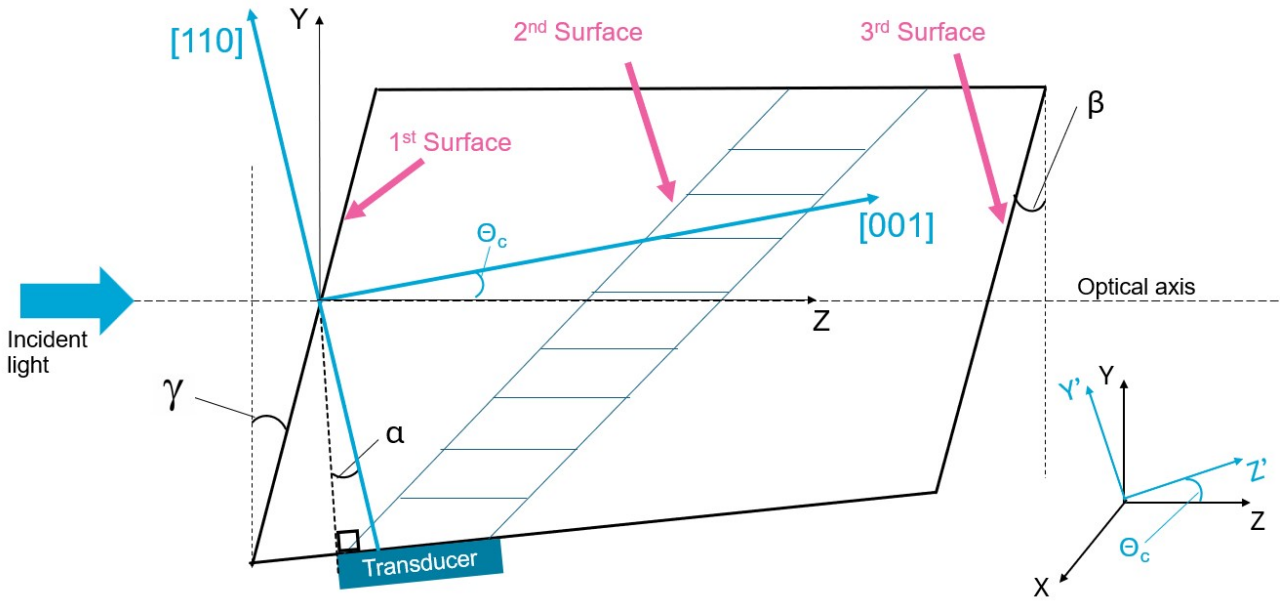


Figure 4.4: Main AOTF surfaces and variables used, also the positioning of the global (black) and crystallographic (blue) coordinate systems in the AOTF.

Throughout the analytical model, two reference coordinate systems will be used interchangeably (Figure 4.4). The O-XYZ is the global coordinate system (shown in black), and the O-X'Y'Z' is the crystallographic coordinate system (shown in light blue). In case, this analytical model is desired to be integrated into an optical simulation software, such as Zemax, the Z-axis in the global coordinate system is selected to be the optical axis of the system [50]. The x-axis is positioned normal to the acoustical field plane [47], leaving the y-axis as the plane to measure the deviations of the incident ray and the diffracted rays along the different points of the simulation.

To switch to the crystallographic axis system O-X'Y'Z' the global coordinate system needs to be rotated anticlockwise around the x-axis by the crystallographic axis angle θ_c , mentioned previously in Section 2.6. This angle represents the incident cut angle relative to the crystallographic plane of [110] [47]. Consequently, the Y' and Z' axes are parallel to the crystallographic axes of [110] and [001] respectively, while the X' axis is kept the same as the X axis [47]. Mathematically, the switch to the crystallographic axis system can be performed with the help of rotational matrix $\mathbf{R}_x(\theta_c)$ around x-axis by angle θ_c , depicted in Equation 4.1. Similarly, to go back to the global axis reference system, a rotational matrix in the opposite direction can be applied ($\mathbf{R}_x(-\theta_c)$).

The last key angle depicted in Figure 4.4 is the acoustical tilt angle, α , which is between the acoustic phase velocity vector and the [110] crystallographic axis [51]. As has been mentioned in Subsection 2.6.1, the tilt angle α influences the AO interaction and if such an angle increases, typically the frequency required for Bragg condition is also expected to be higher[28].

The angles related to crystallographic axis system θ_c and α , as well as the angles related to the AOTF's entrance and exit facet angles, γ and β , vary based on the manufacturing of the crystal. Manufacturers usually do not specify those parameters, due to competitive reasons. However, these angles are essential for characterising the AOTF's behaviour, and to satisfy the requirement CHAR-REQ-001, these angles should be targeted for AOTF's characterization.

4.2.3 Variable notation for the analytical model

After specifying the three surfaces of the AOTF, the next step is to clarify the variable notation that is associated with these three surfaces. This subsection provides an overview of the notation used in the analytical model for defining various ray and wave properties in the AOTF. The model uses three types of variables: r (directional cosines for rays), u (directional cosines for substages), and k (wave vectors). Each variable is defined explicitly, with subscripts used to specify surface interactions and polarization types. This notation system is summarized in Table 4.1.

Table 4.1: Definitions of key variables used in the analytical model.

Variable	Definition
r	Directional cosine of the ray exiting a surface
u	Directional cosine at an intermediate substage
k	Wave vector at a substage for AO interaction
0/1/2/3	Index specifying the surface
e/o	Index specifying polarization type (extraordinary/ordinary) of the ray

The main difference between a ray variable r and a substage variable u lies in their roles within the model. A substage u acts as an intermediate building block between two AOTF surfaces, representing the steps required to construct the final ray. In contrast, the ray variable r represents the resultant ray exiting a surface after all the mathematical substage operations have been completed. Meaning that for each surface, there can be multiple substages u , which together produce the ray r exiting that surface.

While the variable k can also be treated as a substage, it differs from u in that it represents a wave vector rather than a unit directional cosine. This makes k non-normalized, in contrast to the directional cosine vectors u and r . Introduction of variable k was required to apply the theory of AO interaction, which was discussed in Section 2.6.

To clarify how these variable notations are applied in practice, examples are provided in Table 4.2, showing typical use of the ray r , substage u , and wave vector k in the simulation model.

Table 4.2: Examples of variable notation in the model.

Example	Explanation
r_{1e}	Extraordinary ray exiting surface 1 (AOTF's entrance facet)
u_{1a}	Substage 'a' defining the ray at surface 1
k_{2c}	A wave vector at substage 'c' used for defining the ray at surface 2 (Acoustical field)

4.2.4 Stage and ray terminologies

After clarifying the notation of variables used in the analytical model, this subsection aims to present all the variables used in the analytical model and provide an initial overview of what each of the AOTF's surfaces is aiming to achieve.

For ordinary incident ray simulation, all variables are presented chronologically in Figure 4.5, where blue arrows represent ordinary rays (o-rays) and green arrows represent extraordinary rays (e-rays). The simulation's substages are illustrated in square boxes, annotated with the corresponding surface. For example, the substages u_{1a} and u_{1b} will be used to define the output ray at stage one, therefore those two substages are presented together for surface one. The substages in wave vector form, k_{2c} and k_{2d} , appear only at surface two, since there the AO interaction will be simulated and the directional cosines will need to be transformed into the wave vector space. For convenience, substages use alphabetical subscripts, where only the letter e is omitted to avoid a confusion with extraordinary rays.

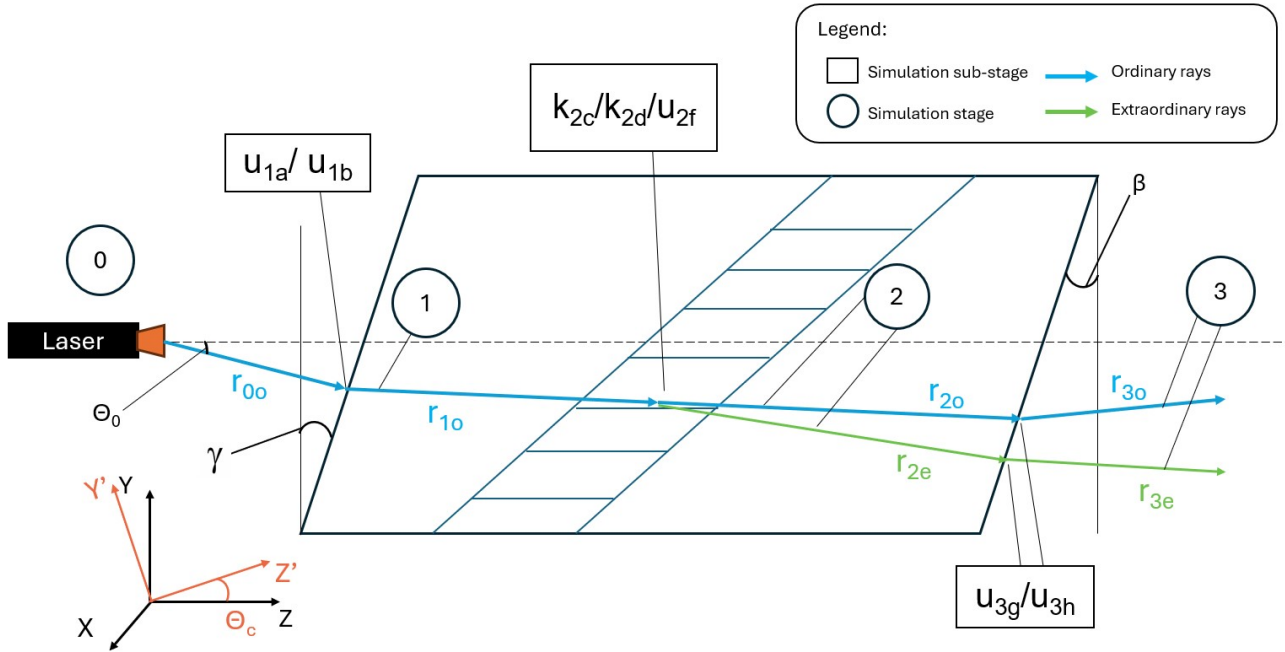


Figure 4.5: Stages and substages of ray propagation in the AOTF model, showing ordinary (blue) and extraordinary (green) rays with key AOTF angles and directions labeled.

Considering that there are multiple substages, surfaces used in the model, for each of the mathematical surface explanations a table with short explanation of each substage at the given AOTF's surface will be provided. For the analytical model overall, Table 4.3 provides a summary of each stage used in the model. The stage zero is used to describe the incident ray as a DCM vector, which will hit the first surface of the AOTF's crystal. This will result in the ray's refraction and a change in ray vector's direction ($\mathbf{r}_{0o} \neq \mathbf{r}_{1o}$). Afterwards, this ray will encounter the acoustical field, where a diffracted ray of opposite polarisation is introduced to the simulation. The two output rays from surface two, propagate until they reach the AOTF's exit surface three, where another refraction takes place and the rays leave the crystal

Table 4.3: Stages of AOTF Surface Simulation

Stage	Simulation Aim
0 - Incidence ray	Define the incidence ray as a directional vector
1 - Entrance facet	Simulate refraction using Snell's law with DCM
2 - Acoustic field	Simulate AO interaction in wave vector space and transform back to DCM
3 - Exit facet	Simulate refraction of (un)diffracted rays exiting the AOTF's crystal

4.3 Analytical Model

After describing the notations and the coordinate systems used in the model, this section focuses on the mathematical operations. The analytical model can work for two cases, either when the incident ray is ordinarily or extraordinarily polarized. The order of calculations does differ between these two cases. Therefore, to avoid confusion, this section will focus on one case when the incident ray is ordinarily polarised as shown in Figure 4.5. The case for extraordinary incident ray will be briefly described in Section 4.4.

Similarly to the stages defined in Subsection 4.2.4, this section is broken down into four parts per each stage. In Subsection 4.3.1 the initial vector parameters of the input laser ray are defined, producing the ray vector \mathbf{r}_{0o} . Subsection 4.3.2 focuses on the first surface, where the transformation of the input ray is performed after it passes through the AOTF's entrance facet. Consequently, Subsection 4.3.3 focuses on the second AOTF surface, where the AO interaction is performed. Finally, Subsection 4.3.4 describes the third surface, where the refraction of two rays at the AOTF's exit facet is performed.

4.3.1 Entrance ray definition

The first stage of the analytical model has a goal to characterize the input ray, from a laser or a light source, as a directional vector. From the Figure 4.5, this stage is marked under the number 0, as it is an initial stage which precedes surface one.

From the requirement SIM-REQ-001, the aim is to make the simulation work in 3D. To accomplish this requirement, the entrance ray should be easily steered in 3D space. Therefore, as a first step, the ray from the laser is imagined to be shining along the optical axis, meaning that only the z-component is present in the ray's propagation, as depicted in Figure 4.6.

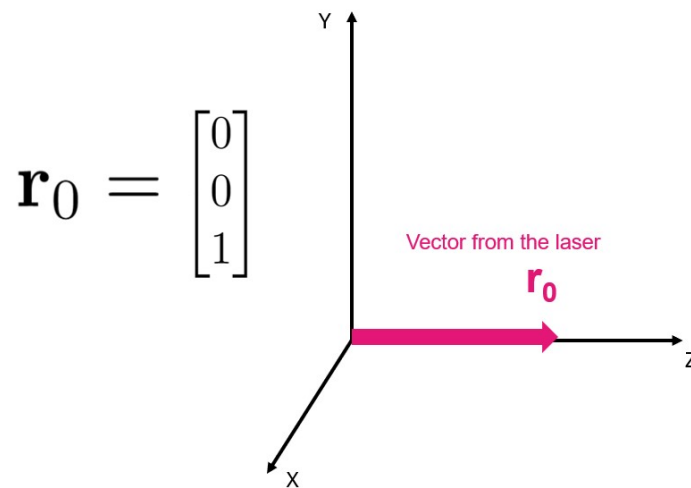
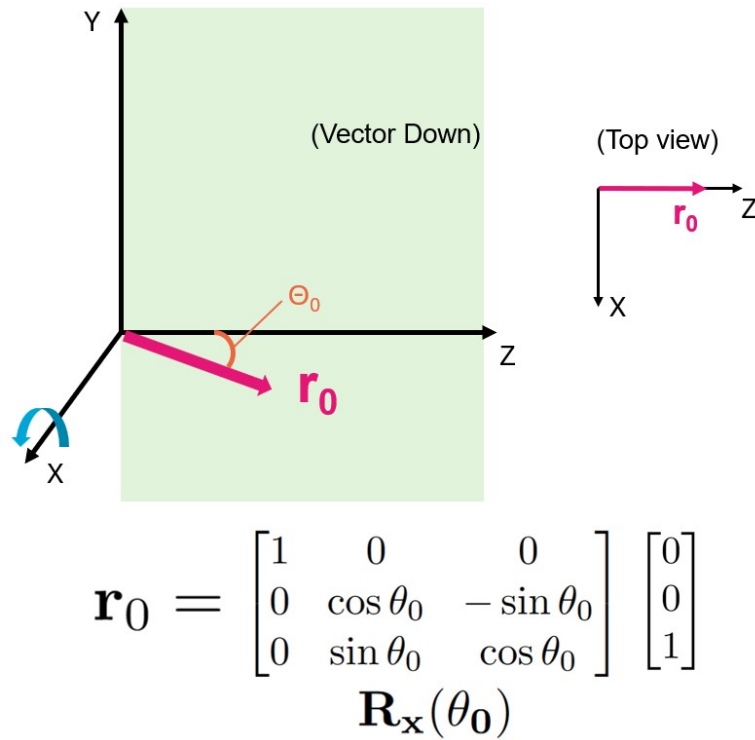


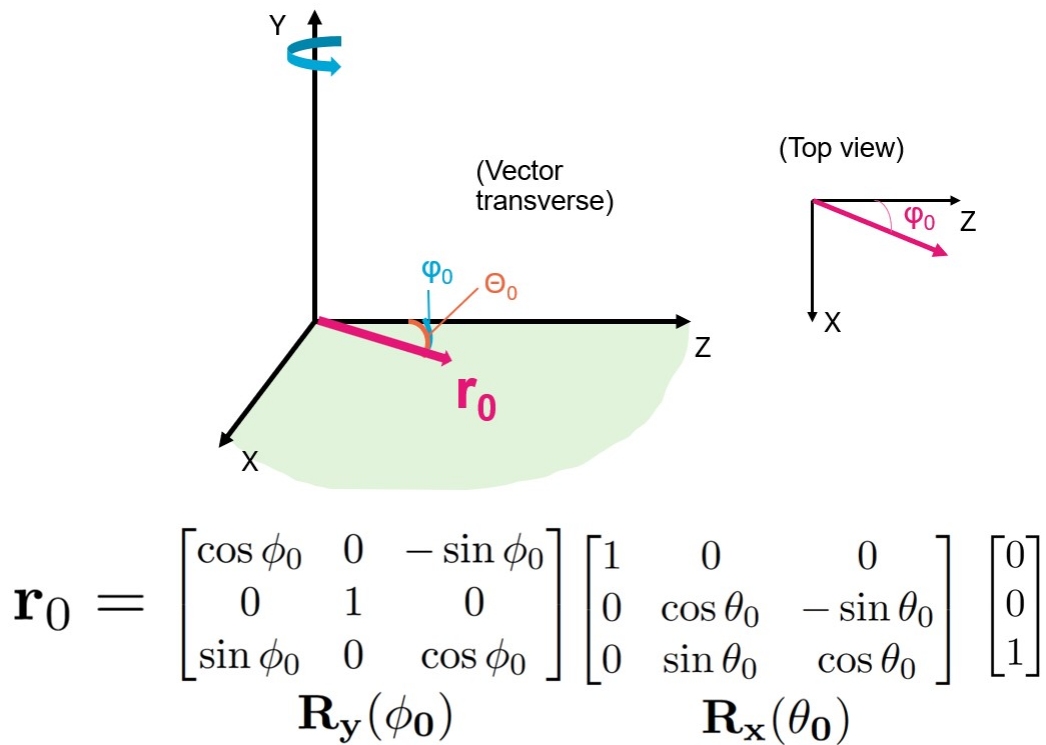
Figure 4.6: Base equation of the initial ray propagating along the optical axis.

Afterwards, this ray vector is influenced by the rotational matrices. The first rotational matrix transformation is depicted on Figure 4.7, where the initial ray is rotated by an angle θ_0 around the x-axis. This angle is used to change the laser's angle of incidence to the AOTF, and it will have a significant influence on the AO interaction [52].

The angle θ_0 is defined positively downwards, or alternatively, rotation towards the negative Y-axis is defined positively. The angle was defined this way for future convenience with the AO interaction calculations, where the wave vectors in literature are defined in the negative crystallographic quadrant as shown in Figure 2.11 [47, 5, 10, 53]. The angle θ_0 is expected to be small, otherwise, the ray vector may not pass through the AOTF's entrance due to acceptance angle constrains.

Figure 4.7: Steering the initial ray by θ_0 in the YZ -plane.

Suppose, the user wants to change the angle along the XZ -axis as well, in the transverse direction. In this case, an additional rotational matrix around the Y -axis can be applied, as depicted in Figure 4.8. This matrix rotates the vector r_0 by an angle ϕ_0 , which can be useful in cases when an optical ray is found to be inclined and the experimental results are still desired to be processed. This angle has a small influence on the AO interaction, but the angle is important to test whether the ray passes through the AOTF successfully.

Figure 4.8: Steering the initial ray by ϕ_0 in the XZ -plane.

Both of those transformations can be combined into one matrix, which is depicted in Equation 4.4. The user can now easily specify the angle of incidence θ_0 and the transverse angle ϕ , which will be used to generate the

initial ray vector r_0 in 3D vector space.

$$\mathbf{r}_0 = \begin{bmatrix} L_0 \\ M_0 \\ N_0 \end{bmatrix} = \begin{bmatrix} \cos(\theta_0) \sin(\phi_0) \\ -\sin(\theta_0) \\ \cos(\theta_0) \cos(\phi_0) \end{bmatrix} \quad (4.4)$$

As a side note, considering that this stage does not use any refractive indices and only uses angles to define the initial ray's direction. This stage, therefore, can be equally applied if the incident ray has an ordinary or an extraordinary polarization. Just the appropriate subscript ('o' or 'e') has to be added to satisfy the notation used.

4.3.2 First surface - Entering Crystal's medium

The first surface describes the AOTF's entrance facet, where the ray enters a new medium. The incident facet contains an inclination angle γ , which is depicted on Figure 4.9 where a closer look at relevant rays and substages are provided. To perform the transformation from r_0 to r_1 correctly, the substages u_{1a} and u_{1b} will be introduced to include the influence of the angle γ and the change of refractive index of propagation from n_{air} to n_o , by the use of Snell's law. By the end of operations for surface one, it is desired to obtain a DCM of a ray vector r_{1o} propagating in the global axis system.

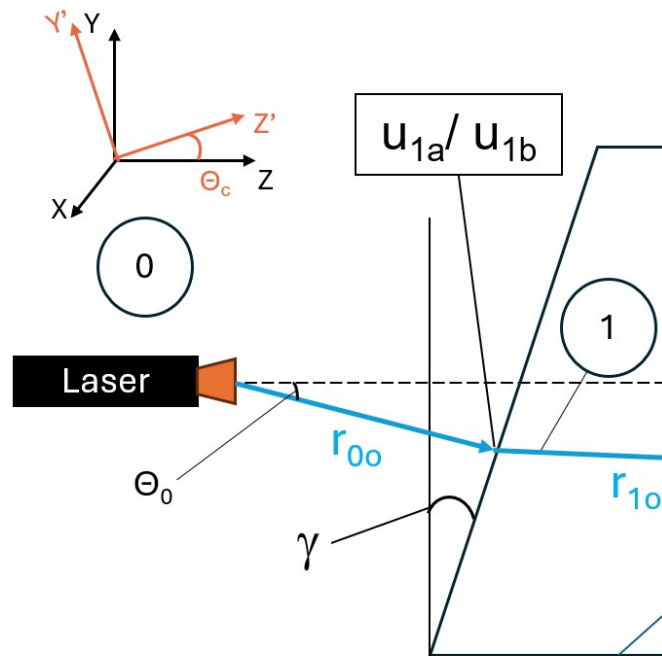


Figure 4.9: Closer view of stage one, involving the rays and substages involved in the model.

An even closer depiction of the first surface is shown in Figure 4.10, where the ray r_0 enters the facet at an angle θ_0 set at the Equation 4.4. The entrance facet has a normal line, depicted as a dashed black line, set at an angle γ relative to the optical axis shown in a dashed blue line. To apply Snell's law, an angle between the surface's normal and the vector needs to be taken [54]. In other words, a new reference axis system needs to be used where the ray vector r_0 is propagating relative to the surface normal rather than the optical axis. The angle between the surface's normal and the r_0 vector is $\gamma - \theta_0$, as depicted in Figure 4.10.

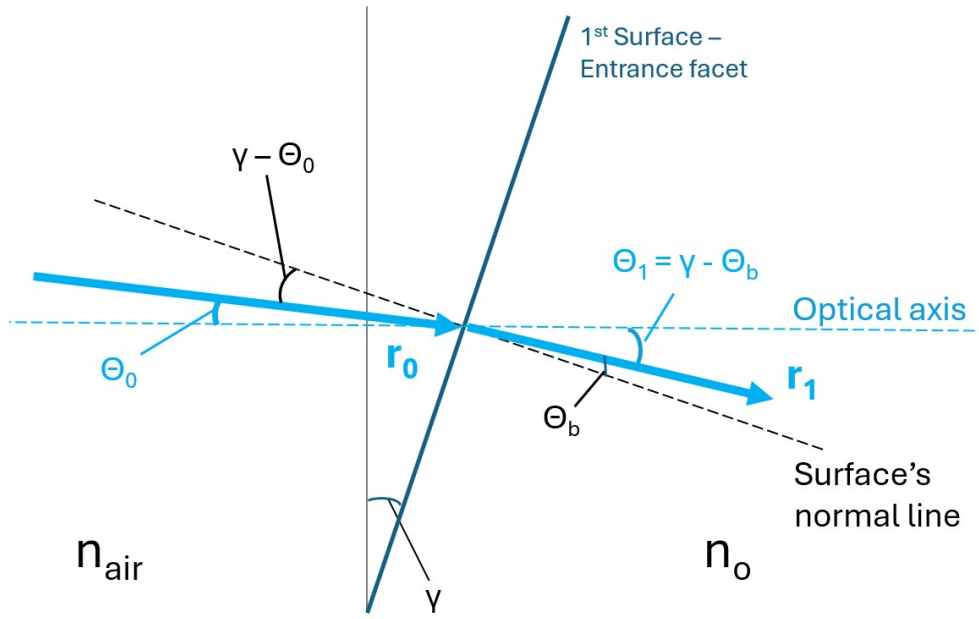


Figure 4.10: Snell's law at the entrance facet schematic.

To achieve such a change of reference axis system, the coordinate system can be temporarily rotated clockwise by an angle γ , as depicted in Figure 4.11. With this rotation, the ray vector now operates along the $O-X_\gamma Z_\gamma$, creating the desired angle of $\gamma - \theta_0$ between the vector r_0 and the entrance surface's normal axis Z_γ . In DCM such a step can be performed by Equation 4.5, where a clockwise rotation by an angle γ is performed, creating a substage u_{1a} , which propagates at an angle $\gamma - \theta_0$ relative to a new reference axis depicted in part (b) of Figure 4.11.

$$u_{1a} = R_x(-\gamma) \begin{bmatrix} L_0 \\ M_0 \\ N_0 \end{bmatrix} \quad (4.5)$$

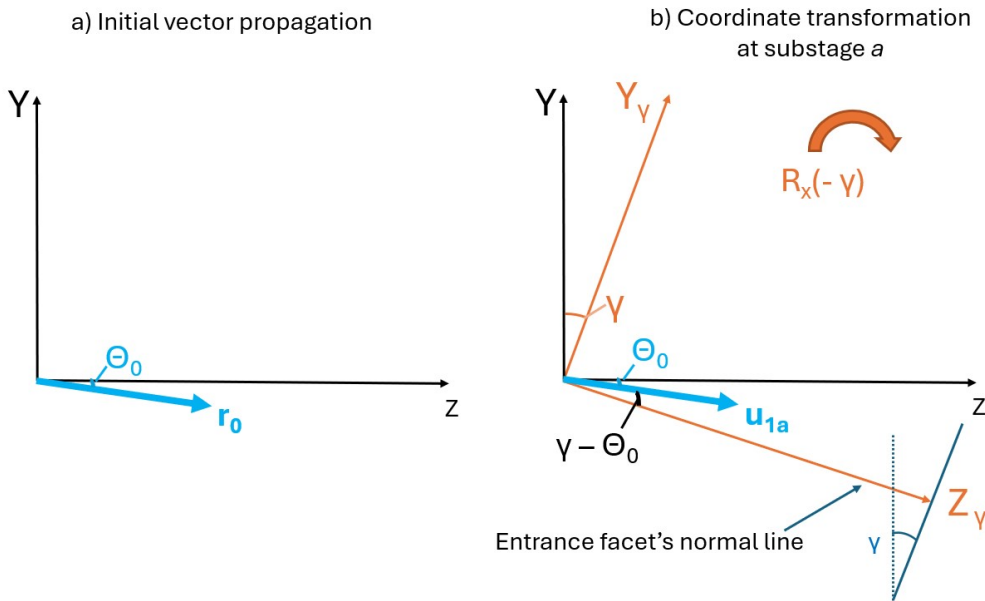


Figure 4.11: (a) Initial ray depiction and (b) coordinate system transformation for the intermediate stage a

After creating substage u_{1a} vector with a desired angle, Snell's law in the vector form can be applied. To represent how the ray vector will change after entering a new medium, Equation 4.6 is provided [47]. The substage u_{1b} still operates in the entrance facet's reference system. Therefore for the Snell's law where the

variables L_a and M_a are divided by the refractive index of the new medium, to find variables L_b and M_b . In this example, the refractive index is n_o since the incoming ray is ordinarily polarized.

$$\mathbf{u}_{1b} = \begin{bmatrix} L_b \\ M_b \\ N_b \end{bmatrix} = \begin{bmatrix} \frac{L_a}{n_o} \\ \frac{M_a}{n_o} \\ \sqrt{1 - L_b^2 - M_b^2} \end{bmatrix} \quad (4.6)$$

To show why a division is used to find DCM variables L_b and M_b , Snell's law is introduced in Equation 4.7 resembling the angles depicted in Figure 4.10, where the variables are rearranged to find $\sin(\theta_b)$, where θ_b represents a refracted angle of a ray inside the AOTF's crystal. However, this angle is still calculated relative to the entrance facet reference frame $O\text{-}XY_\gamma Z_\gamma$, depicted in part (c) of Figure 4.12.

$$\sin(\theta_b) = \frac{1}{n_o} \sin(\gamma - \theta_0) \quad (4.7)$$

$$M_b = \frac{1}{n_o} M_a \quad (4.8)$$

Considering that the refractive index of air is one, and the substage \mathbf{u}_{1a} already contains the angle $\gamma - \theta_0$. Then the variables L_b and M_b of the ray follow the directional cosine and incorporate Snell's law. In other words, a variable M_b can be written as Equation 4.8. The operation on the N_b variable, illustrated in Equation 4.6, is used to reflect the influence of Snell's law on the ray's magnitude along the z-axis and to keep \mathbf{u}_{1b} as the unit vector [55].

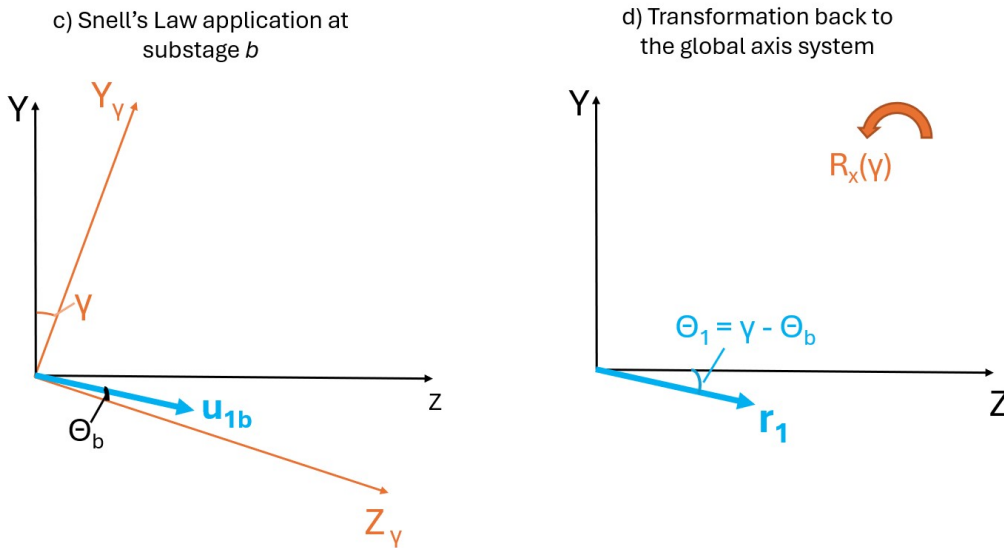


Figure 4.12: (c) Application of the Snell's law and (d) transformation back to the global coordinate system.

The resultant substage \mathbf{u}_{1b} , after Snell's law, is depicted at stage (c) in the Figure 4.12. The vector is still operating at the coordinate axis system where the Z_γ still acts as a normal line to the crystal's entrance facet. For future vector transformations, such a coordinate system is no longer needed, therefore a reverse transformation is performed at Equation 4.9, back to the global coordinate system.

$$\mathbf{r}_{1o} = \mathbf{R}_x(\gamma) \begin{bmatrix} L_b \\ M_b \\ N_b \end{bmatrix} \quad (4.9)$$

The illustration of the final transformation of the first surface is shown in part (d) of Figure 4.12. Which is the desired result, as the ray \mathbf{r}_1 has been influenced by refraction and is now propagating in the global reference axis system. To finalise the operations at the first surface, Table 4.4 provides a summary of all the rays and substages used in this section, stating their purpose, and providing information on the reference frame used per substage.

Table 4.4: First Stage Simulation: Sub-stage Notation and Transformations

Substage notation	Transformation applied	Purpose / Definition of the ray	Ref. axis frame
$\mathbf{r}_{0o} = \text{Definition of incident ray direction}$			Global
\mathbf{u}_{1a}	$R_x(-\gamma)$	Rotation relative to the entrance surface inclination	Entrance Facet
\mathbf{u}_{1b}	-	Application of Snell's law	Entrance Facet
\mathbf{r}_{1o}	$R_x(\gamma)$	Rotation back to the global axis system	Global
$\mathbf{r}_{1o} = \text{Ray exiting first surface}$			Global

4.3.3 Second surface - the AO interaction

At surface two, the goal is to correctly calculate the direction of the diffracted ray \mathbf{r}_{2e} , which will be the output of the surface two. During stage two, a closer schematic of which is shown in Figure 4.13, the ray from surface one \mathbf{r}_{1o} acts as an input, which will be transformed into a wave vector in a crystallographic axis frame \mathbf{k}_{2c} . Using this wave vector, the AO interaction is performed, and the diffracted wave vector \mathbf{k}_{2d} is found by knowing the direction of the acoustical wave vector \mathbf{k}_a in the crystal. Afterwards, both of the wave vectors are normalised at substage \mathbf{u}_{2f} , and transformed back to the global axis system creating a diffracted ray \mathbf{r}_{2e} and undiffracted ray \mathbf{r}_{2o} , which will be the outputs of this surface.

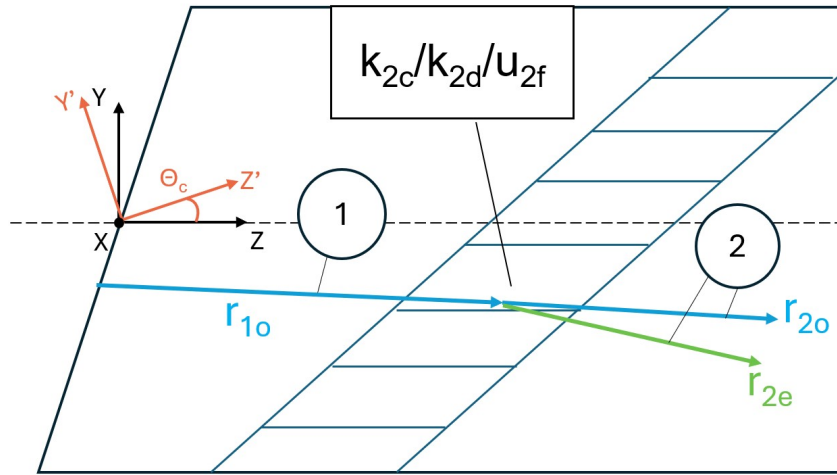


Figure 4.13: Closer view of stage two, involving the rays and substages involved in the model.

From literature for non-collinear AOTFs with TeO_2 as the crystal's material, the crystallographic axis system with [001] and [110] axes are commonly rotated anticlockwise from global axis system by an angle θ_c [10, 26, 27], as depicted in Figure 4.13 or previously in Figure 2.11. As has been mentioned in Section 2.6, the calculations involving the AO interaction are performed in the crystallographic reference frame. Considering the input ray \mathbf{r}_{1o} is already propagating inside the crystal, it is multiplied by rotation matrix $\mathbf{R}_x(\theta_c)$ to change the reference axis frame from global to crystallographic.

Furthermore, it has been mentioned in Section 2.6, that the momentum-matching condition calculations are happening in the wave vector space [10]. Therefore, the ray \mathbf{r}_{1o} is transformed into a wave vector by the multiplication $2\pi n_o/\lambda$, along with the previously mentioned rotation around x -axis. These two transformations applied result in a wave vector \mathbf{k}_{2c} for an ordinarily polarized ray, which can be represented in a simplified form, Equation 4.10, or in a detailed form, Equation 4.11 [47].

$$\mathbf{k}_{2c} = \frac{2\pi n_o}{\lambda} \mathbf{R}_x(\theta_c) \begin{bmatrix} L_1 \\ M_1 \\ N_1 \end{bmatrix} \quad (4.10)$$

$$\mathbf{k}_{2c} = \begin{bmatrix} x_c \\ y_c \\ z_c \end{bmatrix} = \frac{2\pi n_o}{\lambda} \begin{bmatrix} L_1 \\ (M_1 \cos(\theta_c) - N_1 \sin(\theta_c)) \\ (M_1 \sin(\theta_c) + N_1 \cos(\theta_c)) \end{bmatrix} \quad (4.11)$$

The newly found wave vector \mathbf{k}_{2c} for an incident ray, can be visualised in the wave vector space in Figure 4.14, where the refractive ellipses have been added, and the axes represent the crystallographic reference axis system O-XY'Z'. The final goal of this stage is to find the diffracted ray vector \mathbf{r}_{2e} . To achieve this goal, the diffracted wave vector \mathbf{k}_{2d} will firstly need to be found which elongates until point D located along the extraordinary ellipse. To find point D, an acoustic wave vector \mathbf{k}_a will be used which propagates from the end point C of the wave vector \mathbf{k}_{2c} , until point D [47]. This description can be visualised in Figure 4.14, where the acoustical wave vector \mathbf{k}_a fills the space between the two refractive ellipses and travels along the line of transducer's facet location in crystallographic space.

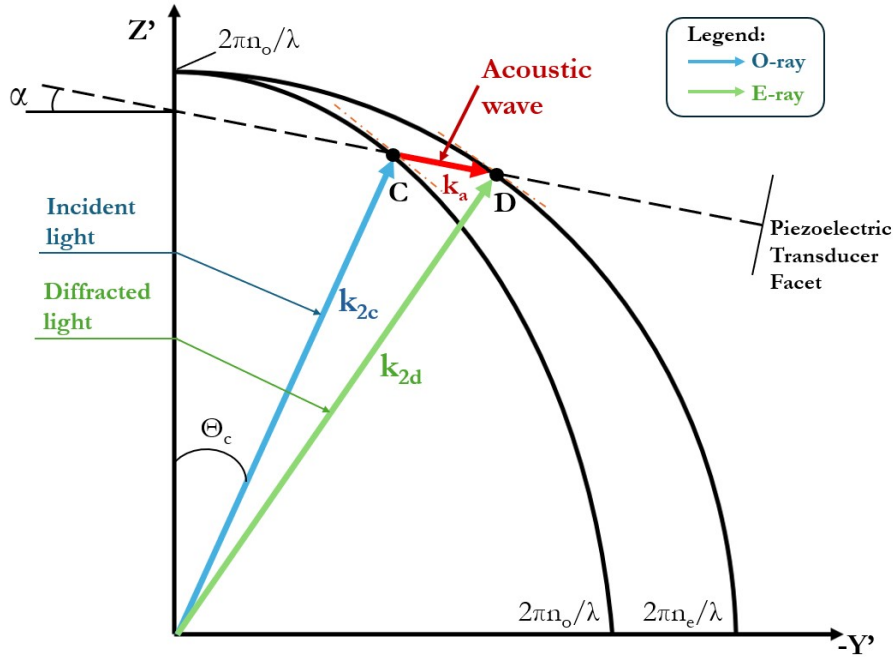


Figure 4.14: Two-dimensional wave vector diagram during the AO interaction in O-XY'Z' axis system - adapted from [47].

To draw the ellipses in the 3D, Equation 4.12 and Equation 4.13 can be used for the ordinary and extraordinary ellipses respectively [47]. To create a similar projection as shown in Figure 4.14, the equations are rearranged to equate to z' .

$$\left(\frac{2\pi}{\lambda_0}\right)^2 = \left(\frac{x}{n_o}\right)^2 + \left(\frac{y'}{n_o}\right)^2 + \left(\frac{z'}{n_o}\right)^2 \quad (4.12)$$

$$\left(\frac{2\pi}{\lambda_0}\right)^2 = \left(\frac{x}{n_e}\right)^2 + \left(\frac{y'}{n_e}\right)^2 + \left(\frac{z'}{n_o}\right)^2 \quad (4.13)$$

To make the connection between the points C and D, the acoustic wave vector \mathbf{k}_a is needed. Conveniently, the acoustical vector \mathbf{k}_a follows a straight line dependent on the tilt-angle α , created during the AOTF manufacturing. In the projection along the negative y' axis, the wave vector \mathbf{k}_a has the directional coordinates represented in Equation 4.14, where t is a scalar value.

$$\mathbf{k}_a = t \begin{bmatrix} 0 \\ -\cos(\alpha) \\ -\sin(\alpha) \end{bmatrix} \quad (4.14)$$

To find the \mathbf{k}_d vector, the acoustical wave vector \mathbf{k}_a is prolonged, by increasing the value t , from the starting point being C until the vector intersects with the extraordinary ellipse. This intersection point is marked as D, which forms the \mathbf{k}_d vector if an arrow is plotted from the origin [47]. A visualisation of such calculation in the model is show in Figure 4.15, where an ordinary refractive ellipse is in blue and extraordinary is in green. The units of the axis were set to $1/\mu\text{m}$ for improved readability.

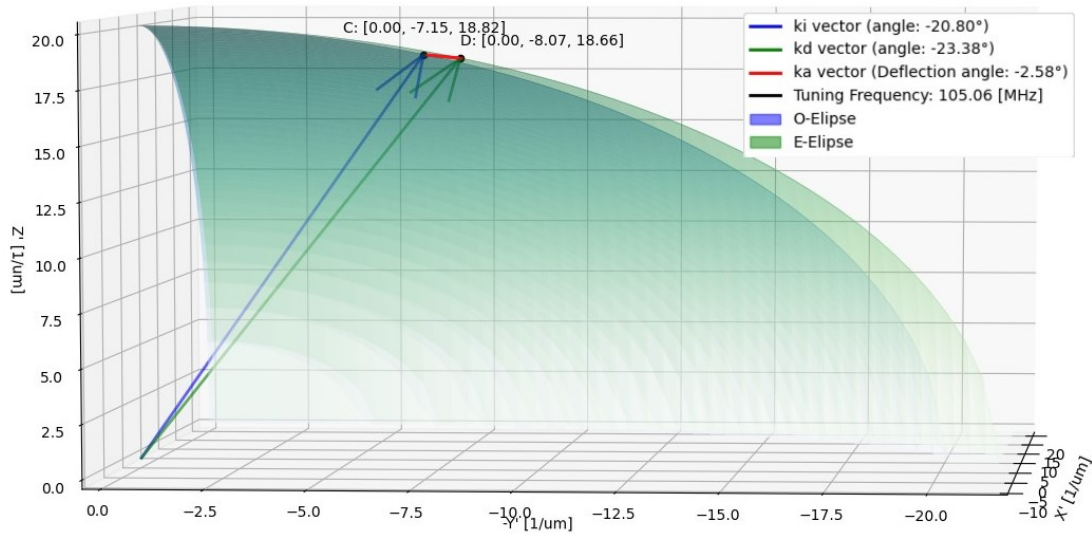


Figure 4.15: Wave vector diagram during the AO interaction in O-XY'Z' axis system

After finding the magnitude of the \mathbf{k}_a wave vector, it is possible to compute the associated tuning frequency for the momentum-matching condition, by re-arranging the wave vector equation presented in Equation 2.9 [25]. This results in Equation 4.15, where $|\mathbf{k}_a|$ is an acoustical wave vector magnitude, V is the acoustical velocity, and f is a tuning frequency. The acoustical velocity V can be calculated by Equation 4.16 [30], where $V_{110} = 616$ m/s and $V_{001} = 2104$ m/s [29, 56]. Considering that the main direction of propagation for the acoustical wave is along [110] axis [27], it follows that the velocity V_{110} is associated with the cosine term, while V_{001} corresponds to the sine term.

$$f = \frac{|\mathbf{k}_a|V}{2\pi} \quad (4.15)$$

$$V = \sqrt{V_{110}^2 \cos^2(\alpha) + V_{001}^2 \sin^2(\alpha)} \quad (4.16)$$

After finding the diffracted wave vector and the frequency required for momentum-matching, the wave vectors are transformed back into unit vectors. Here, the analytical model significantly deviates from the reference simulation from Zhao et al. This is due to the lack of clarity in the explanation of subsequent steps in the reference, though the model's output results remain consistent.

The simplest method for converting wave vectors into unit vectors is through normalization. For the incident wave vector, the normalization results into substage \mathbf{u}_{2fo} , where 'o' stands for o-ray, and can be calculated by Equation 4.17. For the diffracted e-ray, the same operation is performed and illustrated in Equation 4.18.

$$\mathbf{u}_{2fo} = \hat{\mathbf{k}}_{2c} = \frac{1}{\sqrt{x_c^2 + y_c^2 + z_c^2}} \begin{bmatrix} x_c \\ y_c \\ z_c \end{bmatrix} \quad (4.17)$$

$$\mathbf{u}_{2fe} = \hat{\mathbf{k}}_{2d} = \frac{1}{\sqrt{x_d^2 + y_d^2 + z_d^2}} \begin{bmatrix} x_d \\ y_d \\ z_d \end{bmatrix} \quad (4.18)$$

While the substage \mathbf{u}_{2f} still has a crystallographic reference axis system, an effective refractive index n'_e for an extraordinary ray can be found. This value will be needed at stage three of an analytical model to perform a correct refraction of an e-ray at an exit facet. To find n'_e , firstly the angle of the diffracted ray θ_{2fe} with the optic axis [001] is needed to be found, or in this system the Z' axis. Considering that the substage \mathbf{u}_{2fe} is already in DCM form, the simplest way to find the angle with the Z' axis is to use an inverse cosine on the Z variable in the DCM matrix [49], as shown in Equation 4.19.

$$\theta_{2fe} = \arccos(N_{2fe}) \quad (4.19)$$

Afterwards, this angle is inserted into the relation, either based on the P.Gass model (Equation 2.12), or if gyration is a factor then into the Voloshinov's model (Equation 2.25) or Fresnel's model (Equation 2.28). In Equation 4.20, an example is shown with the P.Gass model to find the effective refractive index for the diffracted ray. For an ordinary ray, the refractive index stays the same at n_o , unless gyration is a factor.

$$n'_e(\theta_{2fe}) = \left(\frac{\cos^2(\theta_{2fe})}{n_o^2} + \frac{\sin^2(\theta_{2fe})}{n_e^2} \right)^{-1/2} \quad (4.20)$$

After finding the effective refractive index for an e-ray, both of the rays are transformed back to the global axis reference system. This is done by rotating the axis system by $-\theta_c$, as shown in Equation 4.21 to get the ray \mathbf{r}_2 . This step will be needed to visualise the propagation of the rays leaving the acoustical field.

$$\mathbf{r}_2 = \mathbf{R}_x(-\theta_c) \begin{bmatrix} L_{2f} \\ M_{2f} \\ N_{2f} \end{bmatrix} \quad (4.21)$$

After obtaining the ray propagations for both diffracted (\mathbf{r}_{2e}) and undiffracted (\mathbf{r}_{2o}) rays, the goal of this surface has been achieved. Table 4.5 provides a summary of all the transformations performed at the acoustic field, including the purposes of each substage and in which reference frame an operation was performed.

Table 4.5: Second Stage Simulation: Sub-stage Notation and Transformations

Sub-stage notation	Transformation applied	Purpose / Definition of the ray	Ref. axis frame
$\mathbf{r}_{1o} = \text{Ray from the first AOTF surface}$			<i>Global</i>
\mathbf{k}_{2c}	$R_x(\theta_c) \cdot \frac{2\pi n_o}{\lambda}$	Switch to crystallographic axis and make a wave vector	Crystallographic
\mathbf{k}_{2d}	Acoustic search with k_a	Using the AO interaction theory to find the diffraction wave vector	Crystallographic
\mathbf{u}_{2f}	Normalization	Normalize both vectors to DCM and compute $n'_e(\theta)$	Crystallographic
\mathbf{r}_{2o}	$R_x(-\theta_c)$	Rotation back to the global axis system	Global
\mathbf{r}_{2e}	$R_x(-\theta_c)$	Rotation back to the global axis system for diffracted ray	Global
$\mathbf{r}_{2o} = \text{Undiffracted ray exiting second surface}$			<i>Global</i>
$\mathbf{r}_{2e} = \text{Diffracted ray exiting second surface}$			<i>Global</i>

4.3.4 Third surface - Exit AOTF facet

The last surface of the analytical model is the AOTF's exit facet, where both the undiffracted and diffracted rays experience refraction with the AOTF's exit facet. The procedure for this stage is similar to surface one. Firstly, a temporary reference axis frame of the exit facet inclination is used at substage \mathbf{u}_{3g} , then the Snell's law is applied at \mathbf{u}_{3h} , and finally the rotation back to global axis frame is performed to obtain a refracted ray \mathbf{r}_3 . Depending on the ray's polarization, a different refractive index is used for Snell's law, n_o for the ordinary and n'_e for the extraordinary. A closer visualisation of the exit facet and the input/output rays at surface three are shown in Figure 4.16.

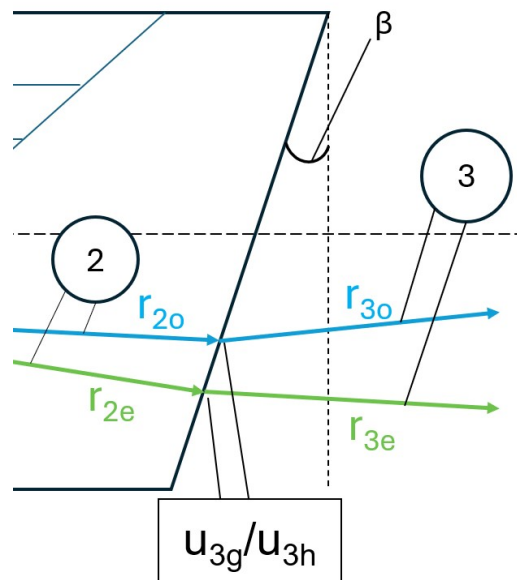


Figure 4.16: Closer view of stage three, involving the rays and substages involved in the model.

Similarly, as for the surface one, to perform the Snell's law, the angle relative to the surface normal is taken, not the angle relative to the optical axis in the global axis system. Based on the Figure 4.17, the angle relative to the surface normal is $\beta - \theta_2$, where β is the exit facet's inclination and θ_2 is the ray's propagation angle relative to the optical axis. To achieve such an angle, the reference axis frame needs to be rotated clockwise by an angle β , which can be visualised in part (b) of Figure 4.18. This substage is the same for both the o-ray or the e-ray entering the third surface, and mathematically such a change in a reference frame can be achieved by Equation 4.22.

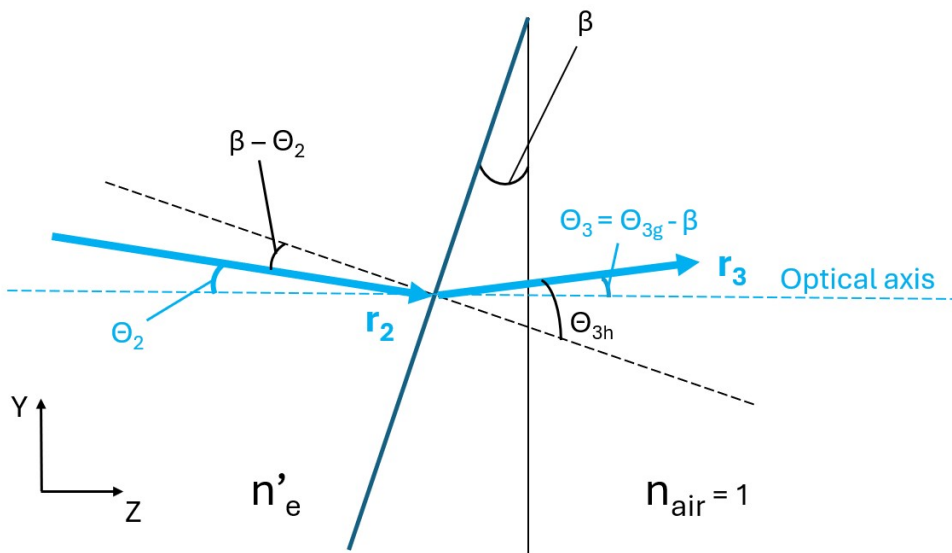


Figure 4.17: Snell's law at the third surface schematic.

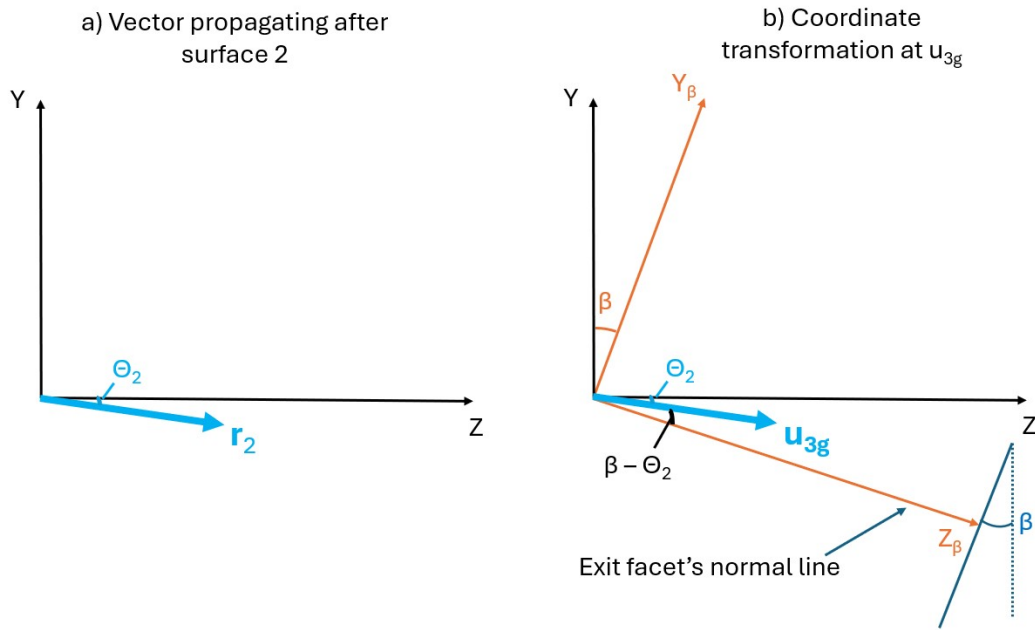


Figure 4.18: Coordinate system transformation at the substage \mathbf{u}_{3g} .

$$\mathbf{u}_{3g} = \mathbf{R}_x(-\beta) \begin{bmatrix} L_2 \\ M_2 \\ N_2 \end{bmatrix} \quad (4.22)$$

After the coordinate transformation, Snell's law can be applied in the next substage \mathbf{u}_{3h} . Similarly to the first surface, the directional cosines for the L_h and M_h components are determined by deriving an appropriate sine expression, based on the Snell's law. This expression is shown in Equation 4.23 where the desired directional variable is $\sin(\theta_{3h})$, Equation 4.24 shows how the Snell's law is applied for the DCM component. In this case, the effective refractive index n'_e appears in the numerator, as the ray is now exiting the crystal, unlike the situation at the first surface.

$$\sin(\theta_{3h}) = \frac{n'_e}{1} \sin(\beta - \theta_2) \quad (4.23)$$

$$M_h = n'_e M_g \quad (4.24)$$

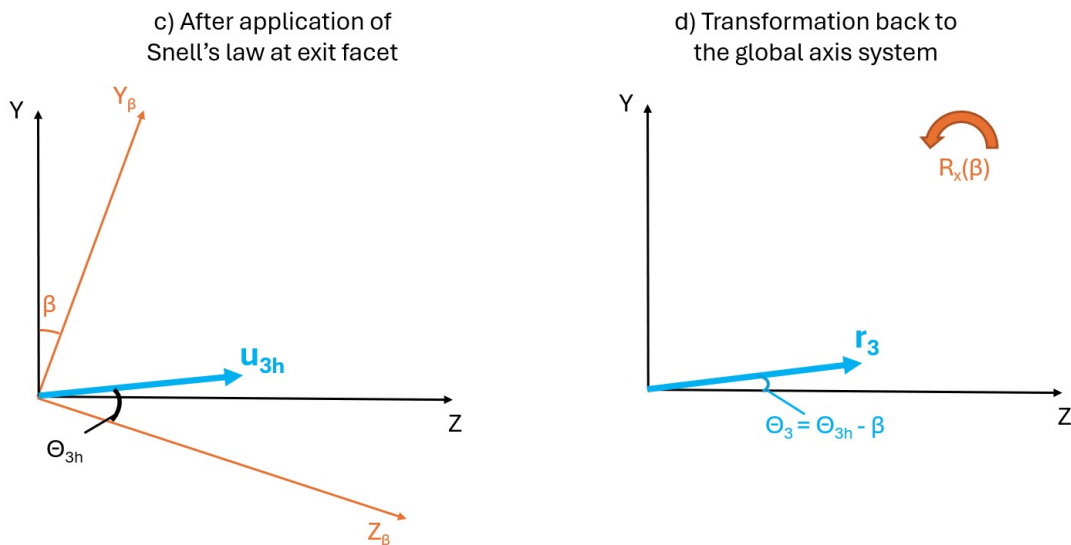


Figure 4.19: Coordinate system transformation at the substage \mathbf{u}_{3h} and the ray \mathbf{r}_3 .

By applying the Snell's law for L_h and M_h components, the DCM component N_h along the Z_β axis takes the expression presented in Equation 4.25 [55], ensuring that the substage \mathbf{u}_{3h} is still a unit vector. This substage is still operating in the exit facet reference system and can be visualised in part (c) of Figure 4.19. Naturally, for the o-ray the multiplication is performed with the refractive index of n_o .

$$\mathbf{u}_{3h} = \begin{bmatrix} L_h \\ M_h \\ N_h \end{bmatrix} = \begin{bmatrix} n'_e \cdot L_g \\ n'_e \cdot M_g \\ \sqrt{1 - L_h^2 - M_h^2} \end{bmatrix} \quad (4.25)$$

After applying the Snell's law relative to the exit facet's normal line, the last step is to rotate the substage \mathbf{u}_{3h} back to the global coordinate system, by rotating the reference axis system by an angle β anticlockwise as depicted in Equation 4.26, and visualised in part (d) of Figure 4.19. The final vector \mathbf{r}_3 represents the ray exiting the AOTF, with which the directional angle θ_3 can be calculated relative to the Z -axis.

$$\mathbf{r}_3 = \mathbf{R}_x(\beta) \begin{bmatrix} L_h \\ M_h \\ N_h \end{bmatrix} \quad (4.26)$$

Considering that at the third surface, two distinct rays with opposite polarizations approach the surface. The transformations at the exit surface are summarised in two tables. Table 4.6 for the undiffracted o-ray, and Table 4.7 for the diffracted e-ray.

Table 4.6: Substage Notation and Transformations for o-ray

Substage notation	Transformation applied	Purpose / Definition of the ray	Ref. axis frame
$\mathbf{r}_{2o} = \text{Undiffracted ray exiting second surface (o-ray)}$			Global
\mathbf{u}_{3g}	$R_x(-\beta)$	Rotation relative to the exit surface inclination	Exit Facet
\mathbf{u}_{3h}	-	Application of the Snell's law with n_o	Exit Facet
\mathbf{r}_{3o}	$R_x(\beta)$	Rotation back to the global axis system	Global
$\mathbf{r}_{3o} = \text{Undiffracted ray exiting the AOTF (o-ray)}$			Global

Table 4.7: Substage Notation and Transformations for e-ray

Substage notation	Transformation applied	Purpose / Definition of the ray	Ref. axis frame
$\mathbf{r}_{2e} = \text{Diffracted ray exiting second surface (e-ray)}$			Global
\mathbf{u}_{3g}	$R_x(-\beta)$	Rotation relative to the exit surface inclination	Exit Facet
\mathbf{u}_{3h}	-	Application of the Snell's law with n_i	Exit Facet
\mathbf{r}_{3e}	$R_x(\beta)$	Rotation back to the global axis system	Global
$\mathbf{r}_{3e} = \text{Diffracted ray exiting the AOTF (e-ray)}$			Global

4.4 Extraordinary ray simulation

The analytical model, described in Section 4.3, provides an example of AOTF simulation when an ordinarily polarized light is sent onto an AOTF. However, for the case of incident extraordinary rays, no published simulations were available at the time of this research, particularly those employing 3D vector analysis for optical simulation of the AOTF. Consequently, it was necessary to develop a custom model for this type of the AO interaction. Especially considering that most of the AOTF analyses in literature were primarily focused on the e-ray incident beams [26].

Rather than explaining the analytical model in full and repeating the explanation of certain steps, this section will instead provide the additional steps that are required to simulate AOTF's behaviour for the incident e-ray. This section can be split into two main parts. Subsection 4.4.1 will explain the e-ray interactions with the AOTF's entrance and exit facets, whereas Subsection 4.4.2 will specify peculiarities of the e-ray AO interaction.

4.4.1 E-ray surface interactions

The entrance surface and the exit surfaces of the AOTF in the analytical model serve a purpose to simulate the refraction of rays interacting with these surfaces. For the entrance surface simulating the incident e-ray, an additional step is required, which is highlighted in yellow in Table 4.8 as substage u'_0 . This notation was chosen to ensure that the subsequent substages continue in the alphabetical order established in Subsection 4.2.4.

Table 4.8: Substage Notation and Transformations for Incident e-ray

Substage notation	Transformation applied	Purpose / Definition of the ray	Ref. axis frame
$r_{0e} = \text{Definition of incident ray direction}$			<i>Global</i>
u'_0	$R_x(\theta_c) \ \& \ R_x(-\theta_c)$	Find incident ray's direction relative to [001] axis and find n'_e	Crystallographic (Temporarily)
u_{1a}	$R_x(-\gamma)$	Rotation relative to the entrance surface inclination	Entrance Facet
u_{1b}	-	Application of the Snell's law with n'_e	Entrance Facet
r_{1e}	$R_x(\gamma)$	Rotation back to the global axis system	Global
$r_{1e} = \text{Ray exiting first surface}$			<i>Global</i>

By sending an extraordinary polarized light onto AOTF the birefringence of the TeO_2 crystal comes into play [52], already at the entrance surface. This means it is no longer possible to apply Snell's law with a refractive index of an o-ray (n_o) like it was done in Subsection 4.3.2. Instead, the refractive index acting on the incident e-ray will depend on the ray's angle (θ') relative to the [001] crystallographic axis of the crystal. Such an angle can be found by using the substage u'_0 , Equation 4.27, where the incident ray r_{0e} is temporarily rotated to the crystallographic axis frame, and the angle θ' is found in Equation 4.28 [49]. Afterwards, the analytical model comes back using the ray r_{0e} for further substages.

$$\mathbf{u}'_0 = \begin{bmatrix} L'_0 \\ M'_0 \\ N'_0 \end{bmatrix} = \mathbf{R}_x(\theta_c) \mathbf{r}_{0e} \quad (4.27)$$

$$\theta' = \arccos(N'_0) \quad (4.28)$$

The value of the effective refractive index n'_e for the incident e-ray interacting with the birefringent crystal can be found by Equation 4.29 [57]. Similarly, as before, the ordinary (n_o) and the extraordinary (n_e) refractive indices depend on the incident ray's wavelength, which can be found by equations in Section 2.5. Furthermore, a different equation can be used to find the effective refractive index, depending on if gyration is the factor that was chosen to be considered. These two considerations are used to satisfy the [SIM-REQ-002] requirement.

$$n'_e(\theta') = \left(\frac{\cos^2(\theta')}{n_o^2} + \frac{\sin^2(\theta')}{n_e^2} \right)^{-1/2} \quad (4.29)$$

After finding the effective refractive index n'_e for the incident e-ray, this value will be used at substage u_{1b} to perform the Snell's law at the entrance surface, as shown in Equation 4.30.

$$\mathbf{u}_{1b} = \begin{bmatrix} L_b \\ M_b \\ N_b \end{bmatrix} = \begin{bmatrix} \frac{L_a}{n_i(\theta')} \\ \frac{M_a}{n_i(\theta')} \\ \sqrt{1 - L_b^2 - M_b^2} \end{bmatrix} \quad (4.30)$$

For the third surface of the AOTF, when the incident ray is e-polarized, both the diffracted and undiffracted rays interact with the surface. The refraction of these rays has already been analysed in Subsection 4.3.4, but in the case of incident e-ray, the polarizations switch: the undiffracted ray becomes e-polarized, while the diffracted ray is o-polarized. For the diffracted o-ray, Snell's law is applied using the ordinary refractive index n_o . For the e-ray, once again, the ray's angle relative to the crystallographic axis must first be determined before calculating the effective refractive index using Equation 4.29, or other formulation if gyration effect is a factor.

4.4.2 E-ray AO interaction

To keep a similar simulation procedure as in Section 4.3, it was decided to continue using the wave vectors and ellipses representing the refractive indices based on their positioning in the crystallographic axis system. Further research into extraordinary interaction revealed that the acoustic wave vector (\mathbf{k}_a) continues to slope upwards after locating the correct point on the extraordinary ellipse. This finding aligns with an example from a conference paper by Batshev et al. (2021) [58].

A Figure 4.20 for the extraordinary AO interaction was created to maintain consistent variable terminology. Unlike previously, the incident light is now an e-ray, meaning that when the global coordinate system is rotated by an angle θ_c , the incident wave vector \mathbf{k}_{2c} should now intersect with the outer ellipse for the extraordinary ray. To keep the order of notations the same, the newly found point on the extraordinary ellipse is noted as point C. The point found through the AO interaction on the ordinary ellipse for the ordinary ray is designated as point D. This ensures the transformation order remains the same with point D being used for the diffracted ray.

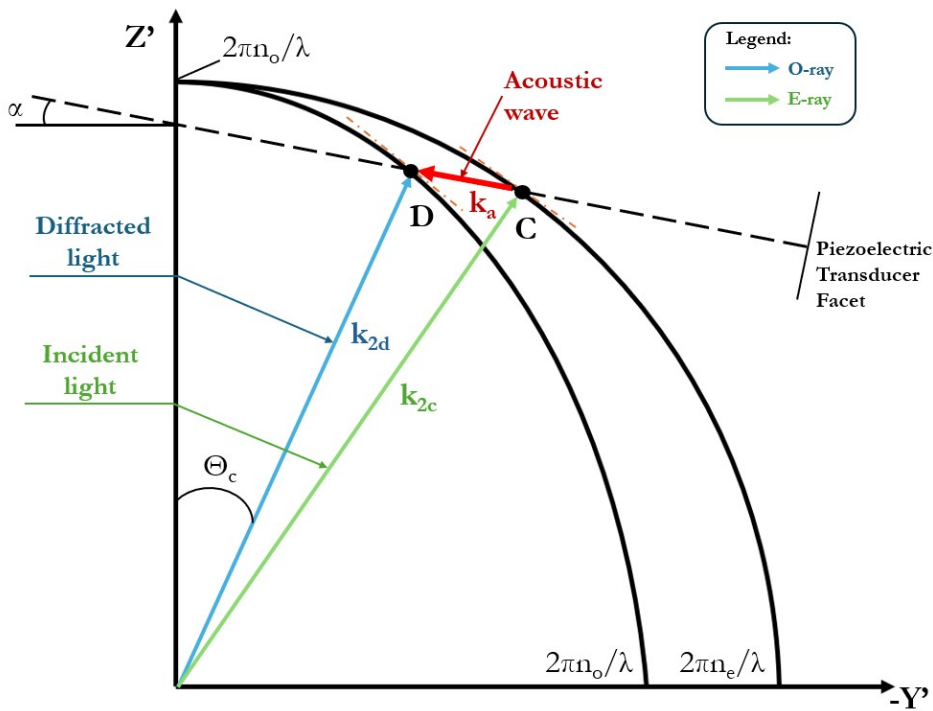


Figure 4.20: Wave vector diagram for the extraordinary polarization AO interaction.

The first step is to find point C on the extraordinary ellipse graph. According to the Figure 4.5, step C comes after obtaining the ray \mathbf{r}_1 from the entrance surface interaction. This time, however, converting the ray \mathbf{r}_1 into a wave vector and keeping the same angle with the crystallographic axis, is trickier, as it involves finding the effective refractive index of e-ray once again instead of using n_o .

This can be done by a similar procedure described in Subsection 4.4.1, involving transformation of \mathbf{r}_1 into the crystallographic reference frame and finding an angle θ_{1c} with [001] axis and finding the effective refractive index $n'_e(\theta_{1c})$, by using Equation 4.29. Finally, this newly found refractive index is used to find the wave vector \mathbf{k}_c , by using Equation 4.31. Using this wave vector, point C is found on the wave vector diagram.

$$\begin{aligned}
 x_c &= \frac{2\pi n_i(\theta)}{\lambda_0} l_1 \\
 y_c &= \frac{2\pi n_i(\theta)}{\lambda_0} m_1 \\
 z_c &= \frac{2\pi n_i(\theta)}{\lambda_0} n_1
 \end{aligned} \tag{4.31}$$

To find the diffracted ray, point D, the acoustic wave \mathbf{k}_a needs to find an intersection with an ordinary ellipse this time. As has been noted and shown in the Figure 4.20, the wave vector \mathbf{k}_a has an upward slope and a different direction compared to the o-ray simulation [58]. The acoustical wave vector \mathbf{k}_a can be expressed by Equation 4.32, with point C acting as a starting point. The wave vector \mathbf{k}_a is being extended until it intersects the ordinary ellipse. Similarly, as in Section 4.3, the magnitude of the wave vector \mathbf{k}_a can be used to find the tuning frequency required for the Bragg condition.

$$\mathbf{k}_a = \begin{bmatrix} 0 \\ \cos(\alpha) \\ \sin(\alpha) \end{bmatrix} \tag{4.32}$$

The intersection point of the vector \mathbf{k}_a and the ordinary ellipse, is the point D, which is then used to convert the wave vector back to the ray notation to perform future manipulations with this ordinary ray and simulate the AOTF's behaviour.

4.5 AOTF rotation

To make the analytical model even more versatile, one adaptation has been created involving the AOTF rotation, allowing the optical designs to be more flexible with the AOTF's positioning, and adaptable to validation testing, allowing to satisfy the [SIM-REQ-004] requirement. This adaptation is quite obvious from the name itself, the AOTF is rotated by an angle ζ_{rot} , defined clockwise positive. However, this rotation introduces several changes to how rays interact with the AOTF. To illustrate these changes, the figures below are provided. Figure 4.21 shows the diagram previously used to define the geometrical angles of the AOTF's crystal, when no rotation is applied. To illustrate the AOTF rotation, the top right corner of the image provides a view of the AOTF and the incoming ray path.

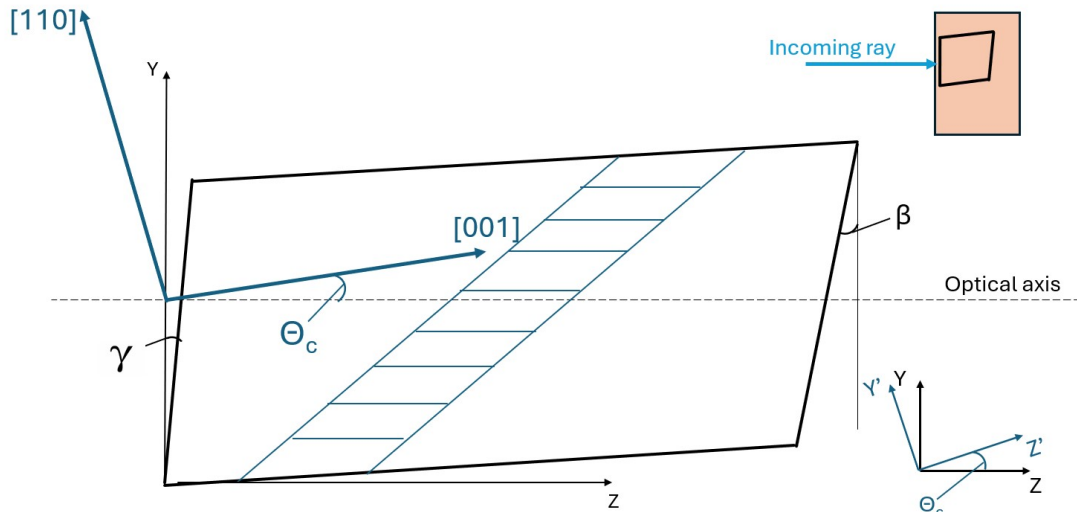


Figure 4.21: AOTF angles with the moved crystallographic axis system.

Figure 4.22 shows the rotated AOTF by an angle ζ_{rot} , with clockwise defined as a positive rotation to match the metric used on the rotational stage. This rotation causes the AOTF's entrance facet and the exit facet to appear more inclined than previously. This inclination increase will subsequently increase the angle of the normal

surface axis, which will then cause an increase in refraction for the incoming rays. Meaning that the output rays from the AOTF will have higher exit angles, as the rotational angle ζ_{rot} becomes higher.

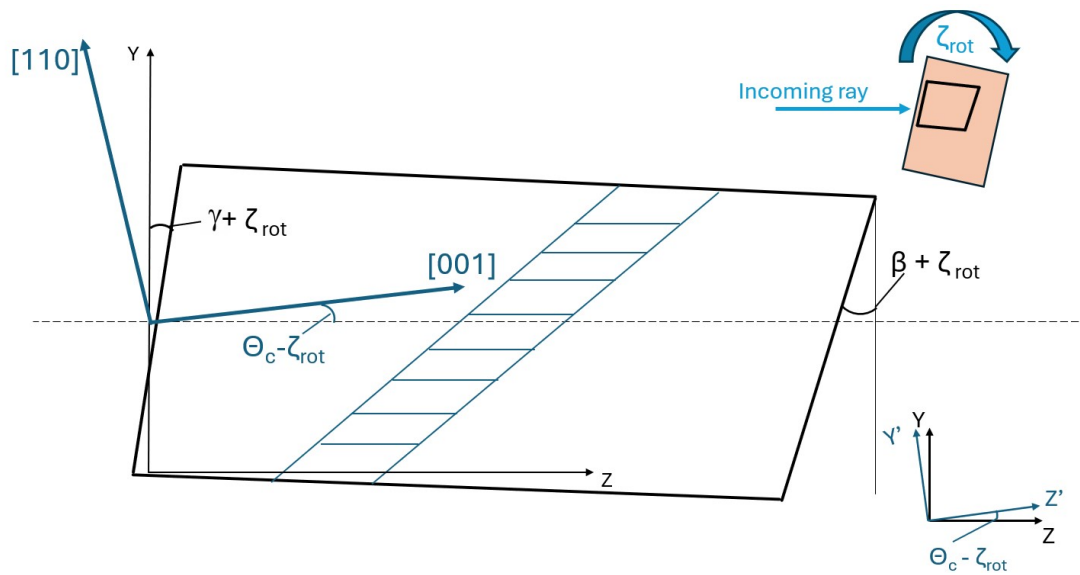


Figure 4.22: Rotated AOTF by an angle ζ_{rot} clockwise.

The mathematical impact of higher inclination angles at the facets is described in Subsection 4.5.1. Whereas the second implication of ζ_{rot} concerns the perceived crystallographic axis angle, how exactly it changes and which parts of the simulation it impacts are described in Subsection 4.5.2.

4.5.1 Surface rotations

As mentioned earlier, introducing the AOTF rotation angle will result in the entrance and exit facets of the AOTF being perceived at a higher inclination. Mathematically, this influences ray interactions at surfaces 1 and 3, which are illustrated in Figure 4.4. Since the implementation steps are similar for both surfaces, the procedure will be demonstrated for surface 1 only. Understanding the adaptations for surface 1 makes it straightforward to apply these transformations to surface 3.

To help with visualisation, Figure 4.23 has been provided showing the new schematic of the ray interaction with the first surface. The main difference is that the new surface inclination is now $(\gamma + \zeta_{rot})$, instead of just γ . This increases the angle of the normal line, the dashed black line, compared to the optical axis, the blue dashed line.

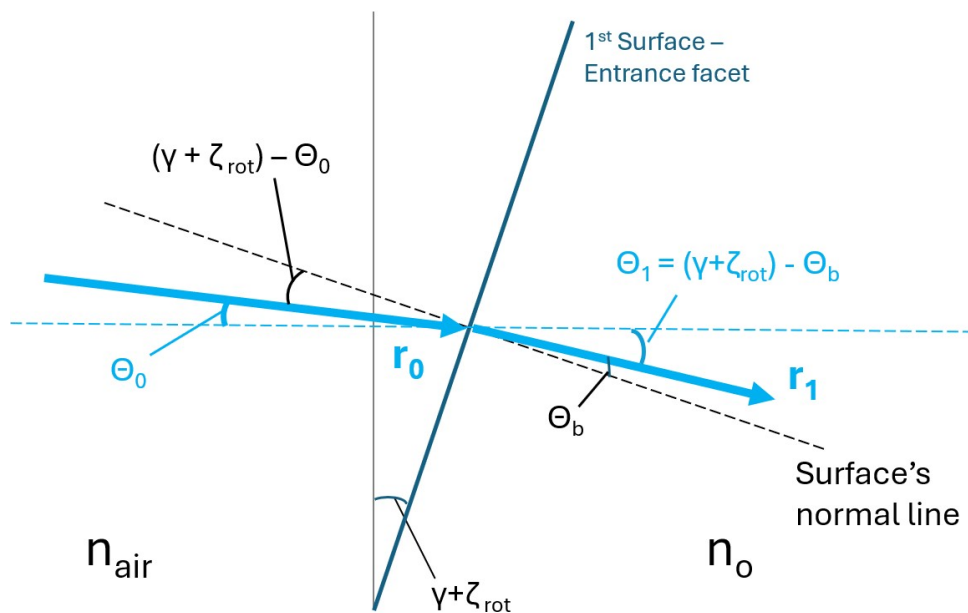


Figure 4.23: Snell's law at the entrance facet schematic, including the ζ_{rot} rotation.

In Subsection 4.3.2 it was explained that the global axis needs to be temporarily rotated clockwise around the X-axis, where the new Z-axis (Z_γ) acts as a normal line of the first surface. In this case, the rotation is clockwise, and involves the two angles γ and ζ_{rot} . This transformation can be visualised in part (b) in Figure 4.24, as well as mathematically in Equation 4.33.

$$\mathbf{r}_a = \mathbf{R}_x(-\gamma - \zeta_{rot}) \begin{bmatrix} L_0 \\ M_0 \\ N_0 \end{bmatrix} \quad (4.33)$$

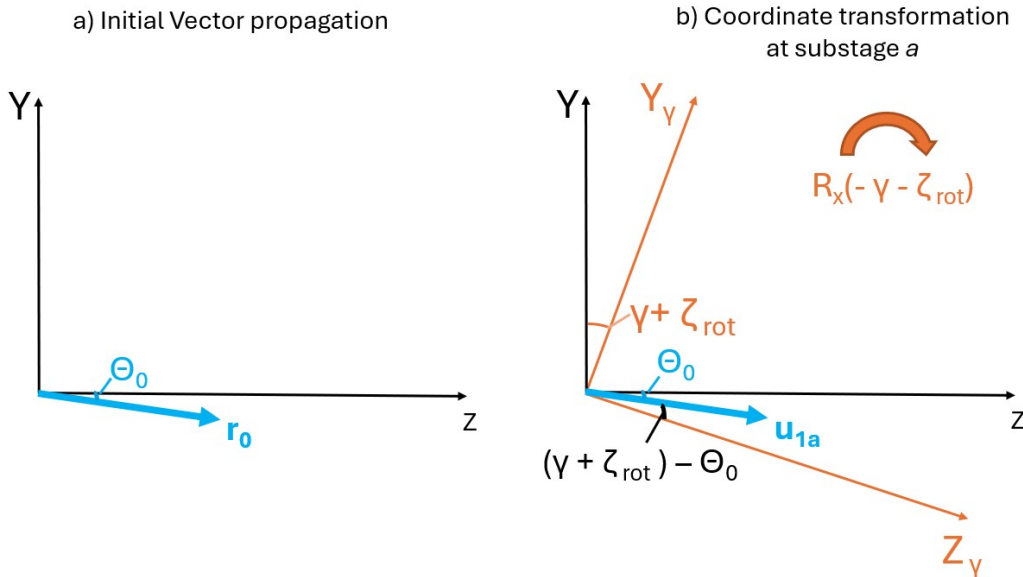


Figure 4.24: (a) New initial ray depiction and (b) coordinate system transformation for the intermediate stage a with angle ζ_{rot} included.

The procedure for the stage where the intermediate ray r_b is created concerning Snell's law stays the same as described in Subsection 4.3.2. The resultant angle θ_b , depicted in part (c) of Figure 4.25, will differ and will be slightly larger if the ζ_{rot} angle is positive.

After the application of Snell's law, it should not be forgotten to transform the substage back to the global axis. This is done by rotating the axis system by γ and ζ_{rot} angles anticlockwise, which is depicted as part (d) of Figure 4.25 and mathematically in Equation 4.34.

$$\mathbf{r}_1 = \mathbf{R}_x(\gamma + \zeta_{rot}) \begin{bmatrix} L_b \\ M_b \\ N_b \end{bmatrix} \quad (4.34)$$

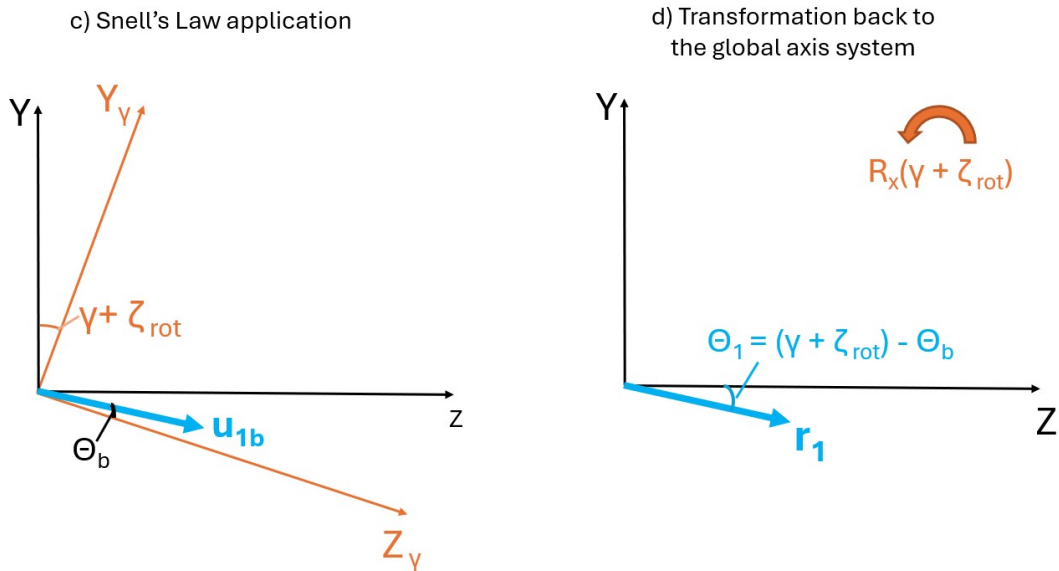


Figure 4.25: (c) Application of Snell's law on the ray with a larger normal angle, and (d) transformation back to the global coordinate system.

For the third surface, the adaptation also involves rotating the global axis system by a higher angle due to the ζ_{rot} angle. In both cases, the outgoing ray from the surface interaction has a higher angle of refraction due to the nature of Snell's law where the input ray has a higher angle with the surface's normal, resulting in a higher angle of refraction compared to if the AOTF was not rotated.

4.5.2 Crystallographic axis rotation

The second implication of ζ_{rot} is a bit more subtle. It has been noted in Subsection 4.2.2, that the crystallographic [001] and [110] axes are fixed inside the crystal, and are rotated relative to the global axis system by an angle θ_c . However, it was realised, that by rotating the AOTF clockwise by an angle ζ_{rot} , the crystallographic axis system also rotates clockwise since it is fixed inside the crystal, which is visualised in Figure 4.22.

This means that the perceived rotation of the crystallographic axis system is described by Equation 4.35, where the perceived crystallographic angle (θ'_c) depends on the AOTF's rotation. Firstly, the user needs to define the angle θ_c when the AOTF is positioned perpendicular to the straight incidence ray, as in Figure 4.21. After finding θ_c , the perceived angle will be smaller if the AOTF is rotated clockwise, which can be observed in Figure 4.22.

$$\theta'_c = \theta_c(\zeta_{rot} = 0^\circ) - \zeta_{rot} \quad (4.35)$$

This change complicates the analysis, as every time a coordinate system switch to the crystallographic axis is performed, the user will need to use θ'_c instead of θ_c .

However, the angle α does not change with the AOTF rotation, as it is defined to be between the [110] axis and the AOTF's bottom surface. Both the surface and the [110] axis rotate by the same angle ζ_{rot} , causing the angle α to remain unchanged. This is an important finding, as it means that the acoustical wave vector \mathbf{k}_a will have the same vector notation at all angles ζ_{rot} .

The introduction of the AOTF's rotational angle to simulation can be an advantageous tool for the user designing optical setups involving the AOTFs. Non-collinear AOTFs do not commonly have significantly large acceptance angles for incident rays, around 2–3 degrees in literature [25] and 6–7 degrees in commercially available AOTFs [59], which is larger in comparison to collinear AOTFs [7]. However, the inclusion of the rotational angle could extend the range of allowed optical paths, allowing versatility as the AOTF's positioning and potentially make the optical paths more compact. More importantly, however, the AOTF testing can be simplified where an AOTF's rotational stage can be used to change the ray's incidence angle rather than realigning the laser for new incidence angles.

4.6 Ray propagation visualisation and verification

After describing the analytical model and what adaptations were made to make the model more versatile, this section aims to show how can the produced rays in the model be visualised. For the example of visualisation, the AOTF parameters from the Voloshinov et al. paper [53] will be used in order to show how would the rays propagate in that AOTF and also to compare if the results produced in the model match the results from the paper.

From the paper, the inputs for the analytical model are presented in Table 4.9, where the parameter notation has been adapted to fit the terminology used in the analytical model. Furthermore, in the paper three outputs were provided, shown in Table 4.10, that can be used to verify the results of the analytical model. The outputs are the acoustic tuning frequency f , and the separation angles inside the crystal (after AO interaction) and outside the crystal (after the exit facet surface). The separation angle is calculated as an angle difference between the diffracted and undiffracted ray [60].

Table 4.9: AOTF parameter inputs from Voloshinov et al. paper [53]

Description	Parameter	Value
Wavelength	λ	700 nm
Polarization of incident light	-	e-ray
Crystallographic axis angle	θ_c	23.4°
AOTF tilt-angle	α	10°
Entrance surface angle	γ	0°
Exit facet angle	β	0°

Table 4.10: AOTF parameter outputs from Voloshinov et al. paper [53]

Description	Parameter	Value
Acoustic frequency	f	105 MHz
Separation angle (in crystal)	$\delta\theta_2$	2.6°
Separation angle (in air)	$\delta\theta_3$	5.8°

Based on the inputs from Table 4.9, the analytical model has provided a visual output of an AO interaction seen in Figure 4.26, where expectedly the incident wave vector \mathbf{k}_i (or \mathbf{k}_{2c} based on previous notation) had an angle of 23.4° relative to the [001] axis. The diffracted wave vector was found to have a separation angle of 2.58° inside the crystal, which is almost the same as in the reference paper. It could even be the same, as the authors have rounded their results to one decimal place. Furthermore, the tuning frequency based on the analytical model is also almost identical to the reference paper, where the analytical model has provided a tuning frequency of 105.06 MHz for the Bragg condition.

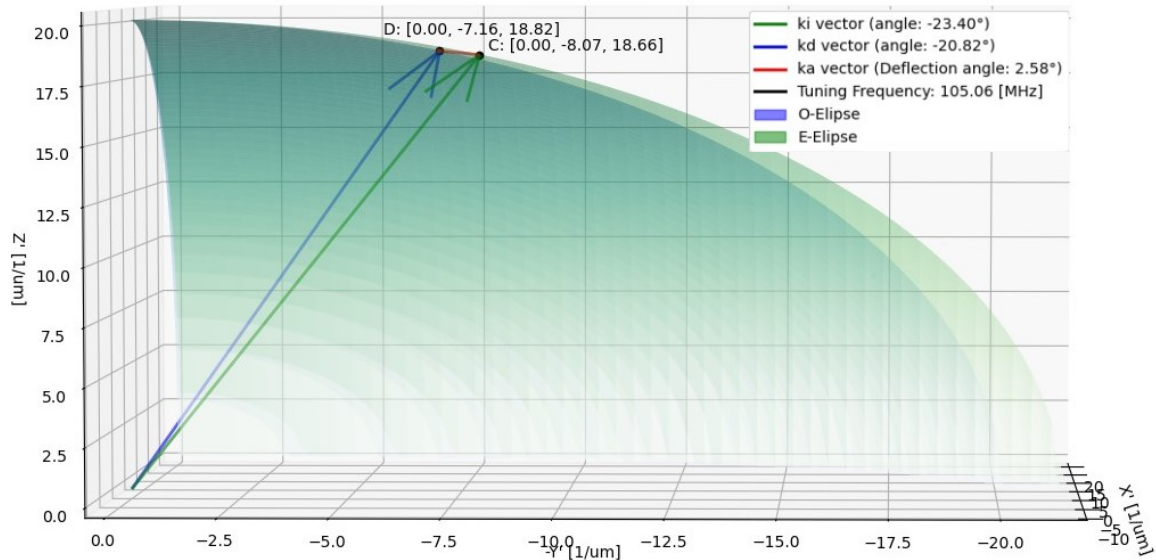


Figure 4.26: AO interaction to verify the results with the results from Voloshinov (2007), $\beta=0^\circ$, and $\gamma=0^\circ$.

By running the analytical model further, a separation angle at the exit surface was also found, resulting in an angle of 5.8° which is exactly the same as in the reference paper. Based on the initial verification, the model is outputting reliable results, which are summarised in Table 4.11.

Table 4.11: Comparison of AOTF parameter outputs from Voloshinov et al. [53] and the analytical model

Description	Parameter	Reference Value	Model Result	Difference
Acoustic frequency	f	105 MHz	105.06 MHz	0.06 MHz
Separation angle (in crystal)	$\delta\theta_2$	2.6°	2.58°	-0.02°
Separation angle (in air)	$\delta\theta_3$	5.8°	5.80°	0.00°

To visualise the rays propagating through the AOTF crystal, a new code has been written in python. This code uses the resultant rays \mathbf{r}_0 , \mathbf{r}_1 , \mathbf{r}_2 , and \mathbf{r}_3 from the analytical model for the visualisation. In this code, the AOTF with given geometrical parameters is drawn as a trapezium surface, and similarly the acoustical field also acts as a surface.

This code starts multiplying the ray vector \mathbf{r}_0 by a scalar value until it reaches the first surface. Afterwards, the ray \mathbf{r}_1 propagates until it reaches the acoustical field. Similarly, as in the analytical model, two rays exit the second surface, \mathbf{r}_{2o} and \mathbf{r}_{2e} , which propagate until the last AOTF surface. After the last surface rays \mathbf{r}_{3o} and \mathbf{r}_{3e} continue propagating until the user specified border. Finally, all the results are being plotted, resulting in Figure 4.27 where the AOTF from Voloshinov et al. paper is used as an example.

Figure 4.27 visualises the AOTF in the middle of the figure, with the acoustical column shown in pink colour. The rays are classified based on the polarisation, where green represents e-rays and blue o-rays. The legend in the top left corner shows relevant AOTF characteristics based on inputs and outputs of the analytical model. The legend in the bottom right corner shows all the ray angles relative to the Z-axis in the global axis system.

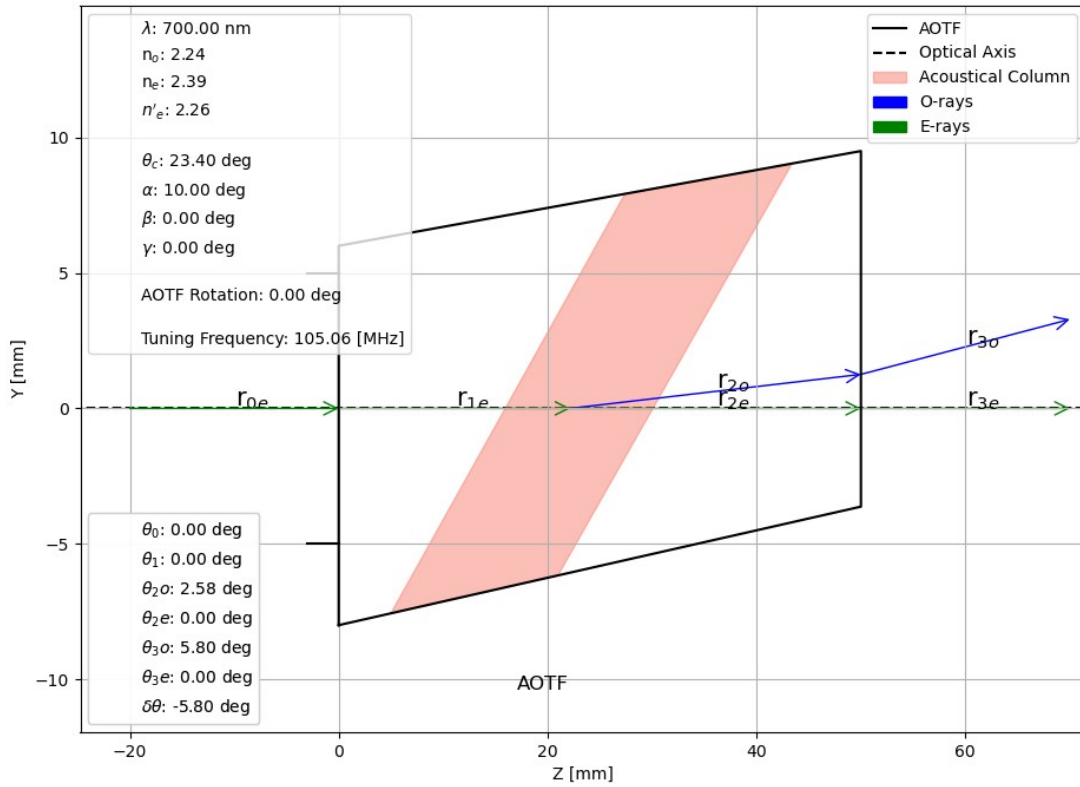


Figure 4.27: Ray propagations throughout the crystal with a 700nm laser input angle of 0 degrees, $\beta=0^\circ$, and $\gamma=0^\circ$.

The ray visualisation code is based on the same principle as ray tracing in the optical software programs such as Zemax, where directional matrices are continuously being multiplied until the ray reaches a surfaces [50]. There are examples in literature of AOTFs being integrated into Zemax by the use of directional matrices for specific wavelengths [61, 62]. However, those sources do not provide the mathematics involved in the ray tracing, but they can be used as an indication that it is possible to integrate this analytical model into optical simulations such as Zemax for future works. This finding together with a working code in python shows ray propagation inside the AOTF crystal satisfies the [SIM-REQ-005] requirement.

With regard to the verification of the analytical model, it was desired to verify the model with AOTF literature results that have facet inclinations and also results regarding the separation angles. The reference source [47] had a similar test performed, but the AOTF used for their proposed model had two transducers, both having different α angle [47]. Neither this model nor the model proposed in the paper had adaptations for the multiple transducer AOTF design, making such an AOTF choice in a paper quite strange for verification, and also not applicable to verify this model. Therefore, due to lack of testing results in literature, a physical validation of the model is required, which will be provided in the following chapter.

4.7 Conclusion on the analytical model

In the chapter on the AOTF's analytical model, a detailed description of an AOTF simulation has been provided, where an AOTF is split into three main surfaces. Namely, the AOTF entrance surface, acoustical field and the exit surface. The analytical model operates in 3D, allowing the user to account for both vertical or transverse ray inclinations, satisfying the [SIM-REQ-005] requirement.

Such model design was possible due to the use of directional cosines, which are not only convenient to be used for matrix transformations between reference axis systems, but are also can easily be used to find relevant ray angles which can then be used for the effective refractive index identifications. Finally, choosing directional cosines for the analytical model makes the model easier integrable into other ray tracing software programs such as Zemax [50].

In Section 4.3 the analytical model was built on the reference of AOTF of Zhao et al. [47], for the case when the incident ray is o-polarized. This model has been broken down into more substages and shorter expressions in comparison to the reference in order to provide detailed reasoning for each substage action and to simplify

potential future model integrations into other AOTF works. The AO interaction is also described, where it was ensured that the acoustical wave vector \mathbf{k}_a has a sufficient magnitude to cover the distance between the two refractive ellipses to satisfy the momentum-matching condition, allowing to simulate the most effective diffraction scenario. From the \mathbf{k}_a magnitude, the tuning frequency is calculated to which AOTF can be tuned to, in order to diffract the desired wavelength at highest efficiency, allowing to answer sub-question 3 from Chapter 3.

Furthermore, the model has been made usable for a range of wavelengths based on the experimental results from Uchida from 400 to 1100nm [23]. Additionally, the model has been adapted, allowing the user to choose between three different equations for effective refractive indices. The model based on P.Gass is the most commonly used model, and if optical activity (gyration) is a factor, a different refractive index equation can be used, either based on Voloshinov's equation or Fresnel where an equation for TeO₂ was derived in Subsection 2.7.3. These additions allow the model to satisfy the [SIM-REQ-002] requirement.

In Section 4.4, a new case scenario for the model has been created, allowing the user to simulate the AOTF's behaviour when the incident ray is e-polarized. This simulation adaptation included the calculation of effective refractive index on the e-ray and how it changes the calculation of Snell's law at the entrance and exit facets of the AOTF. Furthermore, a new AO interaction has been described where the diffracted ray is an o-ray, which involved a different set of equations compared to the previous simulation type. This addition to the model allows satisfying [SIM-REQ-003] requirement, where the user can specify the polarisation type involved in diffraction.

Section 4.5 introduces the AOTF's rotation angle (ζ_{rot}) allowing the user to increase versatility of the model during the testing design or a design for integrating AOTF into a product, allowing to satisfy [SIM-REQ-004] requirement. The AOTF's rotation increases the inclination of AOTF's entrance and exit surfaces, causing the rays to be refracted at higher angles compared to simulation where not AOTF rotation is included. Secondly, the rotational angle alters the perceived crystallographic axis angle once the ray enters the crystal, this does have an impact on the e-ray propagation through the crystal and the AO interaction.

Finally, Section 4.6 showed a visualisation of the analytical model's product based on an AOTF from literature. The visualisation shows the propagation of the incident ray inside the crystal and the propagation of the diffracted ray which underwent the AO interaction. The results of the model were compared with the reference results from the Voloshinov et al. paper, and it was found that the model's outputs match the results from the paper. Providing an initial suggestion that the model is working correctly. However, to fully validate the analytical model more test data is required, which will be obtained in the following chapter.

Simulation verification 5

After describing the model, the proper verification is required to make sure that the model is working correctly in terms of providing correct tuning frequencies and separation angles, satisfying requirements [VER-REQ-001] and [VER-REQ-002] respectively. Furthermore, it was desired to quantify the impact of the material's optical activity on the results, therefore P.Gass and Fresnel models for refractive indices were compared in the results.

To verify the analytical model, an AOTF device is needed where the crystallographic and the facet angles are known. This information is secretive by the manufacturers, which made the model verification a challenging task. Fortunately, educational institutions, such as Université Polytechnique Hauts-de-France (UPHF), can provide an AOTF with known angular properties. This experiment was conducted by Prof. Samuel Dupont at UPHF, the data of which is analysed in this chapter.

5.1 Experimental results

The test aims to analyse whether the analytical model provides the correct separation angle when the AOTF is tuned for the Bragg condition, producing the highest diffraction efficiency. Furthermore, the frequency needed for the Bragg condition was compared between the model and the experiment. The main AOTF angles required for the analytical model are represented in Figure 5.1. Furthermore, the displacements of the rays, to find the separation angle $\Delta\Theta_3$, are shown on the right side of the figure.

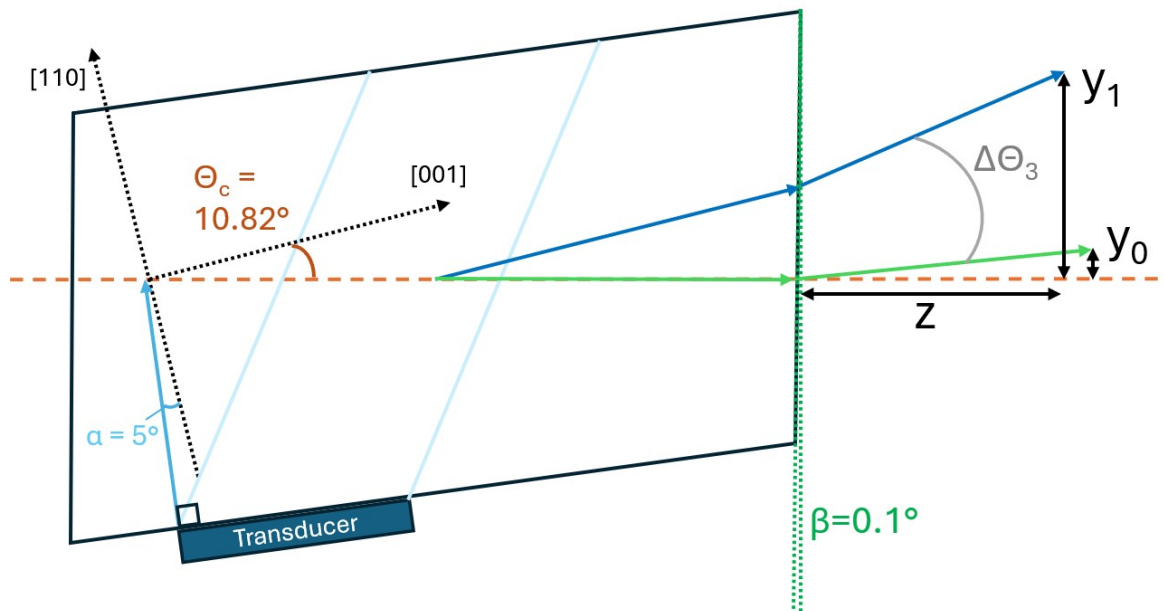


Figure 5.1: AOTF variables for the test conducted at UPHF.

The Table 5.1 represents the results obtained from the experiment at UPHF where linear horizontally (extraordinary) polarized lights at wavelengths 532, 593 and 671nm were sent perpendicularly onto the AOTF's entrance surface. The variables y and y_0 represent the vertical displacements of the diffracted and undiffracted rays coming out from the AOTF. The variable z is the horizontal distance between the AOTF's exit facet and the point where the displacement measurements were taken.

Table 5.1: Experimental Results for AOTF diffraction at different wavelengths, conducted at UPHF.

λ [nm]	Frequency [MHz]	y [cm]	y_0 [cm]	z [cm]	$\Delta\Theta_3$ Separation angle [deg]
532	69.48	16.9	32.5	272	3.28
593	60.90	17.4	32.5	272	3.18
671	52.44	17.8	32.6	272	3.11

By knowing the distances y , y_0 , and z , for each of the wavelengths tested, the separation angle $\Delta\Theta_3$ was calculated by using simple trigonometry, shown in Equation 5.1.

$$\Delta\Theta_3 = \arctan\left(\frac{|y - y_0|}{z}\right) \quad (5.1)$$

From the results, it could be seen that the separation angle and the tuning frequency are the highest at the lower wavelengths. This does go in-line with the theory, as was shown in Figure 2.10, the birefringence for the TeO_2 is the highest at lower wavelengths. This means that the difference between ordinary and extraordinary refractive indices is larger, causing the wave vector \mathbf{k}_a to have a larger magnitude to cover the distance between the two refractive ellipses and for the Bragg condition to occur, as can be seen in Figure 4.14 given that θ_c stays constant. Consequently, the larger value of \mathbf{k}_a results in a higher frequency, which in turn would also increase the separation angle between the incident and diffracted wave vectors, \mathbf{k}_{2c} and \mathbf{k}_{2d} .

Finally, due to the relatively low value of θ_c (below 11°) the gyration effect is expected to be significant, as based on the Figure 2.22 the difference in refractive indices is not zero compared to the P.Gass model. To test if these hypotheses are true, and the simulation model is working correctly, Section 5.2 compares the results of the analytical models and the experimental results. Voloshinov's simplified model for gyration (Equations (2.24) and (2.25)) was not included in this analysis, since that model according to the authors is a good approximation for $\theta_c < 5^\circ$ [37], and therefore this model does not fit this use case.

5.2 Analytical model results

To verify the analytical model, the inputs represented in Table 5.2 were implemented into the model, along with the wavelengths used for the test. Furthermore, 3 different models were used for verification, to test whether the optical activity induced by the gyration along the optic axis, improves the analytical model's results.

Table 5.2: Input Parameters for the Analytical Model

Parameter	Value
Incident Polarization	Extraordinary
θ_c [deg]	10.82°
α [deg]	5°
β [deg]	0.1°
γ [deg]	0°
ζ_{rot} [deg]	0°

The P.Gass model has no gyration effect, and refractive indices are based on the relations presented as n_{e1} and n_{o1} . The Fresnel model does include the gyration effect, which is the strongest along the [001] axis. However, the rotatory power value used for the gyration effect, influences the magnitude, as can be seen in Equation 2.19. The rotatory power for TeO_2 value seemed high according to literature, with $\rho = 87^\circ/\text{mm}$ at 633nm [23], according to Uchida. Therefore, a third model was introduced for comparison, which is also based on the Fresnel relation, but the rotatory power is reduced to $5^\circ/\text{mm}$ at 633nm and scaled based on the graph presented in Figure 2.18. The value of $5^\circ/\text{mm}$ was chosen to match the experimental results found in Figure 7.9, divided by two, since the AO interaction happens roughly in the middle of the AOTF device.

Full results, for each of the analytical models, are shown in Appendix D. However, to summarise the results, the Table 5.3 compares the separation angle results between the three models and the values obtained from the experiment. Similarly, a comparison for the frequency is presented in Table 5.4. The tables show the difference between the experimental value, with plus indicating how much the simulated value is higher and minus indicating if the simulated value is lower than the experimental one. The green colours indicate if the

model satisfies verification requirements, either [VER-REQ-001] for separation angles ($|\delta\Delta\theta_3| < 0.02^\circ$) or [VER-REQ-002] for tuning frequencies ($|\delta f| < 0.5$ MHz). The red colour indicates that the simulated value is far away from the experimental one.

Table 5.3: Separation Angle Comparison Table

λ [nm]	$\Delta\theta_3$ Separation Angle [deg]	$\delta\Delta\theta_3$ P. Gass Model [deg]	$\delta\Delta\theta_3$ Fresnel Model ($\rho_{633} = 87^\circ$) [deg]	$\delta\Delta\theta_3$ Fresnel Model ($\rho_{633} = 5^\circ$) [deg]
532	3.28	0.00	+0.30	+0.01
593	3.18	-0.01	+0.24	+0.01
671	3.11	-0.03	+0.17	0.00

Table 5.4: Frequency Difference Comparison Table

λ [nm]	Frequency [MHz]	δf P. Gass Model [MHz]	δf Fresnel Model ($\rho_{633} = 87^\circ$) [MHz]	δf Fresnel Model ($\rho_{633} = 5^\circ$) [MHz]
532	69.48	-0.29	+6.01	+0.06
593	60.90	-0.75	+3.82	-0.49
671	52.44	-0.73	+2.52	-0.54

From the results, it can be seen that the P.Gass model and the Fresnel model, with an adjusted ρ value, perform well in identifying the separation angle between the two outgoing beams. The adjusted Fresnel model performed especially well, with the separation angle difference being below 0.02° in comparison to the experimental values, satisfying the [VER-REQ-001] for separation angle difference.

The outputs of these two models for the frequency tuning are also close to the experimental results, all the values being within the range of ± 1 MHz. The uncertainty between the results can be either from the experiment itself, where the tuning frequency was close to the Bragg condition, but not exactly there. Alternatively, the TeO₂ crystal could have alternative acoustic velocities along the [110] and [001] axis, compared to the values used in the model. Most likely, it is the combination of both of these factors, that create the uncertainty for tuning frequency.

However, considering that the Fresnel model with adapted rotatory power values performs the best in the frequency tuning and for separation angle data. It is believed that the gyration effect is present inside the AOTF crystal similar to the extent shown in the physical experiments, rather than the rotatory power suggested in the literature.

The Fresnel model, which uses rotatory power values based on the data from Uchida (2nd model), significantly overestimates the separation angle and the frequency required for the Bragg diffraction. This is especially true for the optical wavelength of 532nm, where according to Figure 2.18 the rotatory power is the highest, around 142 deg/mm.

The higher rotatory power creates a larger separation between the two ellipses, seen in Figure 2.21, which causes the vector \mathbf{k}_a to travel a longer distance compared to the P.Gass model. This results in a larger simulated tuning frequency value, and the diffraction angle inside the crystal. These two factors explain the overestimation of values for the second model in the table, for both frequency and the separation angle.

5.3 Conclusion and results evaluation

From the results, it can be said that the experimental results do successfully verify the core of the analytical model. The models based on refractive indices of P.Gass and Fresnel (with low rotatory power values) simulate the separation angles with an accuracy of $\pm 0.01^\circ$ in comparison to the experimental values, where only one value was off by 0.03° for P.Gass model. This finding does successfully match the [VER-REQ-001] verification requirement. Furthermore, both of the models performed well with regard to the frequency tuning values, where the difference between the model and experimental values was within the RF frequency range of ± 1 MHz for both of the models.

The Fresnel model, which uses the rotatory power values based on Figure 2.18, where experimental values from Uchida [23] are taken, does significantly overestimate the separation angles and the frequency tuning values

required for the Bragg condition. This either means that there could be a potential flaw in the Fresnel model for simulating gyration effects, or this model is applicable only for low θ_c values, or finally, the rotatory power values should be lower than was suggested by Uchida.

However, the Fresnel model which used reduced values of rotatory power has performed the best in comparison to the experimental results provided by UPHF. With the difference in separation angles being below 0.01° for all the wavelengths tested, and with the difference in frequency tuning values being within ± 0.55 MHz. Providing results close to satisfying the momentum-matching frequency requirement [VER-REQ-002]. This means that potentially further research is required in the rotatory power in the TeO_2 crystals, as based on this verification, the rotatory power values are expected to be significantly lower than the values represented by Uchida Figure 2.18.

The potential separation of results between the experimental and model values may also lie in an experimental setting where perhaps a not fully collimated light is used, the presence of transverse or vertical ray inclinations, or a rough AOTF surface finishing of the AOTF's facets [47]. The experimental procedure can also influence the results, especially with regard to finding the correct tuning frequency for the Bragg condition. Therefore, a higher variation of results in frequency tuning was expected.

The verification could be improved by repeating the test for more wavelengths, and for different incident polarization types. Furthermore, a test identifying the polarization rotation would benefit in identifying correct rotatory power values that should be used for the analytical model. The inclusion of the AOTF's rotational angle (ζ_{rot}) would also be beneficial as a validation for the analytical model's adaptations. Unfortunately, due to time limitations at UPHF, it was not possible to test for those adaptations with an AOTF that has known crystallographic and geometrical facet angles. However, overall, the results of the verification are positive, suggesting that the analytical model is good at simulating AOTF's behaviour with the P.Gass model, and it is working at various optical wavelengths.

Testing methodology for AOTF and geometry analysis 6

This chapter aims to describe the two physical tests that will be used to characterise the AOTF's behaviour and to validate the analytical model. These two tests are called power and diffraction testing. The first test aimed to record the power intensities of the diffracted and undiffracted beams of light. In contrast, the second test aimed to record the ray exit angles of diffracted and undiffracted rays.

These two tests were used on two different AOTFs one from AA opto-electronics and the other from Brimrose. Even though the tests performed were the same, the data analysis for those AOTFs differed. For the AA opto-electronics AOTF, it was possible to identify the AOTF's geometrical angles, such as γ or β , the procedure for which will be discussed in Section 6.2. However, the Brimrose AOTF was newly bought and the AOTF's crystal was closed off.

The aim of testing the Brimrose AOTF is to answer sub-question five, where the goal is to see whether an analytical model can be used as a tool to characterise an AOTF which is a black box to the user. However, the aim of testing AA opto-electronics AOTF is to develop initial procedures that can be used to identify θ_c or α angles and also to perform further validation of the analytical model on the adaptations added to the model.

Given that the data analysis for the AA Opto-Electronics and Brimrose AOTFs follows distinct approaches while the testing procedures remain consistent, the test descriptions are presented separately in this chapter. Chapter 7 and Chapter 8 are then focused on analysing data specifically for the AA Opto-Electronics AOTF and Brimrose AOTF, respectively.

In this chapter, Section 6.1 describes the procedure and the results of the allowed frequency range within which both of the AOTFs are allowed to operate safely and efficiently. Section 6.2 describes the procedure and results to find the crystal dimensions inside the AA opto-electronics AOTF. Afterwards, Section 6.3 provides the equipment descriptions used in both of the tests and the optical alignment procedure used for the laser. Section 6.4 provides the procedure for the diffraction testing, and similarly Section 6.5 provides a procedure for the power test.

6.1 AOTF's allowed frequency range

Before conducting optical tests, the AOTFs were evaluated electrically to determine the standing wave ratio (SWR), to satisfy the related [TEST-REQ-005] validation requirement. As discussed in Section 2.8, a higher SWR ratio results in more power being reflected back to the amplifier, which can potentially damage the amplifier if the reflected power is excessive. Additionally, a higher SWR value reduces the efficiency of the AOTF, as less power reaches the transducer [4], which in turn means that less power is converted into acoustic waves — reducing the AOTF's diffraction efficiency.

A Vector Network Analyser (VNA) was used to identify the operational frequency range with low SWR values by measuring the SWR across a range of frequencies [46]. To ensure safe and efficient AOTF operation, an SWR threshold of 3 was selected, so only frequencies below this value were considered usable.

In Figure 6.1, the AOTF from AA opto-electronics was analysed. This AOTF will be further used to identify the geometrical and crystal properties. The operational frequency range of this AOTF is between 73.15 and 148.93 MHz, which is judged by the intersection points with the SWR=3.0 line. Additionally, the minimum SWR value of 1.07 was observed at 111.5 MHz, indicating that nearly all the power is efficiently delivered to the AOTF at this frequency, with minimal voltage reflection to the amplifier.

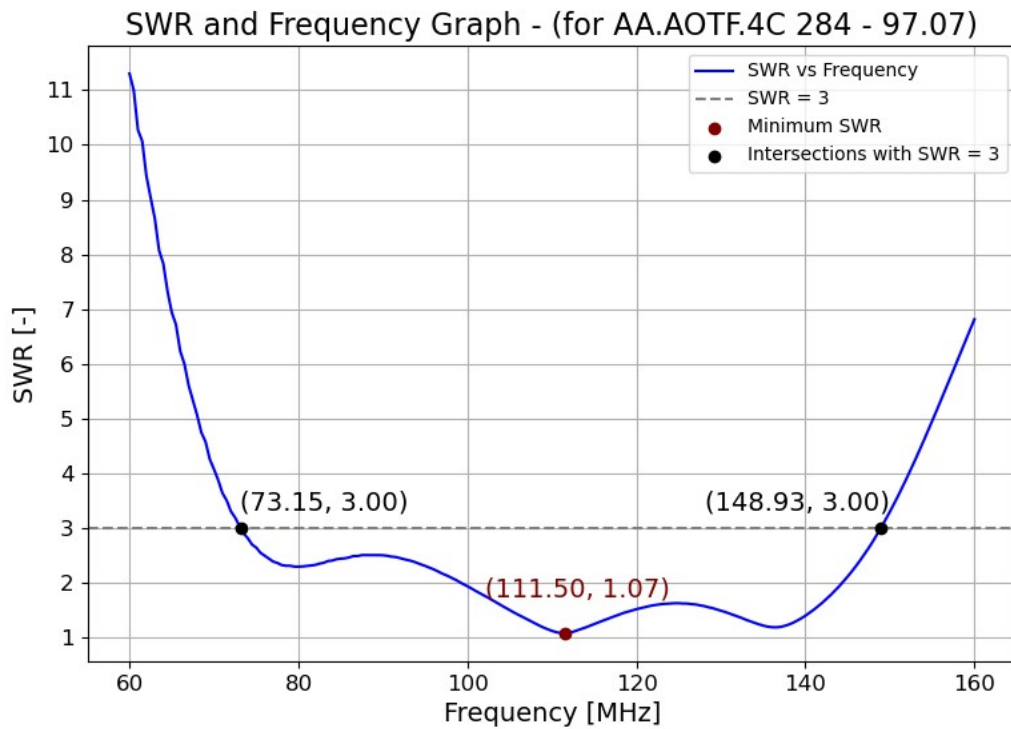


Figure 6.1: The SWR over Frequency graph for the AA opto-electronics AOTF (AA.AOTF.4C 284–97.07)

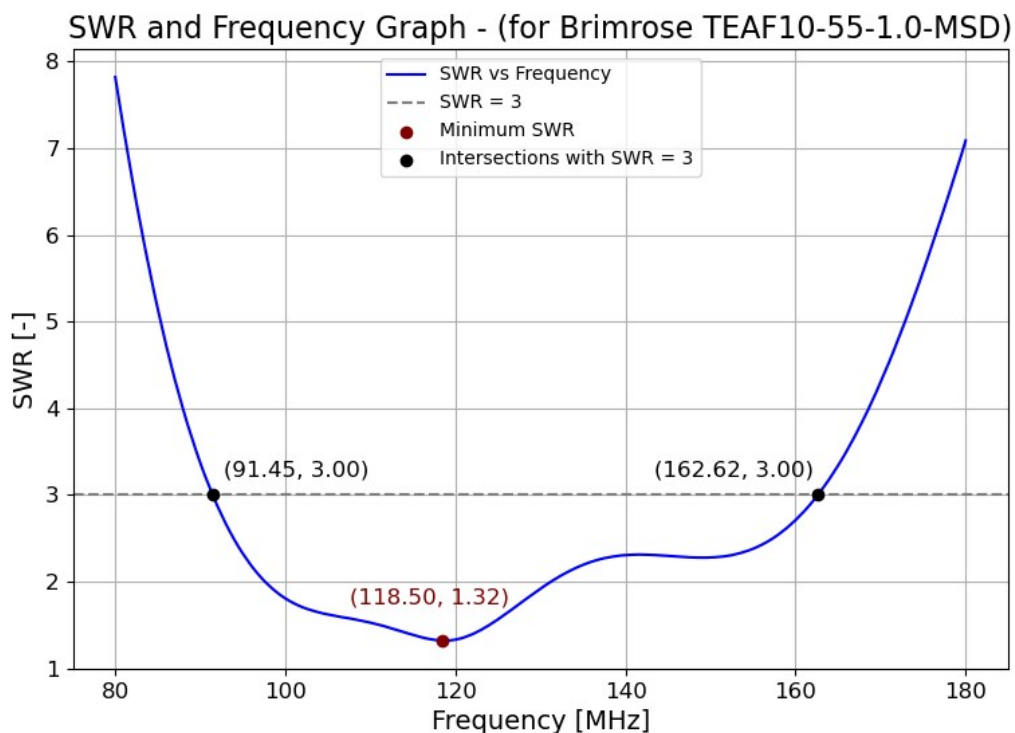


Figure 6.2: The SWR over Frequency graph for the Brimrose AOTF (TEAF10-55-1.0-MSD)

An identical procedure has been performed for the Brimrose AOTF, the results of which are illustrated in Figure 6.2. This AOTF is commercially bought, and it will be used at the end of the report to satisfy the AOTF characterisation requirements. The operational frequency range for Brimrose AOTF is between 91.45 and 162.62 MHz. The higher frequency values, compared to the AOTF from AA opto-electronics, suggest that the Brimrose AOTF will have the transducer positioned at a larger α angle relative to the [110] axis, which can be judged based on the previous description of Figure 2.15.

By knowing the operational frequency ranges for the AOTFs, optical tests can be performed, and satisfy the [TEST-REQ-005] requirement. Such test consideration would ensure that AOTF is operating at high efficiency

from an electrical standpoint. Furthermore, to satisfy the [TEST-REQ-008] requirement, all the AOTFs were limited to the RF power of 100 mW to avoid damaging the transducer.

6.2 AOTF geometrical dimension calculations

In order to validate the simulation in the future and to develop the methods for AOTF characterisation in terms of crystallographic angles such as θ_c and α , some known parameters such as AOTF's geometrical properties shall be known. In this section, the physical dimensions of the AOTF crystal were measured without extracting the AOTF crystal from its housing. This procedure was performed on the AOTF from AA opto-electronics (AA.AOTF.4C 284–97.07).

Due to the AOTF's small size and the precision required, direct manual measurements were impractical. Furthermore, it is undesired to make a direct contact with the AOTF's crystal, and manual measurement could also lead to AOTF damage, as can be seen in Figure 6.3, the transducer is seen relatively fragile. Instead, the digital image-based method was chosen to obtain the necessary AOTF's geometrical dimensions. The process involved the steps outlined below.

Image Capture:

High-resolution photographs of the AOTF using a camera positioned perpendicular to the surface of the AOTF were taken. To ensure accuracy, a scale reference of a one-centimetre grid paper was included in the images.

Software Analysis:

Using an open-source image analysis software, Tracker [63], the captured photographs were imported. The software allows the user to calibrate the image based on the known scale reference, converting pixel measurements to real-world units. For the AOTF measurements, the dimensions were calculated in centimetres. In this case, each pair of squares on the grid paper shown in Figure 6.3 correspond to one centimetre. To calculate the AOTF's angles, the software needs a reference system, which was chosen to be along the AOTF's contour, shown in pink lines in Figure 6.3, since that is the part which will be rotated during the testing. To make sure that the reference system's lines pass along the AOTF's contour, the reference system had to be rotated by 0.2 degrees counterclockwise, suggesting that AOTF itself was not at 90 degrees with the camera.

Dimension Extraction:

The key points on the AOTF in the image, such as edges and corners, were identified and the start and end points of the surface were specified. The software then calculated the distances between these points based on the image's scale reference. By specifying the length of the surface, the software also determined the surface's inclination based on the previously established axis system, shown in purple. This allows to find the angles γ , β , and other relevant AOTF angles.

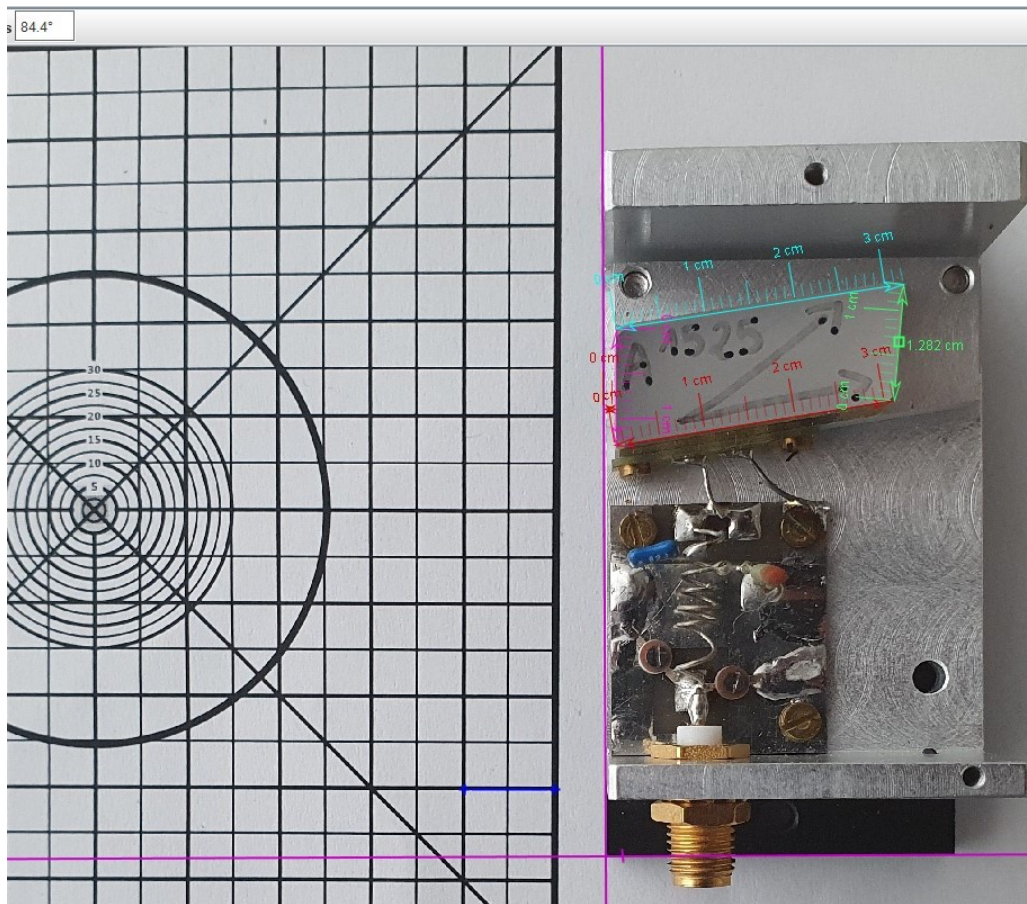


Figure 6.3: AOTF being analysed in image analysis software — Tracker [63].

Based on the procedure described, the AOTF's dimensions and angles were determined and subsequently imported into the analytical model. Figures Figure 6.4 and Figure 6.5 summarize the dimensions obtained from the image analysis.

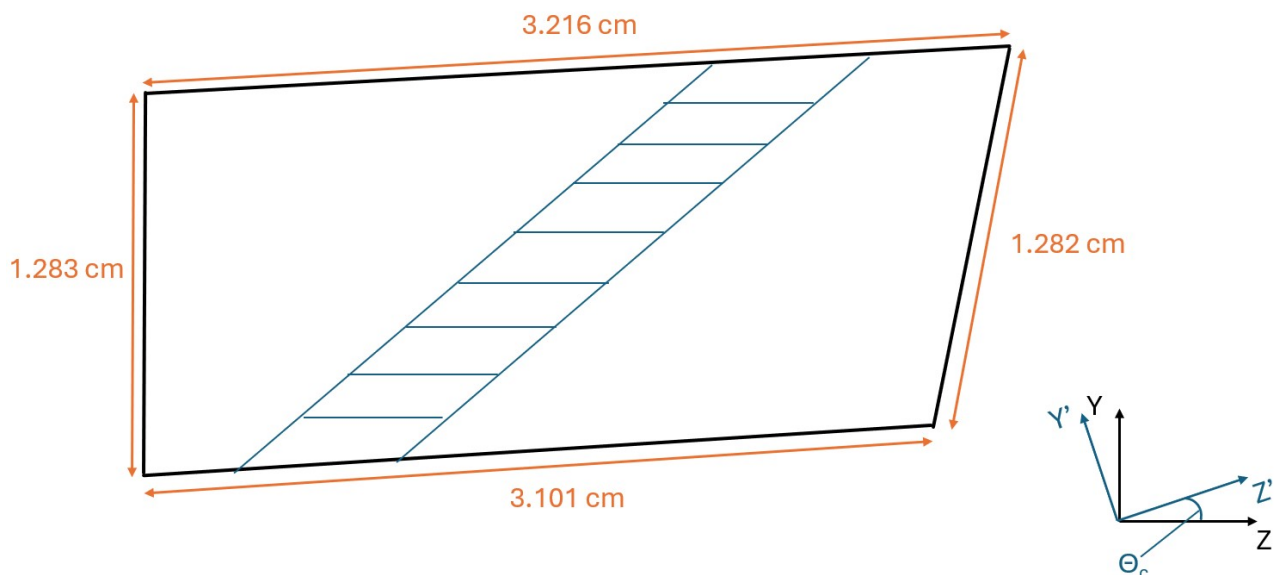


Figure 6.4: AOTF length dimensions obtained from the image analysis.

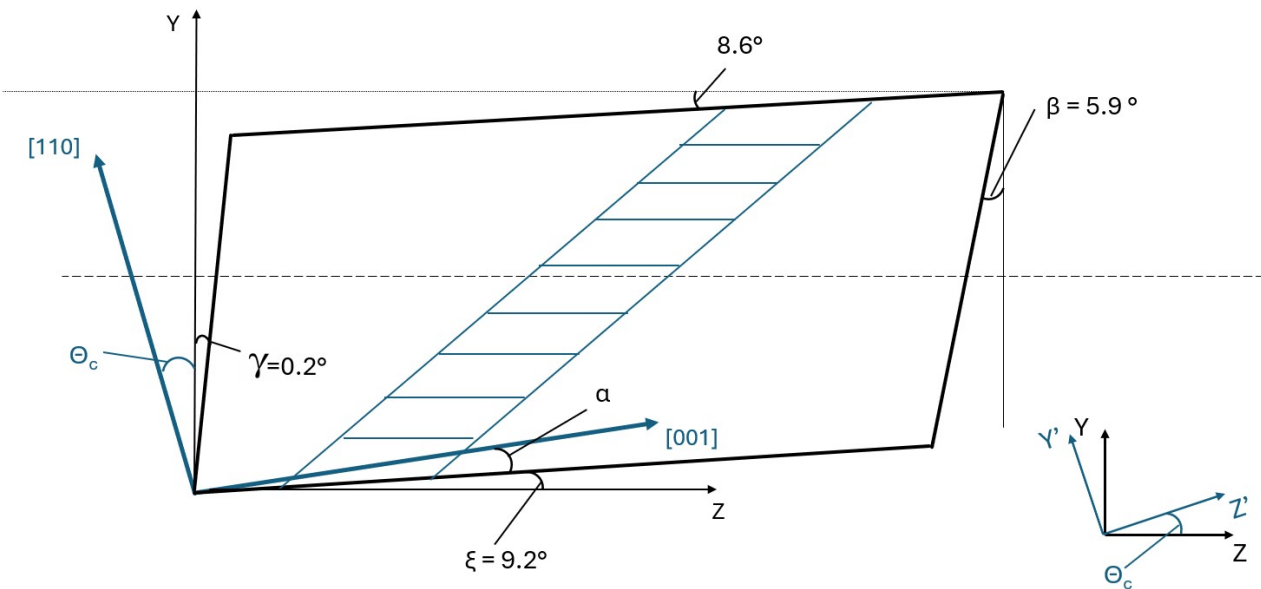
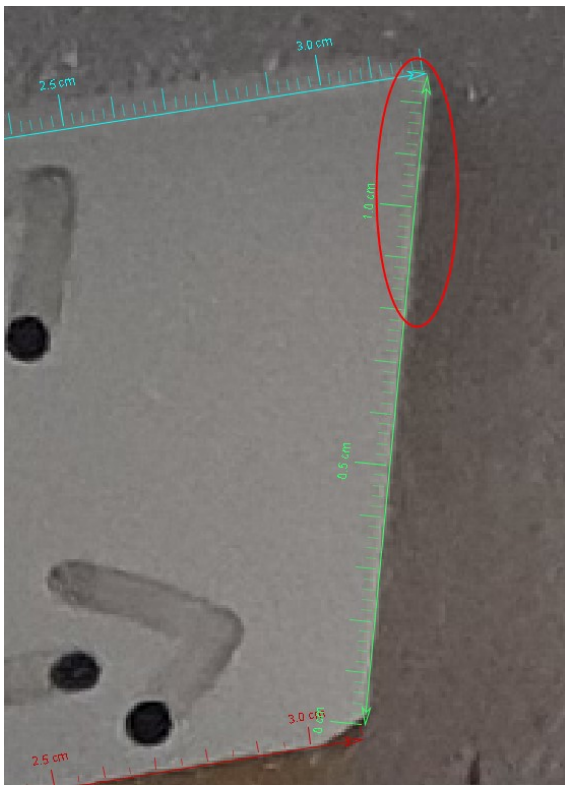


Figure 6.5: AOTF angles obtained from the image analysis.

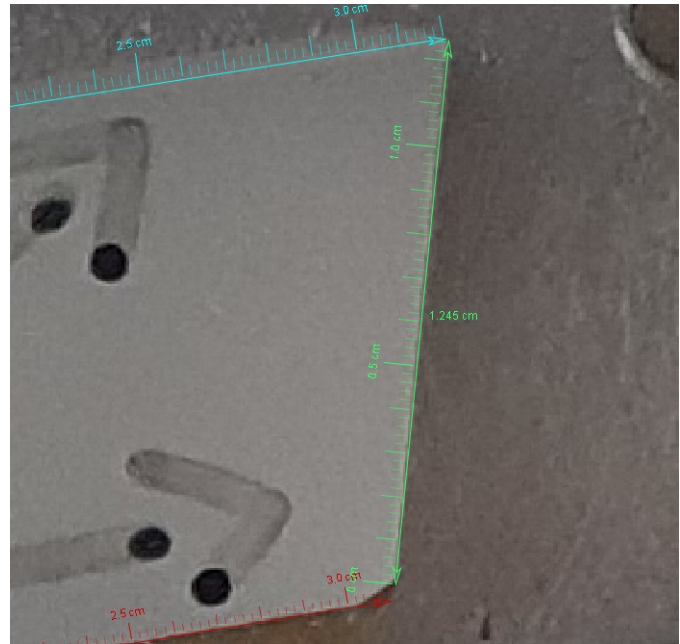
From the angle's perspective, the entrance angle γ was found to be 0.2° relative to the AOTF's contour. The exit angle β was found to be equal to 5.9° . From the AOTF's last surface's orientation, with positive β angle, this AOTF is designed to operate at the e-ray input application [64]. This means that this AOTF will perform better for diffracting an extraordinary (horizontally) polarized light.

It is hypothesised that such AOTF behaviour is related to the transducers positioning relative to the crystallographic axis system. In this case, the crystallographic axis system is rotated anti-clockwise relative to the global axis system and the transducer is positioned at the AOTF's bottom surface. If the transducer is instead glued to the AOTF's top surface, and the crystallographic axis still has an anticlockwise orientation, then that AOTF would be designed for incident ordinary polarization, which is a similar configuration as in [30] paper. However, information from literature confirming such hypothesis could not be found at the time of this topic research.

Identifying the β angle was challenging due to imperfections in the surface finish of the exit facet of the AA opto-electronics AOTF. Such imperfections can occur during the manufacturing process of AOTFs [47]. In this case, the top part of the facet had a different inclination compared to the bottom part. This can be observed in Figure 6.6a, where the bottom part of the facet aligns with a straight line, while the top part, highlighted in red, deviates. To account for this, the overall inclination was re-evaluated, as shown in Figure 6.6b, resulting in $\beta = 5.9^\circ$.



(a) Angle β identification, focusing on the lower part of the facet.



(b) Revised identification considering the overall facet's inclination.

Figure 6.6: Comparison between initial and revised identification of the β angle.

The crystallographic axis angle, θ_c , could not be calculated from the picture and therefore remained an unknown. Similarly, due to the dependence on the angle θ_c the piezoelectric positioning angle α could also not be identified, which can be visualised in Figure 6.5. It will be a goal of Chapter 7 to characterise angles θ_c and α .

6.3 Setup description

As been mentioned, the two main tests which were performed on the AOTF are the power and the diffraction testing. The aim of the power testing is to identify the incidence angles at which the AOTF performs the best in terms of highest diffracted ray intensity. The diffraction test is aiming to record the exit angles of the diffracted and undiffracted beams. The second test purpose is to validate the analytical model's outputs.

To perform those tests, optical setup is required. In this section, firstly in Subsection 6.3.1, the equipment used in those tests would be described. Followed by the alignment procedure in Subsection 6.3.2 to ensure that no additional inclination to the optical ray is introduced. Finally, considering that the tests are being planned to be performed for both e and o polarized lights, Subsection 6.3.3 describes how the polarisation types are changed in the setup.

6.3.1 Setup components

Most of the components used are the same for both of the tests. The purpose and positioning of these components on the optical breadboard is described in this section, with Figure 6.7 being used as an illustration of the setup schematic used for the power testing with an incident e-ray, and similarly Figure 6.8 provides a schematic for the diffraction testing.

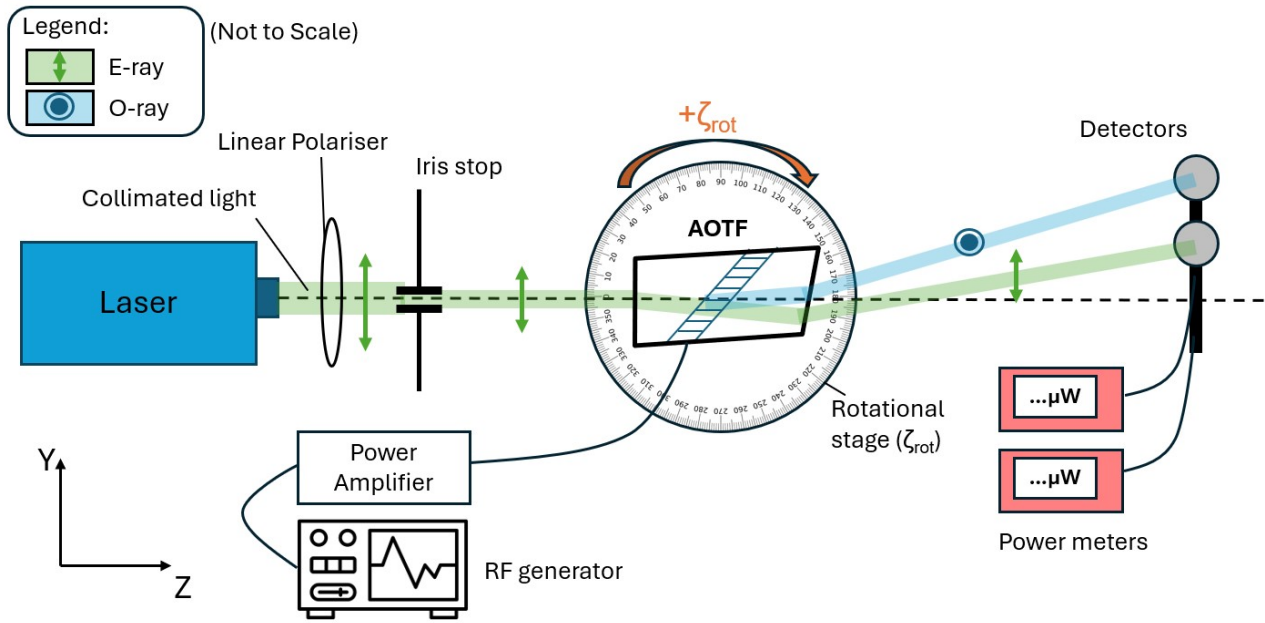


Figure 6.7: Experimental setup schematic for the power testing for the incident e-ray.

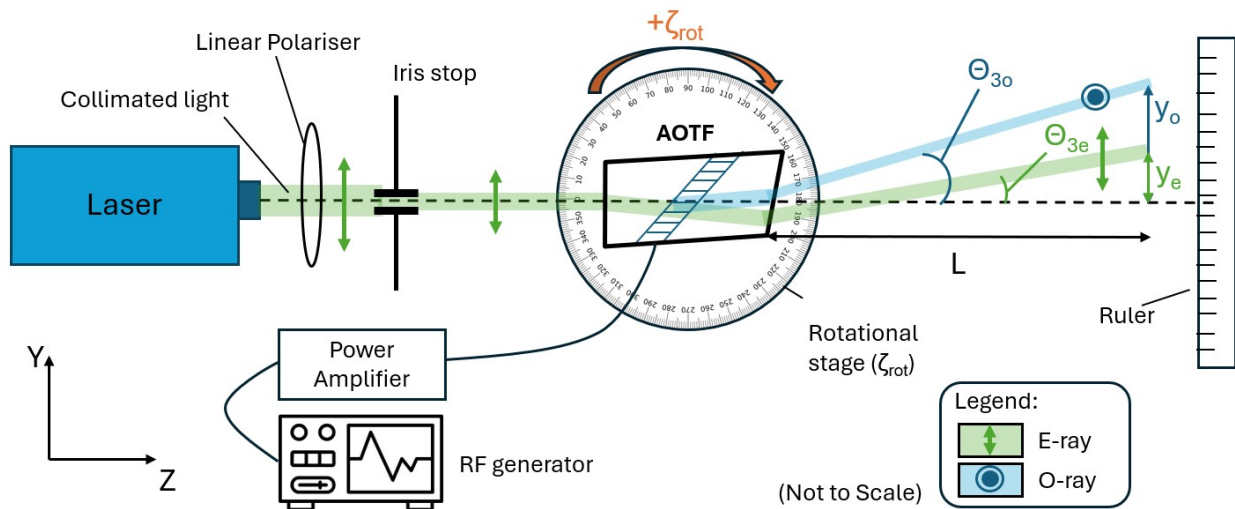


Figure 6.8: Experimental setup schematic for the incident e-ray diffraction test.

Visible Range Laser (LDM635, Thor Labs): This laser was selected for its collimated light with a linear polarization. Collimation is essential for efficient AO interaction within the AOTF [7]. Considering that the laser already produces collimated light, additional collimation lenses were unnecessary. The linear polarization was essential to switch between horizontal (extraordinary) and vertical (ordinary) polarization types [3]. The downside was that the laser produced a wide elliptical beam as an output, which was solved by using an aperture stop (iris).

Linear Polariser: A linear polariser was used to evaluate the AOTF's performance at various polarisation angles. It enabled precise adjustment of the laser's rotational orientation, allowing the selection of a specific polarisation type — either ordinary (vertically linear) or extraordinary (horizontally linear).

Iris stop: To address the elliptical and wide nature of the output beam from the laser, which caused internal reflections at certain AOTF rotation angles, an iris was introduced. This modification shaped the input beam into a circular and smaller form, avoiding unwanted reflections and improving the quality of the AO interaction. A visualisation of iris' frontal view partially blocking laser's profile is shown in Figure 6.9.

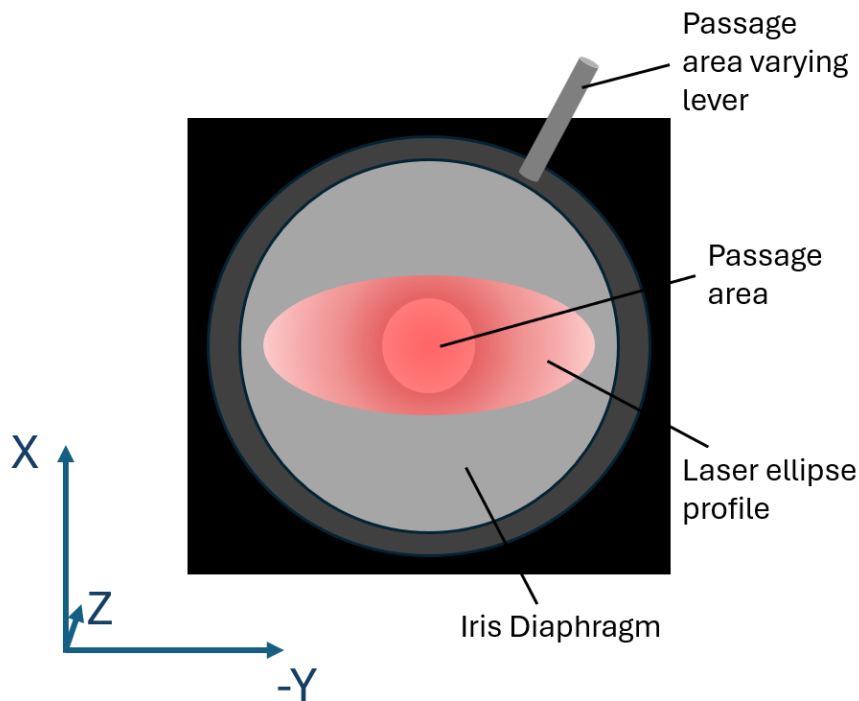


Figure 6.9: Iris Diaphragm and elliptical incident laser profile

Rotational Stage: This component was used to vary the AOTF's angle orientation with respect to the incoming laser ray. This meant that the incidence angle can be changed together with the rotational angle. The rotational stage allowed varying the AOTF's rotational angle up to 5 arcminutes, which is equivalent to 0.0833 degrees.

AOTF: The AOTF itself was the central component, positioned and fixed on the rotational stage. It was also connected to the power amplifier through a cable to send the RF signal to the AOTF's transducer.

Rulers: Two rulers were used for the diffraction test. The first ruler is used to record the distances along the y-axis of the diffracted and undiffracted rays from the AOTF, positioned at the end of the diffraction test optical setup in Figure 6.8. The second ruler is employed to measure and verify the distance L along the Z-axis between the AOTF exit surface and the deviation measuring ruler.

RF Generator: An RF generator was included to generate the necessary RF signals to drive the AOTF. The tuning frequency could be adjusted at the RF generator.

Power Generator: This component amplified the generated RF signal from -20 dBm to 20 dBm, equivalent to 100 mW. This signal is then sent to the AOTF via SMA cable.

Detectors and Power Meters: For power tests, two detectors and two power meters were used. Allowing to measure the power intensity of the diffracted and undiffracted beams.

6.3.2 Setup alignment procedure

The steps regarding the setup alignment are similar for both of the tests. The main objectives of the alignment for such tests is to ensure that the laser is sent along the same optical axis and to ensure that the AOTF is positioned directly perpendicular to the optical axis before the rotation is applied.

To perform the test along a single axis, all equipment was mounted in a straight line on the breadboard, as can be seen in Figure 6.10. To ensure such alignment, screws were added to the poles, allowing to screw the poles along the holes of the breadboard. Such steps ensured that the optical setup is all along the same axis without any deviation in the transverse (y-)axis.

After mounting all the poles, the laser was securely fixed in place. For the extraordinary ray tests, it was essential to confirm that the laser beam was horizontally polarized, which could be judged by observing the horizontal ellipse produced from the laser [65]. Afterwards, it was ensured that the laser was directed to hit the midpoint of the ruler, marked at 250 mm. Then, the double iris was used to adjust the beam's size, and its placement was adjusted to make sure that the laser beam still hit the middle point, as can be seen in Figure 6.10.

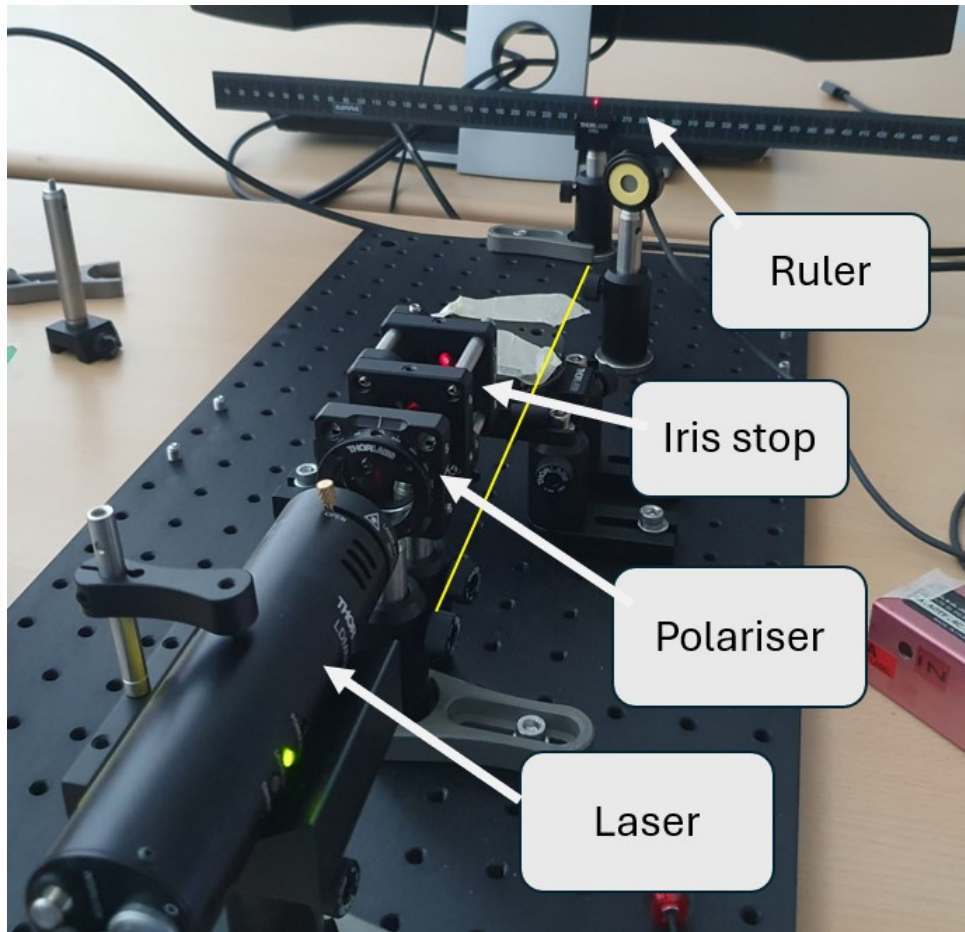


Figure 6.10: Laser alignment along the optical axis.

For the diffraction test, it is desired to have a larger distance between an AOTF and the deviation measuring ruler at the end of the optical setup. Therefore, after the laser alignment is established and the correct heights for all the optical components is picked, the ruler is moved to a further L distance outside the breadboard's length. In the experiments, this distance was around 1.1 meters, which was confined by the dimensions of the optical lab space where the setup could be kept in the dark environment. The new ruler positioning is fixed, and the point where the laser is shone is marked as a point y_0 , based on which other beam exit angles could be calculated with the help of the trigonometry, as shown in Figure 6.11. Moving the deviation measurement ruler straight away at a desired distance is not possible, as the breadboard is needed to know the exact positioning of the optical axis.

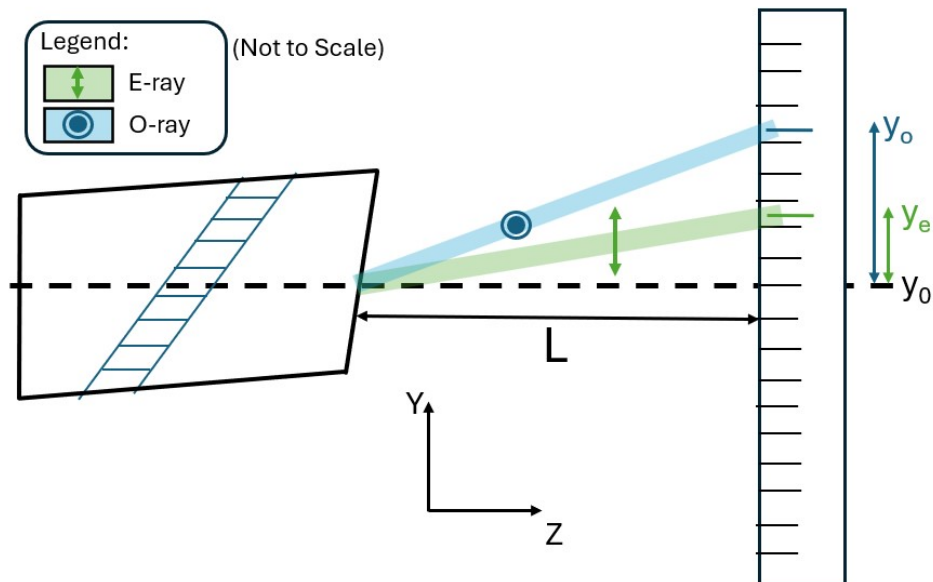


Figure 6.11: Notation used for the positioning of the beams at the ruler

Afterwards, the AOTF was mounted on the rotational stage. Unfortunately, the AOTF's hole sizes did not match with the rotational stage. Therefore, to ensure that the AOTF is firmly placed, the AOTF was thoroughly tapped to the rotational stage. Additionally, it was made sure that the laser ray passed through the middle of the AOTF. To make sure that the AOTF is perpendicular to the ray, a 90-degree ruler was used, as depicted in Figure 6.12. The ruler is firmly placed against the screws on the breadboard, and to ensure that the AOTF is perpendicular, there should be no gap being present between the ruler and the AOTF's surface.

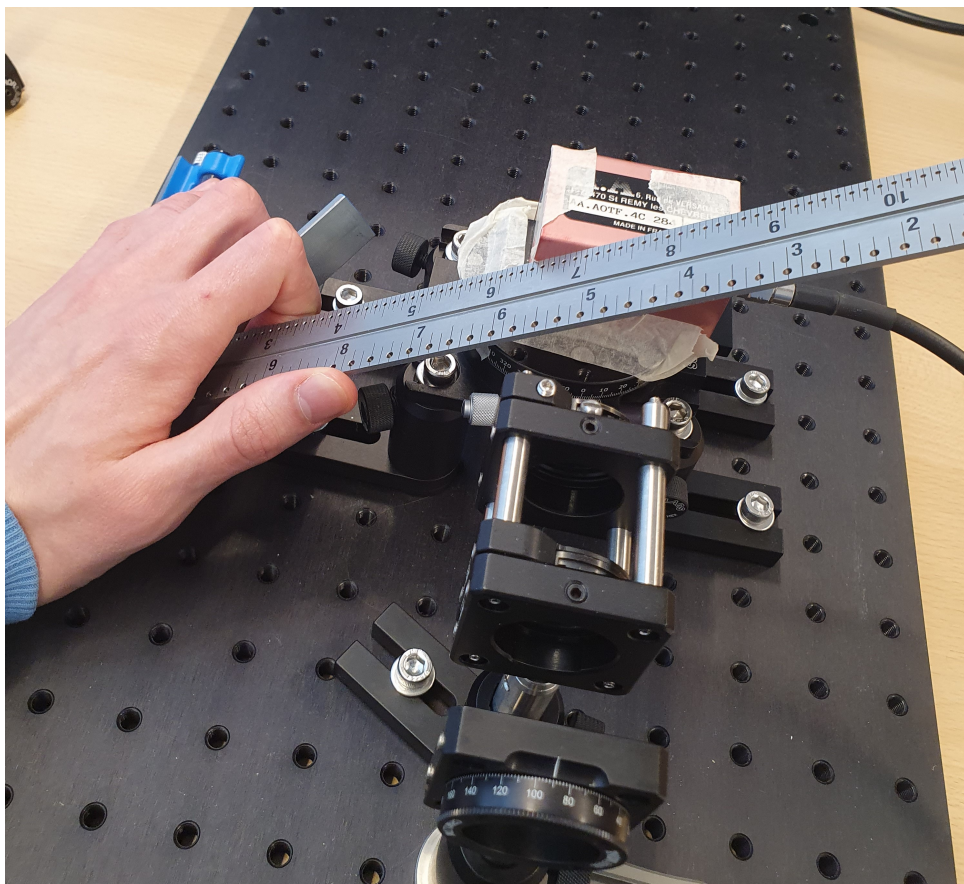


Figure 6.12: Adjusting AOTF to be perpendicular to the optical axis.

After this is done, the rotational stage is fixed, and the reading of the rotational angle is taken. Based on this

reading, the future rotational angles can be easily identified. For identification of the diffraction rays outgoing from the AOTF, the distance from the AOTF to the ruler was also measured.

6.3.3 Polarisation classification

During the testing, both of the AOTFs are tested with two different incident ray polarizations, the extraordinary (horizontal) polarization and the ordinary (vertical polarization) [3]. Explanation of why horizontally polarized ray is extraordinary and vice versa is provided Section 2.4. To avoid the confusion, this section provides the schematics of the global coordinate system during AOTF testing and the output rays notations.

The global axis system for the AOTF in the experimental setting is shown in Figure 6.13, to match the notation used in the simulation. The optical axis is the Z axis, along which the incident ray is propagating before coming into contact with the crystal. The Y axis, shown in orange, is used as a basis to calculate the AOTF output angles. Finally, the X axis completes the system by pointing upwards.

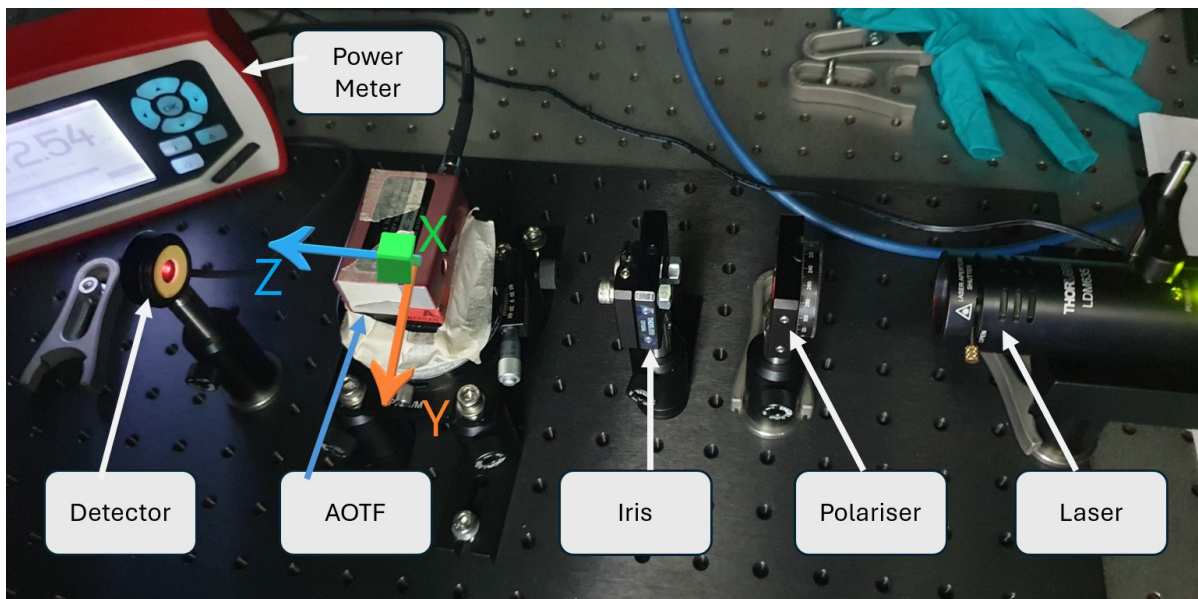


Figure 6.13: Global coordinate system with the setup used

To understand what is meant by the e-ray diffraction case, Figure 6.8 has been shown previously, where the extraordinary ray is marked in green and the ordinary ray in blue. In this testing, the horizontally polarized light is an extraordinary polarization, meaning that the electrical field of the ray is oscillating along the Y-axis. The ordinary ray is where the electric field is oscillating along the X-axis.

To highlight these specifics of the ray polarization states, the p and s-polarization notations were used in the figures, where p-polarization stands for parallel to the incidence plane and s-polarization stands for the light perpendicular to the incidence plane [66]. In this case, the incidence plane is along the y and z axes, meaning that horizontal polarization is p-polarized and has a notation of a double arrow. Similarly, the vertical polarization is s-polarized and has a dot notation on the figures.

In the e-ray diffraction, previously provided in Figure 6.8, the diffracted light is expected to be ordinarily polarized and should have a larger output angle (θ_{3o}) compared to the incident output light's angle (θ_{3e}) which stays extraordinarily polarized. In other words, from the laser's point of view, the diffracted ray is expected to appear to the left of the incident output ray.

Contrary, for the o-ray diffraction case shown in Figure 6.14, the diffracted light is extraordinarily polarized, and it is appeared at a smaller angle compared to the undiffracted beam of light.

To determine the output angles in both of the cases, the length L is measured and the diffracted distance (y_e or y_o) are identified. Afterwards, by using basic trigonometry, the desired angles θ_{3o} or θ_{3e} are calculated for each AOTF rotational angle (ζ_{rot}) which is defined positively clockwise.

6.4 Diffraction testing procedure

After gathering the necessary equipment and ensuring the setup alignment, the tests can begin. The primary goal of diffraction testing is to measure the output angles from the AOTF. As previously mentioned, the AOTF

outputs two rays: the undiffracted ray and the diffracted ray, which results from the AO interaction. By determining the diffraction angles and noting down the required RF signal, the results can be compared with the simulation data, and be used for model validation.

The optical setup schematic used for the diffraction testing is presented in Figure 6.14, where the alignment procedure has already been performed and the AOTF has been added to the setup in the middle, and the ruler at the furthest distance away possible to record the ray deviations along y -axis. The RF generator and the amplifier are connected by coaxial cables to the AOTF, to control the tuning frequency f required for AO interaction.

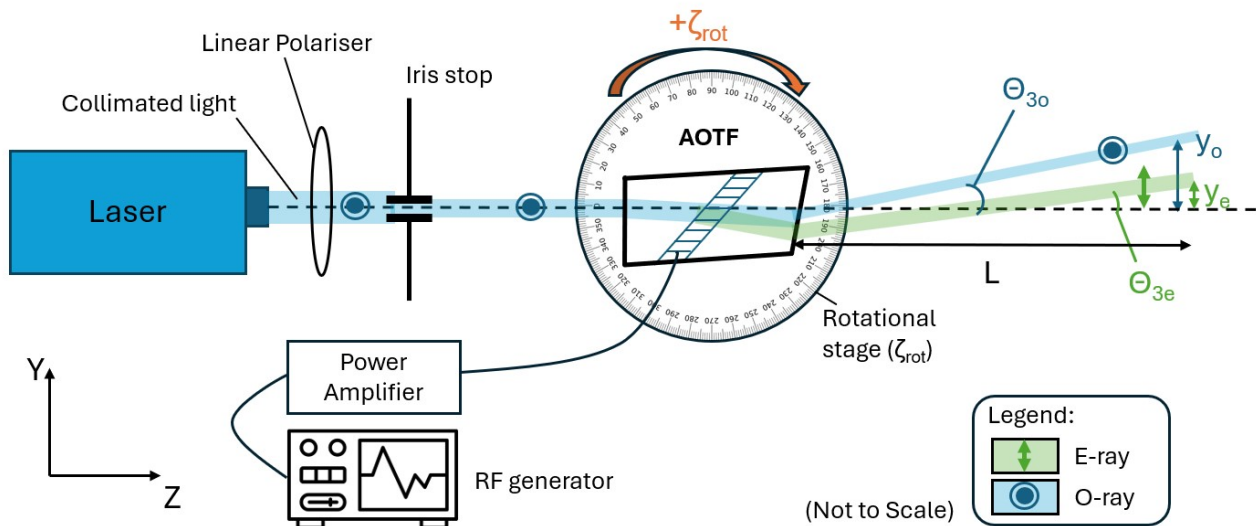


Figure 6.14: Experimental setup schematic for the incident o-ray diffraction test.

The procedure to perform the diffraction testing:

1. Perform the alignment as described in Subsection 6.3.2.
2. Adjust the AOTF's rotational angle by rotating the rotational stage, and record the new rotational angle ζ_{rot} .
3. Generate an RF signal and vary the frequency until the maximum intensity of the diffracted ray is observed. Note the applied RF frequency.
4. The diffracted beam intensity is judged by reading a measurement from a detector placed close to the deviation measurement ruler. After finding the highest diffracted beam intensity, the detector is removed from the path of the diffracted ray.
5. Calculate the output rays' angles by reading the ruler located at the end of the optical setup and using the known distance between the ruler and the AOTF.
6. Repeat steps 2 to 4 for each new AOTF rotational angle.

Angle calculations were performed based on the ruler readings and trigonometric calculations, using the known distance between the AOTF and the ruler. Judging readings with the naked eye on the ruler in the dark setting was challenging; therefore, to enhance detection accuracy, a photo was taken for each AOTF rotation angle. From the photo, the centre of the optical beam could be precisely located along the ruler, thereby improving the accuracy of the measurements, as illustrated in Figure 6.15.

During testing, it was observed that the incident ray often splits into two closely placed rays after passing the crystal due to birefringence. This phenomenon complicates the distinction between the readings on the ruler with the naked eye. However, the photo allows seeing those two rays separately, as can be noted on Figure 6.15. For the extraordinary input ray, measurement of the higher intensity optical beam was taken since that is the e-ray, and it has experienced a higher refractive index while passing through the crystal.

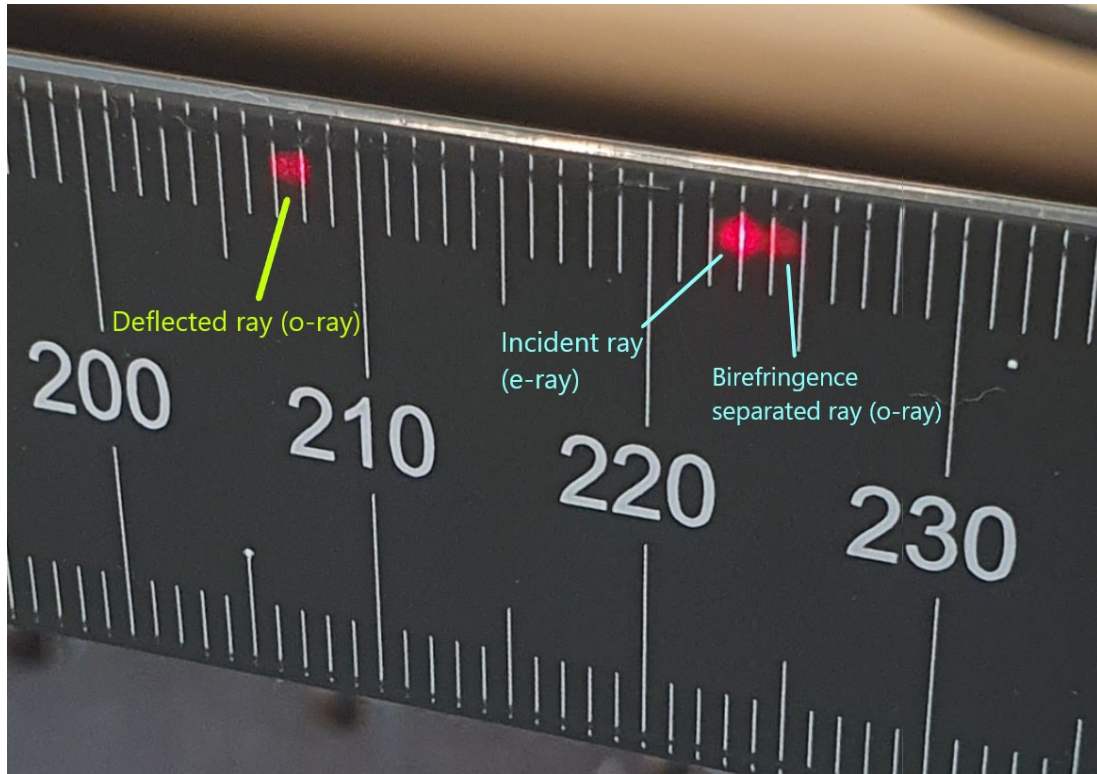


Figure 6.15: Ray separation by birefringence into ordinary and extraordinary rays, sending a horizontally polarized light (e-ray).

The birefringence separated ray, the most right optical beam in Figure 6.15, is caused due to the crystallographic axis being rotated compared to the global axis by angle θ_c , as seen in Figure 4.4. If the input ray's polarization rotated anticlockwise by an angle θ_c , then that optical beam would disappear, which was physically tested with the help of a polarizer in the setup. However, performing the acousto-optical diffraction at such polarization goes against the AOTF's design, resulting in a low diffracted beam intensity.

Measurement correction due to the AOTF rotation

After specifying how the measurements of the rays were recorded on the ruler, it is important to specify how the beam angles were calculated and how a correction due to the AOTF's rotation is applied.

When the AOTF is positioned perpendicularly to the incident ray, $\zeta_{rot} = 0$, as shown in Figure 6.16, the calculation of the diffracted ray angle is just trigonometry (Equation 6.1), involving the length L and the distance between the point on the optical axis (Y_0) and the point of recorded diffracted beam, in this example Y_e .

$$\theta_{3e} = \tan\left(\frac{Y_e - Y_0}{L}\right) \quad (6.1)$$

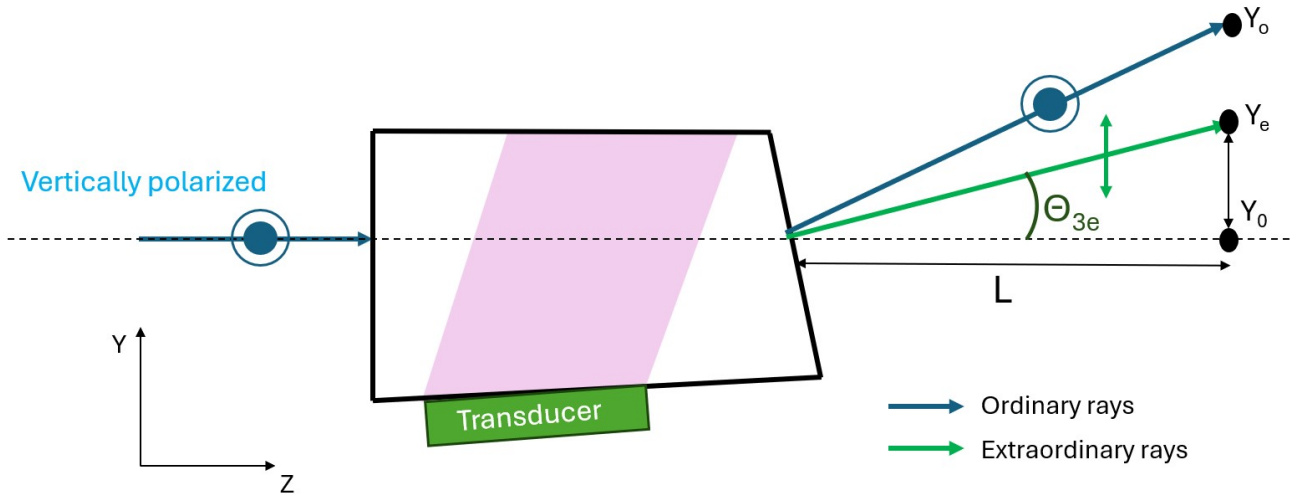


Figure 6.16: Top view of an AOTF diffraction at 0 degrees of rotation.

However, in cases where the AOTF is rotated, the point where the rays leave the AOTF's exit surface changes too. For consistency of the calculation, it is desired to keep the same reference point of where the rays leave the AOTF. As can be seen in Figure 6.17 the anticlockwise rotation causes the ray's exit point to shift positively along the y -axis. If the diffracted ray angle θ_{3e} is calculated based on the old reference point Y_0 , then the test would overestimate the diffraction angle.

To correct for this error, an estimated shift (ϵ_{rot}) of the new reference point is calculated based on half of the AOTF's length, found in Figure 6.4, and the rotation angle ζ_{rot} . This shift allows finding a new reference point Y_{0n} for each rotational angle. With this correction, the diffracted ray angle is found by using Equation 6.4. Similarly, the undiffracted ray angle θ_{3o} is found by using the same equation, but instead of Y_e the point Y_o is used.

$$\epsilon_{rot} = (L_{AOTF}/2) \sin(-\zeta_{rot}) \quad (6.2)$$

$$Y_{0n} = Y_0 + \epsilon_{rot} \quad (6.3)$$

$$\theta_{3e} = \tan\left(\frac{Y_e - Y_{0n}}{L}\right) \quad (6.4)$$

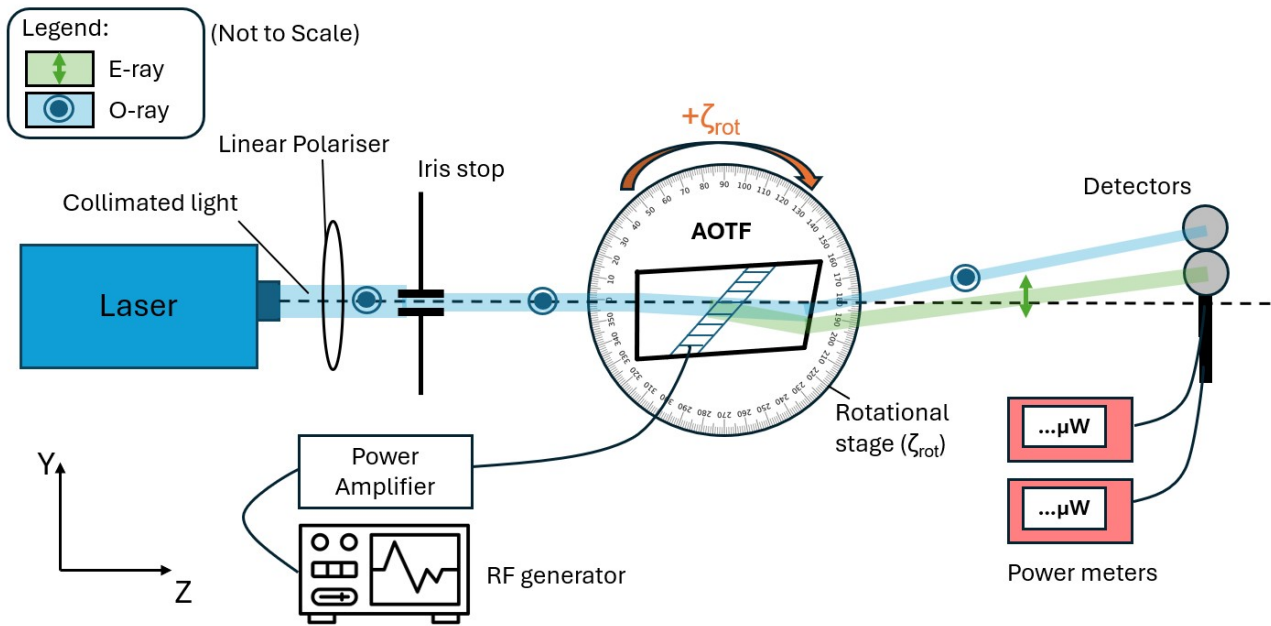


Figure 6.18: Experimental setup schematic for the incident o-ray power test.

The power meters were connected to the detectors to provide the beam intensity reading in watts. To avoid the environmental noise from external light sources, the test was performed in a dark setting. Otherwise, it would be difficult to recognize at which AOTF rotation angle the highest diffracted beam intensity was recorded.

After clarifying the equipment positioning and the setting, the procedure for the power test was as follows:

1. Perform the alignment as described in Subsection 6.3.2.
2. Adjust and fixate the detectors on the breadboard, making sure the optical rays are hitting the detector's centre.
3. Make sure the power meters are adjusted for 635nm reading, and zero the meters for the dark room.
4. Turn on the laser and RF generator.
5. Adjust the AOTF's rotational angle and adjust the generated RF frequency until the maximum intensity of the diffracted beam is detected.
6. Record the intensities of both beams. Turn off the laser and the RF supply to the AOTF, and note down the frequency used for the maximum diffraction.
7. Repeat steps 4-6 until the maximum power intensity has been recorded for a range of rotational angles ζ_{rot} .

Reason for turning on/off the laser and RF generator

During the initial power tests, it was noticed that the combined power intensity of the undiffracted and diffracted beams decreases over time, while incident angle and RF signal remain constant. Such a test feature was undesired, since it meant that the total power supply is inconsistent between the measurements. Therefore, to avoid this inconsistency, in between power measurements the RF supply was stopped as well as the laser power supply was momentarily turned off. The same consideration was added for the diffraction testing.

One explanation of why the total power has reduced during the test can be explained by the laser's internal rise in temperature with time [67]. This temperature increase could impact the electronics inside the laser and therefore reduce the efficiency of the ray production during the test. In fact, it was found that due to the laser temperature increase the supplied current also increases in the laser [67], which may explain the inconsistency of the laser beam intensity with time.

Another reason could be the increase in temperature of the AOTF during the testing. It was researched that a rise in AOTF's temperature could affect its polar angular performance [30]. Therefore, it is advised to switch off the AOTF after each measurement power measurement.

Diffraction Efficiency

To find at what specific rotational angle ζ_{rot} the highest diffraction efficiency (DE) was recorded. A coarse search was firstly performed where ζ_{rot} was changed by one degree per reading, and then a fine-tuning was performed in the interval where the highest diffraction was recorded based on the initial coarse testing. The diffraction efficiency can be found with the help of Equation 6.5, where I_1 is the intensity of the diffracted beam and I_0 of the undiffracted beam [13].

$$DE = \frac{I_1(\lambda)}{I_1(\lambda) + I_0(\lambda)} \quad (6.5)$$

An example of the power test in an experimental setting can be seen in Figure 6.19, where the laser ray passes through all the optical components and two distinct rays leave the AOTF. Those two rays are then captured on the detectors at the end of the breadboard and the power readings are taken.

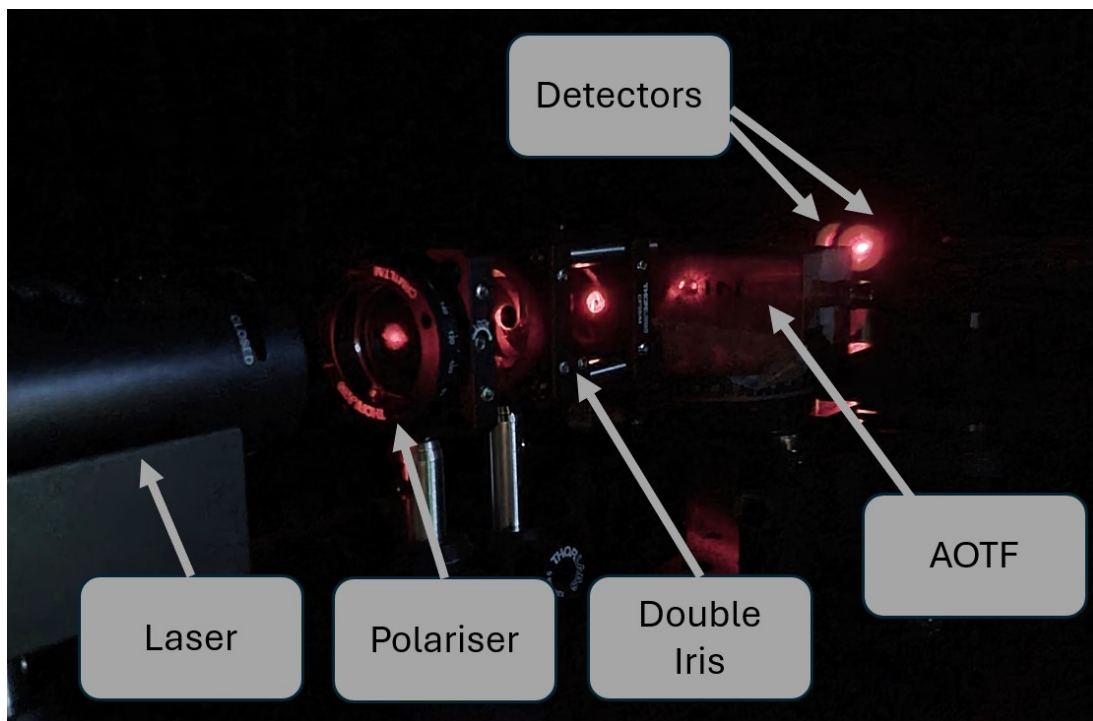


Figure 6.19: Optical setup for the power testing.

6.6 Conclusion

This chapter focused on the physical tests necessary to validate the AOTF simulation program developed earlier, and also to attempt characterising the AOTF crystallographic angles with the help of results from the tests. The chapter described the digital analysis performed on the AOTF to obtain the necessary AOTF dimensions and angles that can be later imported into the AOTF simulation.

Following the digital analysis, the chapter detailed the optical setup, listing all components and their purposes, explaining the alignment procedure for each test, and specifying the differences between the tests when the other incident beam's polarization type is used. The purposes and procedures of the two main tests, diffraction testing and power testing, were also described.

Diffraction testing aims to validate the simulation results by examining the output rays exiting the AOTF. The positioning of the optical rays is recorded on a ruler, and trigonometry is used to calculate the rays' exit angles, which are then compared with the simulation results.

Power testing identifies the AOTF's rotational angle at which the diffracted optical beam has the highest intensity. Conducted in a dark setting, this test can highlight which factors may affect the AOTF's diffraction efficiency.

In summary, the methodologies and descriptions provided in this chapter will guide the physical tests. Throughout this chapter, the test setup requirements under the [TEST-REQ] category from Section 3.2 were satisfied. Table 6.1 provides a summary of these requirements along with descriptions of how each one was met.

Table 6.1: Test Requirements and Achievements

Requirement ID	Requirement's Goal	How it was achieved
[TEST-REQ-001]	Align setup for accurate angles.	Aligned components with laser and ruler.
[TEST-REQ-002]	Measure diffracted and undiffracted angles.	Used ruler and trigonometry for angle calculation. With correction procedure.
[TEST-REQ-003]	Dark setting for intensity accuracy.	Conducted tests in dark optical lab.
[TEST-REQ-004]	Measure diffracted ray intensity.	Added photodetectors with power meters.
[TEST-REQ-005]	RF signal within VSWR limits.	Identified RF range with VSWR values < 3.
[TEST-REQ-006]	Record RF signal at peak diffracted beam intensity.	Measured power at peak diffracted intensity.
[TEST-REQ-007]	Vary incidence angle approaching the AOTF crystal.	Added rotatable stage for adjustments.
[TEST-REQ-008]	Limit power within transducer specs.	Applied low power of 100 mW.

The results for both diffraction and power tests are analysed in the following chapter, to understand the behaviour of the AA opto-electronics AOTF and to develop a method to characterise the AOTF in terms of the crystallographic angles positioning.

Model validation — experimental results 7

In this chapter, the AOTF from AA opto-electronics will be tested in terms of power testing and diffraction testing, using the procedure described in Chapter 6. Considering that the angles θ_c and α are secretive by the manufacturers, but at the same time critical for simulating AOTF's performance. Therefore, the key aim of this chapter is to find a methodology to characterise those AOTF angles, in an attempt to satisfy the [CHAR-REQ-001] requirement.

The second aim is to analyse what aspects affect the diffraction efficiency (DE) of an AOTF, and whether the DE changes with varying rotational angles, answering sub-question six. This will be analysed in Section 7.1, where the results of the power tests are compared between the incident o-ray and e-ray cases.

In Section 7.2 a successful method for the AOTF's characterisation is introduced. The method is frequency-matching, where the analytical model is used to vary θ_c and α angles until the model's curve matches the frequency curve obtained in the diffraction testing.

These obtained θ_c and α are then tested with the diffraction testing results, in Section 7.3, where it is judged with which values the analytical model simulates the diffracted and undiffracted angles more accurately. The second aim, of the diffraction testing section, is to further validate the analytical model. Some aspects such as diffraction in incident e-ray case and application of the model for various optical wavelengths have already been verified in Section 4.6 and Chapter 5. However, the aspects such as AOTF's rotation, or using the model for incident o-ray have not yet been verified. These aspects will be judged based on the trend lines produced by the model and obtained in the experiment for the diffracted and undiffracted angles.

Finally, Section 7.4 will look into the rotatory power influence, where firstly a simple test is performed to judge whether the AOTF rotates the incident polarization, and secondly it is analysed, whether the inclusion of rotatory power can further improve the accuracy of the model in simulating the diffraction testing angles.

7.1 Power testing validation

The aim of the power testing is to identify at which incident angles does the AOTF perform at the highest diffraction efficiency, a calculation based on Equation 6.5. This test follows the procedure described in Section 6.5, where at the end of the optical setup two detectors are positioned which measure the beam intensities of the diffracted and the undiffracted beams, exiting from the AOTF. With the obtained power intensities, it is then possible to determine the diffraction efficiency (DE) of the AOTF at a given rotational angle ζ_{rot} and tuning frequency. The raw data for the power tests is presented in Appendix C.

The initial hypothesis of the power test was that by finding the highest DE at a given rotational angle ζ_{rot} , it would be possible to characterise the AOTF in terms of angles θ_c and α , to satisfy the AOTF characterisation requirement [CHAR-REQ-001]. As will be later discussed, such a hypothesis was false and it did not yield desired results. Therefore, this section will mainly focus on analysing the results when the e-ray (Subsection 7.1.1) and the o-ray (Subsection 7.1.2) incident lights are sent into the AOTF. The differences between the two cases will be compared, and it will also be discussed which factors influence the DE the most.

7.1.1 Incident e-ray power test

For the incident e-ray power test, a horizontally polarized light was sent into an AOTF following the schematic shown previously in Figure 6.7. As previously described in Section 6.5, the power test was performed in the dark setting with the alignment being performed. Initially, the test involved a coarse search, results presented in Table 7.1, where the rotational angle was increased by one degree for each new measurement. The second is the fine search, presented in Table 7.2, where the rotational angles were changed around the values where the highest diffraction efficiency was found.

From the coarse power testing, Table 7.1, it can be seen that the diffraction efficiency increases as the rotational angle ζ_{rot} increases, with the highest diffraction efficiency being recorded around the $\zeta_{rot} = 5^\circ$. The power drop-off, at the rotational angle of 6 degrees, is due to the incident ray being partially blocked by the AOTF's casing at the entrance. That recording has been noted in Table 7.1 by an asterisk.

The fine-tuning was performed around the rotational angle of five degrees, as the highest DE was recorded around that value, and the results are illustrated in Table 7.2, where the ordering of the results is based on the time of recording. Due to continuous adjustment of the RF signal and the rotational angle by small increments, the RF power and the laser were switched on during the fine-tuning. Therefore, it could be noticed that the total power is reducing as new measurements are being recorded.

Table 7.1: Optical Lab Testing incident e-ray - Coarse Power Testing

Angle Reading	Rot. Angle [deg]	RF Freq [MHz]	O-ray Power [μ W]	E-ray Power [μ W]	Total Power [μ W]	DE [%]
-0.33	0	93.48	4.54	12.19	16.73	27.14
0.67	1	94.25	4.76	12.07	16.83	28.28
1.67	2	95.40	5.00	11.86	16.86	29.66
2.67	3	96.96	5.29	11.59	16.88	31.34
3.67	4	99.06	5.60	11.32	16.92	33.10
4.67	5	101.35	5.72	11.12	16.84	33.97
5.67	6	105.13	5.00	10.20	15.20*	32.89

Table 7.2: Optical Lab Testing incident e-ray - Fine Power Testing

Angle Reading	Rot. Angle [deg]	RF Freq [MHz]	O-ray Power [μ W]	E-ray Power [μ W]	Total Power [μ W]	DE [%]
4.92	5.25	102.07	5.75	11.14	16.89	34.04
4.67	5.00	101.39	5.73	11.11	16.84	34.03
4.75	5.08	101.59	5.73	11.11	16.84	34.03
4.92	5.25	102.06	5.68	11.02	16.70	34.01

Based on the fine-tuning results, the highest DE was recorded at the rotational angle of 5.25 degrees, which is highlighted in yellow in Table 7.2. This result also has the highest RF frequency signal applied, in comparison to other measurements where the incident light was not blocked by the casing. In fact, a trend can be noted, where the RF frequency keeps increasing to satisfy the Bragg condition, as the rotational angles increases. This does go inline with the theory outlined in Subsection 2.6.1, as the higher rotational angle increases, the incidence angle of the wave vector \mathbf{k}_i increases too in the wave-vector space. At higher \mathbf{k}_i angles, the distance between the refractive ellipses increases too, causing the frequency to increase too to fill in the gap between the two ellipses.

Initially, it was believed that the angle 5.25 degrees is the Bragg angle of this AOTF based on which the crystallographic angle θ_c search theory was developed and described in Section 7.2. However, later in the research, it was noticed that there is a correlation with the VSWR graph and the increased DE when a higher tuning frequency value is used.

Figure 7.1 represents a zoomed in view of the VSWR graph for the AA opto-electronics AOTF, focusing on frequencies between 90 and 110 MHz. The complete VSWR spectrum is shown in Figure 6.1. As could be noticed in this zoomed region, the VSWR decreases as the applied frequency increases, indicating better impedance matching at higher frequencies. The green-shaded area marks the frequency range where the incident ray was unobstructed by the AOTF's casing during the power test. Notably, at the tuning frequency corresponding to a rotational angle ζ_{rot} of 5.25 degrees, the VSWR reaches its lowest value, signifying optimal power transfer to the transducer. This is the reason why the diffraction efficiency was the highest at $\zeta_{rot} = 5.25^\circ$.

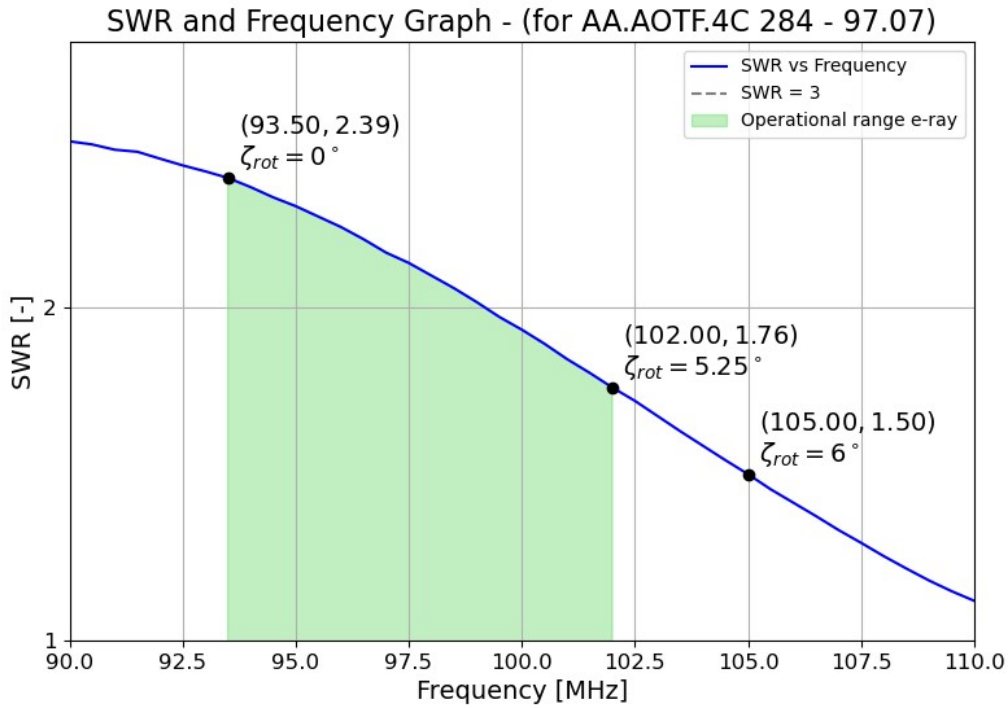


Figure 7.1: Zoomed-in VSWR curve for the AA Opto-Electronics AOTF, focusing on 90-110 MHz range and highlighting the unobstructed ray region during e-ray power test.

This finding also means that, electrically, this AOTF is better optimised for diffracting lower optical wavelengths than $635nm$. Based on Figure 6.1, this AOTF has the lowest VSWR value of 1.07 at a frequency of 111.5 MHz. Combining this information with the theory presented in Figure 2.13, it could be predicted that the DE efficiency would increase if the incident optical wavelength is lower than the wavelength used in the test. Alternatively, the DE could be increased by increasing the RF signal power. However, the user should be mindful that the applied power is within the transducer's handling properties, as been described in 'Section 2.8.

7.1.2 Incident o-ray power test

The same test has been performed in the optical lab, but this time with the ordinarily (vertically) polarized light. To change the polarization, the laser was rotated by 90 degrees with the help of the polarizer and a detector. In this test, the diffracted ray is the e-ray and the undiffracted is the o-ray, as can be visualised in Figure 6.18. Basically, the notations of the exit rays switch, but the test's procedure remains the same.

Coarse testing was performed and results are illustrated in Table 7.3, where it can be noted that the diffraction efficiency keeps increasing with a larger rotational angle. The highest diffraction efficiency has been noted to be at ζ_{rot} equalling to eight degrees, but a significant portion of light was blocked by the AOTF's entrance casing, the same applies for the rotation angle of seven degrees. The maximum allowed rotational angle without casing blockage was found to be 6.33 degrees, where the diffraction efficiency reached 30.46%, for 100 mW of power supplied.

Similarly, as for the e-ray incident power test, a zoomed in VSWR curve for the AA opto-electronics AOTF has been provided in Figure 7.2. This time, the operational range for 635nm laser is highlighted in blue area, standing for the o-ray incident case. Once again, the highest DE was recorded at the highest frequency value within AOTF's operational range.

One notable difference between the two tests is that for the same AOTF rotational angles, the tuning frequency for the incident o-ray is lower than for the incident e-ray case. This does go with the theory provided in literature based on the experimental results [26, 64], as shown in Figure 2.14.

Table 7.3: Vertical Polarization Testing - Coarse Results

Rot. Angle [deg]	RF Signal [MHz]	e-ray Power [μ W]	o-ray Power [μ W]	Total Power [μ W]	Power % Diffracted
-1.00	91.98	2.43	8.31	10.74	22.63
0.00	92.10	2.50	8.01	10.51	23.79
1.00	92.36	2.72	8.07	10.79	25.21
2.00	92.75	2.85	7.98	10.83	26.32
3.00	93.34	2.95	7.88	10.83	27.24
4.00	94.23	3.06	7.73	10.79	28.36
5.00	95.27	3.17	7.63	10.80	29.35
6.00	96.53	3.28	7.55	10.83	30.29
7.00*	98.09	3.22	7.07	10.29	31.29
8.00**	100.30	2.42	4.84	7.26	33.33
6.33	96.95	3.25	7.42	10.67	30.46

SWR and Frequency Graph - (for AA.AOTF.4C 284 - 97.07)

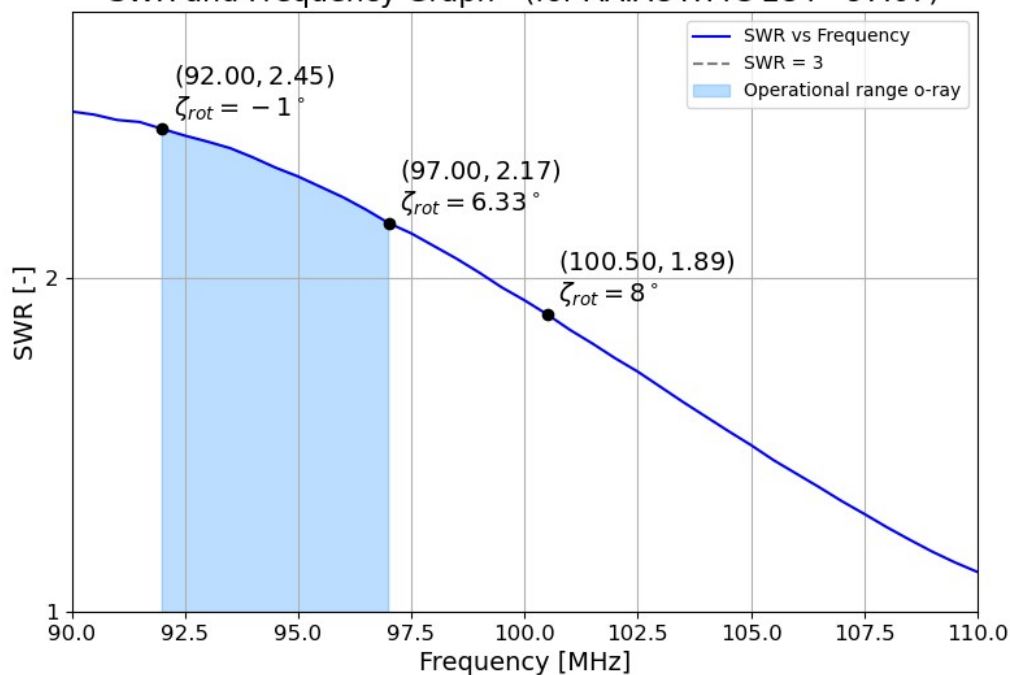


Figure 7.2: Zoomed-in VSWR curve for the AA Opto-Electronics AOTF, focusing on 90-110 MHz range and highlighting the unobstructed ray region during o-ray power test.

To continue comparison to the previous power test, Table 7.4 is provided to compare maximum diffraction efficiency (DE). The incident e-ray test exhibits a higher maximum DE, reaching 34.04% at a tuning frequency of 102.07 MHz where SWR value is around 1.76. The o-ray test, however, achieves its highest DE at a tuning frequency of 96.95 MHz, corresponding to an SWR of 2.17. Explaining why the maximum DE was recorded for the incident e-ray case, for this AOTF at the optical wavelength of 635nm.

Table 7.4: Comparison of e-ray and o-ray test results (Maximum DE, Tuning Frequency, and SWR)

Test Type	Max DE [%]	Tuning Freq [MHz]	SWR
e-ray	34.04	102.07	1.76
o-ray	30.46	96.95	2.17

However, to test whether the AOTF is designed for particular polarisation diffraction based on the AOTF's shape, as been claimed in [64]. A comparison of results from both power tests has been made in Table 7.5, where similar tuning frequencies were used for the Bragg diffraction. At those frequencies, the VSWR value difference is expected to be the same between the pairs. As can be seen, the DE values are almost identical in

all the comparison pairs between the incident e-ray or o-ray power tests. Suggesting that VSWR plays the key role in diffraction efficiency, rather than the AOTF's shape. The shape, however, would impact how the rays refract at the exit surface, where the shape choice would be important for the optical designs.

Table 7.5: Comparison between e-ray and o-ray coarse testing results (Rotational Angle, RF Signal, and DE)

Test Pair	Rot. Angle [deg]	RF Freq [MHz]	DE [%]
1st pair	e-ray: 0.67	94.25	28.28
	o-ray: 4.00	94.23	28.36
2nd pair	e-ray: 1.67	95.40	29.66
	o-ray: 5.00	95.27	29.35
3rd pair	e-ray: 2.67	96.96	31.34
	o-ray: 6.33	96.95	30.46

7.2 Crystallographic axis identification

To satisfy requirement [CHAR-REQ-001], this section introduces the frequency-matching method for characterising the crystallographic angles θ_c and α of the AA opto-electronics AOTF. This AOTF was chosen due to its known geometrical parameters (γ and β angles), allowing a focused search for the crystallographic angles.

The characterisation method that produced reliable results is frequency-matching, which was performed with both incident e-ray (Subsection 7.2.1) and o-ray (Subsection 7.2.2) diffraction testing results. This method involves adjusting the values of θ_c and α within the analytical model so that the model's tuning frequency aligns with the experimental frequency curve obtained from diffraction testing.

The result from the model will be validated by comparing the model's diffracted and undiffracted angles to the experimental results. Notably, a colleague familiar with the AA opto-electronics AOTF indicated that α is approximately eight degrees, providing a useful search reference.

7.2.1 Incident e-ray frequency-matching

The idea to adjust θ_c and α values within the model was inspired by the AOTF calibration paper by Zhang et al. [30], where the authors have developed a polynomial equation to approximate the tuning frequency required for the AOTF's Bragg condition. By using that equation, the authors were altering the angles related to θ_c and α . Considering that not all the variables of the polynomial equation were provided, that same equation was not used to characterise this AOTF. Instead, the analytical model, developed previously, was used to provide frequency tuning values for a range of ζ_{rot} values used in the diffraction test.

During the diffraction testing, the frequency satisfying the momentum-matching condition was noted for each rotational angle ζ_{rot} , as been described in Section 6.4. The Figure 7.3 shows the experimental results in blue for the incident e-ray diffraction test, and the analytical model results with adjusted θ_c and α values in green. For this test, the best match was at $\theta_c = 16.95^\circ$ and $\alpha = 8.07^\circ$. The value for the α angle is close to eight degrees, which is close to the values suggested by the manufacturer, making these frequency matching results promising.

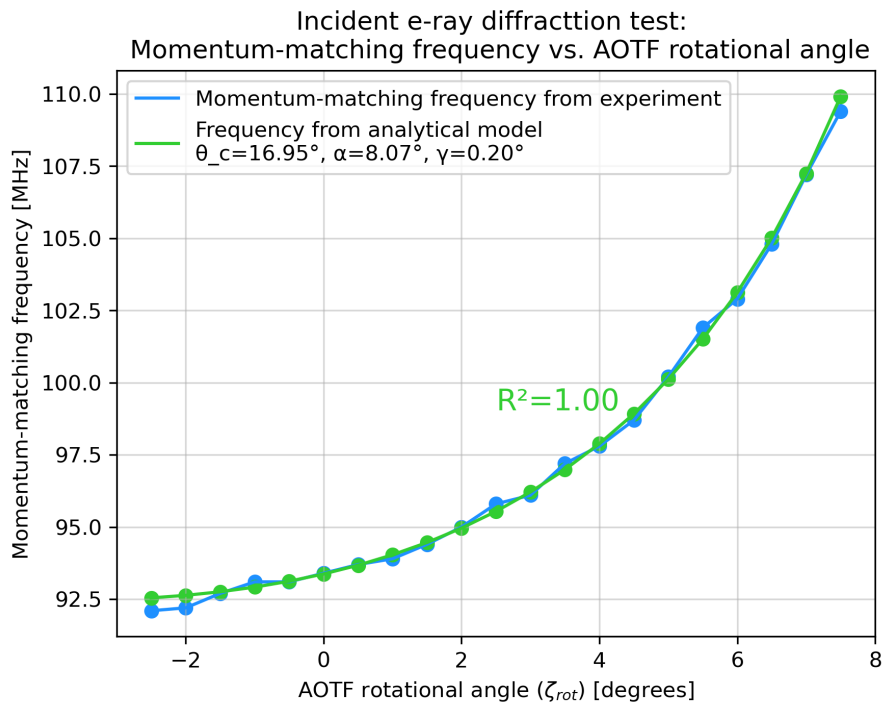


Figure 7.3: Frequency tuning over rotational angle matching curves for incident e-ray.

The R^2 value, or the coefficient of determination, presented in Figure 7.3, is a statistical measure that indicates the proportion of variance explained by a model [68]. The R^2 value of one, as presented in Figure 7.3, suggests a strong correlation between the analytical model and the experimental data. Suggesting that the frequency-matching method was performed correctly.

7.2.2 Incident o-ray frequency-matching

The same procedure has been performed with the incident o-ray diffraction testing, with the experimental results presented in blue in Figure 7.4. The frequency-matching graph for the ordinary ray is represented in purple, where $\theta_c = 15.90^\circ$ and $\alpha = 8.03^\circ$. These values are surprisingly different in-comparison to the frequency matching performed with the e-ray frequency data. However, it was found that AOTFs do have different θ_c angles depending on the incident polarisation used, to satisfy the momentum-matching principle [64]. In one of the papers, the same AOTF had $\theta_c = 14.97^\circ$ for the e-light and $\theta_c = 13.20^\circ$ for the o-light [64].

This finding could explain why the graphs presented in Figure 2.14 have different trough points for different incident polarisation types. Alternatively, it could also be possible that during the growth of the AOTF's crystal, the lattice structure could be inhomogeneous, which could impact the experimental results depending on the incoming light's incidence point during the experiment. The inhomogeneity of the crystal could happen due to the so-called point defects, where during the crystal's solidification a certain atom may be displaced and disrupt regular arrangement of atoms at a localised crystal's area [69].

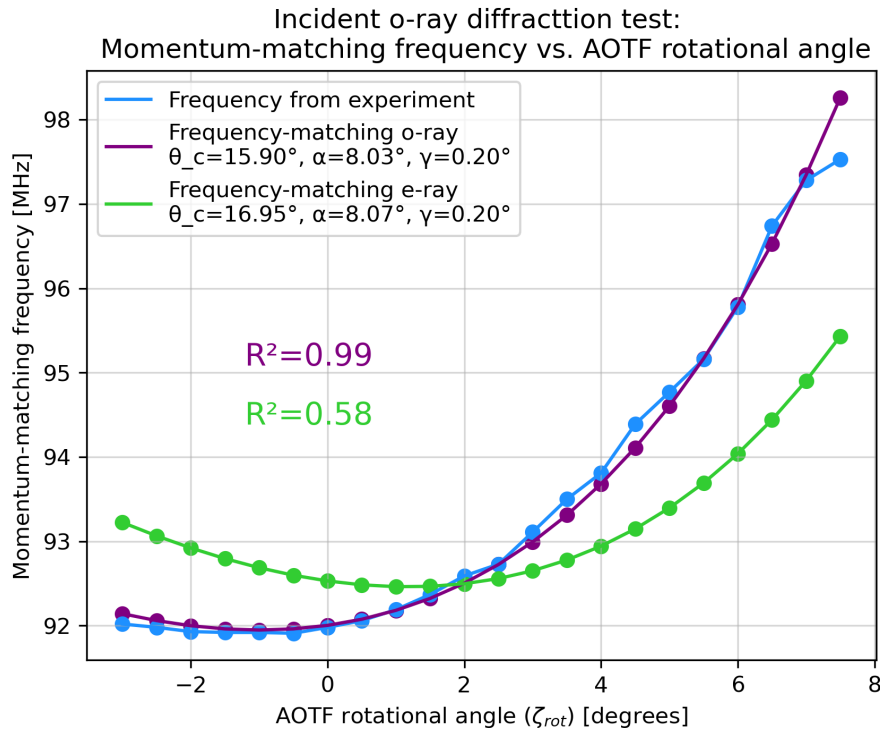


Figure 7.4: Frequency tuning over rotational angle matching curves for incident o-ray.

For comparison reasons, the angles θ_c and α found during frequency-matching for the incident e-ray diffraction were also plotted for the o-ray diffraction case in green, seen in Figure 7.4. As seen, the green curve does not align with the experimental frequency curve for the incident o-ray case.

Furthermore, the green curve projection is not the same, as has been shown in Figure 7.3. The reason is that the analytical model uses the incident o-ray case for Figure 7.4. As has been noted in Section 4.4, the AO interaction procedure does differ per incident polarization case. This variation causes a difference in the momentum-matching frequency profile, even when identical crystallographic angle values are used.

7.2.3 Conclusion on AOTF characterisation method

In this section, the frequency-matching method was applied to both frequency momentum-matching curves obtained from diffraction testing for the incident e-ray and o-ray cases. This method involved adjusting the values of θ_c and α in the analytical model until its frequency curve matched the experimental diffraction testing curves. The resulting values of θ_c and α are summarized in Table 7.6.

Table 7.6: Methods summary to characterise θ_c and α angles for e-ray and o-ray incident cases.

Incident Case	Method	θ_c [deg]	α [deg]
e-ray incident	Frequency-matching e-ray	16.95	8.07
o-ray incident	Frequency-matching o-ray	15.90	8.03

Based on feedback from a previous researcher familiar with this AOTF, the values of α derived from the frequency-matching method appear promising, as they are close to the expected value of eight degrees. However, to confirm these results and further validate the analytical model, the next section will compare the model's predicted diffracted and undiffracted angles with experimental data, using the θ_c and α values obtained in this section.

7.3 Diffraction test validation

This section analyses the diffraction test data, the procedure of which is described in Section 6.4. The primary aim of the section is to compare the experimental results with the outputs of the analytical model using the crystallographic angles θ_c and α obtained from the frequency-matching method. By the end of the section,

it will be evaluated if the frequency-matching method is able to characterise an AOTF and meet the [CHAR-REQ-001] requirement.

The second aim of this section is to further validate the analytical model. While the tests performed at UPHF, Chapter 5, provided a great insight that the model is performing well in terms of simulating the AOTF at various optical wavelengths and in terms of providing a tuning frequency for the Bragg condition. The adaptation made to the model, such as AOTF's rotation, has not yet been validated. Secondly, the verification tests performed so far used incident extraordinary polarization.

To validate these aspects, diffraction tests were conducted for both incident e-ray (Subsection 7.3.1) and o-ray (Subsection 7.3.2) polarizations. The model's performance will be assessed by comparing the predicted diffracted and undiffracted angles (Subsection 7.3.3) to the experimental results. The raw data for the diffraction tests is presented in Appendix B.

The analytical model in this section uses the P.Gass model for refractive indices to avoid introducing additional unknowns related to gyration. As discussed in Section 2.7 and Chapter 5, the rotatory power ρ , responsible for gyration, may vary across different AOTFs.

7.3.1 Incident e-ray diffraction test results

In this part, the model's performance will be compared with the experimental data e-ray diffraction test, for diffracted and undiffracted ray angles exiting the AOTF. The schematic for the incident e-ray diffraction test is illustrated in Figure 6.8. In this test, it is expected that the diffracted ray changes its polarization from extraordinary to ordinary. Furthermore, the undiffracted ray keeps the same polarization as the incident ray. Finally, it is expected that the diffracted ray angle (θ_{3o}) will be larger in comparison to the undiffracted ray angle (θ_{3e}).

Figure 7.5 presents the graph for diffracted ray angle variation with the AOTF rotational angle (ζ_{rot}). The graph in blue represents the values obtained from the diffraction test. In contrast, the curve in green represents the analytical model's output using the values from frequency matching obtained in Subsection 7.2.1. By observing the two graphs, it can be seen that the trend lines of both curves are the same, with a Root Mean Squared Error (RMSE) of 0.14° .

The RMSE is a metric that calculates a mean deviation of results between the model and the reference curve [70], which is the experimental curve. Having an RMSE of 0.14° is a positive result which almost satisfies the [VAL-REQ-002] about the model's accuracy.

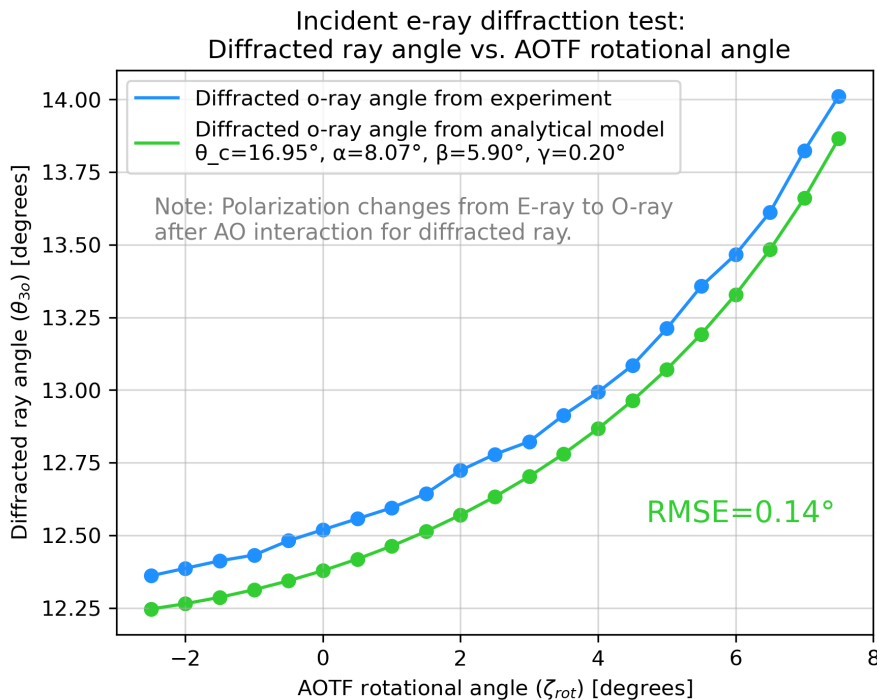


Figure 7.5: Diffracted angles (θ_{3o}) as a function of rotational angle for e-ray diffraction test.

The analytical model also performs well for the undiffracted angles (Figure 7.6) where both trend lines have the same trend as the curve based on the experimental results. As the name suggests, the undiffracted angles are not influenced by the AO interaction. The factors influencing the results are the geometrical angles γ and especially β , and also the effective crystallographic angle θ'_c which influences the effective refractive index on the e-ray.

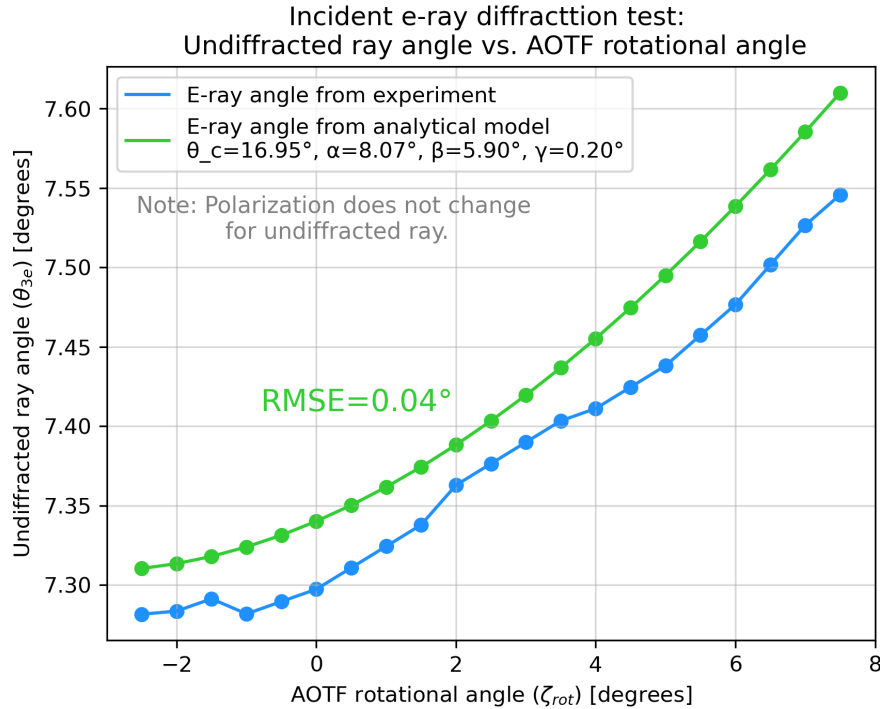


Figure 7.6: Undiffracted angles (θ_{3e}) as a function of rotational angle for e-ray diffraction test.

For the frequency-matching results in green, the difference between the experimental results for undiffracted angles is even lower than for the previous graph comparison. In this case, the RMSE is 0.04 degrees, suggesting that the β value found in the image analysis is close to the real value of this AOTF. Furthermore, a similar trend line of the analytical model and the experimental results does further validate the model in terms of the correct use of the effective refractive index and the adaptation used to include the AOTF's rotation ζ_{rot} .

7.3.2 Incident o-ray diffraction test results

For the incident o-ray diffraction testing, the analytical model was run using the crystallographic angles obtained from frequency-matching for the o-ray diffraction case (Subsection 7.2.2). Similarly, the model was run using the incident o-ray diffraction case, and the model's results were plotted in purple for both diffracted and undiffracted angles.

For the diffracted angles results, presented in Figure 7.7, the purple graph almost perfectly matches the experimental results in blue. This is also reflected in the impressively low RMSE value of 0.02°. A slight deviation in experimental results can be observed at the $\zeta_{rot} = 7.5^\circ$, where it is suspected that the AOTF's exit casing started to block the rays leaving the AOTF.

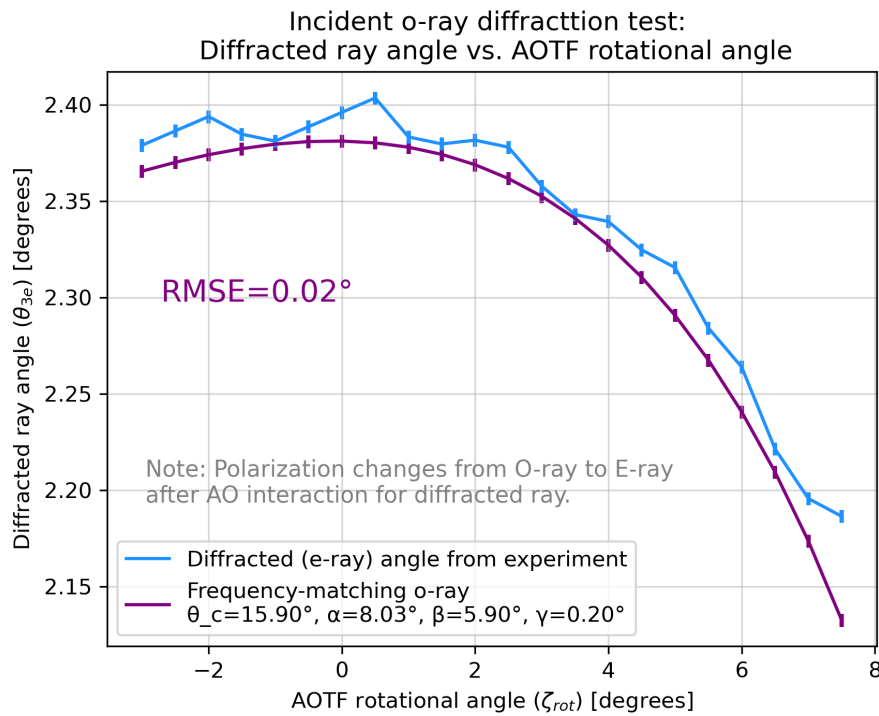


Figure 7.7: Diffracted angles (θ_{3e}) as a function of rotational angle for o-ray diffraction test.

For the undiffracted rays, in the incident o-ray case, the RMSE value is 0.04° , which is low and enough to satisfy the [VAL-REQ-002] requirement for the model's accuracy. Some difference between the experimental and model graphs is present at low rotational angles, between -3 and 1.5 degrees. This value difference never goes beyond 0.07 degrees, and then the difference becomes minimal at higher rotational angles.

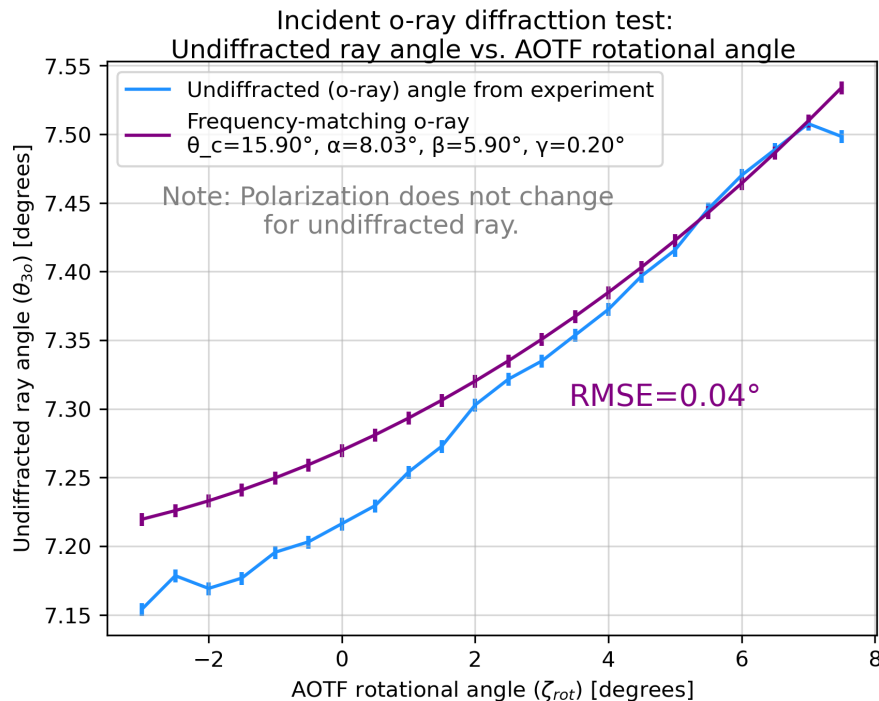


Figure 7.8: Undiffracted angles (θ_{3o}) as a function of rotational angle for o-ray diffraction test.

This difference, at lower rotational angles, could be potentially compensated by introducing the gyration effect. As has been noted in Subsection 2.7.2, the closer the ray is propagating to the [001] crystallographic axis, the larger the effect of gyration effect will be. In other words, the lower the θ'_c angle is, which is the lowest at lower

ζ_{rot} angles, the larger the effect of gyration will be. With higher gyration, the ordinary refractive index would decrease (Subsection 2.7.2), which would result in bringing the model's graphs closer to the experimental curve.

7.3.3 Model's evaluation and result discrepancies

The frequency-matching method for determining θ_c and α enables the analytical model to accurately predict the AOTF's diffracted and undiffracted exit angles, meeting the [CHAR-REQ-001] requirement for AOTF characterisation in terms of crystallographic angles. Discrepancies between model predictions and experimental values are summarized in Table 7.7, where negative values indicate the model's curve lies below the experimental results. An asterisk denotes an outlier removed from the o-ray incident case.

Table 7.7: Bounds of differences for diffracted and undiffracted angles

Incident Case	Angle Type	Lowest Difference	Highest Difference
e-ray incident ($\theta_c = 16.95^\circ$, $\alpha = 8.07^\circ$)	Diffracted Angle	-0.114°	-0.165°
	Undiffracted Angle	0.025°	0.064°
o-ray incident ($\theta_c = 15.90^\circ$, $\alpha = 8.03^\circ$)	Diffracted Angle	-0.002°	-0.023°*
	Undiffracted Angle	-0.006°	0.066°

Based on Table 7.7, the analytical model had an accuracy within 0.1° for all the diffraction test angles, except the diffracted angle curve for incident e-ray, where the analytical model had slightly underestimated the experimentally obtained diffraction angles. There could be multiple factors contributing to this difference, either from the model's input perspective or experimental factors.

From the model perspective, one consideration is that the geometrical angle β could be slightly larger, given a 0.1° uncertainty in image analysis, which would shift the model's curve upward in Figure 7.5 based on Snell's law (Equation 4.23). However, adjusting β could affect other graphs where the model already shows high accuracy, so angle β was deemed accurately determined. Alternatively, increasing α might improve accuracy for e-ray diffraction angles. However, it would increase the frequency needed for momentum-matching condition (Subsection 2.6.1), and disrupt matching between the frequency curves (Figure 7.3). Potentially, the inclusion of the gyration effect may improve results in this regard.

From the experimental perspective, slight misalignments of the incident ray can impact the \mathbf{k}_i and \mathbf{k}_d angles, affecting the tuning frequency and the ray exit angles. Furthermore, potential sources of human error include reading the rotational stage (measured in arcminutes) and positioning the beam's centre on the ruler, which could be challenging to precisely determine, especially in a dark setting. Errors in measuring the distance between the AOTF crystal and the deviation measuring ruler could be minimized by increasing the measurement distance L beyond 1.1 meters. This distance, however, was constrained by the limited space in the dark lab (Subsection 6.3.2).

Despite these potential sources of discrepancy, the analytical model remains highly accurate, further validating its use. The model consistently follows experimental trends across all analysed graphs, suggesting that the model's adaptation with rotational angles works as intended. The model's high accuracy for the o-ray diffraction test also suggests it is robust for various incidence cases.

7.4 AOTF's rotatory power influence

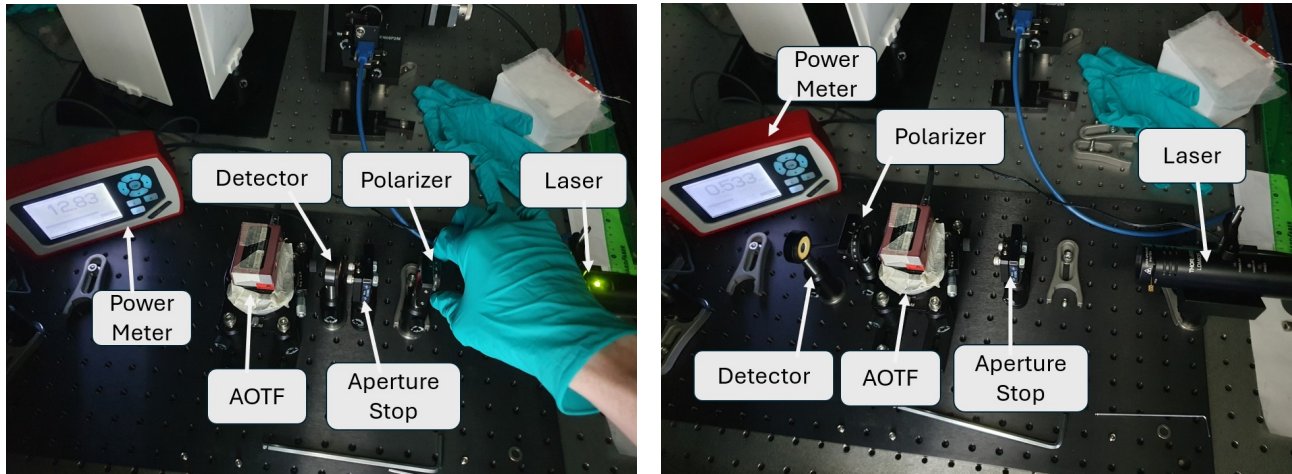
As discussed in Section 2.7, the TeO_2 crystal in the AOTF exhibits significant optical activity, known as rotatory power [33]. This section describes a physical experiment to test if the polarization angle of incident light changes upon passing through the AOTF crystal. According to Uchida's work, TeO_2 has an exceptionally high rotatory power of 87 degrees/mm at a wavelength of 633 nm, along [001] axis [23]. The rotary power does decrease further away from the [001] axis, but even at $\theta_c = 17^\circ$ the rotatory power is still expected to be high, around 78 degrees/mm according to Figure 2.20. This experiment will assess the actual rotatory power of the AOTF crystal and evaluate whether Uchida's values are overestimated, as was already partially confirmed by the UPHF experiment (Chapter 5).

To test if TeO_2 alters the polarization angle, a simple setup was used with a linear polarizer and detector. Firstly, the linear polarizer and the detector were placed before the AOTF, as can be seen in Figure 7.9a, to find the

angle on the polarizer to match the polarization of the laser. This was done by rotating the polarizer until the maximum intensity was detected.

Afterwards, both the polarizer and the detector were placed after the AOTF, as can be seen in Figure 7.9b. The RF signal was not supplied. The AOTF was positioned perpendicularly to the incident ray, and the rotational polarization was only measured for the incident ray. Similarly, the polarizer was rotated until the maximum power intensity was measured, and then the reading of the new angle was taken. By comparing the polarizer angles before and after AOTF, the polarization rotation can be calculated.

The test was conducted in a dark setting to ensure accurate laser intensity readings. The images were taken in the light setting to capture the equipment used. The test was performed for both vertical and horizontally polarized light, to see if certain polarization is more susceptible to rotational polarization of the TeO₂ crystal.



(a) Finding the angle on the polarizer matching the laser's polarization.

(b) Placing the detector and the polarizer after the AOTF to find the maximum power for a polarization.

Figure 7.9: Polarization rotation experiment.

Table 7.8: Polarizer rotation and intensity power measurements for horizontally polarized incident light

Polarizer rotation for the highest intensity power	
Polarizer angle before AOTF:	231°
Polarizer angle after AOTF:	221°
Polarization plane rotation:	10° anti-clockwise
Power Intensity Information	
Power at 231° Before AOTF:	13.31 μW
Power at 231° After AOTF:	12.22 μW
Power at 221° After AOTF:	12.55 μW

Table 7.9: Polarizer rotation and intensity power measurements for vertically polarized incident light

Polarizer rotation for the highest intensity power	
Polarizer angle before AOTF:	321°
Polarizer angle after AOTF:	311°
Polarization plane rotation:	10° anti-clockwise
Power Intensity Information	
Power at 321° Before AOTF:	8.62 μW
Power at 321° After AOTF:	7.49 μW
Power at 311° After AOTF:	7.60 μW

In both of the polarization types, the AOTF causes the polarization to rotate anti-clockwise by ten degrees. The anti-clockwise rotation does confirm that TeO₂ is a dextrorotatory material [40], as was mentioned in Subsection 2.7.1. This can be seen in Table 7.8 for the horizontal incident light, and in Table 7.9 for the vertical

incident light, where the maximum light intensity occurs when the polarizer is rotated by ten degrees from the reference polarization angle.

To visualise these findings, Figure 7.10 shows the polarization changes according to the coordinate system used in the experiments. The letter E stands for the electrical field vector, which characterises the linear polarization, and the subscripts denote whether the ray is before AOTF (subscript 0) or after AOTF (subscript 3).

The power is different between the tests for vertically and horizontally polarized light due to the variable iris opening, which was larger for the horizontally incident light. It is interesting to note, however, that a significant portion of light is absorbed by the AOTF which can be seen from higher power readings before the AOTF, which does impact the efficiency of AOTF.

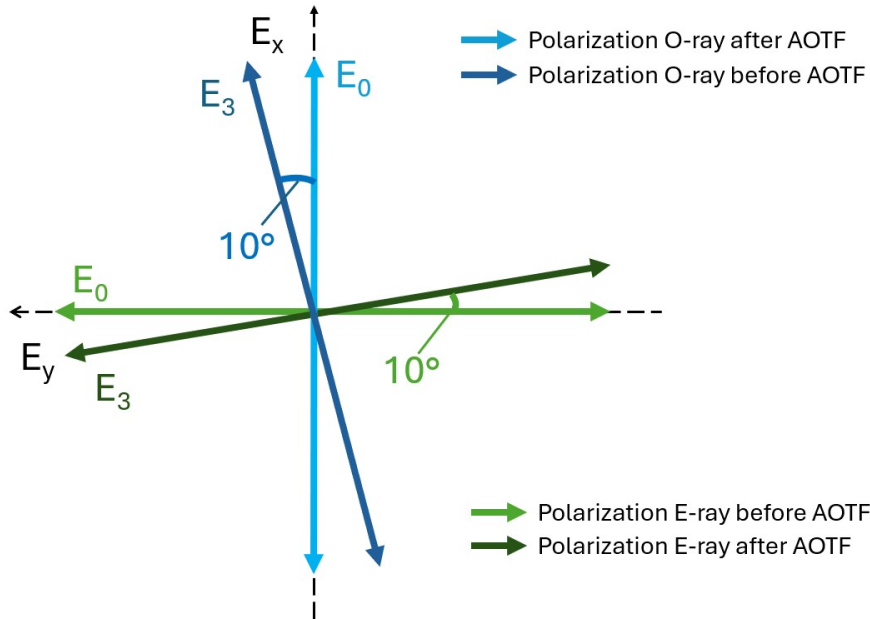


Figure 7.10: AA opto-electronics AOTF polarization angle change

The results of this test indicate that the AOTF has a measurable rotatory power effect on the incident ray's polarization, though it is significantly less than Uchida's reported value of 87 degrees/mm or the adjusted rotatory power with the gyration tensor (78 degrees/mm). This discrepancy could stem from crystal irradiation, which is known to reduce rotatory power [41], although this is unlikely given that the Brimrose AOTF is newly purchased. Alternatively, it could also depend on how the crystal was grown, potentially the θ_c value varies along the crystal causing variability in the rotatory power throughout the crystal.

The change of the AOTF rotational angle, which would impact the distance of propagation inside the crystal, had also no impact on the results, suggesting it is unlikely that the polarization plane has been rotated by 360 degrees or more, before exiting the crystal. This points to a need for further study on rotatory power in future works, as it has an impact on AOTF's behaviour and could have implications on the analytical model's accuracy. An attempt was also made to improve the model's diffraction test predictions by applying Voloshinov's and Fresnel's methods with various rotatory power values. However, results remained inconclusive, as precise values for the crystallographic axis angles (α and θ_c) were not provided by the manufacturer. This lack of information made it challenging to assess the true impact of rotatory power on model accuracy.

7.5 Model validation and experimental results conclusion

In the analysis of the AA Opto-electronics AOTF, three tests were conducted: the power test, diffraction test, and optical activity test.

In the power test (Section 7.1), two types of polarized light were directed into the AOTF at various rotational angles (ζ_{rot}). The results indicated that diffraction efficiency (DE) increased for both polarizations as ζ_{rot} increased. This rise in DE was due to the larger angle of incidence within the crystal, which required a higher frequency to achieve the momentum-matching condition. Specifically, for an optical wavelength of 635 nm, DE rose as the momentum-matching frequency increased.

An examination of the VSWR curve within this frequency range revealed that VSWR values decreased as frequency increased. This suggests that higher frequencies allowed more electrical power to reach the transducer, producing a stronger acoustical wave and thereby increasing the DE. The analysis indicated that DE is not constant across all incident angles but depends on the VSWR curve within the operational frequency range, addressing sub-question 6.

In the diffraction test (Section 7.3), characterisation methods for the θ_c and α angles were evaluated by comparing the analytical model's predictions with experimental results for diffracted and undiffracted exit angles at various rotational positions. The model accurately predicted diffracted and undiffracted angles within 0.1° when θ_c and α values were obtained through frequency-matching. This achievement satisfied the [CHAR-REQ-001] requirement, which called for a method to characterise the crystallographic angles θ_c and α of the AOTF.

Further analysis of the diffraction test results demonstrated that the analytical model's trend lines matched the experimental curves for both o- and e-ray incidences. Combined with high accuracy, this outcome further validated the analytical model's adaptations, such as the introduction of rotational angle and the operational suitability for o-polarized incident rays.

Based on the discussions throughout this chapter and the conclusions drawn, Table 7.10 summarizes all the validation requirements that were achieved.

Table 7.10: Validation Requirements and Achievements

Requirement ID	Requirement's Goal	How it was achieved
[VAL-REQ-001]	Model produces realistic results at various rotational angles.	Model trend lines matched diffraction test results.
[VAL-REQ-002]	Model accuracy within 0.1° for diffracted and undiffracted angles.	Achieved sub 0.1° accuracy except for e-ray diffracted angles (RMSE = 0.14°).
[VAL-REQ-003]	Model supports both extraordinary and ordinary incident polarizations.	Obtained high accuracy and matching trend lines for both incident polarizations.
[VAL-REQ-004]	Identify factors affecting diffraction efficiency.	Factors: θ_c , incident angle, f , λ , and VSWR (from power test).
Sub-Question 6	Does DE remain constant across incidence angles in momentum-matching conditions?	Highest DE recorded at momentum-matching frequencies with lowest VSWR.

The optical activity test confirmed that the AOTF rotated the incident ray's polarization by 10 degrees counter-clockwise. However, this measured optical rotation was significantly lower than values reported in the literature, suggesting either substantial crystal irradiation or lower rotatory power than Uchida's reported values.

To accurately determine the AOTF's true rotatory power, further testing with a crystal of known θ_c and α values is necessary. Alternatively, for those primarily interested in simulating an AOTF, the P. Gass model can be applied. This model has shown reliable performance in diffraction tests, even without adjustments for rotatory power.

Model optimisation and AOTF characterisation 8

One of the main challenges for users wanting to use an AOTF as a commercial off-the-shelf (COTS) component for optical wavelength filtering is the lack of detailed manufacturing information on critical parameters. Manufacturers typically do not provide specifics on the diffraction angles. They also do not provide the precise frequencies required for momentum-matching conditions. Additionally, data for each wavelength across the visible spectrum is often unavailable.

To obtain this information, users must perform physical tests to configure the optimal frequencies, diffraction angles, and incidence angles for each wavelength of interest. However, conducting these tests for multiple wavelengths is labor-intensive and costly, especially if multiple lasers are required. Ideally, users would benefit from a single test that could characterise the AOTF's behaviour across a range of optical wavelengths.

This chapter demonstrates how the analytical model can characterise key angles related to the AOTF's crystallographic axis, such as θ_c and α , as well as facet inclination angles β and γ . With these parameters, the AOTF's behaviour can be extrapolated to multiple wavelengths, which not only saves time on testing but also enables more versatile planning of optical setups.

This process involves diffraction testing on the newly acquired AOTF, by recording both output ray angles and the momentum-matching frequency (Section 8.1). The frequency is determined by using a detector and power meter at each rotational angle. An optimisation algorithm is then chosen and applied to the analytical model to determine the optimal parameters for θ_c , α , γ , and β (Section 8.2). Finally, the model's predicted output angles, based on the optimised parameters, are compared with the experimental results, and the optimisation algorithm's performance is evaluated (Section 8.3).

8.1 Procedure and Brimrose AOTF schematics

Before exploring the combination of the optimisation algorithm and the analytical model, an AOTF device (model TEAF10-0.55-1.0-MSD) was obtained from Brimrose. The entrance and exit views of the AOTF are shown in Figure 8.3. The entrance and the exit view of the AOTF are presented in Figure 8.3. From the figures, it can be noted that the SMA connection for the RF signal is connected to the left side of the crystal's front view, suggesting that the transducer itself is also located on that side. Additionally, while the entrance facet angle (γ) is not clearly visible, the presence of the exit facet angle (β) is evident, as shown in Figure 8.2. Finally, based on the information from the manufacturer, the crystal's material is TeO_2 , which aligns with the previously developed model.

Table 8.1: Brimrose AOTF Specifications

UNITS	SPECIFICATIONS
Substrate	TeO_2
Wavelength Range (nm)	550-1000
RF Frequency Range (MHz)	$85-170 \pm 5$
Angular Aperture (deg)	5-7
Separation Angle (mrad)	Input -1 order 2.8, -1 order-0-order 6.4-7
Spectral Resolution (nm)	2.5-11

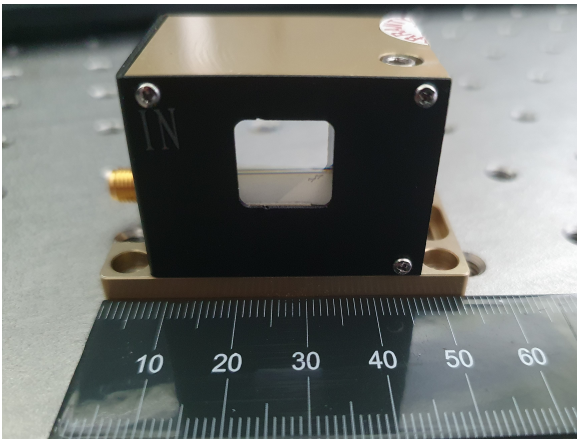


Figure 8.1: Brimrose Entrance View

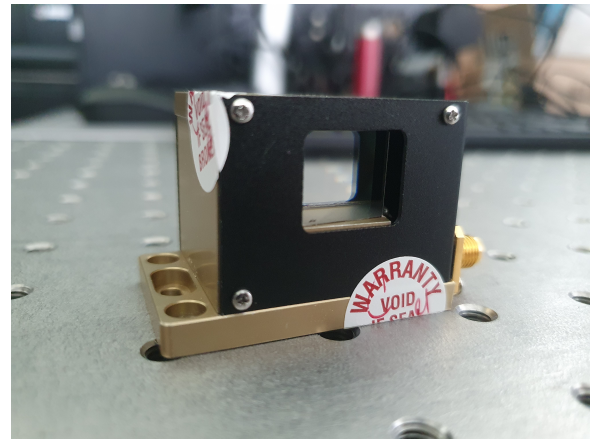


Figure 8.2: Brimrose Exit View

Figure 8.3: Physical pictures of the Brimrose TEAF10-0.55-1.0-MSD AOTF

After the initial examination of the AOTF, it was brought to the optical lab for diffraction testing to determine the momentum-matching frequencies when illuminated by a 635 nm laser. The diffraction occurred only when a vertically (ordinary) polarized light was shone, at around 145 MHz. An example of this diffraction is shown in Figure 8.4, where the diffracted light appears dim to the left of the undiffracted light. The dimness of the diffracted light is due to the RF power being set at 100 mW to prevent potential damage to the AOTF or the amplifier from excessive reflected power, although the manufacturer recommends an input power of 2 W. The raw data of the Brimrose diffraction testing is presented in Appendix E.

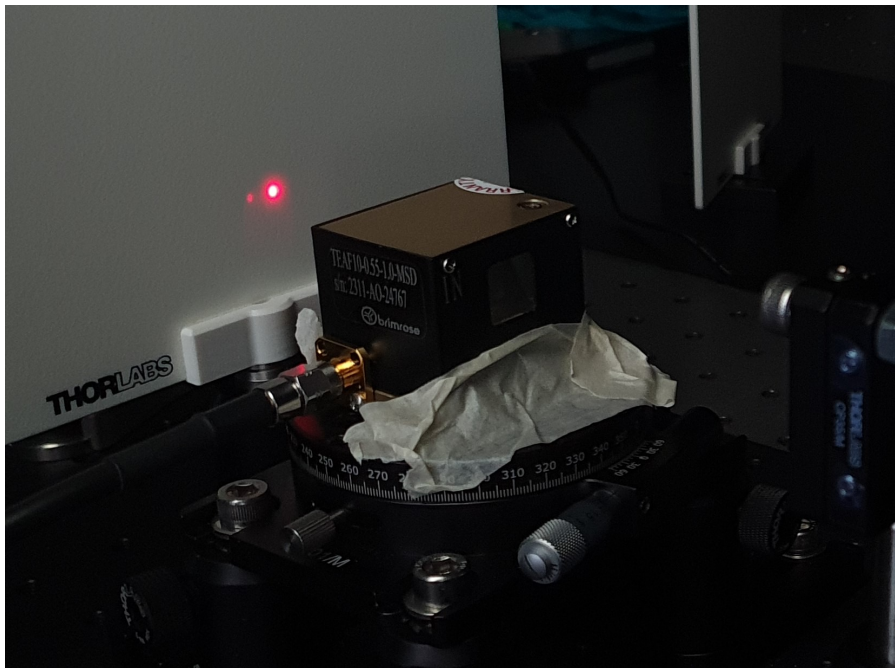


Figure 8.4: Brimrose AOTF diffraction when a vertically polarised light is shone onto the AOTF.

Based on initial information on the AOTF, a preliminary schematic of the AOTF's crystal geometry can be drawn, a top view of which is represented in Figure 8.5. The output rays were both below the optical axis of the experimental setup, with the diffracted (extraordinary) ray appearing close to the Z-axis. Comparing this result with AA AOTF for ordinary diffraction Figure 6.14, the diffraction of the extraordinary ray happens in the opposite direction, which suggests that the crystallographic axes are inverted.

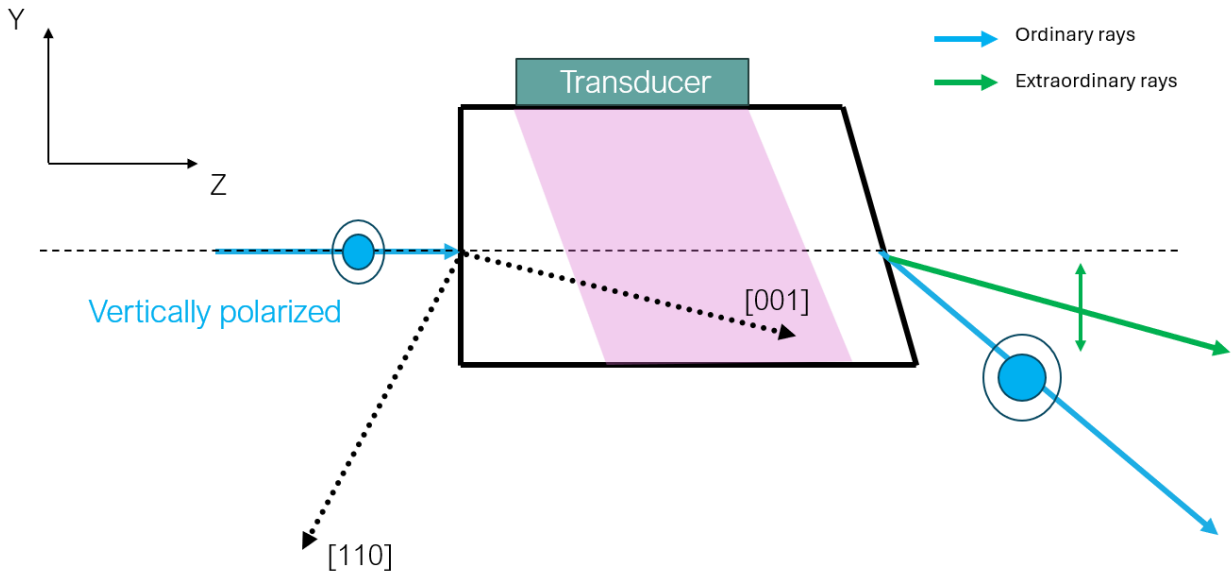


Figure 8.5: Top view schematic of the AOTF crystal in the experimental setup.

To avoid confusion with the inverted crystallographic axis system and the transducer’s position on top of the crystal’s schematic, the AOTF and the experimental results were mirrored along the z-axis. This produced the inverted schematic shown in Figure 8.6. The AOTF in this representation matches the previously defined coordinate systems, such as those in Figure 5.1 and Figure 6.5. The positive angle definitions of the AOTF (θ_c , α , and β) are also shown in Figure 8.6 and will be used later in the model.

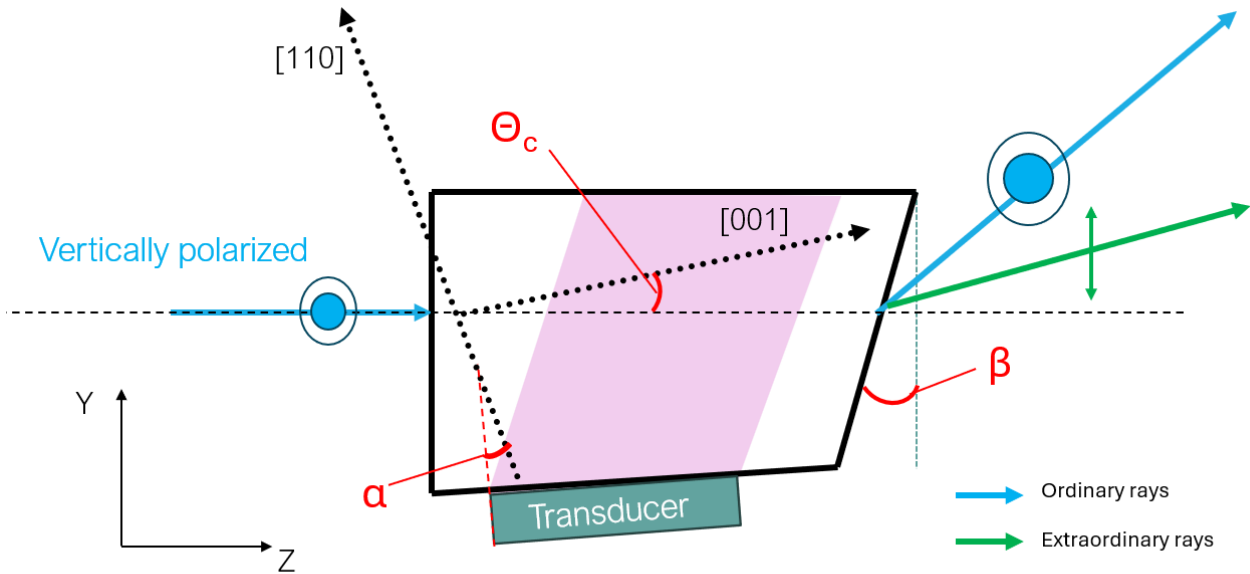


Figure 8.6: AOTF inverted along the z-axis

The diffraction testing results had both output angles (θ_{3e} and θ_{3o}) and the AOTF rotational angle (ζ_{rot}) as negative. To align with the new inverted schematic, these values were also inverted to positive. These adjustments were made to match the already validated analytical model and to make the initial analysis of the AOTF more intuitive.

8.2 Solution with optimisation

A straightforward way to characterise the AOTF’s critical parameters is by manually adjusting angles θ_c , α , γ , and β until the model’s predicted output angles align with experimental results. However, this approach is

highly time-consuming, especially when multiple AOTFs are desired to be characterised, and can be challenging for users unfamiliar with AOTF principles. To automate this process and make it more accessible to new users, the analytical model can be combined with an optimisation algorithm to automatically determine the critical AOTF parameters.

To implement the analytical model within an optimisation algorithm, the first step is to select a suitable algorithm, which will be discussed in Subsection 8.2.1. Next, in Subsection 8.2.2, an objective function must be created for the algorithm to optimise for. Furthermore, the search bounds for the optimisation will be established.

8.2.1 Optimisation algorithm choice

Creating an optimisation algorithm from scratch was not in the requirements, or the goal of this research. Instead, the goal was to select an existing algorithm and adapt the analytical model to work with it. Since the model was created in Python and involves multiple variables influencing the results, the algorithm selection was limited to those available in SciPy that support multi-variable optimisation.

The “L-BFGS-B” algorithm (Limited-memory Broyden-Fletcher-Goldfarb-Shanno) was chosen due to its suitability for multi-variable nonlinear problems and its computational efficiency compared to other quasi-Newton methods [71]. This algorithm supports box constraints, denoted by the letter “B” in the abbreviation, allowing to establish straightforward bounds on variables (θ_c , α , γ , β), within which the algorithm is allowed to manipulate the variables.

Quasi-Newton methods find a local minimum by estimating the objective function’s curvature, focusing on values where the function approaches a local minimum [71]. To find the curvatures for each search variable, these algorithms often use an inverse Hessian matrix (a matrix of second-order partial derivatives). However, calculating a full Hessian becomes exponentially more time-consuming as the number of variables (n) increases [72]. Therefore, this limited-memory method estimates the Hessian matrix by using only recent search iterations, rather than calculating a new Hessian matrix for each search iteration [72].

A detailed mathematical explanation of the algorithm’s workings is beyond the scope of this research. The primary reason for selecting this algorithm is its time efficiency in solving multi-variable problems and its straightforward implementation in Python using the SciPy library, which supports simplified variable constraints. Additionally, the algorithm is relatively efficient at finding a global minimum (optimal value) for the objective function [72].

However, L-BFGS-B can get stuck in local minima, as illustrated in Figure 8.7, where an example objective function with a single variable n shows how the algorithm may converge to a local rather than global minimum [72]. To mitigate this, multiple runs with varied initial guesses can improve the likelihood of finding the global minimum.

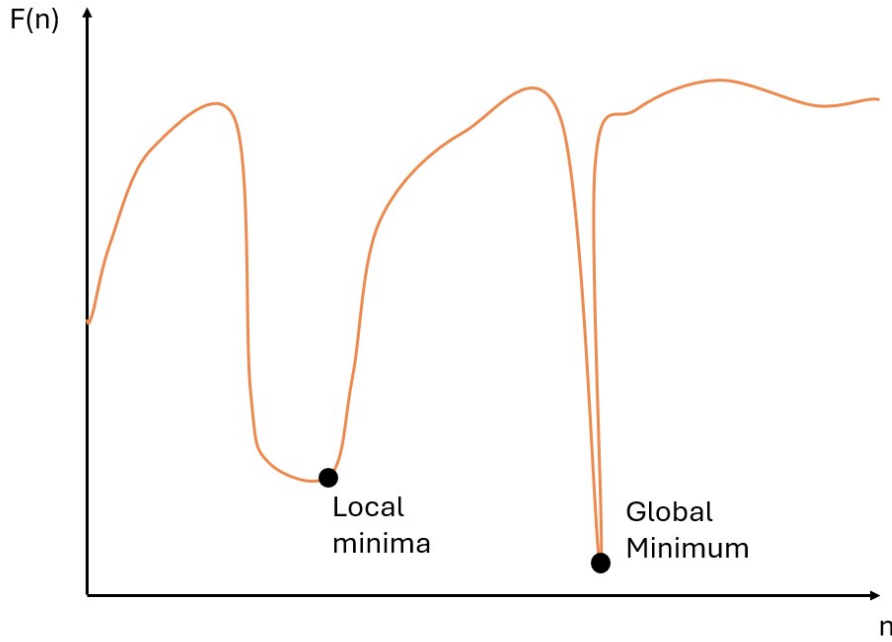


Figure 8.7: Simplified multimodal example where finding global minimum is challenging for Newton methods — adapted from [73]

Genetic algorithms generally perform better for finding the global minimum in such situations but are complex to implement, requiring constraints within the objective function and often have higher computational time [73]. Due to these factors, genetic algorithms were not examined here but could be recommended for future works.

8.2.2 Objective function and bounds selection

Following the selection of the L-BFGS algorithm, the next step is to define its input for optimisation. The primary input is the objective function — a scalar function that the algorithm aims to minimize [72]. Here, the objective is to reduce the discrepancy between the experimental measurements from the Brimrose AOTF diffraction testing and the predictions from the analytical model. This discrepancy is quantified as a total error, represented in Equation 8.1 as the objective function, which includes the sum of squared errors for momentum-matching frequency and diffracted/undiffracted angles.

$$E_{\text{total}} = E_{\text{freq}} + E_{\text{undiff}} + E_{\text{diff}} \quad (8.1)$$

Where each term is defined as follows:

$$E_{\text{freq}} = \sum_{i=1}^n (f_i^{\text{exp}} - f_i^{\text{sim}})^2 \quad (8.2)$$

$$E_{\text{undiff}} = \sum_{i=1}^n (\theta_{o,i}^{\text{exp}} - \theta_{o,i}^{\text{sim}})^2 \quad (8.3)$$

$$E_{\text{diff}} = \sum_{i=1}^n (\theta_{e,i}^{\text{exp}} - \theta_{e,i}^{\text{sim}})^2 \quad (8.4)$$

For each error calculation in Equations (8.2) to (8.4), the squared difference is chosen because it penalizes larger errors more heavily than smaller ones, encouraging the optimisation algorithm to reduce large discrepancies as a priority.

Here, the variable n represents the number of data points inside the experimental results array f^{exp} obtained from diffraction testing, where each point corresponds to a different ζ_{rot} angle. The optimisation algorithm

runs the analytical model for the same span of ζ_{rot} angles as in the experiment, generating a simulation array f^{sim} . For each run, the algorithm tries a different configuration of variables: θ_c , α , γ and β . The algorithm then prioritises the values of these variables when the cumulative error across all three equations reaches its minimum, thus minimizing the objective function.

To ensure the algorithm searches within realistic AOTF values, search bounds were set for θ_c , α , γ and β . The selected bounds for the Brimrose AOTF are provided in Table 8.2, where the first and second values in the brackets represent the lower and upper bounds, respectively.

Table 8.2: optimisation Variables and Their Bounds

Variable	Bounds	Units
θ_c	[10, 55]	Degrees
β	[5, 12]	Degrees
γ	[-0.1, 0.1]	Degrees
α	[5, 16]	Degrees

Diffraction testing on the Brimrose AOTF showed that momentum-matching frequencies are around 145 MHz. These frequency values are significantly higher than those of the AA opto-electronics AOTF or the AOTF used for verification at UPHF. Therefore, according to the theory, it is expected that the Brimrose AOTF operates at higher angles of θ_c and α , resulting in correspondingly high upper search bounds for these parameters. Additionally, from the experiment, the undiffracted angles were significantly greater, than those of the AA opto-electronics AOTF. Indicating that the β angle should also be higher for the Brimrose AOTF, leading to a high upper bound value of twelve degrees. Finally, γ angle is expected to be minimal, judging by Figure 8.1, so a minimal bound was set for this parameter.

8.3 Evaluation of the optimisation results

After specifying the objective function and the bounds for the L-BFGS algorithm, the optimisation was run multiple times with varying initial guesses, to avoid the algorithm being stuck in one local minima, as was explained by Figure 8.7. The results of the optimisation algorithm have converged each time to the optimised parameters given in Table 8.3. The results did match the initial expectations that the angles θ_c , α , and β would be higher in comparison to the AA opto-electronics AOTF.

Table 8.3: Brimrose AOTF Optimised Parameters

Parameter	Optimised values [degrees]
θ_c	25.92°
α	11.97°
β	7.20°
γ	-0.10°

The optimised values were then reapplied in the analytical model, and the resulting predictions (in green) were plotted alongside the experimental data (in blue) for comparison. The frequency tuning plot, shown in Figure 8.8, demonstrates a close match between the two sets of results. Notably, for the Brimrose AOTF, the frequency remains relatively stable with increasing rotational angle, unlike for the AA opto-electronics AOTF. This stability is probably related to a θ_c value, where the rate at which birefringence changes is lower (Figure 4.14). In other words, the distance between the refractive ellipses changes slower at a higher value of θ_c .

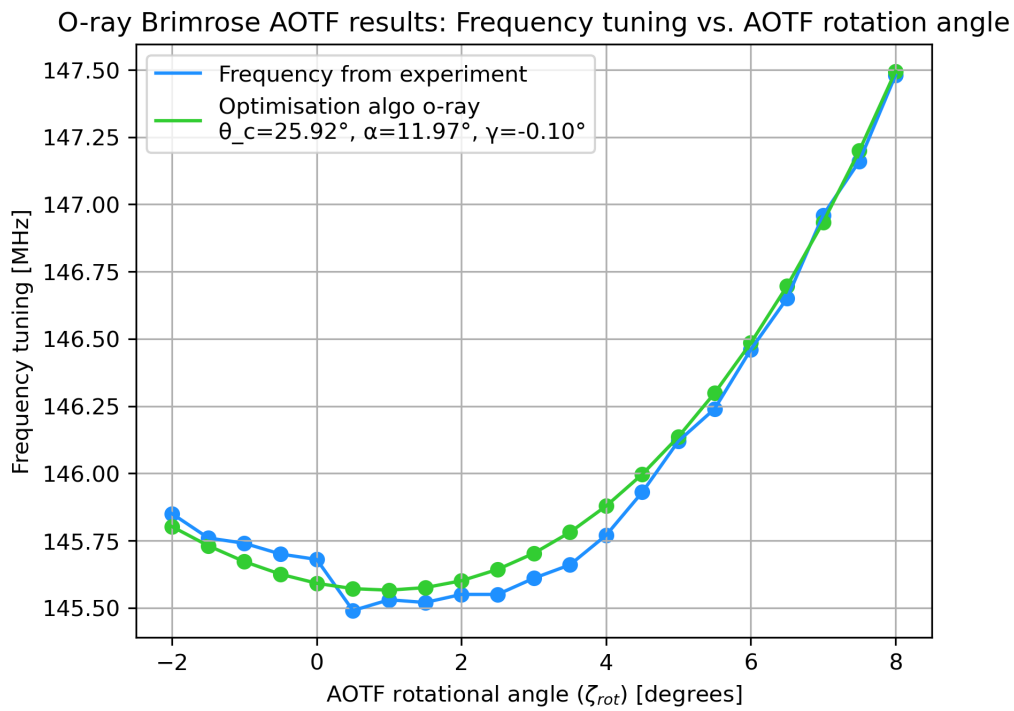
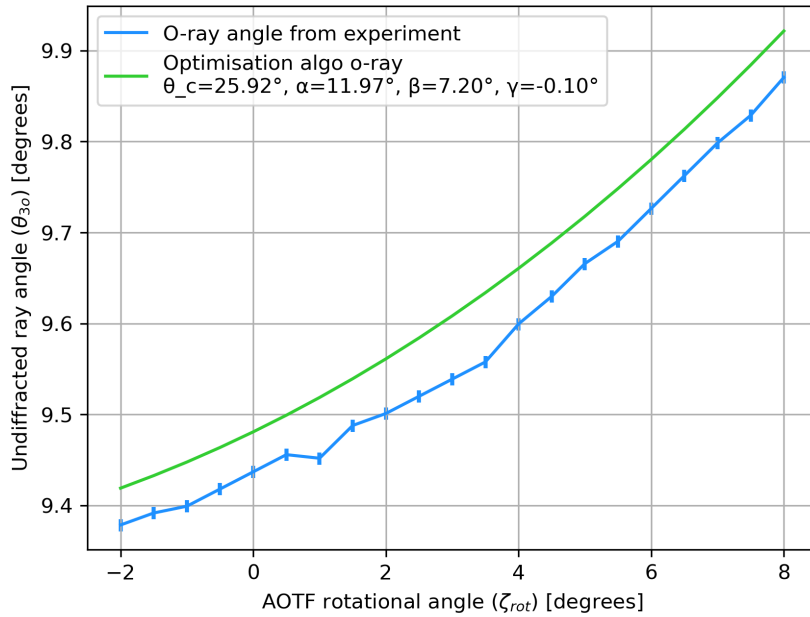


Figure 8.8: Momentum-matching frequencies as a function of AOTF rotational angle for the o-ray diffraction test on the Brimrose AOTF.

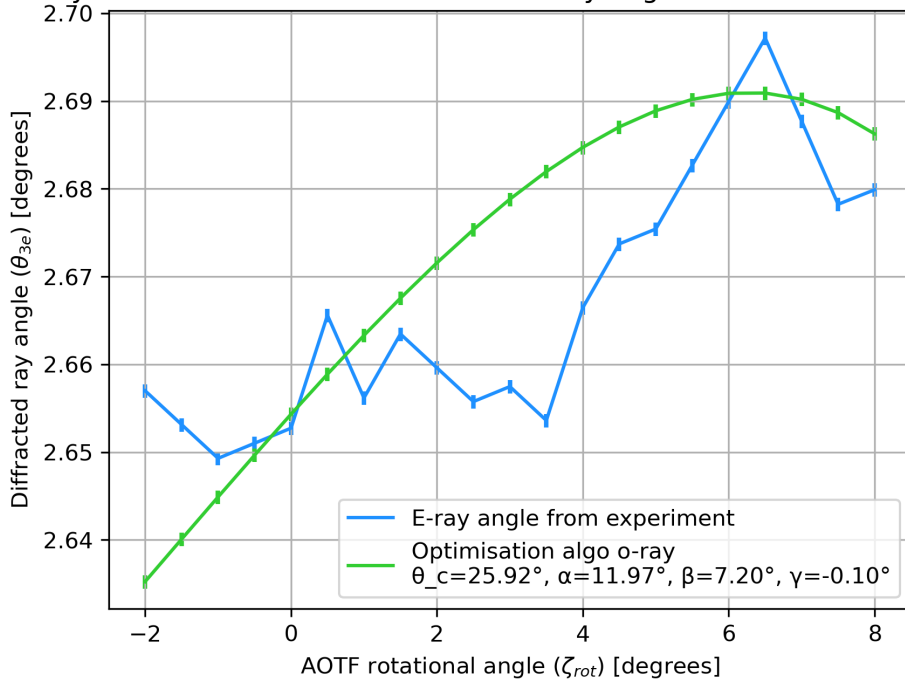
The undiffracted and diffracted angle results are analysed together, as the graphs affect each other. For the undiffracted rays (Figure 8.9), where β significantly impacts the results, the optimisation algorithm slightly overestimates the experimental curve. This adjustment is made to reduce discrepancies between the optimised and experimental curves for the diffracted rays (Figure 8.10).

Interestingly, the diffracted ray angles remain exceptionally stable for this AOTF, ranging between 2.65° and 2.70° . This consistency is advantageous for the optical design, making it straightforward to predict the diffracted ray's propagation and place the CCD accurately. However, this stability also creates a confrontation for the optimisation algorithm. When the algorithm lowers the simulated undiffracted angle values by reducing β , it simultaneously shifts the diffracted angle values downward, which penalizes the algorithm if β is further reduced.

O-ray Brimrose AOTF results: Undiffracted (ordinary) ray angle vs. AOTF rotation angle

Figure 8.9: Undiffracted ray angles (θ_{3o}) as a function of AOTF rotational angle for the o-ray diffraction test on the Brimrose AOTF.

O-ray Brimrose AOTF results: Diffracted ray angle vs. AOTF rotation angle

Figure 8.10: Diffracted ray angles (θ_{3e}) as a function of AOTF rotational angle for the o-ray diffraction test on the Brimrose AOTF.

Overall, the optimisation algorithm has yielded strong results, with all simulation curves closely matching the experimental data. More importantly, the simulation trend lines follow the same shape as the experimental curves. One way to potentially improve the simulation is by reducing the penalty for momentum-matching frequency errors. As observed during verification with the UPHF experimental data in Chapter 5, the simulation results showed only minor discrepancies in the momentum-matching frequency graph, with errors being around ± 0.75 MHz for the P.Gass model.

This frequency mismatch may stem from various factors, such as slight value deviations in the crystal's material properties, like acoustic velocities or refractive indices, from those used in the analytical model. By reducing

penalties on the frequency curve, the algorithm might better align with the diffracted and undiffracted angle curves, although it may slightly compromise performance on the momentum-matching frequency graph.

Alternatively, the algorithm could be refined by including additional variables, such as the material's acoustic velocities (V_{001} and V_{110}) or incorporating Fresnel's model with rotatory power ρ as an additional search variable. These modifications would increase the computational time due to the added search variables but could improve the Brimrose AOTF characterisation. The improved optimisation search could then be used for future AOTF characterisations.

8.4 Conclusion on optimisation

From this chapter, it has been demonstrated that the developed analytical model can characterise an AOTF with unknown θ_c , α , γ , and β parameters. To automate the search for these parameters, the model has been adapted together with an optimisation algorithm, yielding optimal values for the AOTF angles to describe its behaviour. These results satisfy the answer to sub-question 5 from Chapter 3, along with the characterisation requirements summarised in Table 8.4.

Table 8.4: characterisation Requirements and Achievements

Requirement ID	Requirement Goal	Achievement
[CHAR-REQ-001]	Develop a method to characterise an AOTF in terms of θ_c and α .	Frequency-matching in diffraction testing effectively determined θ_c and α angles.
[CHAR-REQ-002]	Automate the AOTF angles characterisation.	L-BFGS optimised model selects variables to match diffraction data, automating the AOTF characterisation.
Sub-Question 5	Can the model characterise a commercial AOTF?	The model accurately characterises an AOTF for θ_c , α , γ , and β angles.

The AOTF characterisation process began with creating preliminary schematics based on AOTF's appearance and diffraction behaviour. From these observations, the transducer's positioning, crystal geometry outline, and the orientation of the [001] and [110] crystallographic axes were identified.

Afterwards, the L-BFGS optimisation algorithm was chosen for its efficiency with multiple variables, computational time efficiency, and its improved ability to locate global minima compared to simpler optimisation algorithms. The algorithm's implementation in Python, facilitated by SciPy, enabled a smooth adaptation between the analytical model and the algorithm. To provide a purpose for the optimisation algorithm, an objective function was set up to minimize discrepancies between the simulation and experimental diffraction test results. Finally, the search bounds were established for the AOTF variables θ_c , α , β , and γ , within which the algorithm was allowed to vary these variables.

The optimised results for these four variables produced curves closely aligned with the experimental results, meeting the characterisation requirements. The characterisation results could be further improved by either reducing a penalty in the objective function for finding a frequency matching curve or including more variables into the optimisation algorithm, such as acoustical velocities or the rotatory power. While the latter recommendation would increase the algorithm's computational time, it could provide an even more accurate AOTF characterisation.

Conclusion 9

Throughout the report, the analytical model simulating the Acousto-Optic Tunable Filter (AOTF) behaviour was developed, validated, and placed into use to characterise commercially available AOTF to answer the following research question:

“How can the performance of the non-collinear Acousto-Optic Tunable Filter (AOTF) based on tellurium dioxide (TeO_2) be accurately simulated, be physically validated, and be effectively characterised?”

To concretise, the main research question has been broken down into six sub-questions. Sub-questions 1–3 address model development, while sub-questions 4–6 focus on the model validation and the AOTF characterisation.

Sub-Questions:

1. Which AOTF parameters are essential for building the analytical model for AOTF optical simulation?
2. How is the propagation through the crystal of the diffracted and undiffracted rays simulated in the analytical model?
3. How can the Acousto-Optic interaction be simulated to provide the RF signal needed for momentum-matching?
4. What test methodology would validate the outputs of the AOTF analytical model for the specific optical wavelength?
5. Can the model characterise a commercially bought AOTF in terms of crystallographic and facet geometrical angles?
6. Does diffraction efficiency stay the same for all incidence angles under momentum-matching, and if not, what factors influence it?

The decision to focus on a non-collinear AOTF configuration based on TeO_2 arose from its wide acceptance angle range and the material’s favourable acousto-optic properties, making this AOTF type the industry’s preferred option [3]. Such a specific configuration choice allows to focus on the identification of essential AOTF parameters for the analytical model building.

Addressing the **sub-question 1**, information regarding the refractive indices of TeO_2 was firstly gathered. The material was found to have a uniaxial birefringence, causing it to refract the incident light differently based on whether the light is ordinarily (o) or extraordinarily (e) polarized. These refractive indices varied with optical wavelength and followed the relationship provided by Polyanskiy’s database [24]. To account for the varying effective refractive index of e-polarized light (n'_e), the P.Gass model was applied, with the value depending on the ray’s propagation angle relative to the material’s fast axis ([001] crystallographic axis) [26].

For the model, the crystallographic axis angle θ_c , defined as the angle between the [001] axis and the optical axis, was crucial. This angle, set during the AOTF’s crystal manufacturing, influences the propagation of extraordinary polarized rays and the Acousto-Optic (AO) interaction. Additionally, the tilt angle (α) affects the acoustic wave propagation within the crystal and the frequency magnitude required for peak diffraction efficiency. The inclination angles of the AOTF’s entrance (γ) and exit (β) facets influence the refraction of both undiffracted and diffracted rays as they exit the AOTF.

After identifying key AOTF parameters, **the sub-questions 2 and 3** were addressed by developing a Python-based analytical model that divides the AOTF into three key surfaces: the entrance facet, the acoustic field,

and the exit facet. The Directional Cosine Matrices (DCMs) were applied to simulate light paths as rays enter, propagate through, and exit the AOTF's crystal in 3D space. Refraction of both ordinary and extraordinary rays was modelled at the entrance and exit facets, while AO interactions were calculated at the acoustic field surface. At the acoustic field, the incident ray was represented as a wave vector and projected alongside refractive ellipses in 3D space. To meet the momentum-matching condition and achieve optimal diffraction efficiency (DE), the acoustic wave vector (\mathbf{k}_a) was calculated to bridge the gap between these refractive ellipses. The magnitude of \mathbf{k}_a provided the required RF signal for momentum-matching, and its endpoint determined the propagation direction of the diffracted wave vector.

The model was then further adapted to accommodate both incident polarisation types, allowing rotation of the AOTF within the optical design, and incorporating simulations for the crystal's optical activity. These additional adaptations enabled the model to be verified and validated for the key output parameters, including the separation angles between diffracted and undiffracted rays and the RF signal necessary for the momentum-matching condition.

Initial model verification showed that the model's outputs aligned precisely with the results from the Voloshinov et al. paper. Further verification, conducted in Chapter 5, with support from Prof. Samuel Dupont at UPHF, demonstrated that the model could predict separation angles with an accuracy of up to 0.03° and the momentum-matching frequency with an accuracy of up to 0.75 MHz when applying the P. Gass model. The refractive index models including the optical activity need to be further studied in future works.

To address **sub-questions 4 and 6**, validation involved physical testing of the AA opto-electronics AOTF, involving the power and diffraction tests. For **sub-question 6**, power testing revealed that DE is not constant across all incident angles but instead varies with dependence on the Voltage Standing Wave Ratio (VSWR) curve, which depends on the transducer's design. This finding emphasizes the importance of ensuring that the momentum-matching frequency for the desired optical wavelengths for diffraction falls within the region of the lowest VSWR values when designing the AOTF for a specific spectral range.

The diffraction testing validated the model's predictions for various incident angles and provided a reliable method to characterize the AOTF's crystallographic angles, partially addressing **sub-question 5**. The results showed that the frequency-matching method accurately determined θ_c and α values, which, when applied in the model, enabled predictions of diffracted and undiffracted angles within 0.1° of experimental values. Additionally, this testing validated the model overall (**answering sub-question 4**), as the model's trend lines closely matched experimental data for both incident polarizations, confirming the effectiveness of adaptations such as rotational angle adjustments and AO interaction simulation for both ordinary and extraordinary rays.

Finally, for the **sub-question 5**, the model has shown the capability to characterize commercially acquired AOTFs in Chapter 8. This characterization was automated by integrating the model with an L-BFGS optimization algorithm, which minimizes the error between the model's outputs and experimental diffraction test data across three graphs: the momentum-matching frequency curve, and the diffracted and undiffracted angle curves. By adjusting θ_c , α , β , and γ , the algorithm was able to identify the optimal parameters (presented in Table 9.1) for a newly acquired Brimrose AOTF. With this characterization, those characterised values can be inserted into the model once again, enabling an accurate AOTF simulation for all optical wavelengths in the visible spectrum.

Table 9.1: Brimrose AOTF Optimised Parameters

Parameter	Optimised values [degrees]
θ_c	25.92°
α	11.97°
β	7.20°
γ	-0.10°

The summary above demonstrates that the analytical model for simulating AOTF behaviour has been successfully developed, validated, and can be used to characterise newly acquired AOTFs, thereby answering the main research question. This optical model bridges the gap between acquiring an AOTF and integrating it into an optical design. Setting a major stepping stone of a versatile optical model, the applicability of which can be further extended, and its validation process further improved, as discussed in the following chapter.

Recommendations and Future Works

10

The recommendations provided in this chapter focus on improving both the analytical model and the experimental testing procedures for the AOTF. The analytical model-based recommendations (Section 10.1) aim to improve the model's understanding and to provide the adaptations that can enhance the model's versatility to be applicable for more AOTF designs. Meanwhile, the test-related recommendations (Section 10.2), suggest adjustments to the experimental setups to enhance the reliability of future tests and data analysis of the analytical model.

10.1 Analytical model based recommendations

Given that the analytical model is central to this report, it is important to provide recommendations for enhancing its capabilities and facilitating its integration into other AOTF applications.

10.1.1 Change in coordinate system

The model's complexity stems from the multiple stages and substages involved, requiring a reference source during its development. Unfortunately, the initial reference material from Zhao et al. used a left-handed coordinate system, which is unconventional in engineering. This left-handed framework was recognized late in the model-development process, leading to an initial understanding of the model's behaviour based on that system. After understanding the model's work, adding adaptations, and performing validation, transitioning to a right-handed coordinate system could have improved clarity and alignment with engineering conventions. However, with limited time, priority was placed on validating the model rather than reworking its coordinate system. Adapting the model to a right-handed system remains a recommendation for future work to ensure better consistency with engineering standards.

10.1.2 Multiple transducers AOTF designs

While performing the literature study, there were some AOTF designs which employed multiple transducer designs [46], which increases the interaction length in the crystal and in turn should improve the AOTF's spectral bandwidth [7]. This model has been developed for AOTF's with a single transducer design. The difficulty with introducing multiple transducer designs into the model relates to the fact that each transducer's positioning may have a different angle α . Furthermore, for each of these transducers a new model stage will need to be added to simulate the AO interaction, further complicating the model. However, to improve the model's versatility, such adaptation may be beneficial in particular AOTF designs.

10.1.3 Model adaptation for other AOTF types and materials

The analytical model in this report has primarily focused on the visible spectrum and the non-collinear AOTF design with a TeO_2 as an AO material. Knowing that AOTFs using TeO_2 for near infra-red (NIR) region do exist [3, 7], this AOTF model can be easily adapted for such case scenario, by employing n_e and n_o relations for the NIR spectrum, instead of currently used relations for the visible spectrum between 400-1100nm.

The same adaptation can be implemented for the AOTFs which use other uniaxial birefringent crystals such as lithium niobate (LiNbO_3), Calcium molybdate (CaMoO_4), and KDP (KH_2PO_4) [4]. However, the user should be mindful of the crystal's fast axis location, the axis of minimal refractive index, and what are the intricacies of an AO interaction with the use of these particular crystals.

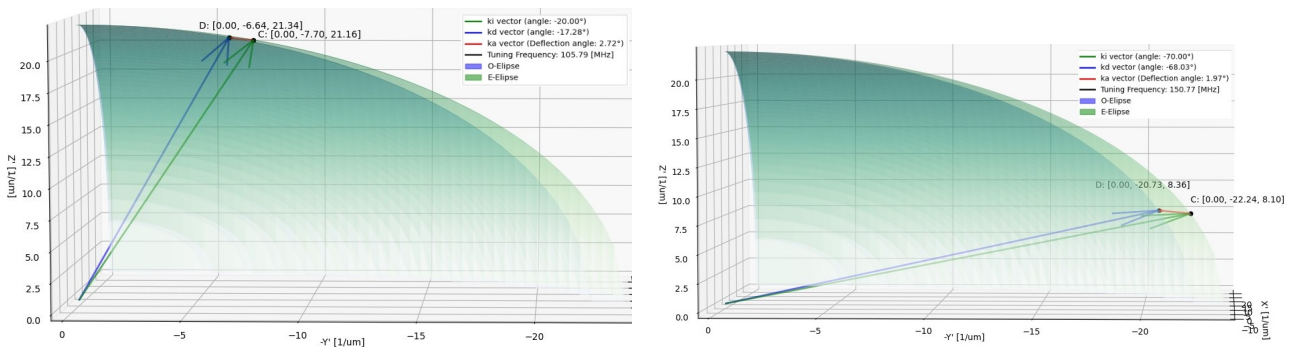
The model adaptation can go even further and be implemented for other materials, such as biaxial materials, or even other AOTF types, such as collinear or quasi-collinear. This adaptation, however, needs a different

procedure at stage two of the model, where the AO interaction is simulated. Furthermore, for biaxial crystals, a different relation will need to be found for calculating the effective refractive indices for ordinary and extraordinary polarization.

These adaptations can be a part of future work, further developing the model for AOTF types and extending the model's versatility. However, proper validation is also required while developing the model for other AOTF types and AO materials.

10.1.4 Far-off axis simulation attempt

This subsection goes a bit off-topic from the research, but some findings were found interesting to share. The far-off axis (FOA) simulation concerns the high angles of incidence AO interaction [51]. Where the incident angle θ_i is larger than 45 degrees, making the interaction closer to the [110] axis rather than [001], along which the refractive indices are equal ($n_e = n_o$). This type of AO interaction could potentially improve the AOTF's spectral bandwidth characteristics, but may reduce the diffraction efficiency.



(a) Close to optical axis AO interaction for $\theta_i = 20^\circ$

(b) Far-off axis AO interaction for $\theta_i = 70^\circ$

Figure 10.1: Comparison of on-axis and off-axis AO interaction in the AOTF with $\alpha = 10^\circ$, $\zeta_{rot} = 0^\circ$

The simulation result has produced the high ultrasound frequency required for the far-off axis interaction, due to the increased length of the acoustic wave vector. This can be noted from the Figure 4.20, where the distance between the two ellipses is larger when the angle θ_c is close to 90° compared to the close axis case. Interestingly, however, the diffraction angle within the crystal is smaller in FOA ($\Delta\theta_d = 1.97^\circ$) compared to the close to optical axis regime ($\Delta\theta_d = 2.72^\circ$). This can be seen from Figure 10.1, where the incident and the diffracted rays are closer together in the FOA regime, compared to close to optical axis interaction.

The idea of using the FOA interaction was quickly discarded in the simulation. Not only the high acoustic frequency of 150 MHz did not produce any AO interaction in the AOTF tested, but it also meant that the crystallographic axis system used in the simulation (Figure 4.4), would need to be inverted, which goes against the currently known theory on the AOTF. Moreover, to justify such an interaction, the incidence ray would need to propagate as shown in example (b) of Figure 10.2, which was not the way AOTFs interact in this research.

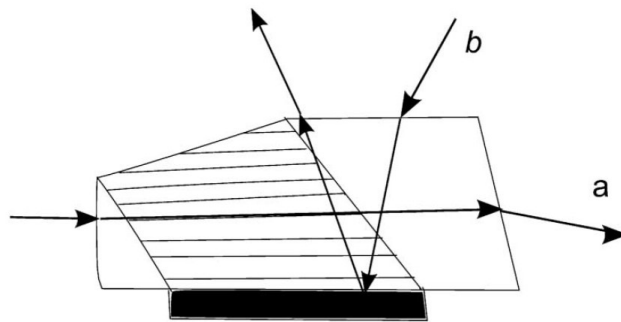


Figure 10.2: Example of (a) Close to the optical axis AO interaction and (b) Far-off axis AO interaction [51].

However, this simulation experiment did go in line with the other research on the FOA performed by Voloshinov and Yukhnevich in 2013 [51]. The frequency of the ultrasound was also higher in FOA, whereas the diffraction within the crystal was smaller in the FOA, for the same cut-off angles α used [51].

What is surprising is that performing the AO interaction at FOA produced a low bandwidth ($\Delta\lambda$) after the diffraction for low birefringent materials, where $\Delta n \ll n_o$ [51]. Low bandwidth means high output resolution of the diffracted ray, which can later produce high-resolution images if spectroscopy is applied. This phenomenon can be observed from Equation 10.1 [51], where in the FOA regime high θ_i values are used, making the denominator values higher and the numerator values lower, resulting in a low spectral bandwidth ($\Delta\lambda$) value.

$$\Delta\lambda = 0.8\lambda^2 \frac{\cos \theta_i}{\Delta n l_1 \sin^2(\theta_i + \alpha)} (1 + \tan \theta_i \tan \psi) \quad (10.1)$$

There is a downside of using AOTFs in the FOA regime, which is the diffraction efficiency. As mentioned, in Section 2.1, the figure of merit (M2) is an important parameter which improves the efficiency of diffraction inside the AO material. The high value of M2 was the reason to use the TeO₂ crystal for the AOTF designs. However, the M2 reduces significantly at high angles of incidence due to the reduction of the effective photoelastic coefficient, which is dependent on the angle of incidence [51].

This implies that the diffracted beam's intensity in FOA regime is substantially lower than in the traditional AOTF designs [51]. This would explain why the FOA based AOTF designs have not been widely adopted or researched. However, for the designs where high-resolution output is desired, and the diffraction efficiency is not a major drawback, the FOA designs can compete with the collinear AOTF designs. For those purposes, it is recommended to validate the model specifically for AOTFs operating in the FOA regime.

10.2 Test related recommendations

The testing and analysis of the AOTF revealed several areas where both the experimental setup and the analytical approach could be improved to achieve more accurate and reliable results. These recommendations are divided into two categories: test-related recommendations (Subsection 10.2.1), focusing on optimizing the physical experimental setup, and test analysis recommendations (Subsection 10.2.2), addressing improvements in the analytical methods and model validation.

10.2.1 Test setup recommendations

The diffraction testing results, as discussed in Section 7.3, were satisfactory, though several improvements could enhance the reliability of future tests. One clear recommendation is to increase the distance between the AOTF and the measuring ruler. While the discrepancies caused by the AOTF's rotation were largely corrected through the calculation adjustments proposed in Section 6.4, a greater distance would further minimize these discrepancies, as the magnitude of the correction would be lower. However, the test should still be implemented in the dark setting so that it is still possible to record the beam intensities without additional light sources and configure the momentum-matching frequency.

An alternative approach would involve creating an optical setup where the diffracted and undiffracted angles are determined based on detector recordings. This method would eliminate uncertainties associated with manually measuring displacements on the ruler. The challenge with this setup, however, is the need for a detector with a large enough active area to precisely capture both diffracted and undiffracted rays, which can be expensive, as photodetector prices increase significantly with size [74]. To mitigate costs, a well-designed optical system would be necessary. However, this would introduce additional time and computational complexity due to the need for angle calculations based on detector data. For this reason, a simpler, more direct testing method was chosen for this report, even though it could be refined for greater accuracy.

Further improvements could include using a sturdier platform for the AOTF during rotation. A straightforward solution would be to utilize a custom 3D-printed platform that securely holds the AOTF and enables precise rotational adjustments. Additionally, to minimize human error when reading angles and manually adjusting the platform, automation could be introduced using an automated rotational stage, as demonstrated in [61]. However, such automation would come with increased costs.

10.2.2 Test analysis recommendations

About the AOTF test analysis, one large limitation was that there was no AOTF with known angles of θ_c and α , which were crucial for the analytical model. This has created difficulties in validating the model. It would

have been beneficial to have more data with the AOTF with known θ_c and α parameters and test it at various rotational angles and with different incident polarization types to verify the model's work.

Such data would have provided a clearer answer on the impact of the optical activity on AOTF's performance, and allow validating the Fresnel's model further. Which has the potential to provide results with even higher accuracy, than the validated model based on the P.Gass model of refractive indices. With such a validation, it would have also been possible to determine the rotatory power of a particular AOTF, with the help of the model. This would give more insight into the topic of the rotatory effect in TeO_2 , as currently, this AOTF parameter is difficult to calculate due to the material's high birefringence [36], and therefore there is a limitation of literature available on this topic.

Based on the frequency curves for the Bragg condition obtained through the diffraction testing, Section 7.2, it was found that the θ_c angle is lower for the incident ordinary polarised rays in comparison to the incident extraordinary rays. This finding is also supported by literature, where the momentum-matching frequency for the incident o-rays was lower than for e-rays [26, 64]. It would be beneficial, to know the physical reasoning why such phenomenon is happening and whether this is the case for all the produced AOTFs. Otherwise, it may result in a faulty AOTF design where the tuning frequency for a desired wavelength may lay in the frequency region with high VSWR.

Regarding VSWR curves, the power testing analysis in Section 7.1 demonstrated a direct correlation between the AOTF's DE and its VSWR curve. To further explore this, another power test using a 550 nm optical wavelength would be beneficial. Comparing the DE values from this test with those from the 635 nm test could confirm whether lower optical wavelengths lead to higher DE, as the model predicts that the momentum-matching frequency for 550 nm should correspond to the lowest VSWR value. Based on Figure 6.1, the frequency of the lowest VSWR is 111.50 MHz. Unfortunately, this test could not be conducted earlier due to the late discovery of this finding, but it would be an intriguing aspect to validate in future research.

Applying any or all of the above recommendations to the analytical model would enhance its versatility and extend the model's applicability to new spectral domains. Additionally, the suggested testing improvements could lead to more accurate and robust validation of the model's performance under different conditions. Implementing these changes would ultimately strengthen the overall reliability of the AOTF simulations and contribute to the advancement of future research in this area.

References

- [1] S. Nag, T. Hewagama, G. Georgiev, B. Pasquale, S. Aslam, and C. Gatebe, “Multispectral snapshot imagers onboard small satellite formations for multi-angular remote sensing,” *IEEE Sensors Journal*, vol. 17, pp. 5252–5268, Aug. 2017. DOI: 10.1109/JSEN.2017.2717384.
- [2] L. Brillouin, “Diffusion de la lumière et des rayons x par un corps transparent homogène: Influence de l’agitation thermique,” *Annales de Physique*, vol. 9, no. 17, pp. 88–122, 1922, Published online: 28 April 2017. DOI: 10.1051/anphys/192209170088.
- [3] S. Valle, “Acousto-optic resonant cavity tunable filters in the uv and mir: Tellurium dioxide, calomel, crystal quartz,” Funded by the Engineering and Physical Sciences Research Council (EPSRC), EngD Thesis, University of Glasgow, College of Science and Engineering, School of Engineering, 2017. DOI: 10.5525/gla.thesis.8323. [Online]. Available: <https://theses.gla.ac.uk/id/eprint/8323>.
- [4] A. Goutzoulis and D. Pape, *Design and Fabrication of Acousto-Optic Devices*. New York-Basel-Hong Kong: Marcel Dekker Inc., 1994.
- [5] E. Dekemper *et al.*, “ALTIUS: A spaceborne AOTF-based UV-VIS-NIR hyperspectral imager for atmospheric remote sensing,” en, R. Meynart, S. P. Neeck, and H. Shimoda, Eds., Amsterdam, Netherlands, Oct. 2014, p. 92410L. DOI: 10.1117/12.2063937. [Online]. Available: <http://proceedings.spiedigitallibrary.org/proceeding.aspx?doi=10.1117/12.2063937> (visited on 12/27/2023).
- [6] S. Valle, J. Ward, C. Pannell, and N. Johnson, “Imaging AOTFs with Low RF Power in Deep-UV and Mid-IR,” *Physics Procedia*, Proceedings of the 2015 ICU International Congress on Ultrasonics, Metz, France, vol. 70, pp. 707–711, Jan. 2015, ISSN: 1875-3892. DOI: 10.1016/j.phpro.2015.08.096. [Online]. Available: <https://www.sciencedirect.com/science/article/pii/S1875389215008378> (visited on 01/08/2024).
- [7] L. Bei, “Acousto-optic tunable filters: Fundamentals and applications as applied to chemical analysis techniques,” en, *Progress in Quantum Electronics*, vol. 28, no. 2, pp. 67–87, 2004, ISSN: 00796727. DOI: 10.1016/S0079-6727(03)00083-1. [Online]. Available: <https://linkinghub.elsevier.com/retrieve/pii/S0079672703000831> (visited on 02/08/2024).
- [8] J. Vanhamel, E. Dekemper, S. Berkenbosch, and R. Clairquin, “Novel acousto-optical tunable filter (AOTF) based spectropolarimeter for the characterization of auroral emission,” en, *Instrumentation Science & Technology*, vol. 49, no. 3, pp. 245–257, May 2021, ISSN: 1073-9149, 1525-6030. DOI: 10.1080/10739149.2020.1814809. [Online]. Available: <https://www.tandfonline.com/doi/full/10.1080/10739149.2020.1814809> (visited on 12/27/2023).
- [9] K. R. Spring, T. J. Fellers, and M. W. Davidson, *Acousto-optic tunable filters*, Company: Olympus. [Online]. Available: <https://www.olympus-lifescience.com/en/microscope-resource/primer/java/filters/aotf/> (visited on 01/09/2024).
- [10] E. Dekemper, J. Vanhamel, B. Van Opstal, and D. Fussen, “The aotf-based no₂ camera,” *Atmospheric Measurement Techniques*, vol. 9, no. 12, pp. 6025–6034, 2016. DOI: 10.5194/amt-9-6025-2016. [Online]. Available: <https://amt.copernicus.org/articles/9/6025/2016/>.
- [11] N. Gupta and R. Dahmani, “Aotf spectrometer for water pollutant monitoring,” in *Proceedings of the 19th Annual International Conference of the IEEE Engineering in Medicine and Biology Society. 'Magnificent Milestones and Emerging Opportunities in Medical Engineering' (Cat. No.97CH36136)*, vol. 2, 1997, 751–752 vol.2. DOI: 10.1109/IEMBS.1997.757745.
- [12] D. Selva and D. Krejci, “A survey and assessment of the capabilities of cubesats for earth observation,” *Acta Astronautica*, vol. 74, pp. 50–68, 2012, ISSN: 0094-5765. DOI: <https://doi.org/10.1016/j.actaastro.2011.12.014>. [Online]. Available: <https://www.sciencedirect.com/science/article/pii/S0094576511003742>.

- [13] J. Vanhamel, E. Dekemper, V. B. Voloshinov, E. Neefs, and D. Fussen, “Electrical bandwidth testing of an AOTF transducer as a function of the optical diffraction efficiency,” en, *Journal of the Optical Society of America A*, vol. 36, no. 8, p. 1361, Aug. 2019, ISSN: 1084-7529, 1520-8532. DOI: 10.1364/JOSAA.36.001361. [Online]. Available: <https://opg.optica.org/abstract.cfm?URI=josaa-36-8-1361> (visited on 12/27/2023).
- [14] N. Gupta and V. Voloshinov, “Hyperspectral imaging performance of a teo2 acousto-optic tunable filter in the ultraviolet region,” *Opt. Lett.*, vol. 30, no. 9, pp. 985–987, May 2005. DOI: 10.1364/OL.30.000985. [Online]. Available: <https://opg.optica.org/ol/abstract.cfm?URI=ol-30-9-985>.
- [15] J. Xu and R. Stroud, *Acousto-Optic Devices: Principles, Design and Applications* (Wiley Series in Pure and Applied Optics). Wiley, 1992.
- [16] R. Oldenbourg, “Chapter 15 - polarization microscopy,” in *Biomedical Optical Phase Microscopy and Nanoscopy*, N. T. Shaked, Z. Zalevsky, and L. L. Satterwhite, Eds., Oxford: Academic Press, 2013, pp. 311–338, ISBN: 978-0-12-415871-9. DOI: <https://doi.org/10.1016/B978-0-12-415871-9.00015-6>. [Online]. Available: <https://www.sciencedirect.com/science/article/pii/B9780124158719000156>.
- [17] E. G. Ehlers, *Optical Mineralogy: Theory and Technique*. Palo Alto: Blackwell Scientific Publications, 1987, vol. 1, p. 28, ISBN: 0-86542-323-7.
- [18] E. Hecht, *Optics*, eng, 5 ed/fifth edition, global edition. Boston Columbus Indianapolis New York San Francisco Amsterdam Cape Town Dubai London Madrid Milan Munich: Pearson, 2017, ISBN: 978-1-292-09693-3.
- [19] P. Piron, *Polarization measurement*, Lecture slides, Spaceborne Instrumentation Section, TU Delft, Mar. 2023.
- [20] C. Kittel, *Introduction to Solid State Physics*, 8th ed. Hoboken, NJ: Wiley, 2005.
- [21] P. Patnaik, *Handbook of Inorganic Chemicals*. McGraw-Hill, 2002, ISBN: 0-07-049439-8.
- [22] L. E. Murr, *Handbook of materials structures, properties, processing and performance*. New York: Springer, 2015, ISBN: 978-3-319-01814-7.
- [23] N. Uchida, “Optical properties of single-crystal paratellurite (teo₂),” *Phys. Rev. B*, vol. 4, Nov. 1971. DOI: 10.1103/PhysRevB.4.3736.
- [24] M. N. Polyanskiy, “Refractiveindex.info database of optical constants,” *Scientific Data*, vol. 11, no. 1, p. 94, Jan. 2024, ISSN: 2052-4463. DOI: 10.1038/s41597-023-02898-2. [Online]. Available: <https://doi.org/10.1038/s41597-023-02898-2>.
- [25] E. Dekemper *et al.*, “Tunable acousto-optic spectral imager for atmospheric composition measurements in the visible spectral domain,” *Appl. Opt.*, vol. 51, no. 25, pp. 6259–6267, Sep. 2012. DOI: 10.1364/AO.51.006259. [Online]. Available: <https://opg.optica.org/ao/abstract.cfm?URI=ao-51-25-6259>.
- [26] P. A. Gass and J. R. Sambles, “Accurate design of a noncollinear acousto-optic tunable filter,” *Opt. Lett.*, vol. 16, no. 6, pp. 429–431, Mar. 1991. DOI: 10.1364/OL.16.000429. [Online]. Available: <https://opg.optica.org/ol/abstract.cfm?URI=ol-16-6-429>.
- [27] I. C. Chang, “Noncollinear acousto-optic filter with large angular aperture,” *Applied Physics Letters*, vol. 25, no. 7, pp. 370–372, Oct. 1974, ISSN: 0003-6951. DOI: 10.1063/1.1655512. [Online]. Available: <https://doi.org/10.1063/1.1655512> (visited on 09/26/2024).
- [28] S. N. Mantsevich, M. I. Kupreychik, and V. I. Balakshy, “Possibilities of wide-angle tellurium dioxide acousto-optic cell application for the optical frequency comb generation,” *Opt. Express*, vol. 28, no. 9, pp. 13 243–13 259, Apr. 2020. DOI: 10.1364/OE.391732. [Online]. Available: <https://opg.optica.org/oe/abstract.cfm?URI=oe-28-9-13243>.
- [29] M. Corporation, *Teo2 (110) 10x10x0.5mm, 1sp - teoe101005s1*, <https://www.mtixtl.com/TeO2-110-10x10x05mm-1sp.aspx>, Accessed: September 29, 2024.
- [30] H. Zhang, H. Zhao, Q. Guo, and Y. Xuan, “Calibration of acousto-optic interaction geometry based on the analysis of aotf angular performance,” *Materials*, vol. 16, no. 10, 2023, ISSN: 1996-1944. DOI: 10.3390/ma16103708. [Online]. Available: <https://www.mdpi.com/1996-1944/16/10/3708>.

- [31] V. Balakshy and S. Mantsevich, "Polarization effects at collinear acousto-optic interaction," en, *Optics & Laser Technology*, vol. 44, no. 4, pp. 893–898, Jun. 2011, ISSN: 00303992. DOI: 10.1016/j.optlastec.2011.11.012. [Online]. Available: <https://linkinghub.elsevier.com/retrieve/pii/S0030399211003483> (visited on 02/29/2024).
- [32] V. I. Balakshy, G. Gondek, T. Katkowski, I. V. Krylov, P. Kwiek, and A. Sliwinski, "Polarization effects at acousto-optic interaction in anisotropic medium," *Proceedings of SPIE*, vol. 2643, pp. 98–107, 1995.
- [33] O. Mys, M. Kostyrko, O. Krupych, and R. Vlokh, "Anisotropy of acoustooptic figure of merit for teo2 crystals. 1. isotropic diffraction," *Ukrainian Journal of Physical Optics*, vol. 16, Mar. 2015. DOI: 10.3116/16091833/16/1/38/2015.
- [34] R. W. Collins and A. S. Ferlauto, "2 - optical physics of materials," in *Handbook of Ellipsometry*, H. G. Tompkins and E. A. Irene, Eds., Norwich, NY: William Andrew Publishing, 2005, pp. 93–235, ISBN: 978-0-8155-1499-2. DOI: <https://doi.org/10.1016/B978-081551499-2.50004-6>. [Online]. Available: <https://www.sciencedirect.com/science/article/pii/B9780815514992500046>.
- [35] Kaidor, *Schematic of a polarimeter showing the principles behind its operation*, [https://commons.wikimedia.org/wiki/File:Polarimeter_\(Optical_rotation\).svg](https://commons.wikimedia.org/wiki/File:Polarimeter_(Optical_rotation).svg), Accessed: 2024-08-18, 2013.
- [36] P. Maák, L. Jakab, A. Barócsi, and P. Richter, "Improved design method for acousto-optic light deflectors," *Optics Communications*, vol. 172, no. 1, pp. 297–324, 1999, ISSN: 0030-4018. DOI: [https://doi.org/10.1016/S0030-4018\(99\)00459-9](https://doi.org/10.1016/S0030-4018(99)00459-9). [Online]. Available: <https://www.sciencedirect.com/science/article/pii/S0030401899004599>.
- [37] V. B. Voloshinov, V. S. Khorkin, L. A. Kulakova, and N. Gupta, "Optic, acoustic and acousto-optic properties of tellurium in close-to-axis regime of diffraction," *Journal of Physics Communications*, vol. 1, no. 2, p. 025 006, Sep. 2017. DOI: 10.1088/2399-6528/aa86ba. [Online]. Available: <https://dx.doi.org/10.1088/2399-6528/aa86ba>.
- [38] A. Yariv and P. Yeh, *Optical Waves in Crystals*. New York: Wiley, 1984.
- [39] Saleh, B.E.A., and M. Teich, "Polarization and crystal optics," in *Fundamentals of Photonics*. John Wiley Sons, Ltd, 1991, ch. 6, pp. 193–237, ISBN: 9780471213741. DOI: <https://doi.org/10.1002/0471213748.ch6>. eprint: <https://onlinelibrary.wiley.com/doi/pdf/10.1002/0471213748.ch6>. [Online]. Available: <https://onlinelibrary.wiley.com/doi/abs/10.1002/0471213748.ch6>.
- [40] M. Karppinen, "Net atomic charges, electric moments, and sign and magnitude of optical rotatory power in -teo2 at 296 k," *Journal of Applied Crystallography*, vol. 53, pp. 1252–1256, Sep. 2020. DOI: 10.1107/S1600576720010791.
- [41] K. McCarthy, A. Goutzoulis, M. Gottlieb, and N. Singh, "Optical rotatory power in crystals of the mercurous halides and tellurium dioxide," *Optics Communications*, vol. 64, no. 2, pp. 157–159, 1987, ISSN: 0030-4018. DOI: [https://doi.org/10.1016/0030-4018\(87\)90043-5](https://doi.org/10.1016/0030-4018(87)90043-5). [Online]. Available: <https://www.sciencedirect.com/science/article/pii/0030401887900435>.
- [42] J. Vanhamel and D. Stutman, "The design of a flexible RF generator for driving Acousto-Optical devices in space applications," en, *Journal of Physics: Conference Series*, vol. 2526, no. 1, p. 012 120, Jun. 2023, ISSN: 1742-6588, 1742-6596. DOI: 10.1088/1742-6596/2526/1/012120. [Online]. Available: <https://iopscience.iop.org/article/10.1088/1742-6596/2526/1/012120> (visited on 12/27/2023).
- [43] Texas Instruments, "Oa-11: A tutorial on applying op amps to rf applications," Texas Instruments, Tech. Rep. SNOA390B, Apr. 2013, Originally published in September 1993, revised in April 2013. [Online]. Available: <https://www.ti.com/lit/an/snoa390b/snoa390b.pdf>.
- [44] R. Rebelo *et al.*, "3d biosensors in advanced medical diagnostics of high mortality diseases," *Biosensors and Bioelectronics*, vol. 130, pp. 20–39, 2019, ISSN: 0956-5663. DOI: <https://doi.org/10.1016/j.bios.2018.12.057>. [Online]. Available: <https://www.sciencedirect.com/science/article/pii/S0956566319300259>.
- [45] V. T. Rathod, "A review of acoustic impedance matching techniques for piezoelectric sensors and transducers," *Sensors*, vol. 20, no. 14, p. 4051, 2020. DOI: 10.3390/s20144051. [Online]. Available: <https://doi.org/10.3390/s20144051>.

- [46] J. Vanhamel, S. Dupont, J.-C. Kastelik, and E. Dekemper, “Design of a radio frequency compensation system, using the electrical characterisation of a multi-transducer acousto-optical tunable filter,” English, in *Proceedings of the 10th Convention of the European Acoustics Association Forum Acusticum 2023*, A. Astolfi, F. Asdrudali, and L. Shtrepi, Eds., ser. Proceedings of Forum Acusticum 2023, Green Open Access added to TU Delft Institutional Repository ‘You share, we take care!’ – Taverne project <https://www.openaccess.nl/en/you-share-we-take-care> Otherwise as indicated in the copyright section: the publisher is the copyright holder of this work and the author uses the Dutch legislation to make this work public. ; Forum Acusticum 2023: 10th Convention of the European Acoustics Association ; Conference date: 11-09-2023 Through 15-09-2023, Jan. 2024, pp. 6355–6360, ISBN: 978-88-88942-67-4. DOI: 10.61782/fa.2023.0379.
- [47] H. Zhao, C. Li, and Y. Zhang, “Three-surface model for the ray tracing of an imaging acousto-optic tunable filter,” *Appl. Opt.*, vol. 53, no. 32, pp. 7684–7690, Nov. 2014. DOI: 10.1364/AO.53.007684. [Online]. Available: <https://opg.optica.org/ao/abstract.cfm?URI=ao-53-32-7684>.
- [48] S. McKnight and C. Zahopoulos, “Rotation matrices,” in *Scientific Foundations of Engineering*. Cambridge University Press, 2015, pp. 57–72.
- [49] A. Patel, A. Papadimitriou, and A. Banerjee, “Chapter 3 - modeling for arws,” in *Aerial Robotic Workers*, G. Nikolakopoulos, S. Sharif Mansouri, and C. Kanellakis, Eds., Butterworth-Heinemann, 2023, pp. 31–47, ISBN: 978-0-12-814909-6. DOI: <https://doi.org/10.1016/B978-0-12-814909-6.00009-3>. [Online]. Available: <https://www.sciencedirect.com/science/article/pii/B9780128149096000093>.
- [50] Zemax, *How to work in global coordinates in a sequential optical system*, <https://support.zemax.com/hc/en-us/articles/1500005487781-How-to-work-in-global-coordinates-in-a-sequential-optical-system>, Accessed: October 4, 2024, 2021.
- [51] V. B. Voloshinov and T. V. Yukhnevich, “Two regimes of wide angle acousto-optic interaction in tellurium dioxide single crystals,” *Appl. Opt.*, vol. 52, no. 24, pp. 5912–5919, Aug. 2013. DOI: 10.1364/AO.52.005912. [Online]. Available: <https://opg.optica.org/ao/abstract.cfm?URI=ao-52-24-5912>.
- [52] P. Wang and Z. Zhang, “Effect of direction of incident light on the basic performance of a teo2 acousto-optic tunable filter,” *Appl. Opt.*, vol. 55, no. 22, pp. 5860–5867, Aug. 2016. DOI: 10.1364/AO.55.005860. [Online]. Available: <https://opg.optica.org/ao/abstract.cfm?URI=ao-55-22-5860>.
- [53] V. B. Voloshinov, K. B. Yushkov, and B. B. J. Linde, “Improvement in performance of a TeO₂ acousto-optic imaging spectrometer,” in *Journal of Optics A: Pure and Applied Optics*, vol. 9, no. 4, pp. 341–347, Apr. 2007, ISSN: 1464-4258, 1741-3567. DOI: 10.1088/1464-4258/9/4/006. [Online]. Available: <https://iopscience.iop.org/article/10.1088/1464-4258/9/4/006> (visited on 02/05/2024).
- [54] C. S. Gardner and G. Papen, “22 - optical communications,” in *Reference Data for Engineers (Ninth Edition)*, W. M. Middleton and M. E. Van Valkenburg, Eds., Ninth Edition, Woburn: Newnes, 2002, pp. 22-1-22–28, ISBN: 978-0-7506-7291-7. DOI: <https://doi.org/10.1016/B978-075067291-7/50024-8>. [Online]. Available: <https://www.sciencedirect.com/science/article/pii/B9780750672917500248>.
- [55] J. B. Almeida, “General method for the determination of matrix coefficients for high-order optical system modeling,” *Journal of the Optical Society of America A*, vol. 16, no. 3, p. 596, Mar. 1999, ISSN: 1520-8532. DOI: 10.1364/josaa.16.000596. [Online]. Available: <http://dx.doi.org/10.1364/JOSAA.16.000596>.
- [56] H. Zhao, C. Cheng, Q. Guo, K. Yu, and Y. Yang, “Angular-spectral characteristics of acousto-optic tunable filters based on mercurous halide crystals,” *Materials*, vol. 17, no. 5, 2024, ISSN: 1996-1944. DOI: 10.3390/ma17050967. [Online]. Available: <https://www.mdpi.com/1996-1944/17/5/967>.
- [57] C. U. Keller, *Lecture 5: Polarization*, https://home.strw.leidenuniv.nl/~keller/Teaching/ATI_2018/ATI_2018_L05_Polarization.pdf, Astronomical Telescopes and Instruments (ATI), Leiden University, 2018.
- [58] V. Batshev, A. V. Gorevoy, V. E. Pozhar, and A. S. Machikhin, “Aberration analysis of aotf-based stereoscopic spectral imager using optical design software,” *Journal of Physics: Conference Series*, vol. 2127, no. 1, p. 012035, Nov. 2021. DOI: 10.1088/1742-6596/2127/1/012035. [Online]. Available: <https://dx.doi.org/10.1088/1742-6596/2127/1/012035>.

- [59] Brimrose Corporation, *Acousto-optic tunable filters (aotf) - free space ao*, Accessed: 2024-10-08, 2024. [Online]. Available: <https://www.brimrose.com/free-space-ao/acousto-optic-tunable-filters>.
- [60] J. Vila-Francés *et al.*, “Configurable bandwidth imaging spectrometer based on acousto-optic tunable filter,” *Review of Scientific Instruments*, vol. 77, Jul. 2006. DOI: 10.1117/12.620640.
- [61] H. Zhao, Z. Ji, G. Jia, Y. Zhang, Y. Li, and D. Wang, “Mwir thermal imaging spectrometer based on the acousto-optic tunable filter,” *Appl. Opt.*, vol. 56, no. 25, pp. 7269–7276, Sep. 2017. DOI: 10.1364/AO.56.007269. [Online]. Available: <https://opg.optica.org/ao/abstract.cfm?URI=ao-56-25-7269>.
- [62] P. Zhou, H. Zhao, Y. Zhang, and C. Li, “Accurate optical design of an acousto-optic tunable filter imaging spectrometer,” in *2012 IEEE International Conference on Imaging Systems and Techniques Proceedings*, 2012, pp. 249–253. DOI: 10.1109/IST.2012.6295512.
- [63] D. Brown, *Tracker video analysis and modeling tool*, Version 6.0.11, 2024. [Online]. Available: <https://physlets.org/tracker/>.
- [64] H. Zhang, H. Zhao, Q. Guo, D. Xu, and W. Teng, “Polarization-multiplexed high-throughput aotf-based spectral imaging system,” *Materials (Basel)*, vol. 16, no. 12, p. 4243, Jun. 2023. DOI: 10.3390/ma16124243.
- [65] Thorlabs, Inc., *Compact laser diode modules*, https://www.thorlabs.com/newgrouppage9.cfm?objectgroup_id=1219, Accessed: 2024-07-02, n.d.
- [66] H. Kim, *Laser polarization: The importance of polarization in laser applications*, <https://www.edmundoptics.com/knowledge-center/application-notes/lasers/the-importance-of-polarization-in-laser-applications/>, Accessed: 2024-08-05.
- [67] Y. Mizuno, N. Motoishi, K. Noda, H. Lee, and K. Nakamura, “Effect of laser temperature control on brillouin optical correlation-domain reflectometry,” *Applied Physics Express*, vol. 13, no. 5, p. 052001, Apr. 2020. DOI: 10.35848/1882-0786/ab827b. [Online]. Available: <https://dx.doi.org/10.35848/1882-0786/ab827b>.
- [68] S. Nakagawa, P. C. D. Johnson, and H. Schielzeth, “The coefficient of determination r^2 and intra-class correlation coefficient from generalized linear mixed-effects models revisited and expanded,” *Journal of the Royal Society Interface*, vol. 14, 2016. [Online]. Available: <https://api.semanticscholar.org/CorpusID:13031504>.
- [69] “4 - strengthening of metal alloys,” in *Introduction to Aerospace Materials*, A. P. Mouritz, Ed., Woodhead Publishing, 2012, pp. 57–90, ISBN: 978-1-85573-946-8. DOI: <https://doi.org/10.1533/9780857095152.57>. [Online]. Available: <https://www.sciencedirect.com/science/article/pii/B9781855739468500042>.
- [70] T. O. Hodson, “Root-mean-square error (rmse) or mean absolute error (mae): When to use them or not,” *Geoscientific Model Development*, 2022. [Online]. Available: <https://api.semanticscholar.org/CorpusID:247518253>.
- [71] K. Kumar, D. Ghosh, A. Upadhayay, J. Yao, X. Zhao, and A. Upadhyay, “Quasi-newton methods for multiobjective optimization problems: A systematic review,” *Applied Set-Valued Analysis and Optimization*, vol. 5, pp. 291–321, Aug. 2023. DOI: 10.23952/asvao.5.2023.2.12.
- [72] T. V. Mikosch, S. I. Resnick, and S. M. Robinson, *Springer Series in Operations Research and Financial Engineering* (Springer Series in Operations Research and Financial Engineering). New York, NY: Springer Science+Business Media, LLC, 2006, p. i, ISBN: 978-0387-30303-1.
- [73] L. Noël and M. Langelaar, *Engineering optimization: Concepts and applications*, Lecture ME46060, 3mE-PME 34-G-1-300, 2023. [Online].
- [74] T. Zhai, L. Li, X. Wang, X. Fang, Y. Bando, and D. Golberg, “Recent developments in one-dimensional inorganic nanostructures for photodetectors,” *Advanced Functional Materials*, vol. 20, no. 24, pp. 4233–4248, 2010. DOI: <https://doi.org/10.1002/adfm.201001259>. eprint: <https://onlinelibrary.wiley.com/doi/pdf/10.1002/adfm.201001259>. [Online]. Available: <https://onlinelibrary.wiley.com/doi/abs/10.1002/adfm.201001259>.

Derivation of refractive index with gyration tensor (G)



The goal of this appendix is to derive the refractive index, which changes with the incidence angle in the crystallographic axis system of the AOTF and includes the impact of the gyration tensor (G). The derived refractive indices are applicable for extraordinary (n_{e3}) and ordinary ellipses (n_{o3}).

Refractive indices of the previous definition by P.Gass have 1 in the subscript [26]

$$n_{o1} = n_o$$

$$n_{e1}(\theta) = \frac{1}{\sqrt{\frac{\cos^2(\theta)}{n_o^2} + \frac{\sin^2(\theta)}{n_e^2}}}$$

Definition of the refractive

$$(n_i^2 - n_{o1}^2)(n_i^2 - n_{e1}^2(\theta)) = G^2$$

$$n_i^4 - n_i^2 n_{e1}^2(\theta) - n_{o1}^2 n_i^2 + n_{o1}^2 n_{e1}^2(\theta) = G^2$$

For simplification introducing the variable x to perform a quadratic equation.

$$x = n_i^2$$

$$x^2 - (n_{e1}^2(\theta) + n_{o1}^2)x + n_{o1}^2 n_{e1}^2(\theta) - G^2 = 0$$

$$x = n_i^2 = \frac{(n_{e1}^2(\theta) + n_{o1}^2) \pm \sqrt{(n_{e1}^2(\theta) + n_{o1}^2)^2 - 4 \cdot 1 \cdot (n_{o1}^2 n_{e1}^2(\theta) - G^2)}}{2}$$

After finding the quadratic equation, values for both ordinary and extraordinary ellipse can be found.

$$n_{o3}(\theta) = \left(\frac{(n_{e1}^2(\theta) + n_{o1}^2) - \sqrt{(n_{e1}^2(\theta) + n_{o1}^2)^2 - 4(n_{o1}^2 n_{e1}^2(\theta) - G^2)}}{2} \right)^{1/2}$$

$$n_{e3}(\theta) = \left(\frac{(n_{e1}^2(\theta) + n_{o1}^2) + \sqrt{(n_{e1}^2(\theta) + n_{o1}^2)^2 - 4(n_{o1}^2 n_{e1}^2(\theta) - G^2)}}{2} \right)^{1/2}$$

If the ray is propagating along the optical axis [001], then the refractive index with the gyration tensor is the same as in the Voloshinov's method.

$$\text{If } \theta = 0^\circ \Rightarrow n_{o3} = n_{o2} \quad n_{e3} = n_{e2}$$

If the ray is propagating along [110] axis, then the refractive index with the gyration tensor is the same as in the normal ellipse method.

$$\text{If } \theta = 90^\circ \Rightarrow n_{o3} = n_{o1} \quad n_{e3} = n_{e1}$$

Diffraction testing raw data

B

This data was used for the diffraction test with AA opto-electronics AOTF and used for model's validation. In this data, the "recording" means the ray's position on the measuring ruler, and "displacement" is the distance between the optical axis (Y_0) position and the "recording" value.

B.1 Incident e-ray diffraction test

In this case, the e-ray stands for undiffracted ray recordings, and o-ray for diffracted ray recordings. The values from Table B.1 were used for "recordings" and "displacement" calculations as described in Chapter 6.

Table B.1: Reference parameters for the AA opto-electronics for the incidence e-ray diffraction testing

Parameter	Value [mm]
Distance to deviation ruler (L)	1012
Optical axis position (Y_0)	323.5
AOTF midpoint (L_{AOTF})	15.45

Table B.2: Diffraction Test — incident e-ray raw data

Recorded Angle [deg]	Rotation Angle [deg]	RF Freq. [MHz]	o-ray Recording [mm]	e-ray Recording [mm]	Displacement o-ray [mm]	Displacement e-ray [mm]	o-ray Angle [deg]	e-ray Angle [deg]
-3.58	-2.50	92.1	107.8	194.9	215.03	127.93	12.36	7.28
-3.08	-2.00	92.2	107.5	195.0	215.46	127.96	12.39	7.28
-2.58	-1.50	92.7	107.2	195.0	215.90	128.10	12.41	7.29
-2.08	-1.00	93.1	107.0	195.3	216.23	127.93	12.43	7.28
-1.58	-0.50	93.1	106.3	195.3	217.07	128.07	12.48	7.29
-1.08	0.00	93.4	105.8	195.3	217.70	128.20	12.52	7.30
-0.58	0.50	93.7	105.3	195.2	218.33	128.43	12.56	7.31
-0.08	1.00	93.9	104.8	195.1	218.97	128.67	12.59	7.32
0.42	1.50	94.4	104.1	195.0	219.80	128.90	12.64	7.34
0.92	2.00	95.0	102.9	194.7	221.14	129.34	12.72	7.36
1.42	2.50	95.8	102.1	194.6	222.07	129.57	12.78	7.38
1.92	3.00	96.1	101.5	194.5	222.81	129.81	12.82	7.39
2.42	3.50	97.2	100.1	194.4	224.34	130.04	12.91	7.40
2.92	4.00	97.8	98.9	194.4	225.68	130.18	12.99	7.41
3.42	4.50	98.7	97.5	194.3	227.21	130.41	13.08	7.42
3.92	5.00	100.2	95.5	194.2	229.35	130.65	13.21	7.44
4.42	5.50	101.9	93.2	194.0	231.78	130.98	13.36	7.46
4.92	6.00	102.9	91.5	193.8	233.61	131.31	13.47	7.48
5.42	6.50	104.8	89.2	193.5	236.05	131.75	13.61	7.50
5.92	7.00	107.2	85.8	193.2	239.58	132.18	13.82	7.53
6.42	7.50	109.4	82.8	193.0	242.72	132.52	14.01	7.55

B.2 Incident o-ray diffraction test

In this case, the o-ray stands for undiffracted ray recordings, and e-ray for diffracted ray recordings.

Table B.3: Reference parameters for the AA opto-electronics for the incidence o-ray diffraction testing

Parameter	Value [mm]
Distance to deviation ruler (L)	1036
Optical axis position (Y_0)	321.8
AOTF midpoint (L_{AOTF})	15.45

Table B.4: Diffraction Test — incident o-ray raw data

Recorded Angle [deg]	Rotation Angle [deg]	RF Freq. [MHz]	o-ray Recording [mm]	e-ray Recording [mm]	Displacement o-ray [mm]	Displacement e-ray [mm]	o-ray Angle [deg]	e-ray Angle [deg]	Angle Difference [deg]
-0.67	-3.00	92.02	192.3	278.0	128.69	42.99	7.15	2.38	4.78
-0.17	-2.50	91.98	192.0	278.0	129.13	43.13	7.18	2.39	4.79
0.33	-2.00	91.93	192.3	278.0	128.96	43.26	7.17	2.39	4.78
0.83	-1.50	91.92	192.3	278.3	129.10	43.10	7.18	2.38	4.79
1.33	-1.00	91.92	192.1	278.5	129.43	43.03	7.20	2.38	4.81
1.83	-0.50	91.91	192.1	278.5	129.57	43.17	7.20	2.39	4.81
2.33	0.00	91.98	192.0	278.5	129.80	43.30	7.22	2.40	4.82
2.83	0.50	92.06	191.9	278.5	130.03	43.43	7.23	2.40	4.83
3.33	1.00	92.19	191.6	279.0	130.47	43.07	7.25	2.38	4.87
3.83	1.50	92.37	191.4	279.2	130.80	43.00	7.27	2.38	4.89
4.33	2.00	92.59	191.0	279.3	131.34	43.04	7.30	2.38	4.92
4.83	2.50	92.73	190.8	279.5	131.67	42.97	7.32	2.38	4.94
5.33	3.00	93.11	190.7	280.0	131.91	42.61	7.33	2.36	4.98
5.83	3.50	93.50	190.5	280.4	132.24	42.34	7.35	2.34	5.01
6.33	4.00	93.81	190.3	280.6	132.58	42.28	7.37	2.34	5.03
6.83	4.50	94.39	190.0	281.0	133.01	42.01	7.40	2.32	5.07
7.33	5.00	94.77	189.8	281.3	133.35	41.85	7.42	2.32	5.10
7.83	5.50	95.16	189.4	282.0	133.88	41.28	7.45	2.28	5.16
8.33	6.00	95.78	189.1	282.5	134.31	40.91	7.47	2.26	5.21
8.83	6.50	96.74	188.9	283.4	134.65	40.15	7.49	2.22	5.27
9.33	7.00	97.28	188.7	284.0	134.98	39.68	7.51	2.20	5.31
9.83	7.50	97.53	189.0	284.3	134.82	39.52	7.50	2.19	5.31

Power testing raw data



This appendix shows the results of all power tests performed, where only the optical lab test results made it to the final data analysis.

C.1 Power tests - bright setting

Results from this test were not further used, as they had light-based noise in the readings.

These tests were performed in the bright room. The reading on the rotational stage was -2.66667 degrees when the AOTF was perpendicularly aligned with the incoming optical ray. The Table C.1 was performed as scanning for potential Bragg angle, and Table C.2 involves the results of the fine-tuning where the Bragg angle was found.

Angle Reading [deg]	Rotation Angle [deg]	RF Freq. [MHz]	O-ray Power [μ W]	E-ray Power [μ W]	Total Power [μ W]	Power % Diffracted [-]
-2.67	0.00	94.00	7.46	18.5	26.0	28.737
-1.67	1.00	95.12	7.86	18.1	26.0	30.277
-0.67	2.00	96.40	8.13	17.7	25.8	31.475
-0.17	2.50	97.37	8.32	17.5	25.8	32.223
0.33	3.00	98.45	8.48	17.2	25.7	33.022
0.83	3.50	99.21	8.67	17.1	25.7	33.463
1.33	4.00	100.85	9.13	16.9	26.0	35.075
1.83	4.50	102.56	9.15	16.8	25.9	35.260
2.33	5.00	104.49	9.01	16.9	25.9	34.774

Table C.1: Power Testing Results - Part 1

Angle Reading [deg]	Rotation Angle [deg]	RF Freq. [MHz]	O-ray Power [μ W]	E-ray Power [μ W]	Total Power [μ W]	Power % Diffracted [-]
1.50	4.17	101.55	9.13	16.9	26.0	35.074
1.67	4.33	102.00	9.14	16.8	25.9	35.235
1.75	4.42	102.36	8.93	16.5	25.4	35.116
2.00	4.67	102.85	8.77	16.1	24.9	35.263

Table C.2: Power Testing Results - Part 2

C.2 Power tests - Dark room setting

Tests were performed in the dark room, but the testing conditions were not optimal. The base for the optical setup was prone to movement during the test inducing the inclinations. The Table C.3 provides the coarse results and Table C.4 provides fine search results. The fine search was performed after the coarse search and the total power of the AOTF output rays was lower than at the start of the experiment.

The reason why this data was not included in the data analysis, is that potential ray inclinations were created during the testing. This can be seen by looking at the rotation angle of 3 degrees in both tables. The RF signal is higher in the fine search, suggesting that the laser itself or the optical path has produced an additional inclination causing an increase in the incidence ray.

Angle Reading [deg]	Rotation Angle [deg]	RF Freq. [MHz]	O-ray Power [μ W]	E-ray Power [μ W]	Total Power [μ W]	Power % Diffracted [-]
-7.42	0.00	94.41	15.53	45.5	61.03	25.447
-6.42	1.00	95.54	16.47	44.8	61.27	26.881
-5.42	2.00	97.23	17.20	43.8	61.00	28.197
-4.42	3.00	99.19	17.60	42.6	60.20	29.236
-3.42	4.00	101.82	17.60	41.6	59.20	29.730
-2.42	5.00	105.91	16.09	41.6	57.69	27.890
-1.42	6.00	111.52	15.09	39.8	54.89	27.491
-0.42	7.00	119.92	7.05	37.5	44.55	15.825

Table C.3: Power Testing Results in Dark Room - Coarse search

Angle Reading [deg]	Rotation Angle [deg]	RF Freq. [MHz]	O-ray Power [μ W]	E-ray Power [μ W]	Total Power [μ W]	Power % Diffracted [-]
-4.42	3.00	99.42	17.50	42.7	60.20	29.070
-4.67	2.75	98.81	17.00	43.4	60.40	28.146
-4.50	2.92	99.22	17.80	42.5	60.30	29.519
-4.33	3.08	99.86	17.70	42.3	60.00	29.500
-3.67	3.75	101.34	17.60	41.9	59.50	29.580
-3.50	3.92	101.92	17.50	41.7	59.20	29.561
-3.17	4.25	103.02	17.10	41.8	58.90	29.032
-4.08	3.33	100.30	17.60	42.2	59.80	29.431

Table C.4: Power Testing Results in Dark Room - Fine Search

C.3 Optical lab - horizontal polarization power test

These results were used since they were performed in the dark and controlled setting.

Table C.5: Optical Lab Testing incident e-ray - Coarse Power Testing

Angle Reading	Rot. Angle [deg]	RF Freq [MHz]	O-ray Power [μ W]	E-ray Power [μ W]	Total Power [μ W]	DE [%]
-0.33	0	93.48	4.54	12.19	16.73	27.14
0.67	1	94.25	4.76	12.07	16.83	28.28
1.67	2	95.40	5.00	11.86	16.86	29.66
2.67	3	96.96	5.29	11.59	16.88	31.34
3.67	4	99.06	5.60	11.32	16.92	33.10
4.67	5	101.35	5.72	11.12	16.84	33.97
5.67	6	105.13	5.00	10.20	15.20*	32.89

Table C.6: Optical Lab Testing incident e-ray - Fine Power Testing

Angle Reading	Rot. Angle [deg]	RF Freq [MHz]	O-ray Power [μ W]	E-ray Power [μ W]	Total Power [μ W]	DE [%]
4.92	5.25	102.07	5.75	11.14	16.89	34.04
4.67	5.00	101.39	5.73	11.11	16.84	34.03
4.75	5.08	101.59	5.73	11.11	16.84	34.03
4.92	5.25	102.06	5.68	11.02	16.70	34.01

C.4 Optical lab - vertical polarization power test

Vertical polarization means that the sent ray is ordinarily polarized for the AA opto-electronics AOTF. At the rotational angle of 1, AOTF had to be readjusted as it was noticed that the caliper was screwed out too far. The incident ray from the laser was partially blocked by the casing at the angle of 7 degrees, and even more at the angle of 8 degrees. Therefore, the last reading is the maximum rotational angle (6.33 degrees) where the casing does not block the incident ray.

Table C.7: Vertical Polarization Testing - Coarse Results

Angle Reading [deg]	Rot. Angle [deg]	RF Signal [MHz]	e-ray Power [μW]	o-ray Power [μW]	Total Power [μW]	Power % Diffracted
1.6666667	-1.00	91.98	2.43	8.31	10.74	22.62569832
2.66667	0	92.1	2.5	8.01	10.51	23.78686965
3.83333333	1.00*	92.36	2.72	8.07	10.79	25.20852641
4.833333	2.00	92.75	2.85	7.98	10.83	26.31578947
5.833333	3.00	93.34	2.95	7.88	10.83	27.23915051
6.833333	4.00	94.23	3.06	7.73	10.79	28.35959222
7.833333	5.00	95.27	3.17	7.63	10.8	29.35185185
8.8333333	6.00	96.53	3.28	7.55	10.83	30.28624192
9.83333333	7.00*	98.09	3.22	7.07	10.29	31.29251701
10.8333333	8.00**	100.3	2.42	4.84	7.26	33.33333333
9.166667	6.33	96.95	3.25	7.42	10.67	30.45923149

Samuel Verification results



D.1 Experimental Results

Table D.1: Experimental Results

lambda [nm]	Frequency [MHz]	y [cm]	y0 [cm]	Separation angle [deg]
532	69.48	16.9	32.5	3.28
593	60.9	17.4	32.5	3.18
671	52.44	17.8	32.6	3.11

D.2 Analytical Model Results E-ray

Table D.2: Simulation Results - e-ray

Wavelength [nm]	Frequency [MHz]	Theta_3o [deg]	Theta_3e [deg]	Separation angle [deg]
532	69.19	3.41	0.13	3.28
593	60.15	3.30	0.13	3.17
671	51.71	3.21	0.13	3.09

Table D.3: Simulation Results - e-ray gyration no adaptation (Uchida)

Wavelength [nm]	Frequency [MHz]	Theta_3o [deg]	Theta_3e [deg]	Separation angle [deg]
532	75.49	3.71	0.13	3.58
593	64.72	3.55	0.13	3.42
671	54.96	3.41	0.13	3.28

Table D.4: Simulation Results - e-ray gyration adaptation

Wavelength [nm]	Frequency [MHz]	Theta_3o [deg]	Theta_3e [deg]	Separation angle [deg]
532	69.54	3.42	0.13	3.29
593	60.41	3.32	0.13	3.19
671	51.90	3.23	0.12	3.11

Brimrose tests for AOTF characterisation



This data was used for AOTF characterisation with an optimisation algorithm. In this case the diffracted ray is e-ray and undiffracted the o-ray.

Table E.1: Reference parameters used for the Brimrose diffraction testing

Parameter	Value [mm]
Distance to deviation ruler (L)	1031
Optical axis position (Y_0)	49.7
AOTF midpoint (L_{AOTF})	15

Table E.2: Incident o-ray Brimrose Diffraction Testing

RF Freq. [MHz]	e-ray Pos. [mm]	o-ray Pos. [mm]	Displ. e-ray [mm]	Displ. o-ray [mm]	e-ray Ang. [deg]	o-ray Ang. [deg]	Angle Diff. [deg]
147.48	95.80	223.50	-48.19	-175.89	-2.68	-9.87	7.19
147.16	95.90	222.90	-48.16	-175.16	-2.68	-9.83	7.15
146.96	96.20	222.50	-48.33	-174.63	-2.69	-9.80	7.11
146.65	96.50	222.00	-48.50	-174.00	-2.70	-9.76	7.07
146.46	96.50	221.50	-48.37	-173.37	-2.69	-9.73	7.04
146.24	96.50	221.00	-48.24	-172.74	-2.68	-9.69	7.01
146.12	96.50	220.70	-48.11	-172.31	-2.68	-9.67	6.99
145.93	96.60	220.20	-48.08	-171.68	-2.67	-9.63	6.96
145.77	96.60	219.80	-47.95	-171.15	-2.67	-9.60	6.93
145.66	96.50	219.20	-47.72	-170.42	-2.65	-9.56	6.90
145.61	96.70	219.00	-47.79	-170.09	-2.66	-9.54	6.88
145.55	96.80	218.80	-47.75	-169.75	-2.66	-9.52	6.86
145.55	97.00	218.60	-47.82	-169.42	-2.66	-9.50	6.84
145.52	97.20	218.50	-47.89	-169.19	-2.66	-9.49	6.82
145.53	97.20	218.00	-47.76	-168.56	-2.66	-9.45	6.80
145.49	97.50	218.20	-47.93	-168.63	-2.67	-9.46	6.79
145.68	97.40	218.00	-47.70	-168.30	-2.65	-9.44	6.78
145.70	97.50	217.80	-47.67	-167.97	-2.65	-9.42	6.77
145.74	97.60	217.60	-47.64	-167.64	-2.65	-9.40	6.75
145.76	97.80	217.60	-47.71	-167.51	-2.65	-9.39	6.74
145.85	98.00	217.50	-47.78	-167.28	-2.66	-9.38	6.72